First principles studies of Si-C alloys

by
Richard Charles Andrew

Submitted in partial fulfilment of the requirements
for the degree
PhilosophiæDoctor (PhD)
in the Department of Physics
in the Faculty of Natural and Agricultural Sciences
University of Pretoria
Pretoria

Supervisor: Prof. Nithaya Chetty
Co-Supervisor: Prof. Max Braun

February 28, 2013

UNIVERSITEIT VAN PRETORIA
UNIVERSITY OF PRETORIA
YUNIBESITHI YA PRETORIA

UNIVERSITY OF PRETORIA

DECLARATION OF ORIGINALTY

This document must be signed and submitted with every essay, report, project, assignment, dissertation and/or thesis.

Full names of student: RICHARD CHARLES ANDREW

Student number: s22315340
Personel number: p2632217

Declaration

1. I understand what plagiarism is and am aware of the University's policy in this regard.
2. I declare that this thesis is my own original work. Where other people's work has been used (either from a printed source, Internet or any other source), this has been properly acknowledged and referenced in accordance with deparmental requirements.
3. I have not used work previously produced by another student or any other person to hand in as my own.
4. I have not allowed, and will not allow, anyone to copy my work with the intention of passing it off as his or her own.

SIGNATURE STUDENT:.....

DATE:.....

SUMMARY

This study involves the investigation of silicon-carbon systems using *ab initio* techniques. It was motivated by the search for off-50:50 alloys and a way to quantify the strengths of 2D silicon-carbon materials. The study also predicts some under-reported properties for three previously proposed hypothetical allotropes of carbon. Preferably stable off-50:50 structures are identified from a set of trial structures for silicon-rich and carbon-rich candidates and their conditions of stability and physical properties are identified. A two-dimensional equation of state is introduced and applied to analyze the relative strengths of various 2D silicon-carbon materials.

Of the possible off-50:50 alloy combinations and candidate structures considered, only the pyrite-FeS_2, glitter-SiC_2 and t-BC_2 structures for SiC_2 are elastically and dynamically stable. Analysis of the instability of Si_2C reveals that it seems likely that carbon rich alloys are more favorable to their silicon-rich counterparts due to the smaller size of the carbon atoms and the more compact carbon-carbon bonds which result in less distorted bonding that is less metallic.

The stiffness of the silicon dicarbide structures rank, in increasing order with 3C-SiC included for comparison, as glitter $\rightarrow$ pyrite $\rightarrow$ 3C-SiC $\rightarrow$ t-SiC_2. The moduli values for t-SiC_2 are very comparable to 3C-SiC since for both materials, all atoms are four-fold coordinated with t-SiC_2 having similar but slightly distorted, strong covalent tetrahedral bonding. The pyrite and glitter structures exhibit metallic character whereas t-SiC_2 is a semi-conductor.

Not only has this work demonstrated that, in principle, off-50:50 alloys of carbon and silicon are plausible, it has also provided information on how the strength and elastic properties of these materials are effected by increased

silicon content. This has filled in a significant lack of knowledge about these bulk systems.

For 2D systems, an equation of state is proposed that equates in-plane pressure with a change in surface area. It extracts the layer modulus as one of its fit parameters, which measures a material's resilience to hydrostatic stretching and predicts the material's intrinsic strength. Graphene is the most resilient to stretching with the highest intrinsic strength of all structures considered followed by SiC. Buckled Si is the least resilient with the lowest strength. An off-50:50 planar alloy, called silagraphene, differs elastically from SiC but has a comparable strength due to the similarity of their layer modulus.

The novel 2D equation of state presented here opens up new ways to study and compare the strength properties of mono or multi-layered 2D materials, especially how their resilience to isotropic stretching responds to in-plane pressure.

I would like to dedicate this thesis to my mother for all she has done, provided and put up with to help me to achieve this milestone in my life. And to my father for having faith in my abilities when I had none.

Acknowledgements

And I would like to acknowledge the National Institute of Theoretical Physics, Protea Holdings and the University of Pretoria for funding my work, my supervisors for their guidance and lastly, Michelle Van Den Heever for her unwavering support and friendship.

Contents

List of Figures

List of Tables

Acronyms

***β*-Sn** isostructural to beta-tin (white tin). 1, 3, 6–8, 51

Cmca space group #65 also a phase of silicon. 1, 51

LOA longitudinal optical and acoustic modes. 6

LO longitudinal optical mode. 11

LTO longitudinal and transverse optical modes. 6

TA transverse acoustic mode. 6

TO transverse optical mode. 6, 11

bcc body-centered cubic. 7, 8

cd cubic diamond. 1, 3, 7, 8, 51

fcc face-centered cubic. 1, 3, 7, 8, 44, 51, 52, 58, 89, 107

hcp hexagonal closed-packed. 1, 3, 7, 8, 51

sc simple cubic. 7–9

sh simple hexagonal. 1, 3, 7, 8, 51

2D two dimensional. 4, 5, 14, 48, 136–140, 144, 148, 149, 151, 153, 154, 157–159, 161–164

AE all-electron. 28, 29, 31–33, 45

ANNI axial next-nearest-neighbor Ising. 12

BC8 8-atom primitive cell with a 16-atom body-centered conventional cell. 1, 8, 9, 51, 55, 79

BZ Brillouin Zone. 27, 28, 46

CVD chemical vapor deposition. 13

DFT density functional theory. 13, 17, 19, 21, 22, 27, 42, 46, 48, 140

DOS density of states. 122

ELF electron localization function. 4, 52, 55, 57, 58, 104, 106, 110, 117, 118, 122, 124, 125, 127, 143

EOS equation of state. 4, 14, 40, 61, 66, 76–80, 83, 84, 95, 98, 99, 102, 103, 137–139, 144, 145, 147, 148, 151, 154, 157, 158, 161, 162

GGA generalized gradient approximation. 24, 25, 140, 141

GPT generalized pseudopotential method. 7

HF Hartree-Fock. 18, 23

KKR Korringa-Kohn-Rostoker. 25

KS Kohn-Sham. 22, 25–28, 30, 32, 33

LCAO linear combination of atomic orbitals. 143

LDA local density approximation. 13, 55, 140, 141, 143, 159

LMTO linear muffin-tin orbital. 7, 10

LSDA local spin-density approximation. 24, 43

MAO mean absolute offset: giving a measure of average absolute offset of a set of values from an ideal value. 55, 76, 80, 113, 117, 118, 122, 124, 125

MBE molecular beam epitaxy. 13

MD molecular dynamics. 13

PAW projector augmented wave. 30, 42, 46, 49, 140

SCF self-consistent field. 25, 26, 46, 48, 52, 110

XC exchange-correlation. 23, 31, 42, 88

1

Introduction

1.1 The search for stable Si-C alloy structures

Silicon and carbon are arguably the two elements that have been the main driving forces behind human development. Carbon is not only the basis for all biological life on this planet but, along with silicon, has also been central to the technological advancements of the last century.

Carbon has always been used as a traditional fuel source and was the driving force behind the industrial revolution of the 19^{th} century. It is known to exist in many different allotropes ranging from extremely soft graphite to extremely hard diamond with the two most commonly known forms being graphite and diamond. Each allotrope has its own unique properties and possible applications. In diamond form, carbon has found application as an abrasive due to its extreme hardness. In graphitic form, it has made possible many advancements in technological areas from military applications to sports equipment because of its use as a strong, heat resistant fiber to create flexible composite materials. In its recently researched forms of graphene, nanotubes and nano-strips, it promises to be a very important resource for future electronic technological advancements.

Silicon is the second most abundant element in the earth's crust comprising 27.7 % of all crustal rocks [1]; mostly in the form of SiO_2 silica. The different known allotropes of silicon are Si-I cubic diamond (cd), Si-II beta-tin (β-Sn), Si-III 8-atom body-centered (BC8), Si-V simple hexagonal (sh), Si-VI $Cmca$, Si-VII hexagonal closed-packed (hcp), and Si-X face-centred cubic (fcc) with Si-I being the stable form at ambient conditions

while the others are all high pressure phases. The use of diamond silicon as a substrate for semi-conductor devices has allowed for the integration of millions of circuit elements on a single chip and this has been the main driving force behind the transition from the largely industrial age to our new information age.

Silicon and carbon both occupy group IV on the periodic table and therefore share some chemical characteristics. Both elements have a valency of four and can form sp^3 covalent bonding with a coordination of four. For this reason, they both exist in the diamond structure although while this structure is the stable form for silicon at ambient conditions, it is a metastable form of carbon. Both elements, however, have some significant differences. Whereas silicon prefers sp^3 bonding under ambient conditions, carbon has the ability to form sp^2 and sp hybridized bonding. Carbon is the smaller atom with closely bound valence electrons whereas silicon is larger with loosely bound electrons. Because of this, tetrahedrally bonded carbon atoms in diamond have a bond length approximately $\frac{2}{3}$ of those in diamond silicon. Carbon is also more electronegative than silicon with the better ability to attract other electrons.

Despite these differences, they co-exist in the stable 50:50 Si-C alloy, silicon carbide, with its many stacking polytypes. This stability is mainly due to the fact that all atoms are tetrahedrally bonded to each other with all bonds being homogeneous Si-C bonds of the same length. The question remains, can silicon and carbon exist in other structured alloys besides 50:50 silicon carbide?

Experimental evidence shows that there is a low solubility of C in Si [2] and even though low concentrations of metastable C defects in Si have been created experimentally using molecular beam epitaxy [3,4] and chemical vapor deposition [5], off-50:50 alloys do not seem to readily exist. An extensive search of the literature shows a dearth of ordered, disordered, random, as well as amorphous and thin film structures for off-50:50 alloy concentrations.

Clearly, the reasons for this must center more on the differences between Si and C rather than their similarities. Since SiC under ambient conditions exhibits tetrahedral coordination, this suggests that in an alloyed configuration under ambient conditions, sp^3 bonding may also be preferred. Is it possible for off-50:50 alloys to be fabricated where the atoms maintain their tetrahedral coordination? The sizable difference in the bond lengths of these two elements in the diamond structure will make this difficult. As

mentioned, the stability of 50:50 SiC is largely due to the presence of single-length homogeneous Si-C bonds. The presence of Si-Si, C-C and Si-C bonds in any single system will result in strains which can, in principle, only be relieved in complex geometries.

It turns out that under conditions of high pressure, SiC transforms to the rock-salt (NaCl) structure, which gives the silicon and carbon atoms six-fold coordination with homogeneous Si-C bonds. Silicon also has high pressure phases which exhibit coordination greater than four. Under increasing pressure it transforms from *cd* (coordination 4) $\rightarrow$ β-*Sn* structure (coordination 6) $\rightarrow$ *sh* (coordination 8) $\rightarrow$ *hcp* (coordination 12) $\rightarrow$ *fcc* (coordination 12). Perhaps pressure would be a useful tool to search for off-50:50 alloys involving Si and C. Grumbach and Martin[6], in their theoretical work on high-pressure/high-temperature phases of C, discovered a dense liquid whose melting temperature decreased with pressure, which is a behavior that is very similar to that of Si and Ge at lower pressures. This liquid resembles the simple cubic structure with six-fold coordination, a structure similar to that of Si and Ge under pressure. This suggests that for off-50:50 alloys, simple high coordination ordered structures might form under conditions of high pressure with bonding that differs from simple sp^3.

1.2 Aims and objectives

1.2.1 Off-50:50 Si-C alloys

The first part of this study is motivated by the search for bulk off-50:50 alloys involving Si and C. A number of different structures and stoichiometries are considered involving these elements. The guiding principle in looking for candidate structures is to look for open structures with a strong covalent component to the bonding as well as those with high coordination that could be accessible under conditions of pressure. Model alloy structures from existing crystal structures as well as theoretically proposed structures from other *ab initio* calculations are considered as possible candidates.

For this study, four candidate structures are considered. The known perovskite structure of $CaTiO_3$ is considered because it could represent a range of possible off-50:50 alloys (SiC_4, Si_2C_3, Si_3C_2 and Si_4C), all with high coordination. The next three candidate structures represented the two alloy stoichiometries silicon dicarbide (SiC_2) and disilicon carbide (Si_2C). These open structures have the possibility of bonding between the atoms with a strong covalent component. They are the pyrite structure

based on FeS_2, a previously suggested tetragonal structure based on a hypothetical carbon allotrope called glitter [7] and another tetragonal structure based on a suggested hypothetical structure for diamond-like boron dicarbide [8].

The following are investigated in order to determine the stability of the various candidate structures:

- The coordination of the atoms which indicates the plausibility of the locations for each carbon and silicon atom
- The charge density and electron localization function (ELF) plots which show where charge is concentrated and where bonding electrons are likely to be localized. This is to give an indication of the amount of covalent, ionic or metallic bonding
- The electronic band structure which shows if there is any metallic character to the bonding
- The distances between atoms which also give an indication of bonding type
- The eigenvalues for the elastic stiffness matrix and the elastic moduli which test for elastic stability
- The phonon dispersion which tests for dynamic instability

From these determinants, a set of plausible structures may be deduced and the conditions for their existence and stability investigated.

1.2.2 Two dimensional Si, C and Si-C alloys

The second part of this study considers two dimensional (2D) silicon-carbon systems where the strengths of various structures are calculated and compared. With the relatively recent discovery of the 2D carbon allotrope graphene [9] (which resulted in the 2010 Nobel prize for Physics), silicon and SiC have also been considered as 2-dimensional materials. The iso-structural nature of these materials prompts questions about their relative hardness and strength. This notion of hardness in two dimensional systems is yet to be fully investigated and tested. For instance, there exists no equation of state (EOS), as for bulk materials, where this property can be deduced

from the relationship of the hydrostatic change in surface area to 2D pressure. In this study, such an EOS is proposed and is used on a variety of 2D Si-C systems to extract equilibrium fit parameters including the layer modulus (symbol γ) which measures a material's resilience to hydrostatic stretching. It is used to compare the strengths and elastic properties for the various structures.

1.3 Thesis structure

This thesis is structured in the following manner:

- Chapter 2 reviews previous work done on bulk silicon, carbon, silicon carbide and off-50:50 Si-C systems. It especially emphasizes the use of *ab initio* techniques to the study of bulk systems and their different phases
- Chapter 3 goes through the theory used to develop and implement density functional theory as a practical method to study many-body systems. It covers the methods and algorithms used to make the calculations tractable for large bulk systems. It also covers elasticity theory and lattice dynamics which will be used to study structural strength and stability
- Chapter 4 contains the preliminary calculations used to choose appropriate computational calculation parameters for the rest of the study. Studies on the known bulk systems of silicon, carbon and silicon carbide are done to validate the methods to be used for the study of the proposed silicon-carbon alloys. It also includes original calculations on three novel carbon structures, studying their elastic properties and possible phase transitions
- Chapter 5 presents the studies on the various bulk off-50:50 candidate structures. It presents a detailed study on Si_2C and SiC_2 which evaluates their stability and feasibility
- Chapter 6 introduces the 2D equation of state and investigates the strength properties of various 2D materials. Elemental carbon and silicon as well as 50:50 SiC and off-50:50 silagraphene are studied and compared
- Finally, general conclusions are drawn in Chapter 7

2

Review of previous work

2.1 Silicon and Carbon

Silicon has been much studied over the last few decades due to its importance in many technological applications. It was one of the first materials to be used as a prototype to validate the applicability of computational *ab initio* techniques for the study of the structural, electronic, lattice dynamic and phase transition properties of bulk materials.

In 1980, Yin and Cohen [10] used a pseudopotential method within the local density formalism based on density functional theory to correctly calculate the ground state properties for cubic diamond silicon. By fitting calculated total energy versus volume values to an equation of state, they obtained values for the lattice constant, bulk modulus and cohesive energy all to within 1% of their experimental values. It had also been known since 1962, using resistivity measurements, that diamond Si transforms into a more metallic phase under pressure [11], and that the structure for this new phase was identified through x-ray diffraction measurements in 1963 to be β-Sn [12]. Yin and Cohen theoretically validated this pressure-induced phase transition by identifying a 9.9 GPa tangent pressure line between the two equation of state curves for each phase. This value is smaller than the 16 to 20 GPa values reported in the 1962 and 1963 findings but close to the value of 8.8 GPa reported later in 1983 by Olijnyk et al. [13]. Yin and Cohen also calculated phonon frequencies for $LTO(\Gamma)$, $TA(X)$, $TO(X)$ and $LOA(X)$ all within 3% of their observed values. These first tentative calculations gave credence to the suitability of these methods to study crystal solids.

In 1982, they formalized these computational *ab initio* methods using Si and Ge

as prototypes [14]. They studied the crystal stability for each element by considering cubic diamond (cd), simple hexagonal (sh), beta-tin (β-Sn), simple cubic (sc), body-centred cubic (bcc), hexagonal closed-packed (hcp) and face-centred cubic (fcc) phases. The calculations correctly predicted the stable ground states as being cubic diamond and they reproduced the expected cd to β-Sn transitions. Ground state structural properties based on equation of state fits were in good agreement with experimental values. The valence electron density contour plots for cd Si reproduced the same features as those found in plots synthesized from x-ray data. Contour plots for each phase showed that cd Si had the most covalent bonding character with the β-Sn phase showing a more metallic nature. They obtained good agreement between calculated x-ray structure factors and those derived from experiments. The calculated electronic band structure for both elements gave density of states peak positions that compare well to observed angle-integrated photo-emission data. Based on these results, the claim was made that these methods could be used to accurately describe static structural and electronic properties as well as crystal stability and pressure-induced phase transitions for solids. This laid the foundations for *ab initio* methods to be used to predict yet unobserved crystal phases.

In 1963, it was already known that two new phases for Si exist [15]; a dense body-centered phase created by pressure reduction from the β-Sn phase and a simple hexagonal (sh) phase created by heat treatments. In the 1980's, the *ab initio* methods developed by Yin and Cohen [14] were now used to explain these transitions and predict possible new high pressure phases.

In 1982, McMahan and Moriarty [16] used the generalized pseudopotential method (GPT) [17] and the linear muffin-tin orbital (LMTO) method [18] to predict the following possible phase transition sequence for Si

$$cd \rightarrow \beta\text{-}Sn \rightarrow hcp \rightarrow fcc \rightarrow bcc$$

with the $hcp \rightarrow fcc$ transition occurring at 76 GPa for LMTO and 80 GPa for GPT, and based on extrapolation of the results of Yin and Cohen, the β-$Sn \rightarrow hcp$ transition occurring at 41 GPa. This prediction was partially confirmed in 1983 when Olijnyk et al. [13] experimentally observed the following phase transitions:

$$cd \rightarrow \beta\text{-}Sn \rightarrow sh \rightarrow \text{ an unknown intermediate phase } \rightarrow hcp$$

occurring at 8.8, 16, 35-40, and 40 GPa [13]. The β-$Sn \rightarrow sh$ transition was theoretically described in 1984 by Needs and Martin [19] and in 1986, Duclos et al. [20] observed the $hcp \rightarrow fcc$ transition at 78 GPa. The phase transition from β-Sn to the 8-atom body-centered (BC8) phase under pressure reduction was independently described by Biswas et al. [21] and Yin [22].

Hu et al. [23], in 1986, compared their experimental results with these previous theoretical results which prompted them to state that "it is gratifying to note the good overall agreement between theory and experiment, and the ability of this theory to predict new phases". In fact, during 1993-94 theoretical and experimental results were used to complement each other to explain a newly observed body-centered orthorhombic intermediate phase [24] between the β-Sn and sh structures [25,26].

The first two known forms of carbon were the stable graphite form produced by simple combustion and meta-stable diamond produced in the earth by high pressure and temperature. In 1967, Bundy and Kasper [27] produced a new meta-stable hexagonal form of C using the static pressure compression of graphite at high temperature. It was noted that this form of carbon is found in meteorite diamonds created by large impact collisions with the earth. Strel'nitskii et al. [28] reported in 1978, a novel new allotrope of carbon with body-center symmetry obtained by the deposition of carbon plasma onto a cooled substrate. *Ab initio* techniques were employed to find suitable structures for this new allotrope, these being the supercubane phase [29] and the now generally accepted 8 atom BC8 structure [30]. New methods such as shock-compression [31,32] were then used to create this and other new allotropes in the laboratory. Experimental evidence of new C allotropes spurred theoretical research into possible structures to match the observed x-ray diffraction patterns [33]. It also initiated the search for plausible but not yet observed new phases [34,35,36].

Since the advent of diamond-anvil cell [37] experiments to investigate pressure transitions for other solids, it became important to know the upper pressure bound for the stability of diamond. After their seminal paper in 1982, Yin and Cohen [38] in 1983 studied the crystal stability of carbon considering β-Sn, sc, bcc, hcp and fcc phases and were able to predict a carbon pressure-induced phase transition from diamond to sc at 2300 GPa. A new upper limit was place on diamond when in 1984, Biswas et al. [21] and Yin [22] both predicted a cubic diamond (cd) to BC8 transition at 1200 GPa. It was later suggested in 1987 by Fahy and Louie [39] that the sc and BC8 carbon cannot

be metastable phases at low pressures and that diamond first transforms into BC8 at 1.11 TPa.

It is known that carbon exists under conditions of high pressure and temperature inside planets and for this reason it was important to predict the phase diagram for carbon. Grumbach and Martin [40] in 1996 used first principles molecular dynamics to predict the pressure/temperature phase diagram for C. Their diagram showed that the *sc* phase is most probably a thermodynamically stable high pressure phase with BC8 existing between diamond and *sc*. Liquid C at high pressure was predicted to behave very much like lower pressure Si preferring six-fold coordination. Similar results were obtained by Wang et al. [41] in 2005 also using *ab initio* molecular dynamics.

2.2 Silicon Carbide

Silicon carbide is the oldest known stable alloy involving C and Si and has long been used for its abrasive properties. It was not extensively studied until the 1990's when there was a large interest in new electronic applications for SiC. Although experimental efforts mainly contributed to the progress in SiC growth, it was important to be able to adequately model the main polytypes and understand their properties and stability in the hope of overcoming various technical problems involved in the manufacture of SiC devices.

The first studies into the ground state properties of SiC were done in the mid to late 1980's. Churcher et al. [42] in 1985, using an *ab initio* pseudopotential method based on density functional theory, calculated the theoretical properties of cubic 3C-SiC. They obtained a lattice constant within 1% of the experimental value and a bulk modulus within 10% by fitting their total energy calculations at various volumes to an equation of state. The accuracy of their values is largely due to their well converged energy calculations. Calculated phonon frequencies for X and Γ using the "frozen phonon" method, were in good agreement with measured values to within 5%. Their charge density contour plot suggested SiC had an ionic nature to the bonding. Other calculations were attempted in the same year and in 1988 by Denteneer and Haeringen [43,44] for 3C and hexagonal wurtzite 2H-SiC but the usefulness of their results is in question since their energy calculations were not well converged (they used the same parameters for the plane waves as for previous calculations on Si).

The first *ab initio* study of SiC pressure transitions using a pseudopotential density functional method was done on 3C-SiC in 1987 by Chang and Cohen [45]. Their calculated ground state properties for the lattice constant, bulk modulus and cohesive energy all agreed well with measured values. Calculated valence charge density showed a transfer of charge from the Si atoms into the bonding region indicative of a slight ionic nature and explained why the equilibrium lattice constant for cubic SiC violates Vegard's rule, the empirical relationship believed to exist between the lattice parameter of an alloy and those of the constituent elements. 3C-SiC was also shown to have an indirect band gap between Γ and X with a predicted value of 1.21 eV (smaller than the measured value of 2.39 eV). This band gap was shown to decrease with pressure as is found for Si. They considered the high pressure phases of rocksalt and β-Sn and predicted a pressure transition from 3C-SiC to a semi-conducting rocksalt (NaCl) structure at a pressure of 66 GPa. This transition was only observed experimentally in 1993 by Yoshida et al. [46] and was measured to occur at 100 GPa. They also predicted that since the calculated energies for 3C and 2H only differ by 3 meV, it is expected that 2H also transforms into the NaCl structure at high pressure.

In 1991, Lambrecht et al. [47] calculated the structural and elastic properties of 3C-SiC using both a density functional *ab initio* method and the LMTO. The elastic constants (transformed to a trigonal symmetry tensor) compared well with known values measured from hexagonal 6H-SiC to within 10%.

Electronic and structural properties were calculated in 1994 by Park et al. [48] and separately by Käckell et al. [49,50] for the 3C, 2H, 4H and 6H polytypes. The lattice parameters and bulk moduli compared well with available experimental values with the calculated band structures indicating indirect band gaps for all polytypes. An important result of the work by Käckell et al. [50], is that it was found that in order to obtain correct structural properties, all atoms had to be relaxed before any further calculations could be done. They observed that 4H was the energetically favored type with all cohesive energies for the polytypes being very similar and only differing within an interval of 3.5 meV. The band structure of the polytypes was observed to show a shift in the position of the conduction-band minimum from $X \rightarrow M \rightarrow K$ with increasing percentage of hexagonal close packing ($3C \rightarrow 4H \rightarrow 2H$). Since during crystal growth, the thermal energies would be larger than the differences in cohesive energy for the

polytypes, effects such as the lattice-vibrational properties were thought to play an important role in polytype growth.

That same year, Hofmann et al.[51] presented a semi-empirical method to study these effects by fitting parameters for the semi-empirical bond-charge model to known Raman and luminescence measurements. The calculated lattice dynamical properties for these polytypes and the derived elastic constants from the acoustic velocities were found to be in reasonable agreement with existing experimental and calculated values.

Separately in the same year, Karch et al.[52] using linear-response theory within the pseudopotential density functional method, calculated lattice dynamical properties for 3C, 2H and 4H as well as the expansion coefficient and specific heat of 3C using the quasi-harmonic approximation. They also calculated elastic constants for 3C from *ab initio* stress calculations which agreed well to available experimental data. They noted that the valence charge densities along bonding directions are nearly identical for all polytypes. The phonon dispersion curves for 3C were found to be closer to those of diamond carbon than diamond silicon with a few noted differences that made SiC unique to other tetrahedral III-V semiconductors. For instance, the polar nature of SiC and the mass differences between the two elements caused a splitting of the *LO* and *TO* modes at Γ. The theoretical second-order Raman spectra deduced from the calculated phonon frequencies and eigenvectors agreed with existing measured spectra. The polytypes exhibited similar dynamical properties along their stacking directions indicative of their static structural similarity. Calculated expansion coefficients followed the general shape of the experimental values with discrepancies at higher temperatures most probably due to failure to include higher ordered anharmonic effects. These calculations formed the basis for further studies into the temperature dependent properties of SiC.

In 1996, Karch et al.[53,54] used the pseudopotential density functional method to calculate the pressure dependent structural, lattice-dynamical and dielectric properties of 3C, 2H and 4H-SiC. Looking at various possible high pressure structures, they predicted a 3C transition into one of NaCl, NiAs, anti-NiAs or CsCl phases at 66, 79.8, 206.3 and 360.7 GPa. A study of the continuous structural change from β-Sn to 3C indicated that the β-Sn structure is not a stable or metastable phase of SiC. Similar studies of continuous structural changes from 3C into either the CsCl or NaCl structures found that the NaCl phase is metastable with a small energy barrier per cell, while the CsCl

structure is not stable at zero pressure. From this they concluded that the strong bonding properties of the carbon atoms prevented stable phases with coordination number greater than 6. The high c/a ratio for the NiAs structure also indicated instability. It was also found that the anti-NiAs phase was energetically unfavorable. Unlike Chang and Cohen [45], their results indicated that the NaCl phase is semi-metallic, not semiconducting, with the discrepancy most probably due to a better convergence in the energy calculations. Their results found that whereas the pressure dependence of the ground state properties were largely independent of polytype, the pressure dependence of the dynamical and optical properties behaved differently depending on the polytype.

The next year, Bechstedt et al. [55] investigated some of the possible driving forces behind SiC polytypism and polytype growth using similar methods. They noted an internal relationship between the exact atomic positions and the stability of hexagonal polytypes. The observed decrease in cell volume with hexagonality is only reproduced theoretically if the atoms are relaxed from their ideal tetrahedron structure. Without atomic relaxations, the cubic phase would be shown to be favored over the other polytypes. Looking at the vibrating lattice, they found that in the thermodynamic equilibrium, the vibrations stabilized 4H since it had the lowest free energy over a temperature range from 0 to 1200 K. Using an axial next-nearest-neighbor Ising (ANNI) model to describe the interactions of the stacking layers, they observed a tendency away from the stable cubic phase, towards the hexagonal phases with increasing temperature. They predicted that polytype growth selection is independent of the substrate polytype and is most probably due to thermodynamics. They also showed that combinations of hexagonal and cubic polytypes may give rise to novel heterocrystalline SiC structures. Also using the ANNI model and *ab initio* methods, Käckell et al. [56] found that their calculated stacking faults for SiC were negative, indicating a preference for hexagonal polytypes. Future study of stacking faults would try to address technical problems such as producing stable SiC diodes [57].

The end of the 1990's saw the start of *ab initio* studies into the structural and electronic properties of SiC surfaces [58] which would lead to the creation of novel devices such as graphene diodes on SiC [59].

2.3 Off-50:50 SiC alloys

In 1990, Posthill et al. [60] opened up a new research area in band gap engineering when they suggested that dilute C_xSi_{1-x} hetero-epitaxial films would be good candidates for the production of wide band gap heterojunction bipolar transistors. It was suggested that the C concentration would increase the band gap of the material somewhere between that of Si and SiC. They succeeded in producing these layers on a Si substrate using plasma-enhanced chemical vapor deposition (CVD) that could achieve metastable C concentrations of ~ 3 at.% (well over the small solubility of C in Si). In the following year, Soref [61] did theoretical calculations based on an interpolation technique to study the variation of the band gap with the C alloying concentration which suggested that this increase would occur.

In 1992, Demkov and Sankey [62] used a tight-binding *ab initio* molecular dynamics method to study the microscopic atomic structure of random Si-C alloys. They found that the band gap gets smaller, not larger, with increasing concentrations of C with a minimum at around 10 at.% possibly indicating a metallic nature. molecular beam epitaxy (MBE) was used as a successful method to create $Si_{1-x}C_x$ layers [63] and Eberl et al. [4] experimentally observed that the band gap reduces below Si for small C concentrations below 7%. They also observed an increase in the electron mobility for n-doped strained layers. This effect was studied in 1998 by Knief and Niessen [64] and later used to increased electron mobility in the Si channels of strained FET transistors using C concentrations of around 2% [65].

To understand the chemical ordering of these alloys, various theoretical studies were carried out during the early 1990's to late 2000's using molecular dynamics (MD) [66,67,68] and density functional theory (DFT) [69]. They suggested that amorphous Si-C alloys prefer partial chemical ordering rather than full random ordering. A result confirmed by Chehaidar et al. [70] in 2001 using Raman spectroscopy.

Ordered alloy research is mainly found in the area of nano-cluster research and the study of molecules. There has been interest in the off-50:50 stoichiometry clusters of Si and C (SiC_2, Si_2C, Si_2C_2, Si_3C, SiC_4, Si_2C_3, Si_3C_2 and Si_2C_4 species). The research using local density approximation (LDA) methods has studied the stability of these structures [71,72,73,74] by computing their structural properties, binding energies, and phonon/vibrational frequencies.

There is no research into bulk ordered alloys beyond the cluster level except for a study in 2005 on silicon dicarbide (SiC_2) by Bucknum et al. [75]. In their study, they considered a hypothetical tetragonal structure based on a previously suggested structure for carbon called "glitter" [7]. They presented structural data and made an estimate of the bulk modulus using a semi-empirical formula developed by Cohen [76].

Why is there such a dearth of information on off-50:50 alloys? Are such structures possible? What are some plausible candidates? What governs their stability/instability? These questions form the foundation for the first part of this study. The previous work on Si, C and SiC has laid down some traditional *ab initio* methods used to predict crystal stability and phase transitions. Using these methods and those discussed in the Introduction, this study aims to partially fill in the gap of knowledge on ordered Si-C alloys.

2.4 2D silicon-carbon systems

Graphitic carbon is composed of layered sheets, each in the honeycomb structure, bonded together by the weak van der Waals force. These single layers, called graphene, have been used as theoretical constructs to describe other known carbon materials such as nanotubes [77]; a nanotube is composed of a rolled up sheet of graphene. For this reason, the properties of graphene were studied long before it was actually observed by Novoselov et al. [9] in 2004.

For instance, Sanchez-Portal et al. [77] calculated the phonon dispersion for graphene in order to interpret the phonon properties of single-walled nanotubes and similarly Thomsen et al. determined the phonon deformation potentials for graphene for the same reason.

After 2004, the physical properties of graphene were studied due to the growing interest in the possible applications for this new 2D carbon allotrope. In 2005, Mounet and Marzari studied the linear expansion of graphene showing it to be negative at lower temperatures, a result later verified by Singh et al. in 2010. In 2008, the elastic properties were calculated [81,82] and the 2D Young's modulus was experimentally measured [83]. The following year, the Young's modulus values for other honeycomb structures (including monolayer Si and SiC) were calculated and compared to graphene [84]. In spite

of this, the notion of hardness in two dimensional systems is yet to be fully defined and tested.

For instance, although the 2D bulk modulus for graphene[81] has been calculated, it has not been formally compared to other 2D materials. This modulus is a measure of a material's resilience to in-plane stretching. Does this modulus provide a way to rank the relative strengths of 2D materials and is there, as in the case of bulk systems, a 2D EOS which provides a simple way to extract this value? This question forms the basis for the second part of this study.

In the next chapter, the theoretical framework for this study is introduced with emphasis placed on density functional theory and bulk elasticity. The theoretical framework used for the study of 2D systems is introduced separately in chapter 6.

3

Theoretical framework

In this chapter, the theoretical framework used for this study is introduced. The many-body problem is discussed first along with the difficulties associated with its solution. One possible method to solve this problem, Hartree-Fock, is then introduced and its limitations discussed. Another method, the theoretically exact density functional theory, is discussed in section 3.3 along with the proofs of its two main tenants. The Kohn-Sham ansatz is given in section 3.4 as a way to make this theory tractable. Sections 3.4.1 to 3.5.5 present the algorithmic implementations based on the Kohn-Sham equations along with the various approximations used for their solution. Lastly, the theory used to analyze the elastic and lattice dynamical properties of bulk systems is presented in the last two sections.

3.1 The many-body problem

Any material may be considered as comprising K positive nuclei (referred to as the ions), with positions and atomic numbers $\{\mathbf{R}_\alpha, Z_\alpha\}$, surrounded by N electrons with positions and spins $\{\mathbf{r}_i, \sigma_i\}$. Ignoring relativistic effects, this quantum system is described by solving the following many-body Schrödinger equation [85]:

$$\begin{gathered}\hat{H}\Psi = E\,\Psi \\ \left[\hat{T}_I + \hat{T}_e + \hat{V}_{II} + \hat{V}_{ee} + \hat{V}_{eI}\right]\Psi(\{\mathbf{R}_\alpha\},\{\mathbf{r}_i,\sigma_i\}) = E\;\Psi(\{\mathbf{R}_\alpha\},\{\mathbf{r}_i,\sigma_i\})\end{gathered} \tag{3.1}$$

where Ψ is the many-body wavefunction dependent on both the ionic and electronic degrees of freedom. The kinetic energy terms are given below as:

$$\hat{T}_I = -\frac{\hbar^2}{2}\sum_{\alpha=1}^{K}\frac{1}{m_\alpha}\nabla_\alpha^2 \qquad \hat{T}_e = -\frac{\hbar^2}{2m_e}\sum_{i=1}^{N}\nabla_i^2 \tag{3.2}$$

whereas the potential energy terms describing the various interactions are given by:

$$\hat{V}_{II} = \sum_{\alpha=2}^{K}\sum_{\beta=1}^{\alpha-1}\frac{e^2\ Z_\alpha Z_\beta}{|\mathbf{R}_\alpha - \mathbf{R}_\beta|} \qquad \hat{V}_{ee} = \sum_{i=2}^{N}\sum_{j=1}^{i-1}\frac{e^2}{|\mathbf{r}_i - \mathbf{r}_j|} \qquad \hat{V}_{eI} = -\sum_{\alpha=1}^{K}\sum_{i=1}^{N}\frac{e^2 Z_\alpha}{|\mathbf{R}_\alpha - \mathbf{r}_i|}. \tag{3.3}$$

In order to greatly simplify the problem, one uses the Born-Oppenheimer approximation to separate the ionic and electronic degrees of freedom by assuming that the faster moving electrons obtain an instantaneous ground state for any given configuration of the slowly moving ions.

Therefore, for a given fixed ionic configuration, the N-electron wavefunction Ψ satisfies the following Schrödinger equation:

$$[\hat{T} + \hat{V}_{int} + \hat{V}_{ext} + E_{II}]\,\Psi(\mathbf{r}_i, \sigma_i) = E\,\Psi(\mathbf{r}_i, \sigma_i) \tag{3.4}$$

where $\hat{V}_{int}$, $\hat{V}_{ext}$, E_{II} and $\hat{T}$ are the full electron-electron interaction, electron-ion potential, the classical interaction of the ions with one another and the electron kinetic energy as given in equations 3.2 and 3.3.

It now remains to find the ground state wavefunction that minimizes

$$E = \langle\Psi|\hat{H}|\Psi\rangle = \langle\hat{T}\rangle + \langle\hat{V}_{int}\rangle + \int d^3\mathbf{r}\, V_{ext}(\mathbf{r})\, n(\mathbf{r}) + E_{II} \tag{3.5}$$

where $n(\mathbf{r})$ is the electronic density.

The difficulty in solving the electronic system is due to the incorporation of all of the electron-electron interactions that correlate the positions and kinetic energies of all the electrons. For example, one correlation effect is the fact that all electrons repel each other due to their charge. Another effect is that electrons of the same spin repel each other due to the Pauli Exclusion Principle. Various approximation methods have been developed that incorporate some or all of these correlations to varying degrees of accuracy in a way which makes the problem more tractable. Two such methods are the Hartree-Fock approximation and the theoretically exact Kohn-Sham formulation of density functional theory (DFT).

3.2 The Hartree-Fock approximation

The Hartree-Fock (HF) approximation neglects all electron correlations except those required by Pauli exclusion. The electronic wavefunction is approximated by an anti-symmetric Slater determinant [86]:

$$\Psi_e(\{\mathbf{r}_i,\sigma_i\}) = \Phi = \frac{1}{\sqrt{N!}}\begin{vmatrix} \Phi_1(\mathbf{r}_1,\sigma_1) & \Phi_1(\mathbf{r}_2,\sigma_2) & \Phi_1(\mathbf{r}_3,\sigma_3) & \dots \\ \Phi_2(\mathbf{r}_1,\sigma_1) & \Phi_2(\mathbf{r}_2,\sigma_2) & \Phi_2(\mathbf{r}_3,\sigma_3) & \dots \\ \Phi_3(\mathbf{r}_1,\sigma_1) & \Phi_3(\mathbf{r}_2,\sigma_2) & \Phi_3(\mathbf{r}_3,\sigma_3) & \dots \\ \vdots & \vdots & \vdots & \ddots \end{vmatrix} \tag{3.6}$$

where each single particle spin-orbital is separated into a spatial and spin variable:

$$\Phi_i(\mathbf{r}_j,\sigma_j) = \Psi_i^\sigma(\mathbf{r}_j)\alpha_i(\sigma_j). \tag{3.7}$$

The expectation of the N-electron Hamiltonian of Eqn. 3.4 using this form for the wavefunction is given below in units where $\hbar = m_e = e = 4\pi/\varepsilon_0 = 1$ (called atomic units):

$$\begin{aligned} E_{HF} = & \sum_{i,\sigma}\int d^3\mathbf{r}\,\Psi_i^{\sigma*}(\mathbf{r})[-\frac{1}{2}\nabla^2 + V_{ext}]\,\Psi_i^\sigma(\mathbf{r}) + \frac{1}{2}\int d^3\mathbf{r}\,d\mathbf{r}'\,\frac{n(\mathbf{r})\,n(\mathbf{r}')}{|\mathbf{r}-\mathbf{r}'|} + E_{II} \\ & -\frac{1}{2}\sum_{i,j,\sigma}\int d^3\mathbf{r}\,d^3\mathbf{r}'\,\Psi_i^{\sigma*}(\mathbf{r})\,\Psi_j^{\sigma*}(\mathbf{r}')\frac{1}{|\mathbf{r}-\mathbf{r}'|}\,\Psi_j^\sigma(\mathbf{r})\,\Psi_i^\sigma(\mathbf{r}') \end{aligned} \tag{3.8}$$

where the electron density is defined as

$$n = \sum_\sigma\sum_i^{N^\sigma}|\Psi_i^\sigma|^2. \tag{3.9}$$

The first term in Eqn. 3.8 involves single-body expectation values whereas the second and fourth terms involve interactions between electrons. The second term, called the Hartree energy, describes the Coulomb energy of a self-interacting continuous classical charge distribution of density $n(\mathbf{r})$. The fourth term, called the exchange energy, defines the Coulomb interaction between an electron and its positive hole. This hole defines the region of space around each electron which electrons of the same spin avoid.

Minimizing Eqn. 3.8 while keeping the many-body wavefunction in the form of Eqn. 3.6 leads to the single-electron Hartree-Fock equations [87]

$$\left[-\frac{1}{2}\nabla^2 + V_{ext}(\mathbf{r}) + V_H(\mathbf{r}) + V_x^{i,\sigma}(\mathbf{r}) + E_{II}\right]\Psi_i^\sigma(\mathbf{r}) = \epsilon_i^\sigma\,\Psi_i^\sigma(\mathbf{r}) \tag{3.10}$$

where the Coulomb effects of all the other electrons are approximated by that of a smooth background electron density $n(\mathbf{r})$ giving

$$V_H(\mathbf{r}) = \int d^3\mathbf{r}' \frac{n(\mathbf{r}')}{|\mathbf{r} - \mathbf{r}'|} \tag{3.11}$$

and the effects of Pauli exclusion are incorporated by

$$V_x^{i,\sigma}(\mathbf{r}) = -\left[\sum_j \int d^3\mathbf{r}' \, \Psi_j^{\sigma *}(\mathbf{r}') \, \Psi_i^{\sigma}(\mathbf{r}') \, \frac{1}{|\mathbf{r} - \mathbf{r}'|}\right] \frac{\Psi_j^{\sigma}(\mathbf{r})}{\Psi_i^{\sigma}(\mathbf{r})}. \tag{3.12}$$

The consequence of V_x is that if an electron of spin σ is at $\mathbf{r}$, it cannot be where there is another electron of the same spin. This effect of "exact exchange" fails however to take into account any other correlation effects between electrons such as the Coulomb repulsion felt by all electrons.

The energy difference between the exact energy and the energy given by Eqn. 3.8 for an uncorrelated state with orbitals that give the exact electron density is called the correlation energy. It represents all the missing information when the Coulomb interactions are approximated by a mean field and all the electron correlations are excluded except for exact exchange.

In general, the Hartree-Fock equations are solved self-consistently by choosing basis functions and writing out Eqn. 3.8 in terms of the expansion coefficients for the orbitals. Hartree-Fock is well suited to quantum chemistry for describing single atoms or molecular systems where great numerical accuracy is needed. It is not well suited for large systems due to the large scaling in computational effort required for the number of electron basis functions needed. Hartree-Fock also fails for metals since it incorrectly describes even a simple electron gas such as incorrectly predicting infinite velocities for the electrons near the Fermi level. Improvements to results derived from the Hartree-Fock method require post processing methods that incorporate approximations to the neglected correlation effects.

3.3 Density functional theory

DFT is an exact theory describing the non-relativistic, fully interacting many-body problem and paves the way for a tractable *ab initio* method to solve the N-electron

problem. It shifts the problem from a solution involving N internal degrees of freedom to that of a single quantity: the ground state electron density of the system.

The basis for DFT was set in the 1964 paper by Hohenberg and Kohn [88] that proved the following two theorems (as written in the book by Richard Martin [89])

- **Theorem I:** For any system of interacting electrons in an external potential $V_{ext}(\mathbf{r})$, the potential $V_{ext}(\mathbf{r})$ is determined uniquely, except for a constant, by the ground state particle density $n_0(\mathbf{r})$.
  Corollary I: Since the Hamiltonian is thus fully determined, except for a constant shift of the energy, it follows that the many-body wavefunctions for all states (ground and excited) are determined. *Therefore all properties of the system are completely determined given only the ground state density* $n_0(\boldsymbol{r})$.

- **Theorem II:** A *universal functional*[, where a functional is the mapping of an entire function to a scalar value,] for the energy $E[n]$ in terms of the density $n(\mathbf{r})$ can be defined, valid for any external potential $V_{ext}(\mathbf{r})$. For any particular $V_{ext}(\mathbf{r})$, the exact ground state energy of the system is the global minimum value of this functional, and the density $n(\mathbf{r})$ that minimizes the functional is the exact ground state density $n_0(\mathbf{r})$.
  Corollary II: The functional $E[n]$ alone is sufficient to determine the exact ground state energy and density.

Theorem I is proved by *reductio ad absurdum* as follows:

Proof. If there exists two external potentials $V_1(\mathbf{r})$, $V_2(\mathbf{r})$ that differ by more than just a constant that define two differing Hamiltonians $\hat{H}_1$ and $\hat{H}_2$ each with a differing ground state wave function Ψ_1 and Ψ_2 but give rise to the same ground state density $n_0(\mathbf{r})$ then by the Rayleigh Ritz variational principle

$$E_1 = \langle \Psi_1 | \hat{H}_1 | \Psi_1 \rangle < \langle \Psi_2 | \hat{H}_1 | \Psi_2 \rangle \tag{3.13}$$

giving

$$\begin{aligned} E_1 &< \langle \Psi_2 | \hat{H}_2 | \Psi_2 \rangle + \langle \Psi_2 | \hat{H}_1 - \hat{H}_2 | \Psi_2 \rangle \\ &< E_2 + \int d^3\mathbf{r} [V_1(\mathbf{r}) - V_2(\mathbf{r})]\, n_0(\mathbf{r}). \end{aligned} \tag{3.14}$$

Similarly one can obtain

$$\begin{aligned} E_2 &< \langle \Psi_1 | \hat{H}_1 | \Psi_1 \rangle + \langle \Psi_1 | \hat{H}_2 - \hat{H}_1 | \Psi_1 \rangle \\ &< E_1 + \int d^3\mathbf{r} [V_2(\mathbf{r}) - V_1(\mathbf{r})]\, n_0(\mathbf{r}) \end{aligned} \tag{3.15}$$

which added together give the resulting paradox

$$E_1 + E_2 < E_1 + E_2. \tag{3.16}$$

Therefore there cannot exist two external potentials that differ by more than a constant that yield a solution with the same ground state density. □

It then follows that if all components of the Hamiltonian are uniquely determined, the Schrödinger equation can be solved to find the many-body wavefunction for any state and the ground state is the one that has the lowest energy.

Theorem II is proved as follows:

Proof. Since all properties are uniquely determined by the particle density, there exists a functional for the energy

$$\begin{aligned} E_{HK}[n] &= T[n] + E_{ee}[n] + \int d^3\mathbf{r}\, V_{ext}(\mathbf{r})\, n(\mathbf{r}) + E_{II} \\ &= F_{HK}[n] + \int d^3\mathbf{r}\, V_{ext}(\mathbf{r})\, n(\mathbf{r}) + E_{II} \end{aligned} \tag{3.17}$$

where $F_{HK}[n]$ is a *universal functional* applicable to all fully interacting many-body systems that contains all the internal energies of the electronic system.

If there is a system with an external potential V_1 that corresponds to a ground state density n_1 with wave function Ψ_1, and a differing density n_2, corresponding to a wave function Ψ_2, then

$$\begin{aligned} E_1 &= E_{HK}[n_1] = \langle \Psi_1 | \hat{H}_1 | \Psi_1 \rangle \\ E_2 &= E_{HK}[n_2] = \langle \Psi_2 | \hat{H}_1 | \Psi_2 \rangle > E_1 \end{aligned} \tag{3.18}$$

showing that the value of the energy functional at the ground state density n_1 is indeed a global minimum and is the ground state energy for the Hamiltonian with the external potential determined by n_1. □

It then follows that if the universal functional $F_{HK}[n]$ was known, then by minimizing $E_{HK}[n]$ with respect to variations in $n(\mathbf{r})$, the exact ground state density and energy would be found.

The genius of DFT is that it reduces the N-body problem of Eqn. 3.4 to that of finding a 3-D function $n(\mathbf{r})$ that minimizes a functional $E_{HK}[n(\mathbf{r})]$. Unfortunately it is unsolvable since the exact form of the universal energy functional $F_{HK}[n]$ is unknown and there are no known ways to extract general properties from the density.

3.4 The Kohn-Sham ansatz

DFT was made into a practical method when Kohn and Sham in 1965 [90] changed the problem from solving a fully-interacting electronic system to one of solving a system of non-interacting electrons (with the same ground state electronic density as the fully-interacting system) moving through an effective potential that somehow incorporates the effects of the electron-electron interactions. The ground state density is

$$n(\mathbf{r}) = \sum_{\sigma} n^{\sigma}(\mathbf{r}) = \sum_{\sigma} \sum_{i}^{N^{\sigma}} |\Psi_i^{\sigma}(\mathbf{r})|^2 \tag{3.19}$$

for all Kohn-Sham electron orbitals $\Psi_i^{\sigma}(\mathbf{r})$ where $\sigma = \uparrow$ or $\downarrow$.

The form of the energy functional for the auxiliary system is now [91]

$$E_{KS}[n] = T_s[n] + E_H[n] + \int d^3\mathbf{r}\, V_{ext}(\mathbf{r})\, n(\mathbf{r}) + E_{xc}[n] + E_{II}$$

$$T_s[n] = \sum_{\sigma} \sum_{i}^{N^{\sigma}} \langle \Psi_i^{\sigma} | \hat{T} | \Psi_i^{\sigma} \rangle \tag{3.20}$$

$$E_H = \frac{1}{2} \int d^3\mathbf{r}\, d\mathbf{r}'\, \frac{n(\mathbf{r})\, n(\mathbf{r}')}{|\mathbf{r} - \mathbf{r}'|}$$

where the Hartree energy is as before. Since the Kohn-Sham energy functional must minimize to the same ground state energy as the fully interacting functional, the exchange-correlation energy E_{xc} represents all the missing information when the fully interacting system was replaced by a non-interacting Kohn-Sham system operating in a mean field.

Using the variational equation

$$\frac{\delta E_{KS}}{\delta \Psi_i^{\sigma *}(\mathbf{r})} = \frac{\delta T_S}{\delta \Psi_i^{\sigma *}(\mathbf{r})} + \left[\frac{\delta E_{ext}}{\delta n^{\sigma}(\mathbf{r})} + \frac{\delta E_H}{\delta n^{\sigma}(\mathbf{r})} + \frac{\delta E_{xc}}{\delta n^{\sigma}(\mathbf{r})} \right] \frac{\delta n^{\sigma}(\mathbf{r})}{\delta \Psi_i^{\sigma *}(\mathbf{r})} = 0 \tag{3.21}$$

subject to the constraint of orbital orthonormalization, one derives the Kohn-Sham (KS) equations

$$\begin{aligned}
\left[-\tfrac{1}{2}\nabla^2 + V_{ext} + V_H + V_{xc}^{\sigma}\right] \Psi_i^{\sigma} &= \varepsilon_i^{\sigma}\, \Psi_i^{\sigma} \\
V_{ext}(\mathbf{r}) &= \frac{\delta\, E_{ext}}{\delta\, n^{\sigma}(\mathbf{r})} \\
V_H(\mathbf{r}) = \frac{\delta\, E_H}{\delta\, n^{\sigma}(\mathbf{r})} &= \int d^3\mathbf{r}'\, \frac{n(\mathbf{r})}{|\mathbf{r}-\mathbf{r}'|} \\
V_{xc}^{\sigma}(\mathbf{r}) &= \frac{\delta\, E_{xc}}{\delta\, n^{\sigma}(\mathbf{r})}.
\end{aligned} \tag{3.22}$$

Since the exact form of the exchange-correlation (XC) is not known, various approximations have been developed in order to carry out practical calculations.

3.4.1 Local spin density approximation

The first practical approximation to E_{xc} assumes the exchange-correlation energy per electron at each point $\varepsilon_{xc}(\mathbf{r})$, depends only on the local density and is the same as that for a homogeneous electron gas with the same spin polarized density $(n^{\uparrow}, n^{\downarrow})$ as the system under investigation [92]:

$$\begin{aligned}
E_{xc}^{LSDA}[n^{\uparrow}, n^{\downarrow}] = &\int d^3\mathbf{r}\, n(\mathbf{r})\, \varepsilon_{xc}^{hom}(n^{\uparrow}, n^{\downarrow}) \\
\varepsilon_{xc}^{hom}(n^{\uparrow}, n^{\downarrow}) = &\ \varepsilon_x^{hom}(n^{\uparrow}, n^{\downarrow}) + \varepsilon_c^{hom}(n^{\uparrow}, n^{\downarrow})
\end{aligned} \tag{3.23}$$

The exchange energy per electron is the "exact exchange" term for an electron gas given by the HF approximation [93]

$$\varepsilon_x^{\sigma} = -\frac{3}{4}\left(\frac{6}{\pi}\, n^{\sigma}\right)^{1/3}. \tag{3.24}$$

The spin polarization is represented through the parameter ζ and the density through the parameter r_s where

$$n = n^{\uparrow} + n^{\downarrow} \quad \zeta = \frac{n^{\uparrow} - n^{\downarrow}}{n} \qquad r_s = \left(\frac{3}{4\pi n}\right)^{1/3}. \tag{3.25}$$

The exchange energies for an unpolarized ($\zeta = 0$) and polarized ($\zeta = 1$) homogeneous electron gas are

$$\begin{aligned} \varepsilon_x(r_s, \zeta = 0) &= -\frac{3}{4\pi\, r_s}\left(\frac{9\pi}{4}\right)^{1/3} \\ \varepsilon_x(r_s, \zeta = 1) &= -\frac{3}{4\pi\, r_s}\left(\frac{18\pi}{4}\right)^{1/3}. \end{aligned} \tag{3.26}$$

In order to estimate the correlation energy per electron, Perdew and Zunger in 1981 [94] parametrized the Monte Carlo results of Ceperley and Alder [95] for the high and low densities of a polarized $i = 1$ and unpolarized $i = 0$ electron gas to obtain the PZ form of the local spin-density approximation (LSDA):

$$\begin{aligned} \varepsilon_c(r_s \geq 1, i) &= \gamma_i/(1 + \beta_1^i\sqrt{r_s} + \beta_2^i\, r_s) \\ \varepsilon_c(r_s < 1, i) &= A_i \ln r_s + B_i + C_i\, r_s \ln r_s + D_i\, r_s \end{aligned} \tag{3.27}$$

where $\gamma, \beta_1, \beta_2, A, B, C$ and D are fit parameters.

The exchange and correlation energies per electron are interpolated for fractional polarizations as follows

$$\begin{aligned} \varepsilon_{x/c}(r_s, \zeta) &= \varepsilon_{x/c}(r_s, 0) + \left[\varepsilon_{x/c}(r_s, 1) - \varepsilon_{x/c}(r_s, 0)\right] f(\zeta) \\ f(\zeta) &= \frac{(1+\zeta)^{4/3} + (1-\zeta)^{4/3} - 2}{2^{4/3} - 2}. \end{aligned} \tag{3.28}$$

The success of the LSDA is due to the fact that the energy errors in the exchange and correlation terms mostly cancel each other out fortuitously and the fact that it correctly determines that the sum rule for the exchange hole is exactly one removed electron. In general, LSDA over binds atoms, therefore underestimating bond lengths.

3.4.2 Generalized gradient approximation

In order to improve on LSDA, the generalized gradient approximation (GGA) includes information about the gradient of the density. The GGA functional proposed by Perdew et al. [96] (referred to as PBE) has separate functionals for exchange and correlation, each modifying those for a homogeneous gas.

For the correlation energy, a gradient contribution H is added to that of a homogeneous gas as follows

$$E_c^{PBE}[n^\uparrow, n^\downarrow] = \int d^3\mathbf{r}\, n(\mathbf{r})\, \left[\varepsilon_c^{hom}(r_s, \zeta) + H(r_s, \zeta, t)\right] \tag{3.29}$$

where t is the dimensionless gradient of the density. The exchange energy is given as

$$E_x^{PBE}[n] = \int d^3\mathbf{r}\, n(\mathbf{r})\, \varepsilon_x^{hom}(r_s, 0)\, F_x(s) \tag{3.30}$$

where the exchange energy per electron for a homogeneous gas is enhanced by a factor F_x which is a function of s, the reduced dimensionless gradient of the density. The spin scaling is given as

$$E_x[n^\uparrow, n^\downarrow] = \frac{E_x[2n^\uparrow] + E_x[2n^\downarrow]}{2}. \tag{3.31}$$

In general, GGA under binds atoms thereby overestimating bond lengths. Other GGA functionals have been proposed to accurately describe surfaces (rPBE) and bulk solids (PBEsol and AM05)[97,98,99].

3.5 Algorithmic implementation of the KS equations

The KS equations can be implemented in three equally valid ways:

- Localized atomic orbitals which are used in chemistry to study the atomic-like features of molecules
- Atomic sphere methods such as the augmented plane wave (APW), Green's function Korringa-Kohn-Rostoker (KKR) and muffin-tin orbital (MTO) methods
- Plane wave grid methods which provide fast and efficient ways to solve the KS equations for periodic systems through the use of fast Fourier transforms

All use the self-consistent algorithm as shown in Fig. 3.1 where the KS equations are solved in a self-consistent manner always looking for convergence in the density and the total energy. The repeating loop cycle achieving a converged solution is referred to as a self-consistent field (SCF) calculation.

This study uses the plane wave grid method as implemented in the VASP[101] and QUANTUM ESPRESSO codes[102].

3.5.1 Plane-waves

In a periodic crystal system, the single electron Schrödinger equation for independent electrons under the influence of a periodic potential is given as[103]

$$\left(-\frac{1}{2}\nabla^2 + U(\mathbf{r})\right)\Psi = \varepsilon\Psi \tag{3.32}$$

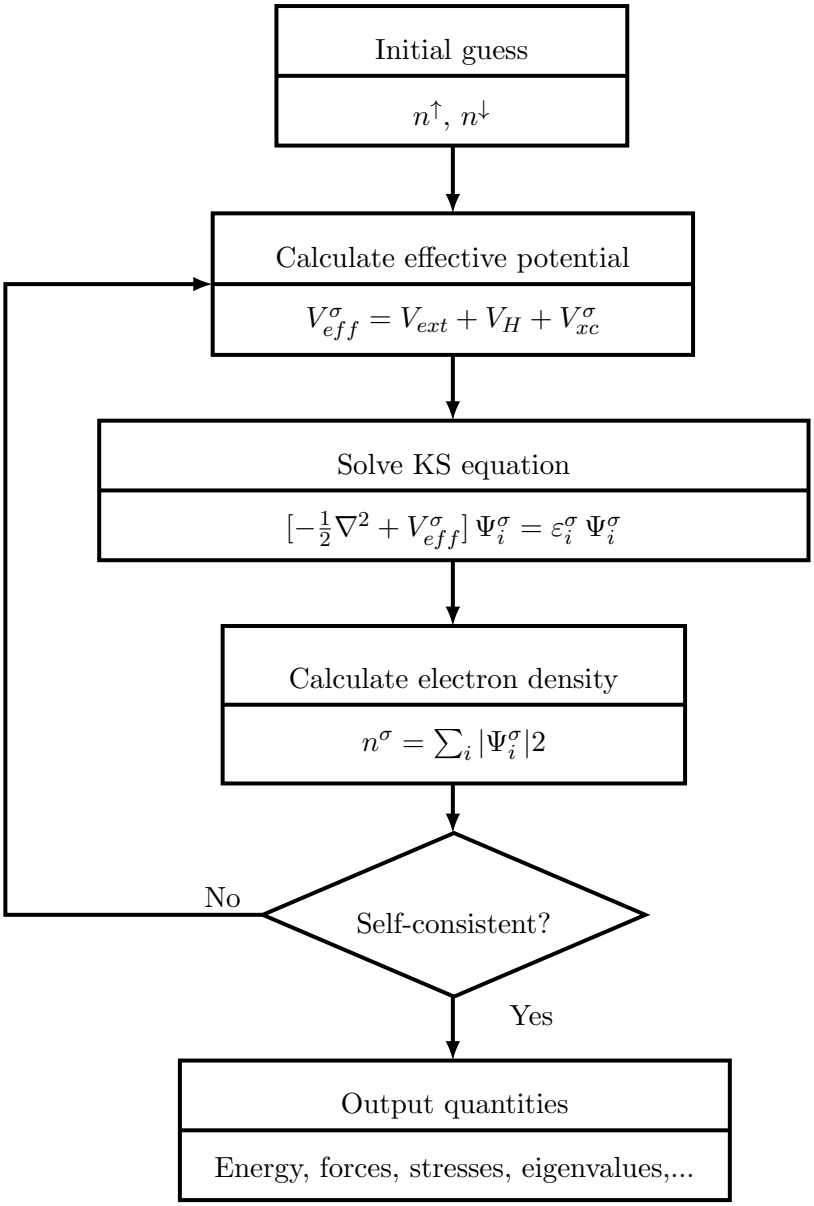

Figure 3.1: Self-consistent field (SCF) algorithm to solve the KS equations. [100]

where the potential U has the periodicity of the underlying Bravais lattice. Bloch's theorem states that

$$\Psi_{\mathbf{k}}(\mathbf{r}) = e^{i\mathbf{k}\cdot\mathbf{r}}\, u_{\mathbf{k}}(\mathbf{r}) \tag{3.33}$$

where $u_{\mathbf{k}}$ has the periodicity of the lattice. Because of this, the electron wavefunction can be written as a plane-wave expansion

$$\Psi_{i,\mathbf{k}}(\mathbf{r}) = \sum_{\mathbf{G}} c_{i,\mathbf{k}+\mathbf{G}}\, e^{i(\mathbf{k}+\mathbf{G})\cdot\mathbf{r}} \tag{3.34}$$

where $\mathbf{G}$ define the reciprocal lattice vectors.

The KS equations in $\mathbf{k}$ space reduce to a matrix eigenvalue equation as shown below[104]

$$\begin{aligned}\sum_{\mathbf{G}'}\{\frac{1}{2}|\mathbf{k}+\mathbf{G}|^2\,\delta_{\mathbf{G}\mathbf{G}'} + V_{ext}(\mathbf{G}-\mathbf{G}') \\ +V_H(\mathbf{G}-\mathbf{G}') + V_{xc}(\mathbf{G}-\mathbf{G}')\}c_{i,\mathbf{k}+\mathbf{G}} = \varepsilon_i\, c_{i,\mathbf{k}+\mathbf{G}}.\end{aligned} \tag{3.35}$$

In practice, the size of the array is made finite by limiting the maximum length for the $\mathbf{G}$ vectors by defining a kinetic energy cut-off

$$E_{cut} = \frac{1}{2}|\mathbf{k}+\mathbf{G}_{max}|^2 \tag{3.36}$$

Solving this equation efficiently and accurately is the motivation behind the iterative methods developed for DFT code.

3.5.2 Integrating over the Brillouin Zone: k-point grid sampling

DFT codes for periodic systems require functions to be integrated over the Brillouin Zone (BZ) in order to calculate such properties as the band energy and charge density. For insulators, there is no discontinuity in sums over the energy bands due to the existence of a band gap separating the valence and conduction bands. All integrations have the form below

$$\tilde{f}_i = \frac{1}{N_k}\sum_{\mathbf{k}} f_i(\mathbf{k}) \tag{3.37}$$

where the quantity f_i is averaged over the entire BZ. Since f_i is a smoothly varying function over the filled bands, it can be expanded into Fourier components

$$f_i(\mathbf{k}) = \sum_{\mathbf{R}} f_i(\mathbf{R}) e^{i\mathbf{k}\cdot\mathbf{R}}. \tag{3.38}$$

This sum can be truncated due to the exponential decrease of the terms at large $\mathbf{R}$. Since these functions have similar values around any given point, the integration sum can then be done over all filled bands using a discrete set of "special points" in the BZ. The scheme proposed by Monkhorst and Pack [105] uses points on a grid based on

$$\mathbf{k}_{n_1\, n_2\, n_3} = \sum_{i=1}^{3} \frac{2n_i - N_i - 1}{2N_i}\mathbf{G}_i. \tag{3.39}$$

Eqn. 3.37 integrates exactly over these points if the Fourier components for each f_i extend only to $N_i\,\mathbf{R}_i$ in each direction.

Metals with their partially filled bands, require careful attention since integrals over the BZ have the form

$$I = \int_{BZ} S(E(\mathbf{k} - E_F))f(\mathbf{k})d^3\mathbf{k} \tag{3.40}$$

where $E(\mathbf{k})$ is the band energy, $S(E(\mathbf{k} - E_F))$ is the unit step function with a drop off at the Fermi energy and $f(\mathbf{k})$ is the function to be integrated. The sharp drop in electron occupation across the Fermi level would require a very dense mesh of $\mathbf{k}$ points to properly resolve the Fermi surface. To avoid the resulting slow convergence of the integral sums, various methods have been developed to integrate around the Fermi surface with a smaller $\mathbf{k}$ grid size:

- The tetrahedral interpolation method proposed by Blöchl [106] fills the space between grid points with tetrahedra that approximate the variation in the integrated periodic function between the grid points. This way the Fermi surface can be adequately resolved using a reasonably sized grid
- The method proposed by Methfessel and Paxton [107] in 1989 uses a smearing function to smooth out the sharp drop in electron occupation across the Fermi surface. By having partial occupancies around the Fermi level, faster convergence is achieved for smaller grid sizes

3.5.3 Pseudopotentials

Another barrier to a fast and efficient solution of the KS equations is that the ionic potentials require a large sized Hamiltonian matrix requiring a large number of terms for the wavefunctions. The rapidly oscillating electronic wavefunctions of the ionic core also require a large number of plane waves for the all-electron (AE) calculation. The solution

is to freeze out the core electrons, since the valence electrons are mostly involved in bonding and chemical properties, and to smooth out the strong ionic potentials so that they act on pseudo valence wavefunctions. This mimics the core behavior with an effective potential while preserving the electron scattering behavior.

Each norm-conserving pseudopotential satisfies the following five conditions for each valence state[108]

1. AE and pseudo valence eigenvalues must agree
2. The all-electron and pseudo wavefunctions must agree beyond a chosen cut-off radius R_{cut}
3. Logarithmic derivatives of the two wavefunctions must agree at R_{cut}
4. The integrated charge inside the cut-off for both cases must agree
5. The first energy derivative of the logarithmic derivatives must agree at R_{cut}

Points 1 and 2 ensure that electrons see the same scattering while point 3 ensures a smooth pseudo wavefunction at R_{cut}. Point 4 ensures that the charge inside the core is correct and point 5 ensures that a given pseudopotential obtained from the spherical atom will adequately describe the ion in a quantum system. R_{cut} for each valence state is chosen to be small enough to accurately describe the wavefunction near the atom and large enough to give smooth wavefunctions requiring a reasonable size of Fourier components and therefore a smaller E_{cut}.

The pseudopotential is separated into a local part and an angular momentum l dependent non-local part

$$V_l(\mathbf{r}) = V_{local}(\mathbf{r}) + \delta V_l(\mathbf{r}). \tag{3.41}$$

Outside R_{cut}, the non-local part is zero and the pseudopotential is the same as the non-local AE potential. The potential operator for the atom is written as

$$\hat{V} = V_{local}(\mathbf{r}) + \sum_{l,m} |Y_{lm}\rangle \delta V_l(\mathbf{r}) \langle Y_{lm}| \tag{3.42}$$

where the last term projects out the spherical-harmonic part of the wavefunction for a given value of l and m.

Various ways to parametrize the pseudo functions are possible:

- Bachelet, Hamann and Schlüter [109] method of expansion in Gaussians
- Vanderbilt [110] method using an assumed form for the potential and variable parameters
- Troullier and Martins [111] method using an exponential form for the wavefunction to the power of a high order polynomial

The Kleinman-Bylander construction [112] constructs a separable pseudopotential operator where the $\delta V_l(\mathbf{r})$ term in Eqn. 3.41 can be replaced by

$$\hat{V}_{NL} = V_{local}(\mathbf{r}) + \sum_{l,m} \frac{|\Psi_{lm}^{PS}\delta V_l\rangle\langle\delta V_l\Psi_{lm}^{PS}|}{\langle\Psi_{lm}^{PS}|\delta V_l|\Psi_{lm}^{PS}\rangle} \tag{3.43}$$

where the second term is fully non-local in angles ϕ, θ and $\mathbf{r}$. The functions $\langle\delta V_l\Psi_{lm}^{PS}|$ operate on the wavefunction and act as projectors. The advantage of this form is that it leads to savings in the number of computations required but can lead to the appearance of artificial "ghost states".

Pseudopotentials are generated as shown in Figure. 3.2 by creating pseudo wavefunctions that satisfy all five points and inverting the radial Schrödinger equation to obtain the pseudopotentials. It is important for the generated pseudopotentials to be transferable to a variety of chemical environments.

To fully describe the electron-ion interaction potential, each pseudopotential for a given ion species V_α is centered on the relevant ionic positions though ionic structure factors [104]

$$S_\alpha(\mathbf{G}) = \sum_I e^{i\mathbf{G}\cdot\mathbf{R}_I} \tag{3.44}$$

where the sum is over positions for that ion type. Therefore, V_{ext} is given by

$$V_{ext}(\mathbf{G}) = \sum_\alpha S_\alpha(\mathbf{G})V_\alpha(\mathbf{G}). \tag{3.45}$$

3.5.4 PAW method

Pseudopotential methods reduce the complexity of electron-ion interactions by smoothing out the valence wavefunctions near the core. The projector augmented wave (PAW) [113] method retains this information in a format that gives computationally efficient calculations to solve the KS equations. The idea behind the PAW method

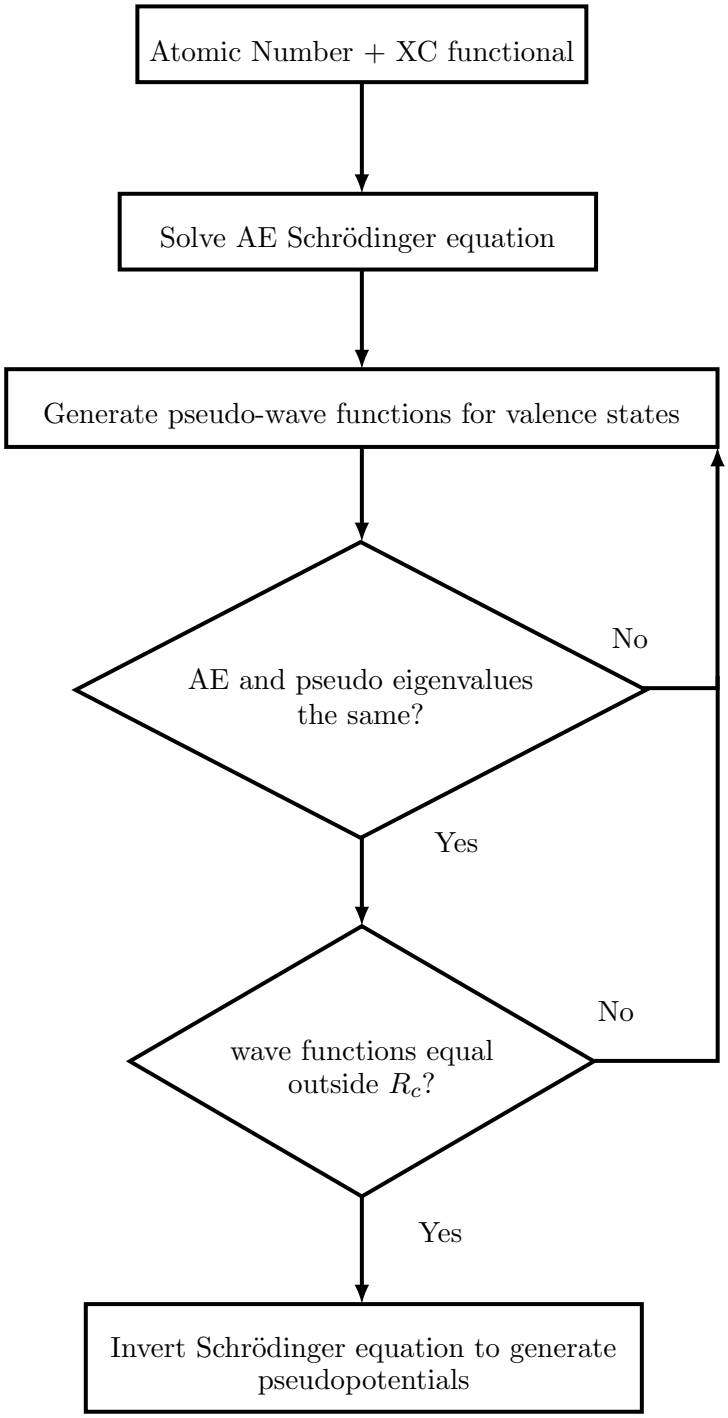

Figure 3.2: Pseudopotential generation

is to transform the AE Kohn-Sham wavefunctions Ψ for single electrons into more convenient pseudo wavefunctions $\tilde{\Psi}$ using a linear transform T where

$$|\Psi\rangle = T|\tilde{\Psi}\rangle. \tag{3.46}$$

The expectation value of an operator A using KS AE wavefunctions can then be done using the pseudo functions

$$\langle A\rangle = \langle\tilde{\Psi}|\tilde{A}|\tilde{\Psi}\rangle \qquad \tilde{A} = T^{\dagger}AT. \tag{3.47}$$

The transformation T is of the form

$$T = 1 + \sum_{R} \tau_R \tag{3.48}$$

where each τ_R is centered at ion position R and only acts within an enclosed augmentation region Ω_R enclosing each ion similar to the cut-off region defined using pseudopotentials. Given a set of complete AE single atom partial waves $|\phi_i\rangle$ in each augmentation region that are orthogonal to the core states of the ion, there is a set of complete pseudo partial waves $|\tilde{\phi}_i\rangle$ such that

$$|\phi_i\rangle = (1 + \tau_R)|\tilde{\phi}_i\rangle \tag{3.49}$$

within the augmentation region Ω_R, where i represents a given R and orbital momentum quantum numbers lm. The set of pseudo partial waves must equal their corresponding AE partial waves outside Ω_R. The AE valence wavefunctions $|\Psi\rangle$ and the valence pseudo wavefunctions $|\tilde{\Psi}\rangle$ can now be expanded in terms of these partial waves as follows

$$\begin{aligned} |\Psi\rangle &= \sum_i c_i|\phi_i\rangle \\ |\tilde{\Psi}\rangle &= \sum_i c_i|\tilde{\phi}_i\rangle \end{aligned} \tag{3.50}$$

and the AE wavefunctions can be written as

$$|\Psi\rangle = |\tilde{\Psi}\rangle - \sum_i c_i|\tilde{\phi}_i\rangle + \sum_i c_i|\phi_i\rangle. \tag{3.51}$$

The linearity of T requires that

$$c_i = \langle\tilde{p}_i|\tilde{\phi}_i\rangle \tag{3.52}$$

for projector functions $\tilde{p}_i$ localized in Ω_R. Therefore T becomes

$$T = 1 + \sum_i (|\phi_i\rangle - |\tilde{\phi}_i\rangle)\langle\tilde{p}_i| \tag{3.53}$$

and the AE wavefunctions can be obtained from the pseudo wavefunctions through

$$|\Psi\rangle = |\tilde{\Psi}\rangle + \sum_i (|\phi_i\rangle - |\tilde{\phi}_i\rangle)\langle\tilde{p}_i|\tilde{\Psi}\rangle. \tag{3.54}$$

It only remains to

1. Obtain the single atom AE partial waves for each ion
2. Define pseudo partial waves outside each augmentation region
3. Find a set of suitable projection functions such that the following is satisfied

$$\langle\tilde{p}_i|\tilde{\phi}_j\rangle = \delta_{ij} \tag{3.55}$$

Thus the rapidly varying nature of the valence wavefunctions in the augmentation region enclosing the core is retained while the functions are smoothed outside the region. All expectation value calculations can now be performed using only the pseudo wavefunctions, the projector functions and the partial waves which allows for fast and efficient calculations.

3.5.5 Atomic relaxations

The Born-Oppenheimer approximation ensures that the KS equations can be solved for a given fixed set of ionic positions. The question remains how one can then move the ion positions to perform atomic relaxations. The answer is provided by the Hellmann-Feynman theorem [114] that states that the force on an ion is given by

$$\mathbf{F}_I = -\frac{\partial E}{\partial \mathbf{R}_I} = -\langle\Psi|\frac{\partial \hat{H}}{\partial \mathbf{R}_I}|\Psi\rangle - \frac{\partial E_{II}}{\partial \mathbf{R}_I} \tag{3.56}$$

where E is the total electronic energy of the system and $\mathbf{R}_I$ is the ionic position. The movement of the ions to new atomic positions defines a new set of KS equations with a different solution and as long as the solution is properly converged, this will define the forces acting on the ions. It then remains to classically move the ions according to the forces.

Atomic relaxations are built around self-consistent total energy calculations in the following manner

1. Move the ions slightly to new positions
2. Recalculate the total energy for the new configuration then calculate the forces on each ion
3. Move ions slightly according to the calculated forces
4. repeat from step 2 until the forces are all within some tolerance

This way, the ions can be relaxed into their zero force equilibrium positions.

3.6 Bulk elasticity

3.6.1 Strain

During a deformation, a point $\vec{r} = x_i\,\hat{e}_i$ in a reference body is moved to a new position $\vec{r}' = \overline{x}_i\,\hat{e}_i$ in the deformed body. The two positions are displaced by a displacement vector $\vec{u} = u_i\,\hat{e}_i$ so that[115]

$$\overline{x}_k = x_k + u_k \quad k = 1, 2, 3. \tag{3.57}$$

Similarly, two neighboring points with separation $d\vec{r}$ will move so that their new separation $d\vec{r}'$ is given by equation (3.58).

$$d\overline{x}_k = dx_k + du_k. \tag{3.58}$$

For infinitesimal deformations, the change in $\vec{u}$ is given by (3.59)

$$\begin{aligned} du_k &= \mu_{kj}\,dx_j \\ \mu_{ij} &= \frac{\partial u_i}{\partial x_j} \end{aligned} \tag{3.59}$$

where μ is the displacement gradient tensor.

We can now define the symmetrical part of μ as being the infinitesimal strain tensor with 9 elements:

$$\varepsilon_{ij} = \frac{1}{2}\left(\mu_{ij} + \mu_{ji}\right). \tag{3.60}$$

For small strains

$$d\overline{x}_k = \left(\delta_{kj} + \varepsilon_{kj}\right) dx_j. \tag{3.61}$$

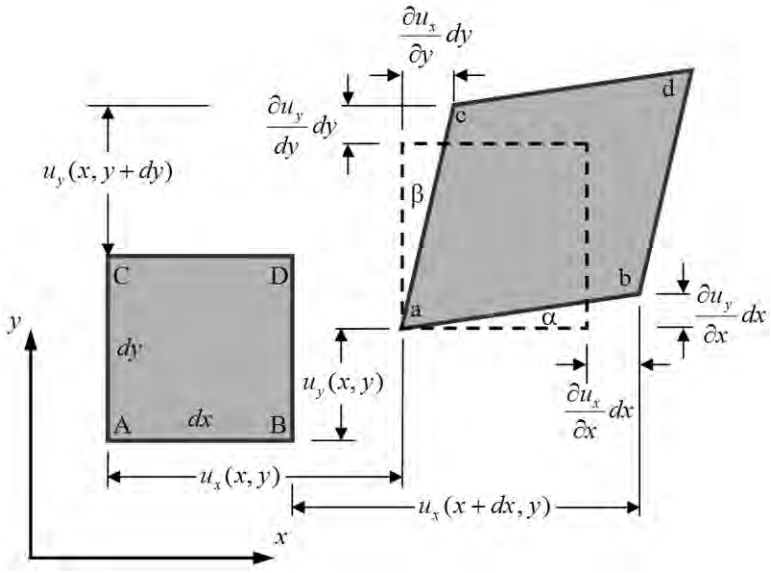

Figure 3.3: 2D geometric strain -[116] Showing the effect of strain deformation on a square body in the xy plane.

Since the strain tensor is symmetrical, the subscripts obey

$$ij = ji$$

reducing the number of independent elements to 6. To see the meaning behind these strain elements, we consider a deformation in the x/y plane as is shown in Fig. 3.3. The length of $\overline{ab}$ is given below:

$$\overline{ab} = \sqrt{dx^2 + (\frac{\partial u_x}{\partial x} dx)^2} \simeq \left(1 + \frac{\partial u_x}{\partial x}\right) dx \simeq (1 + \varepsilon_{xx})\, dx \tag{3.62}$$

meaning the strain in the x direction (direction $\hat{e}_1$) is given by ε_{xx} (or ε_{11} in our tensor notation.) Similarly, ε_{22} and ε_{33} represent strains in the y and z direction respectively. These strain elements are known as normal strains.

The tangent of the angle α in Fig. 3.3 is given by:

$$\tan\alpha = \frac{\dfrac{\partial u_y}{\partial x}}{\left(1 + \dfrac{\partial u_x}{\partial x}\right) dx} \simeq \alpha$$
$$\alpha \simeq \frac{\partial u_y}{\partial x} = \mu_{yx} = \mu_{21}. \tag{3.63}$$

Similarly, angle $\beta = \mu_{12}$ meaning

$$\alpha + \beta = \mu_{12} + \mu_{21} = 2\,\varepsilon_{12} = 2\,\varepsilon_{21} \tag{3.64}$$

therefore the angle between $\overline{ac}$ and $\overline{ab}$ is

$$\frac{\pi}{2} - 2\,\varepsilon_{12}. \tag{3.65}$$

These strain elements with mixed indices are the shear strains.

3.6.2 Stress

When external forces are exerted on a body, the infinitesimal stresses σ_{ij} in the body are as is shown in Fig. 3.4.

The relationship between stress and strain in a general anisotropic material is not a straight forward linear one. Instead the relationship is given by an 81 element stiffness tensor C as is shown in the equation below (where repeated indices indicate summation)

$$\sigma_{ij} = C_{ijkl}\,\varepsilon_{kl}. \tag{3.66}$$

Since no torques occur in the stressed body, the stress tensor subscripts obey

$$ij = ji.$$

The stiffness tensor subscripts obey the added condition that

$$ijkl = klij. \tag{3.67}$$

This ensures that the stiffness tensor is symmetrical leaving only 21 unique elements (called elastic constants) to be specified. The stress in a solid can be calculated using *ab initio* techniques using the stress theorem of Nielsen and Martin [118]. It states that the stress tensor is

$$\sigma_{ij} = -\frac{1}{\Omega}\frac{\partial E}{\partial \varepsilon_{ij}} \tag{3.68}$$

where Ω is the unit cell volume of the crystal and E is the total energy.

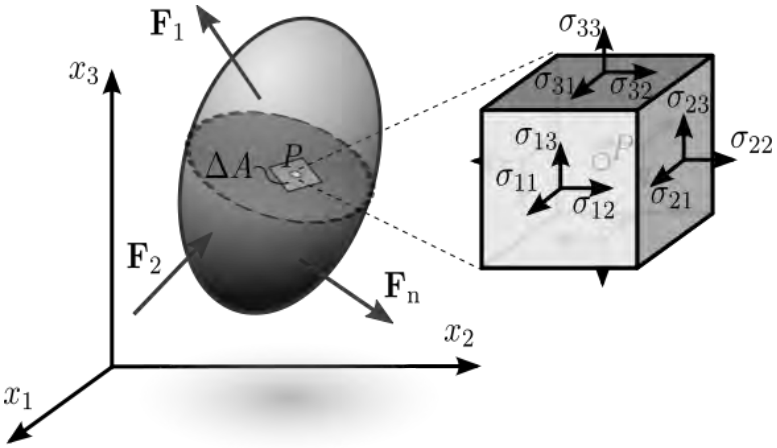

Figure 3.4: Infinitesimal stress components - [117] Showing internal stress components due to external forces applied to a body.

3.6.3 Crystal symmetry

Crystal symmetry provides added relationships between the elastic constants. In the 1959 paper by Waterman [119], additional relationships for the elastic constants are defined by

$$C_{ijkl} = Q_{ip}Q_{jq}Q_{kr}Q_{ls}\,C_{pqrs} \tag{3.69}$$

where the Q's represent tensor components of the symmetry transformations.

To simplify the tensor notation, Voigt notation with the following mapping is used

$$p = i\delta_{ij} + (1-\delta_{ij})(9-i-j), \quad q = k\delta_{kl} + (1-\delta_{kl})(9-k-l) \tag{3.70}$$

so that

$$\begin{matrix} ij \to p \\ kl \to q \end{matrix} \quad 11 \to 1 \quad 22 \to 2 \quad 33 \to 3 \quad 23 \to 4 \quad 13 \to 5 \quad 12 \to 6 \tag{3.71}$$

Using this notation, the stresses σ_{ij}, elastic constants C_{ijkl} and strains ε_{ij} map as

$$\sigma_p = \sigma_{ij}, \quad C_{pq} = C_{ijkl}, \quad e_q = (2-\delta_{kl})\,\varepsilon_{kl}. \tag{3.72}$$

Various crystal systems are invariant under certain rotational symmetry operations $\mathbb{R}_i^\theta$ where θ is the angle rotated and i is the rotation axis. This allows further reduction of the number of unique elastic constants needed by each system.

Cubic systems are symmetrical with respect to $\mathbb{R}_x^{\pi/2}$, $\mathbb{R}_y^{\pi/2}$, $\mathbb{R}_z^{\pi/2}$ resulting in the fact that

$$\begin{array}{c} C_{11} = C_{22} = C_{33} \\ C_{44} = C_{55} = C_{66} \\ C_{12} = C_{23} = C_{13} \end{array} \tag{3.73}$$

leaving 3 unique elastic constants with all other constants not listed set to zero. This gives the resulting stiffness matrix

$$\begin{pmatrix} C_{11} & C_{12} & C_{12} & 0 & 0 & 0 \\ C_{12} & C_{11} & C_{12} & 0 & 0 & 0 \\ C_{12} & C_{12} & C_{11} & 0 & 0 & 0 \\ 0 & 0 & 0 & C_{44} & 0 & 0 \\ 0 & 0 & 0 & 0 & C_{44} & 0 \\ 0 & 0 & 0 & 0 & 0 & C_{44} \end{pmatrix}. \tag{3.74}$$

A hexagonal system is invariant under the rotation $\mathbb{R}_z^{\pi/3}$ which results in

$$\begin{array}{c} C_{11} = C_{22} \\ C_{33} \\ C_{12} \\ C_{23} = C_{13} \\ C_{44} = C_{55} \\ C_{66} = \left(C_{11} - C_{12}\right)/2 \end{array} \tag{3.75}$$

leaving only 5 unique constants. The resulting stiffness matrix is

$$\begin{pmatrix} C_{11} & C_{12} & C_{13} & 0 & 0 & 0 \\ C_{12} & C_{11} & C_{13} & 0 & 0 & 0 \\ C_{13} & C_{13} & C_{33} & 0 & 0 & 0 \\ 0 & 0 & 0 & C_{44} & 0 & 0 \\ 0 & 0 & 0 & 0 & C_{44} & 0 \\ 0 & 0 & 0 & 0 & 0 & \dfrac{C_{11} - C_{12}}{2} \end{pmatrix}. \tag{3.76}$$

The total strain energy for a deformed body is given by:

$$E = E_0 + \frac{1}{2} V C_{pq} e_p e_q \tag{3.77}$$

where V is the unit cell volume. In order to ensure positive energy changes with respect to strain, the determinants of the principle minors of the stiffness matrix (therefore the eigenvalues as well) must all be positive. Negative values indicate elastic instability.

3.6.4 Calculating elastic constants

Traditionally, Eqn. 3.77 was used to obtain elastic constants for a material using *ab initio* methods. Total energies were calculated for a set of carefully chosen strains placed on the crystal and these values were fitted to quadratic equations derived from Eqn. 3.77.

A different approach suggested by Le Page and Saxe [120] uses the method of least-squares to extract out the elastic constants. Given a large initial strain E with a stress $S(E)$, any small strains e around E will give small stress changes s so that

$$S(E+e) = S(E) + s = S(E) + C(E)e. \tag{3.78}$$

Calculating a suitable number of $S(E+e)$ using *ab initio* methods, the 21 elastic constants can then be extracted from Eqn. 3.78 using a least-squares fit. These values can then by used to calculate various elastic properties. This is the method used by the VASP/MedeA [101] software package.

3.6.5 Elastic moduli

The elastic behavior of a material is determined by its elastic moduli. The bulk modulus B is defined as

$$B = -V\frac{\partial P}{\partial V} \tag{3.79}$$

and is a measure of how compressible a material is to hydrostatic strain. The Young's modulus Y is a measure of how a material reacts to tensile stress while the shear modulus G is a measure of how a material reacts to shear stress. Positive values are an indication of elastic stability. All of these properties can be defined for a single crystal material but it is more useful to find the value for polycrystalline material. The bulk and shear elastic moduli for polycrystalline materials are bounded [121] above by the Voigt values

$$\begin{aligned} B_V &= \tfrac{1}{9}\left(C_{11}+C_{22}+C_{33}\right) + \tfrac{2}{9}\left(C_{12}+C_{13}+C_{23}\right) \\ G_V &= \tfrac{1}{15}\left(C_{11}+C_{22}+C_{33}\right) - \tfrac{1}{15}\left(C_{12}+C_{13}+C_{23}\right) + \tfrac{1}{5}\left(C_{44}+C_{55}+C_{66}\right) \end{aligned} \tag{3.80}$$

and below by the Reuss values

$$\begin{aligned} 1/B_R &= \left(S_{11}+S_{22}+S_{33}\right) + 2\left(S_{12}+S_{13}+S_{23}\right) \\ 15/G_R &= 4\left(S_{11}+S_{22}+S_{33}\right) - 4\left(S_{12}+S_{13}+S_{23}\right) + 3\left(S_{44}+S_{55}+S_{66}\right) \end{aligned} \tag{3.81}$$

where S_{ij} denotes the elements of the compliance matrix (the inverse of the stiffness matrix). The geometric mean of the two limits (the Hill value) is a reasonable approximation to describe the polycrystalline material. Using the fact that polycrystalline material is isotropic, the Young's moduli can be obtained from

$$Y = \frac{9BG}{3B + G}. \tag{3.82}$$

Another important quantity is the Poisson ratio which is a measure of how the cross sectional area changes with tensile stress. It is given by

$$\nu = \frac{3B - 2G}{2G + 6B}. \tag{3.83}$$

From the moduli, one can then calculate the shear (s), longitudinal (l) and mean (m) acoustic velocities [122]

$$v_m = \left(\frac{1}{3}\left(\frac{2}{{v_s}^3} + \frac{1}{{v_l}^3}\right)\right)^{-1/3} \tag{3.84}$$

$$v_s = \sqrt{G/\rho} \tag{3.85}$$

$$v_l = \sqrt{\left(B + \frac{4}{3}G\right)/\rho} \tag{3.86}$$

and from v_m obtain the Debye temperature:

$$\theta_D = \frac{\hbar}{k_B}\left(\frac{6\pi q}{V_0}\right)^{1/3} v_m \tag{3.87}$$

where q are the number of ions in the unit cell and V_0 is the equilibrium unit cell volume.

3.6.6 Bulk equation of state

There exist relationships between the pressure and the volume for a solid when under hydrostatic strain though there is an ambiguity in which frame of reference to use to define the finite strain. It has been empirically proven that the Eulerian-Finite-strain used in the Birch-Murnaghan equation of state (EOS) [123] works very well. Describing

hydrostatic volume compressions in terms of Eulerian strain components, the Eulerian-Finite-strain measure becomes

$$f_E = \left[\left(\frac{V_0}{V} \right)^{2/3} - 1 \right] /2 \tag{3.88}$$

and the related EOS is given by

$$P = 3B_0 f_E \left(1 + 2f_E\right)^{5/2} \left(1 + \frac{3}{2} \left(B'_0 - 4 \right) f_E \right) \tag{3.89}$$

where V_0, B_0 and B'_0 are the equilibrium volume, bulk modulus and pressure derivative at zero pressure. The double pressure derivative B''_0 is implicitly defined by

$$B''_0 = -\frac{1}{B_0}((3 - B'_0)(4 - B'_0) + \frac{35}{9}). \tag{3.90}$$

Given that

$$P = -\partial E/\partial V, \tag{3.91}$$

integrating the pressure with respect to volume results in the third order Birch-Murnaghan energy/volume equation of state

$$E = E_0 + (9/8)B_0V_0 \left(2f_E\right)^2 + (9/16)B_0V_0 \left(B'_0 - 4\right) \left(2f_E\right)^3 . \tag{3.92}$$

This provides a way to calculate the single crystal bulk modulus using *ab initio* calculations of the total energy at various volumes around the equilibrium point.

The pressure derivatives of the structure indicate how the bulk modulus responds to pressure through the following equation:

$$B(P) = B_0 + B'_0 \, P + \frac{1}{2} B''_0 \, P^2. \tag{3.93}$$

3.6.6.1 Phase Transitions

Pressure transitions occur when a material is compressed causing a structural change into another phase. The fitted energy versus volume EOS curves for two structures of a given material can indicate such a transition if there exists a positive pressure tangent line between the two curves. This can be seen in Figure. 3.5 where a positive pressure tangent line exists between two generic phases A and B indicating a transition from A to B. Using Eqn. 3.91, the negative slope of this tangent line gives a transition pressure of 640 GPa.

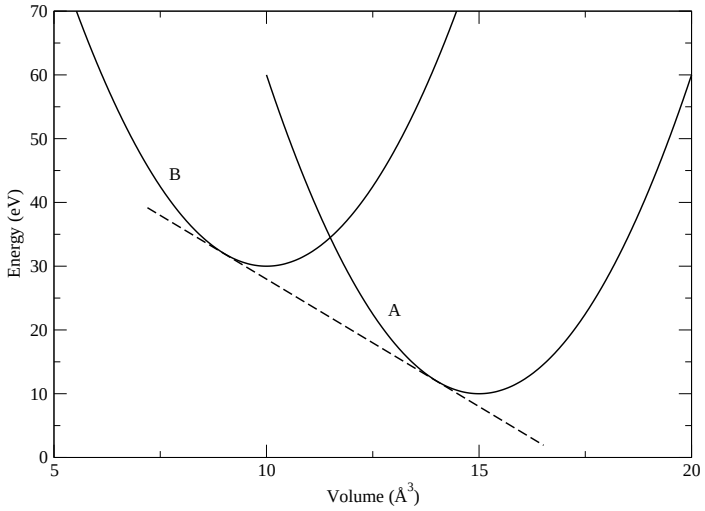

Figure 3.5: EOS fits - Showing a transition between phase A and phase B at 640 GPa.

It is known that two phases can co-exist if their Gibb's energies are equal where

$$G = E + PV - TS = H - TS \tag{3.94}$$

Under conditions of zero temperature, this reduces to the Enthalpies (H) being equal. Calculating the enthalpies for two phases over a range of pressures can also indicate a phase transition as can be seen in Figure. 3.6.

3.7 Lattice dynamics

The lattice dynamics of a crystal indicate the nature of the lattice vibrations. The motions of the ions is described by coupled classical equations of motion [124]

$$M_I \frac{\partial^2 \mathbf{R}_I}{\partial^2 t} = \mathbf{F}_I(\mathbf{R}) = -\frac{\partial E(\mathbf{R})}{\partial \mathbf{R}_I}. \tag{3.95}$$

At zero force, the ions are at their equilibrium positions $\mathbf{R}^0$. Any vibrations around these positions in the harmonic approximation are given by

$$\mathbf{u}_I(t) = \mathbf{R}_I(t) - \mathbf{R}^0 = \mathbf{u}_I e^{i\omega t} \tag{3.96}$$

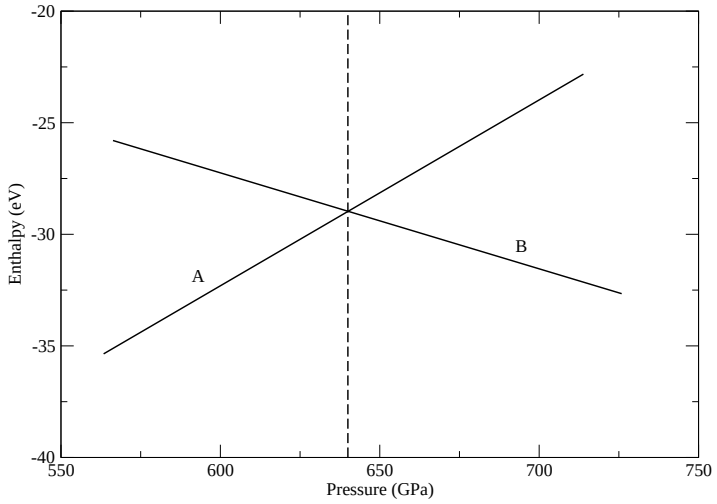

Figure 3.6: Enthalpy plots - Showing a transition between phase A and phase B at 640 GPa.

which with Eqn. 3.95 gives [125]

$$-\omega^2 M_I u_{I\alpha} = -\sum_{J\beta} C_{I,\alpha;J,\beta} u_{J\beta}$$
$$C_{I,\alpha;J,\beta} = \frac{\partial^2 E(\mathbf{R})}{\partial \mathbf{R}_{I,\alpha} \partial \mathbf{R}_{J,\beta}} \tag{3.97}$$

where α and β are the Cartesian components and $C_{I,\alpha;J,\beta}$ is the reduced force matrix. Using Bloch's theorem, a unit cell with S atoms will have dispersion curves of allowed vibrational frequencies given by

$$\det[\frac{1}{\sqrt{M_s\, M_{s'}}} C_{s,\alpha;s',\alpha'}(\mathbf{k}) - \omega^2_{i\mathbf{k}}] = 0$$
$$C_{s,\alpha;s',\alpha'}(\mathbf{k}) = \frac{\partial^2 E(\mathbf{R})}{\partial \mathbf{u}_{s,\alpha}(\mathbf{k}) \partial \mathbf{u}_{s',\alpha'}(\mathbf{k})} \tag{3.98}$$

for $s, s' = 1, \ldots S$ and $i = 1, \ldots 3S$ which define phonons with energy $\hbar\omega_{i\mathbf{k}}$. Positive phonon frequencies indicate lattice stability whereas the appearance of imaginary values indicate that the structure is no longer stable and will transform into another phase. For phonon dispersion curves a convention is used where these imaginary frequencies are plotted as negative numbers.

The direct method for calculating the phonon dispersion for a crystal moves ions off their equilibrium positions and using an *ab initio* method, calculates the reduced force matrix.

The method using linear response calculates the force matrix by determining the response of the charge to ion displacements which perturb the ionic potential.

While the direct method can use the output from any DFT code (as with the PHONON code[126] implemented in VASP/MedeA[101]), the linear response method has to be embedded into the code since it uses perturbation DFT[127] (as implemented in the QUANTUM ESPRESSO codes[102]).

3.8 Software codes

All calculations in this study were done within the framework of density functional theory (DFT) as implemented in the VASP and QUANTUM ESPRESSO codes. Both PAW and ultrasoft pseudopotentials were used using non-spin polarized calculations.

Elastic constants were obtained using the method of least-squares fit[120] as implemented in the VASP/MedeA-MT module. Phonon dispersions were obtained using the direct method as implemented in the VASP/MedeA-PHONON module.

The PBEsol XC functional was chosen based on the comparative study by Csonka et al.[128] on the ability of various XC functionals to describe bulk solids. This functional was introduced in 2008 by Perdew et al.[97] and it was found that this GGA functional was especially apt at describing the bulk properties of densely packed bulk solids, especially under extreme compression.

For layered systems like graphite, LSDA was used in VASP since it provides an interlayer interaction which mimics the weak van der Waals force.

The next chapter presents results for elemental silicon and carbon and 50:50 silicon carbide. The properties of three under-reported carbon allotropes are also presented. The various methods used to characterize the bonding, structural, pressure-transition, elastic and lattice dynamical properties of these systems are investigated and validated. These methods and results are later used to explain the stability conditions for various off-50:50 candidate alloy structures.

4

Bulk elemental and 50:50 Si-C systems

In order to investigate Si-C alloys, preliminary calculations on the elemental and 50:50 Si-C systems must be fully investigated. This is to establish how bonding trends affect the strength and stability properties of these systems. Each system is also studied in turn to validate the methods used later for the study of off-50:50 alloys. In section 4.2, the known silicon allotropes are studied in order to characterize their bonding, strength, and pressure properties and trends in their metallicity. Carbon and silicon carbide structures are studied in sections 4.3 and 4.4 to investigate their covalent and ionic bonding properties.

4.1 Atomic carbon and silicon

Silicon and carbon both occupy group IV on the periodic table and consequently share some characteristics. They have a valency of four and can form sp^3 bonding with a coordination of four. It is no surprise that they both come in the diamond structure although while diamond is the stable form for silicon at ambient conditions, it is a metastable form for carbon. Carbon has the added property of forming sp^2 bonds as seen in its stable graphite structure, thus it can have 3-fold coordination. Under conditions of high pressure, Si and C are known to have 6-fold coordination (as in the rocksalt NaCl structure of SiC) with Si having the ability to have as high as 12-fold coordination in the fcc structure. The work by Wang et al. [41] suggests from their ab

initio molecular dynamics studies, that molten carbon under high pressure does not exceed a coordination of six and Grumbach and Martin [6] predicted a transition from a four-coordinated liquid to a six-fold coordination at high pressure. The work by Karch et al. [53] led them to conclude that phases of SiC with coordination greater than six were unstable due to the strong bonding properties of the carbon atom. All of this seems to place an upper limit on the possible coordination of carbon in silicon-carbon systems.

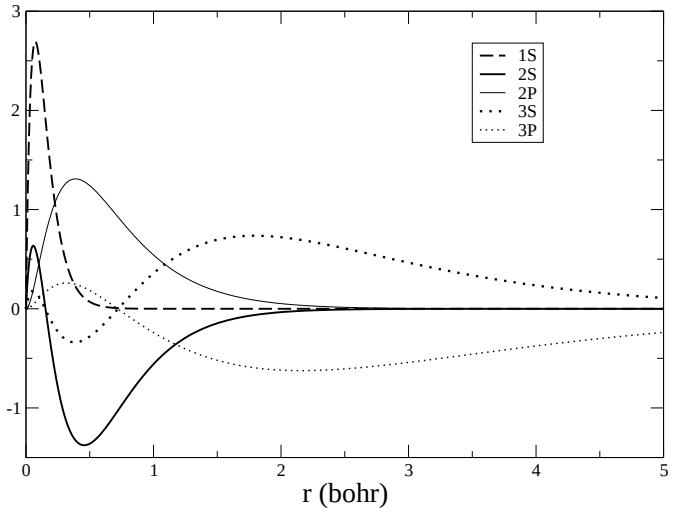

Figure 4.1: Silicon AE KS wavefunctions - Showing loosely bound valence states (dotted curves) pushed outside of the core.

The Si atom has atomic number $Z = 14$ with 10 electrons in $1s^2\,2s^2\,2p^6$ and its valence electrons in $3s^2\,3p^2$ while the C atom has $Z = 6$ with 2 core electrons in $1s^2$ with the 4 valence electrons in $2s^2\,2p^2$. The all-electron (AE) wavefunctions for the states for both atoms are shown in Fig. 4.1 and Fig. 4.2, respectively. Silicon has a p orbital in the core, effectively pushing the valence states to the outside, resulting in loosely bound valence electrons with a well defined core. Carbon, on the other hand, has no p state inside the core resulting in tightly bound valence electrons. The "frozen core" approximation is more applicable to the Si atom due to its loosely bound valence electrons, therefore the smoothing function for the pseudo function can have a much larger (softer) cut-off radius. Since the oscillating part of the wavefunction

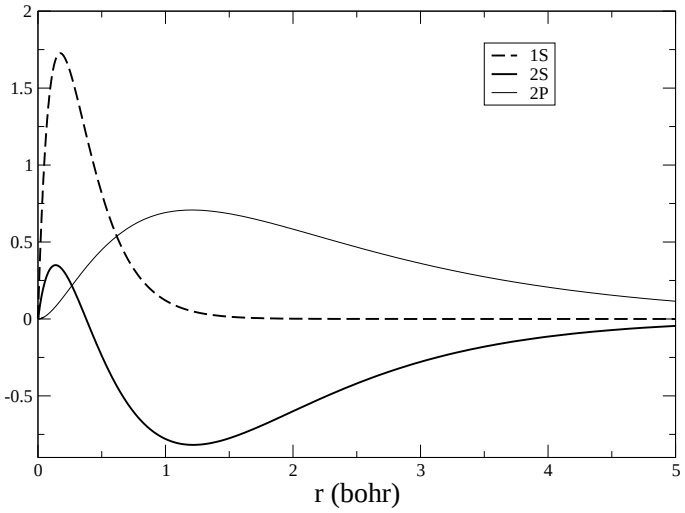

Figure 4.2: Carbon AE KS wavefunctions - Showing tightly bound valence states (solid curves).

does not have to be described, a lesser number of terms are required in the plane wave expansions, meaning a reasonable kinetic energy cut-off. For C the cut-off radius has to be smaller (harder) in order to adequately describe the oscillations near the core, resulting in the need for a larger number of plane wave terms and a larger kinetic energy cut-off for carbon and carbon based systems. This can be seen when comparing the cut-off radii for C in Fig. 4.4 to those for Si in Fig. 4.3. The node-less $2p$ state of C has a lower cut-off radius as compared to the $3p$ state for Si that only contains one node. Fortunately, PAW pseudofunctions are equivalent to ultrasoft pseudopotentials [129] and can therefore have softer cut-off radii with more reasonable kinetic energy cut-offs.

4.1.1 Choice of k-point sampling and kinetic energy cut-off

For accurate DFT calculations, it is important that the Brillouin Zone (BZ) is properly sampled and that an adequate number of plane wave terms are used in order to calculate such properties as the band energy and charge density. The use of "special points" greatly reduces the amount of **k**-points needed to obtain accurate integration over the BZ. It still remains to choose an adequate number of "special points" and a suitable

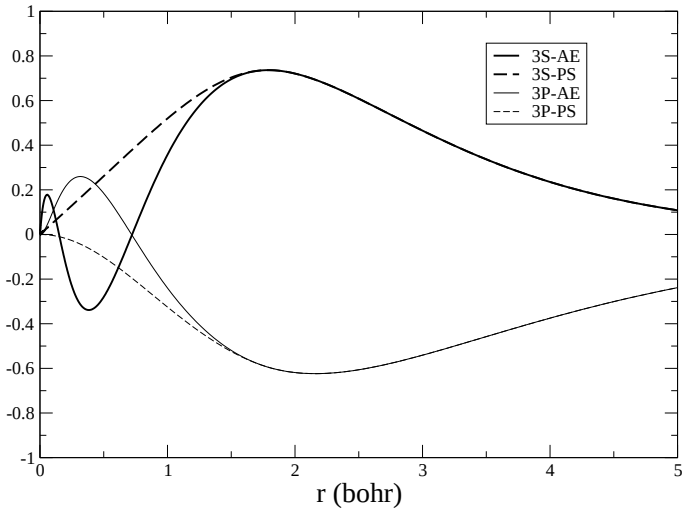

Figure 4.3: Silicon PAW pseudo KS wavefunctions - Showing smoothed valence states with softer cut-off radii.

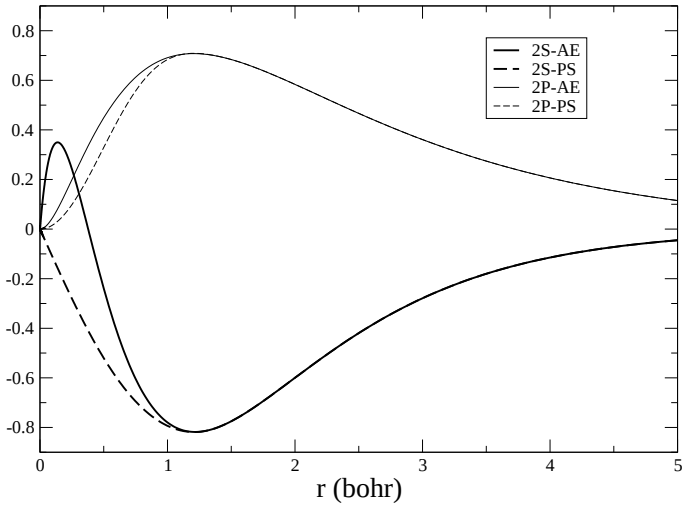

Figure 4.4: Carbon PAW pseudo KS wavefunctions - Showing smoothed valence states with harder cut-off radii closer to the core.

kinetic energy cut-off. This can be done by doing SCF total energy calculations over a range of **k**-point grids at a fixed energy cut-off and a range of energy cut-offs at a fixed **k**-point grid size and observing the convergence behavior for the total energy. This method has the disadvantage that the 2D parameter space is only sampled along fixed lines that may not find the lowest, most optimum values. It has the advantage of being a straightforward method to obtain values that will give the desired accuracy in total energy.

Some DFT software codes such as VASP/MedeA, have automated convergence tools that suggest values for the **k**-point grid size and energy cut-off for the system under consideration and even for the type of calculation to be done (total energy or structure optimization). The 2D parameter space is sampled while testing various convergence criteria set by the user to see if the desired accuracy is met for the desired calculation. Total energy convergence is tested for SCF calculations while the convergence of various criteria such as bond-length and unit cell angle are also tested in the case of structure optimization calculations. Although these automated methods greatly simplify the process of choosing suitable calculation parameters, they are not infallible, as discussed below, and must be verified and not taken at face-value.

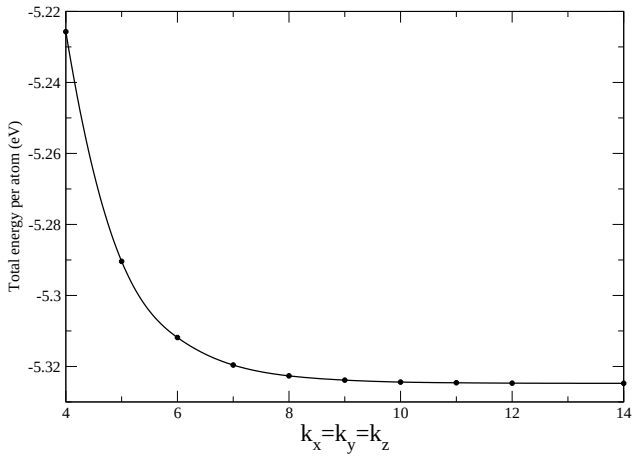

Figure 4.5: Silicon k-point convergence - Showing grid size versus total energy taken with $E_{cut} = 500$ eV.

In order to find suitable **k**-point and cut-off energy parameters, convergence tests

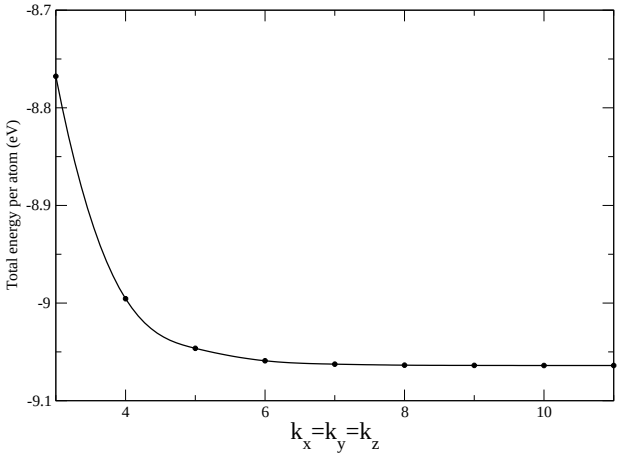

Figure 4.6: Carbon k-point convergence - Showing grid size versus total energy taken with $E_{cut} = 700$ eV.

were done on VASP for C and Si in the diamond structure (at their experimental lattice constants) using non-spin polarized calculations. The values must be chosen such that a reasonable compromise exists between numerical accuracy and the computational effort required. The **k**-point grid for Si was varied from 4×4×4 to 14×14×14 at an energy cut-off of 500 eV (slightly higher than the recommended value suggested by VASP/MedeA for its PAW pseudopotential) as shown in Fig. 4.5. It shows that the total energy is adequately converged to within 1 meV at a grid size of 11×11×11.

The **k**-point convergence test for C, shown in Fig. 4.6, was done at an energy cut-off of 700 eV, indicating that the same grid size as for Si will give a similar convergence to within 1 meV.

These grid sizes were then used to test the convergence of the energy cut-off for each atomic species. The test for Si, shown in Fig. 4.7, shows that an energy cut-off of 400 eV is a suitable value to use and will only result in errors in the energy of no more than 1 meV. Fig. 4.8 shows that the test for C indicates that a value of 800 eV is a reasonable compromise, and will also result in similar errors. As expected, the cut-off for C is larger than the cut-off for Si due to the node-less p state.

It is interesting to note that the automated convergence tool for VASP/MedeA gave a cut-off value of 400 eV for C since the convergence criteria was satisfied at the onset

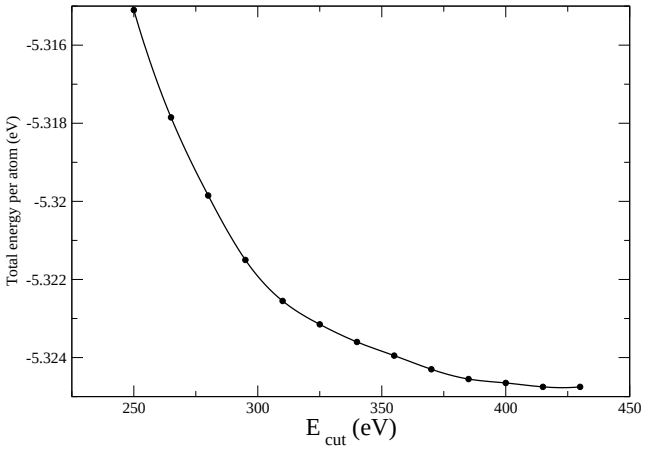

Figure 4.7: Silicon cut-off kinetic energy convergence - Showing E_{cut} versus total energy taken with $k_x = k_y = k_z = 11$.

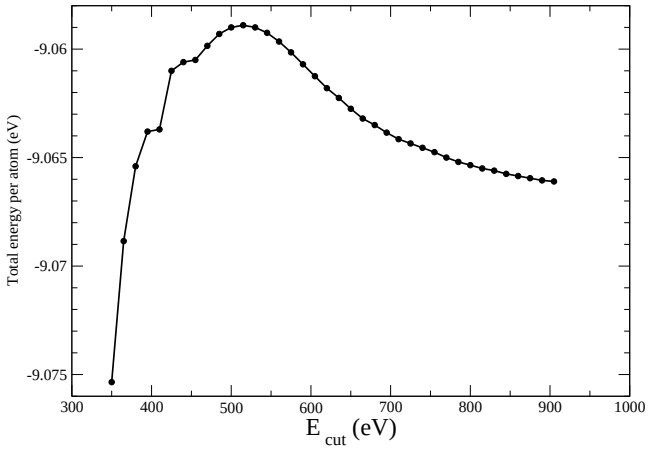

Figure 4.8: Carbon cut-off kinetic energy convergence - Showing E_{cut} versus total energy taken with $k_x = k_y = k_z = 11$.

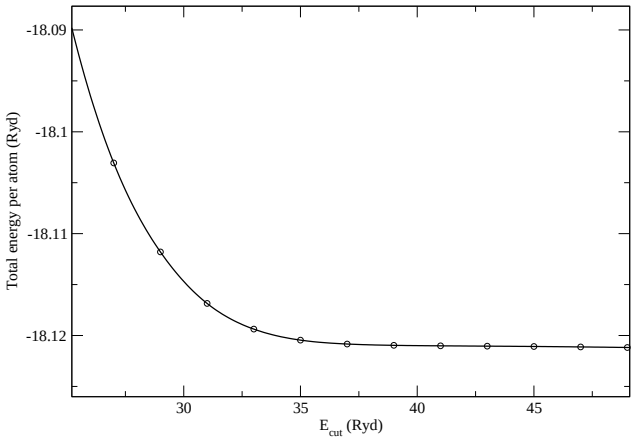

Figure 4.9: Carbon cut-off kinetic energy convergence using QUANTUM ESPRESSO - Showing E_{cut} versus total energy taken with $k_x = k_y = k_z = 11$.

of the energy hump seen in Fig. 4.8. Usually for structure optimizations, the cut-off should be increased by 30% to ensure a well converged energy therefore correct diagonal components for the stress tensor[130]. If this is done using a value of 400 eV, the increased cut-off, located further up the energy hump, results in a worse energy convergence. This shows the importance of verifying the results of automated methods.

In contrast, doing a similar convergence test on QUANTUM ESPRESSO with its carbon PAW did not yield this feature. This can be seen in Fig. 4.9 which shows that the total energy is reasonably converged at a cut-off value of ~36 Ryd (~500 eV). This shows that the hump seen in Fig. 4.8 is a consequence of how VASP implements the PAW method. It is known that VASP uses an automatic convergence correction based on the kinetic energy of the wavefunctions. For bulk materials, this correction is only partial and may cause the total energy to increase with increasing energy cut-off[131], as is the case here.

4.1.2 Chosen calculation parameters

All calculated material properties used the criteria of total energy convergence. Subsequent calculations done on VASP were done using the carbon energy cut-off value of 800 eV except for calculations that relied on energy differences, such as finding phase

transitions and EOS fits, where a lower cut-off of 500 eV was used. All calculations on QUANTUM ESPRESSO used a value of 500 eV.

The total number of **k**-points used for both plane-wave codes was chosen to be 11×11×11 except for calculations that comparing various allotropes. For these calculations, the **k**-point density of the Brillouin Zone for each structure has to be kept constant. When the number of chemical units scales when comparing a second allotrope structure to a first, the unit cell volume of the second structure approximately scales by the same factor. This results in its Brillouin Zone decreasing by approximately the same factor. For these reasons, the **k**-point density for the second structure can be kept more or less the same as the first by scaling down the total number of **k**-points used by the first structure by the same factor and using this recalculated number to define the **k**-point grid for the second structure. In the case of finding phase transitions for metallic systems, a larger number of **k**-points were used to better resolve the Fermi surfaces.

Calculations done on the silicon, carbon and silicon carbide systems to verify the methods to be used to investigate off-50:50 Si-C alloy systems are reported. For the silicon and silicon carbide systems, known and well established phases were used for method verification. For the carbon system, in addition to the well studied diamond and graphite phases, three under-reported theoretical phases were studied in detail namely the supercubane, C_4 and glitter phases. The calculations looked at bonding characteristics, electronic properties, as well as elastic and dynamical stability while verifying possible phase transitions.

4.2 Silicon allotropes

The different known allotropes of silicon are Si-I cubic diamond (*cd*), Si-II beta-tin (β-*Sn*), Si-III 8-atom body-centered (BC8), Si-V simple hexagonal (*sh*), Si-VI *Cmca*, Si-VII hexagonal closed-packed (*hcp*), and Si-X face-centred cubic (fcc) with Si-I being the stable form at ambient conditions while the others are all high pressure phases.

The symmetry group, Wyckoff positions, crystal system and lattice type for each structure are given in Table. 4.1. In the symbol notation for space groups, the letter at the beginning of the group name indicates the lattice type where F indicates a face-

centered lattice, I indicates a body-centered lattice, P indicates a primitive centered lattice while C indicates a base-centered lattice.

Table 4.1: Symmetries of silicon allotrope structures.

Structure	Symmetry Group	Wyckoff positions	Crystal system	Lattice type
Si-I cd	$Fd\bar{3}m$	$8b$	cubic	face-centered
Si-II β-Sn	$I4_1/amd$	$4b$	tetragonal	body-centered
Si-III BC8	$Ia\bar{3}$	$16c$	cubic	body-centered
Si-V sh	$P6/mmm$	$1a$	hexagonal	primitive-centered
Si-VI $Cmca$	$Cmca$	$8f$, $8d$	orthorhombic	base-centered
Si-VII hcp	$P6_3/mmc$	$2c$	hexagonal	primitive-centered
Si-X fcc	$Fm\bar{3}m$	$4a$	cubic	face-centered

4.2.1 Bonding and electronic properties

Bonding in bulk materials is made up mainly of four types, namely directional covalent, electrostatic ionic, delocalized metallic and for layered materials, the weak van der Waals interaction. By looking at the bonding characteristics of silicon allotropes, we see various mixtures of covalent and metallic types. The bonding influences the electronic properties of the material, determining whether the material is metallic or an insulator. The number of valence electrons for Si is even and therefore both possibilities exist.

Bonding properties are determined by the structure of the charge density and the localization of bonding electrons. These are given by charge density and electron localization function (ELF) plots.

Charge density plots show the concentration of valence charge after the SCF for a given plane slice through the structure. The charge density is shown as a contour plot with dense lines indicating a large gradient in the charge density and a greyscale indicating increasing concentration of charge.

An ELF plot is an indication of where valence electron pairs are likely to be located in a given plane slice through the structure. The function outputs a value of 1 for complete localization of electron pairs and 0 for complete delocalization. It is also shown as a contour plot with a greyscale where white represents 0 and the darkest grey

represents a value of 1. These dark regions define areas of localization. For any given structure, the values lie somewhere between 0 and 1.

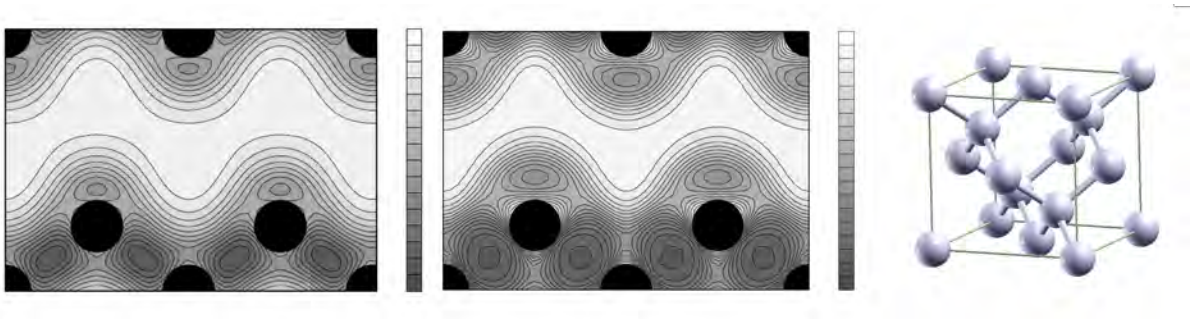

Figure 4.10: Si-I diamond structure - Showing a charge density plot (left) and an ELF plot (middle) for the (110) plane.

The first structure to be considered is a good example of strong sp^3 covalent bonding with eight four-fold coordinated atoms arranged in a face-centered cubic (fcc) lattice. The geometrically optimized Si-I diamond structure is shown in Figure. 4.10 with an ELF plot for the (110) plane (shown in the middle) and a charge density plot for the same plane shown on the left. The charge density plot shows large concentrations of charge between nearest neighbors with a lack of charge in the interstitial sites. The ELF plot shows well defined regions of strongly directional localization between nearest neighbors (dark grey circular contours henceforth referred to as covalent lobes) with white space between atoms indicating complete delocalization (due to lack of charge). This is indicative of strongly directional (covalent) bonding between atoms where bonding pairs of electrons are located in the strongly localized regions with none being available for conduction. The calculated band structure is given in Figure.4.11 where an indirect band gap of 0.4 eV is clearly seen showing this material to be an insulator with a completely filled valence bands. The actual band gap of silicon-diamond is wider with a value of 1.17 eV[132]. This is not surprising since although PBEsol is known to better describe physical properties does not guarantee that it will accurately describe the electronic properties. Other methods, such as the GW method, provide better values but at great computational expense[133]. The diamond structure is a good example of strong tetrahedral covalent bonding where the atoms share a valence electron with each neighbor allowing them to satisfy the octet rule. The atoms are

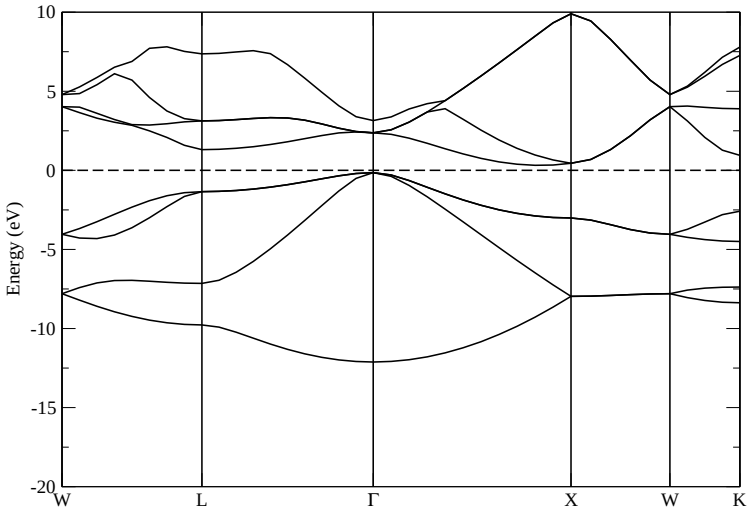

Figure 4.11: Si-I band structure - Showing an indirect band gap of 0.4 eV. Energies shifted to Fermi level.

tetrahedrally bonded with an internal bonding angle of 109.47° and bond lengths of d_{Si-Si}=2.35 Å.

Si-III, shown in Figure. 4.12, is a 16-atom body-centered cubic structure with an internal parameter x to describe the internal positions of the atoms. It has an 8-atom unit cell and is therefore referred to as BC8. The charge density plot for the (110) plane shows a large concentration of charge between nearest neighbors while the ELF plot shows well defined covalent lobes between nearest neighbors. This indicates covalent bonding with four-fold coordination, with distorted tetrahedral bonding with three angles of 98.4° and three of 117.9°. We define a measure of the bonding distortion called the MAO (mean absolute offset)[1]. It is the mean offset of these angles from their ideal values, assuming four-fold atoms should ideally be tetrahedrally bonded with six internal angles of 109.47°. This gives an MAO of 8.9%. The band structure plot in Figure. 4.13 shows that this phase is a semi-metal with the upper valence and lower conduction bands meeting at the symmetry point H. This is in agreement with the 1984

[1]where $MAO = \frac{1}{N}\sum_{n=1}^{N}\left|\frac{X_0 - X_n}{X_0}\right| \times 100\%$

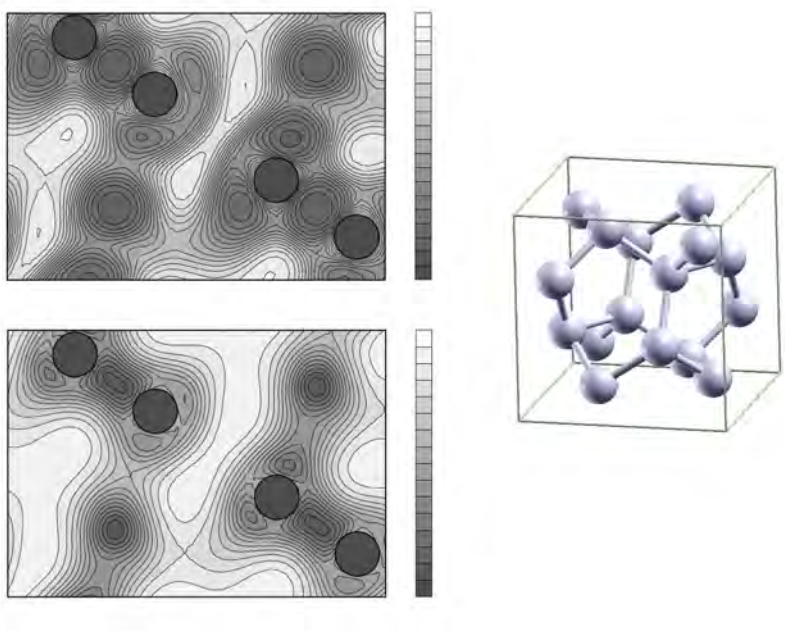

Figure 4.12: Si-III BC8 structure - Showing an ELF plot (top) and a charge density plot (bottom) for the (110) plane.

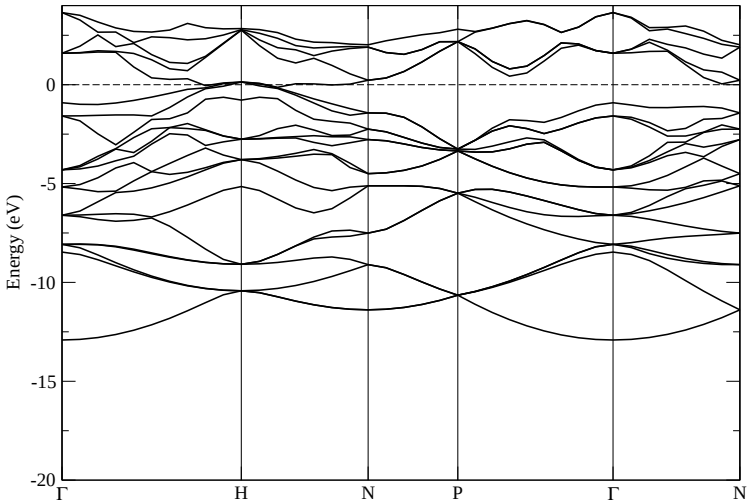

Figure 4.13: Si-III band structure - Showing it to be semi-metallic. Energies shifted to Fermi level.

LDA calculations of Biswas et al. [21] which predicted the same result.

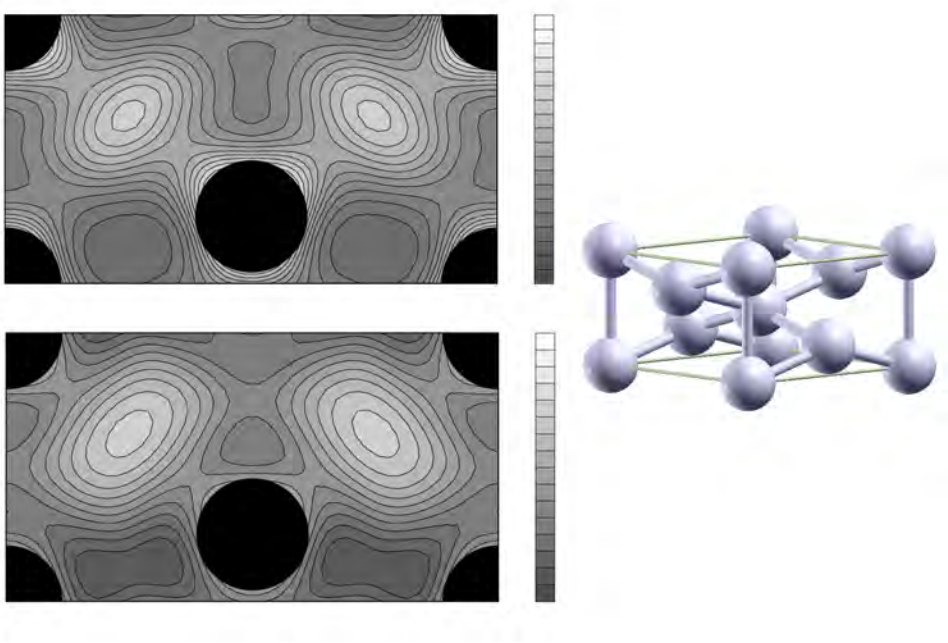

Figure 4.14: Si-II β-Sn structure - Showing an ELF plot (top) and a charge density plot (bottom) for the (100) plane.

The next allotrope, Si-II, has a body-centered tetragonal lattice. Its six-fold coordinated silicon atoms shows directional covalent bonding with a strong metallic component. The structure is shown in Figure. 4.14 with an ELF and charge density plot taken in the (100) plane. The ELF plot shows that for each silicon atom, there is some localization between neighbors but that the localization is less intense and more spread out compared to that in Si-I and Si-III. The charge density plot shows lateral concentrations of charge between these atoms. This gives the bonding a mix of directional covalent bonding (mainly in the horizontal plane) along with a general metallic character. This is not uncommon since, as stated before, bonding in many materials is not strictly covalent, ionic or metallic, but a combination of two or more of these. It is expected that this material should be a metal since there is a significant delocalization component to the bonding. This is indeed the case as can be seen in the band structure plot in Figure. 4.15.

Si-V is another example of a covalent/metallic mix with 8-fold coordinated silicon atoms arranged in a hexagonal conventional cell with a primitive-centered lattice. The

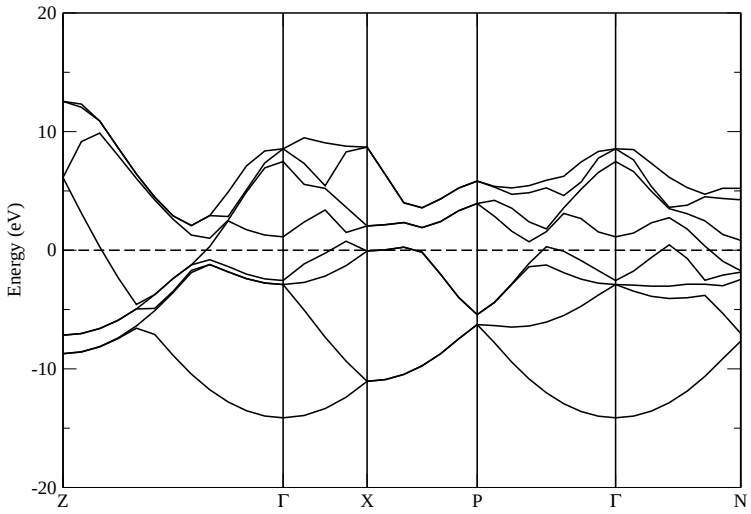

Figure 4.15: Si-II β-Sn band structure - Showing it to be metallic. Energies shifted to Fermi level.

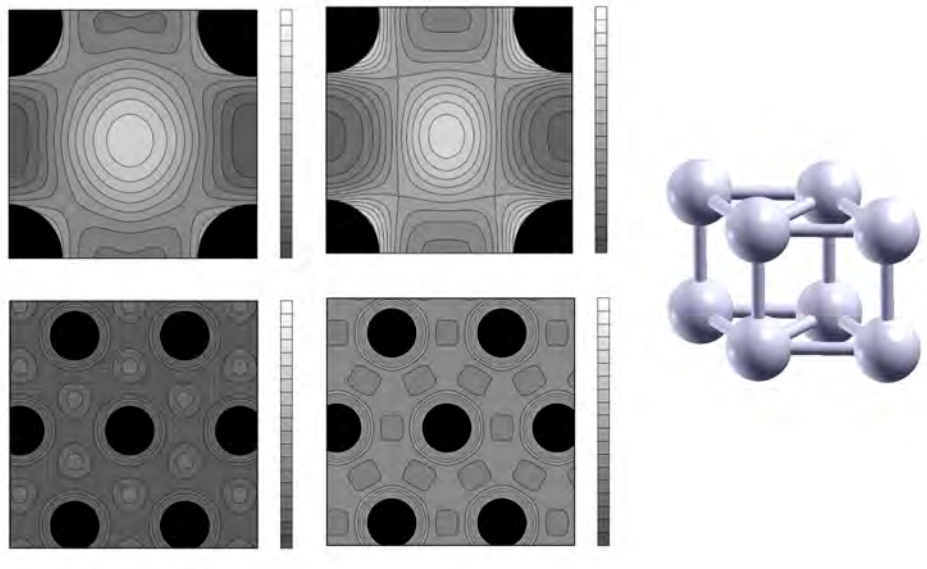

Figure 4.16: Si-V simple hexagonal structure - Showing two sets of charge density (left) and ELF (middle) plots. The upper set for the (100) plane and the lower set for the (001) plane.

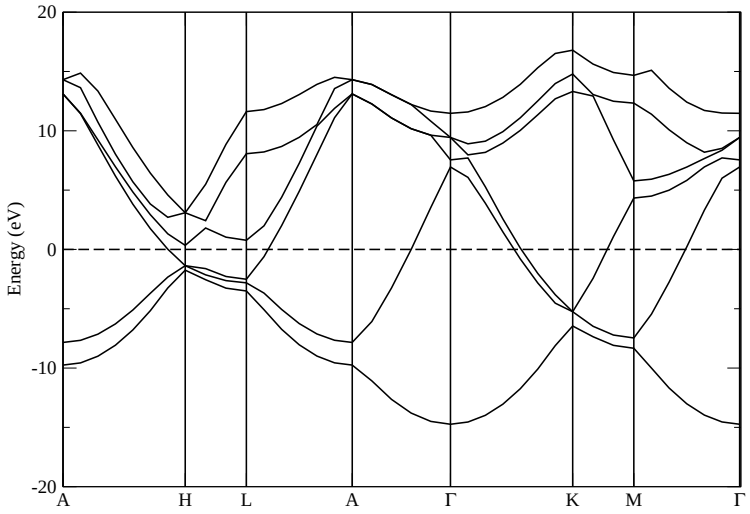

Figure 4.17: Si-V band structure - Showing it to be metallic. Energies shifted to Fermi level.

ELF and charge density plots for Si-V are shown in Figure. 4.16. They show that there is slight covalency in the bonding between layers with greater delocalization within the layers indicating metallic bonding. This covalent admixture has been noted before by Chang and Cohen [134]. The delocalized metallic bonding makes this material a metal, as can be seen in the band structure plot of Figure. 4.17.

The last two structures, both with 12-fold coordinated silicon atoms, are examples of strong metallic bonding. The ELF and charge density plots for primitive-centered hexagonal Si-VII, shown in Figure. 4.18, show that there is extensive delocalization of the valence electrons throughout the structure, the hallmark of a material with metallic bonding. The charge density and ELF plots for the (100) plane in fcc Si-X, shown in the upper row of Figure. 4.20, show a slight directionality to the charge distribution and bonding with the ELF plot showing significant delocalization of bonding pairs of electrons between atoms. The plots for the (110) plane (bottom row) show significant charge in the interstitial sites along with electron delocalization. This is indicative of strong metallic bonding. The metallic bonding in both structures is reflected in their

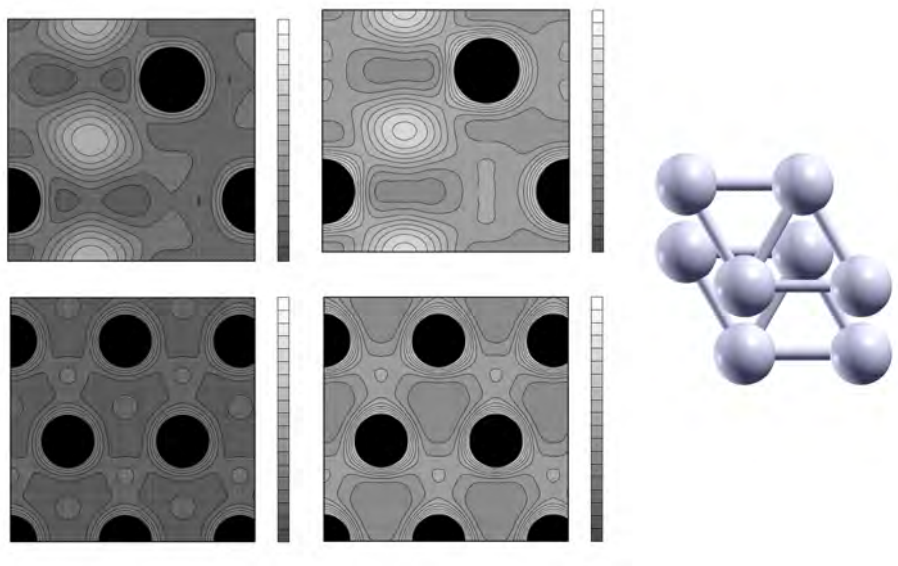

Figure 4.18: Si-VII hexagonal closed packed structure - Showing two sets of charge density (left) and ELF (middle) plots. The upper set for the (100) plane and the lower set for the (001) plane. The overlapping hexagonal layers as seen from the top are shown on the right.

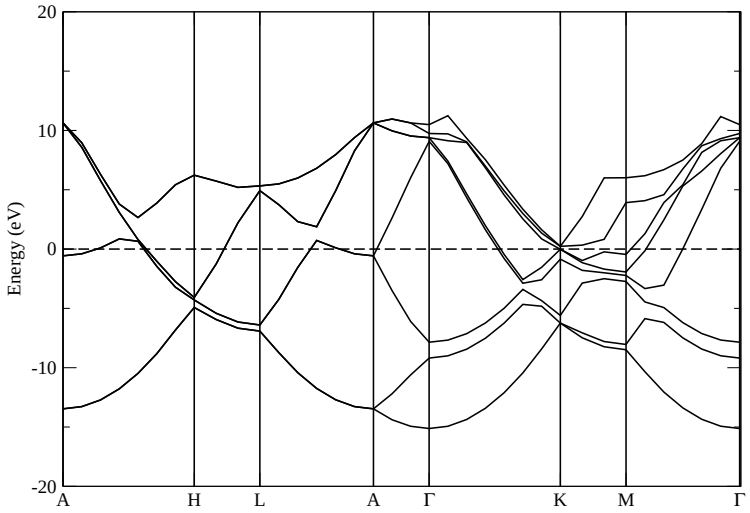

Figure 4.19: Si-VII band structure - Showing it to be metallic. Energies shifted to Fermi level.

band structures shown in Figures. 4.19 and 4.21.

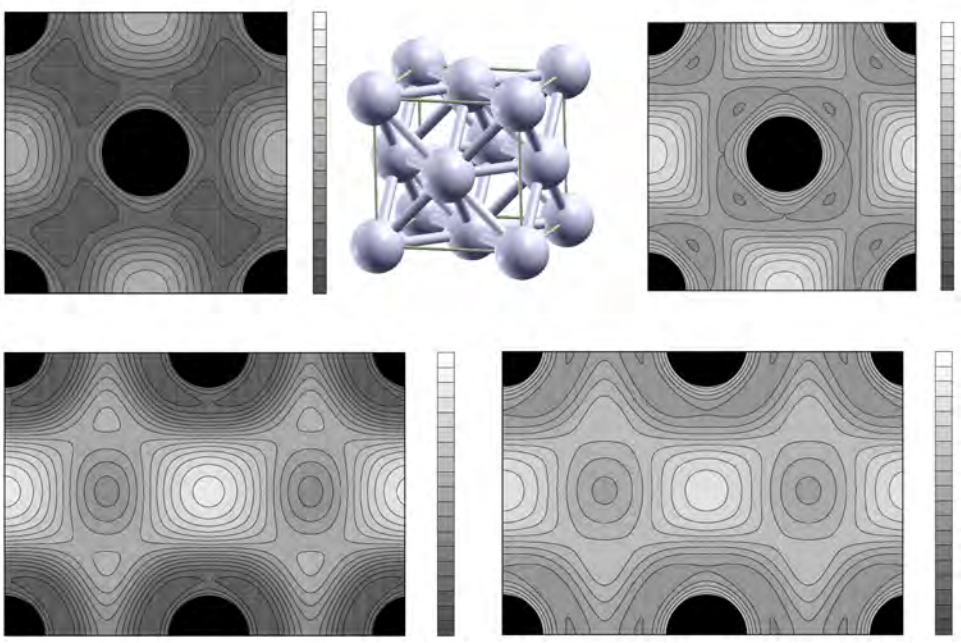

Figure 4.20: Si-X FCC structure - Showing a charge density plot (left) and an ELF plot (right) for the (100) plane (top) and the (110) plane (bottom).

4.2.2 Equation of state

Birch-Murnaghan equation of state (EOS) fits were done on total energy versus volume data obtained by doing full structural optimization on each structure at different external pressures in a range from -8 GPa to 8 GPa . The pressure range gave structure volumes within ±10 % of their equilibrium values (a volume range for which the Birch-Murnaghan EOS provides valid fit parameters). The EOS fit parameters are given in Table. 4.2 and the fitted curves in Figure 4.22. The results for Si-VI are not given since it was found to always relax into Si-V during the structural optimizations (this occurred since Si-VI is a transition structure for the pressure transition from Si-V into Si-VII). The EOS fitted curves in Figure 4.22 are all to the left and higher than Si-I. This indicates that diamond silicon is the most energetically stable allotrope with the other phases accessible through pressure transitions. For example, a positive pressure tangent line is shown in Figure. 4.22 between diamond and β-Sn representing a

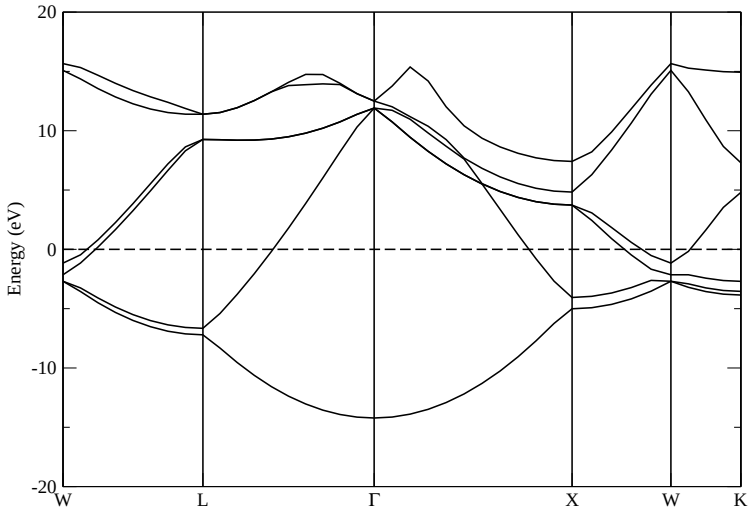

Figure 4.21: Si-X band structure - Showing it to be metallic. Energies shifted to Fermi level.

Table 4.2: Silicon allotrope Birch-Murnaghan EOS fits (volume V_0 per atom in Å^3, lattice parameter a_0 in Å, bulk modulus B_0 in GPa and heat of formation H_f per atom in kJ mol^{-1}).

		V_0	a_0	c/a	b/a	B_0	B_0'	B_0''	H_f
Si-I	*cd*	20.09	5.44	1.0	1.0	94.0	4.26	-0.045	0
Si-II	β-Sn	15.02	4.78	0.549	1.0	117.3	4.66	-0.043	18.3
Si-III	BC8[a]	18.00	6.60	1.0	1.0	90.8	4.24	-0.046	11.6
Si-V	*sh*	14.80	2.63	0.938	1.0	114.4	4.40	-0.039	19.8
Si-VII	*hcp*	13.96	2.67	1.691	1.0	97.0	4.36	-0.045	37.3
Si-X	*fcc*	14.08	3.83	1.0	1.0	94.4	3.87	-0.040	40.3

[a] x=0.10

transition path between the phases. BC8 is a meta-stable phase accessible by slow decompression of Si-II as shown by the negative pressure tangent line from Si-II to Si-III. In Table. 4.2, the bulk moduli for all the allotropes are all comparable to that of Si-I. The results show that the bulk moduli all respond in a near linear manner to changes in pressure around P=0 through Eqn. 3.93 since $|B_0''| < B_0'$.

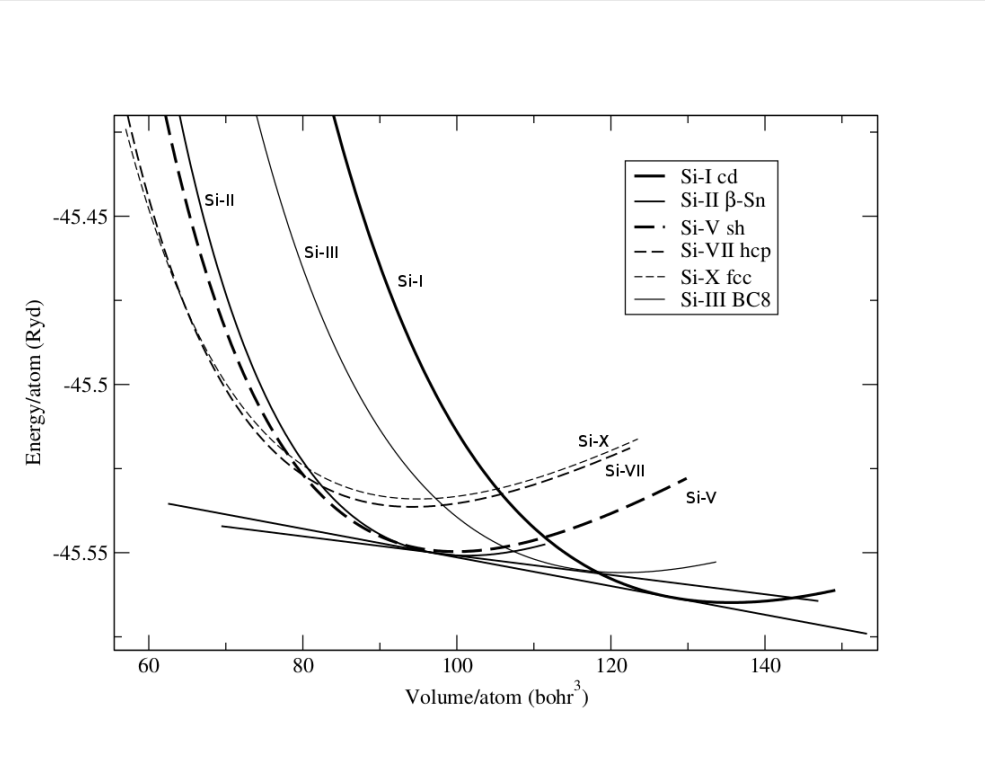

Figure 4.22: Silicon Birch-Murnaghan EOS fits - Showing energy vs volume EOS fits, a positive pressure tangent line from *cd* to β-Sn and a decompression pressure line from β-Sn to BC8.

The heats of formation H_f increase down the column (except for Si-III which is between Si-I and Si-II), indicating that energy is required to form the other structures.

The value for the equilibrium lattice constant a_0 for Si-I is very close to the experimental value to within 0.2% and the bulk modulus is within 5%[135]. The energy of formation for this structure is set at 0 kJ mol^{-1}, since it is the naturally occurring stable phase for silicon at ambient conditions.

The values for Si-II compare well with the PBEsol results of Hennig et al.[136] who obtained a=4.79 Å, c/a=0.548, B_0=115.0 GPa and B_0'=4.52.

The values for Si-III compare well with the values of Biswas et al. [30] who calculated B_0=91.8 GPa, B_0'=3.79 with an internal parameter of 0.1022. The lattice parameter also compares well with the experimental value of a=6.64 Å reported by Wentorf and Kasper [15].

A detailed analysis of the bulk modulus values is given in subsection 4.2.4.

4.2.3 Phase transitions

The phases transform from Si-I (coordination 4) → Si-II (coordination 6) → Si-V (coordination 8) → Si-VII (coordination 12) → Si-X (coordination 12). The trend in the bonding, as the pressure is increased, is from fully covalent Si-I with increasing delocalization to fully metallic Si-X.

The predicted transition pressures were obtained by first geometrically relaxing each structure at different pressures and calculating the enthalpies. Enthalpy versus pressure curves were then plotted for two candidate structures to establish where the two curves crossed, indicating the pressure at which the two phases co-exist. The first phase has the lower curve below this transition pressure and the higher curve after. This indicates that after the transition pressure, the material is transformed from the first phase into the second. Although both LDA and PBEsol calculations were done, only the LDA calculated Enthalpy-Pressure plots for each phase transition are given in Figures 4.23 to 4.26.

To ensure comparable accuracy in the energies, $8000/n$ **k**-points were used for the metallic structures where n is the number of atoms per unit cell.

A summary of the values predicted by enthalpy versus pressure data for LDA and PBEsol are given in Table. 4.3 along with the experimental ranges. It is clear that the PBEsol values become more accurate for the higher pressure transitions.

4.2.4 Elastic properties and stability

The stability of a structure can be evaluated by calculating the elastic constants and plotting the phonon dispersion curves. Positive eigenvalues for the stiffness matrix and positive elastic moduli indicate elastic stability while soft modes (imaginary phonon frequencies indicated by negative numbers) in the phonon dispersion indicate that the structure tends to re-arrange into a new phase.

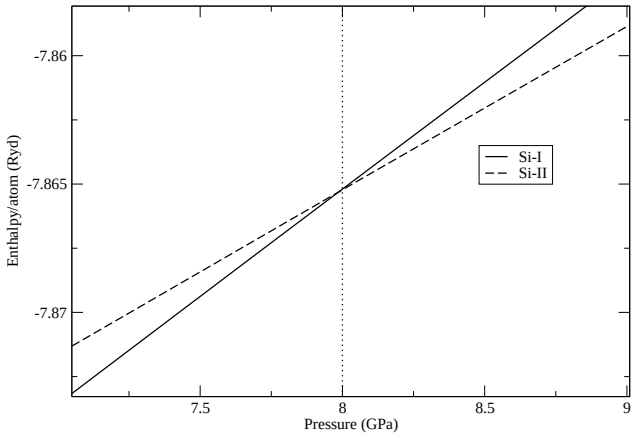

Figure 4.23: Si-I to Si-II phase transition - Showing LDA calculated transition pressure at 8.0 GPa.

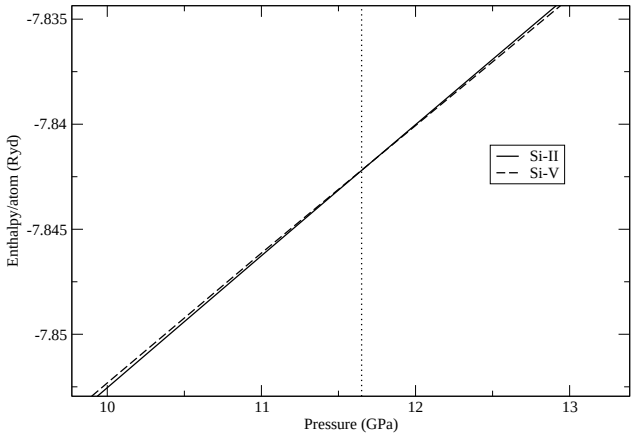

Figure 4.24: Si-II to Si-V phase transition - Showing LDA calculated transition pressure at 11.7 GPa.

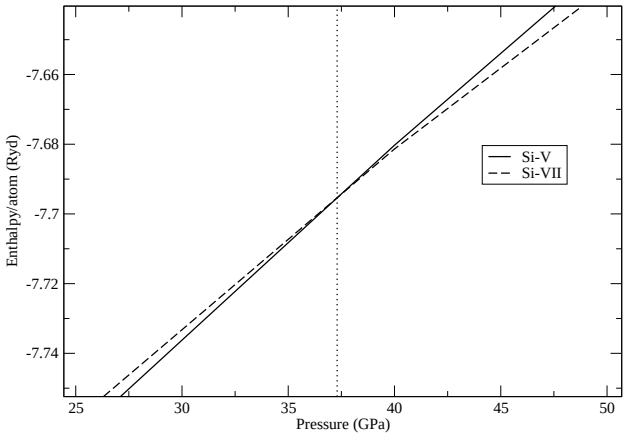

Figure 4.25: Si-V to Si-VII phase transition - Showing LDA calculated transition pressure at 37.3 GPa.

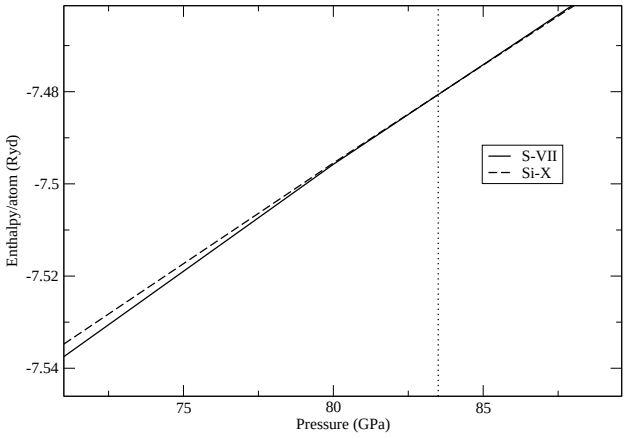

Figure 4.26: Si-VII to Si-X phase transition - Showing LDA calculated transition pressure at 83.5 GPa.

Table 4.3: Silicon phase transition pressures in GPa.

Transition	LDA	PBEsol	Experiment
I→II	8.0	6.4	11.3∼12.5[a]
II→V	11.7	9.6	13.2∼16.4[a]
V→VII	37.3	31.8	41.8±0.5[b]
VII→X	83.5	73.0	79±2[b]

[a] Hu et al.[23]

[b] Duclos et al.[137]

The calculated elastic constants of the equilibrium structures are shown in Table. 4.4 and the calculated elastic properties are listed in Table. 4.5. The modulus values in Table. 4.5 show the upper bound Voigt, lower bound Reuss and averaged Hill values. All structures are elastically stable since the eigenvalues of the stiffness matrices are all positive as are the elastic moduli. This is also reflected in the fact that their elastic moduli are all positive as well. The elastic constants for Si-I in Table. 4.4 are within 8% of the experimental values of McSkimin[138].

Table 4.4: Calculated elastic constants for Si allotropes (in GPa) showing numerical error estimates.

	C_{11}	C_{12}	C_{13}	C_{33}	C_{44}	C_{66}
Si-I	156.6 ± 0.5	62.6 ± 0.5			73.8 ± 0.7	
Expt. Si-I[a]	167.4	65.23			79.57	
Si-II	148.8 ± 2.2	129.8 ± 2.2	83.8 ± 1.6	157.4 ± 2.2	40.1 ± 3.1	91.2 ± 3.1
Si-III	179.1 ± 0.6	51.3 ± 0.6			71.7 ± 0.6	
Si-V	172.5 ± 2.7	120.4 ± 2.6	36.5 ± 1.9	311.7 ± 2.7	83.1 ± 3.8	
Si-VII	157.6 ± 6.2	101.0 ± 6.2	53.3 ± 4.4	135.9 ± 5.5	42.3 ± 8.8	
Si-X	113.0 ± 1.6	78.4 ± 1.6			4.55 ± 2.3	

[a] McSkimin[138]

The EOS derived bulk modulus values, show in parentheses in Table. 4.5, are reasonably close to the Hill values. It is apparent that Si-I and Si-III have quite similar bulk, shear and Young's modulus values. This is due to their tetrahedral covalent bonding. Si-II and Si-V also have very similar bulk moduli due to their metallic bonding with

a mostly uni-directional covalent admixture (planar in Si-II and along the c direction for Si-V). It is interesting to note that both structures have values greater than that for Si-I. The mostly metallic, closed packed structures of Si-VII and Si-X have differing bulk moduli of 94.6 and 89.9 GPa respectively, which can be explained by Si-VII having the higher packing fraction.

In general, Si-V has a similar shear and Young modulus to Si-I due to the covalent bonding between its hexagonal layers. The shear and Young's moduli decrease from Si-V to Si-X due to the increasing delocalization of the valence electrons, with Si-X having very low values due to its weaker metallic bonding.

The Debye temperatures in Table. 4.5 rank in the same order as the Young's and shear modulus also giving an indication of the increase in structural weakness.

Table 4.5: Calculated elastic moduli for Si allotropes (in GPa) showing Voigt, Reuss and geometric mean Hill values. EOS derived bulk moduli are given in parentheses. Debye temperature is expressed in Kelvin.

	B_V	B_R	B_H	G_V	G_R	G_H	Y_V	Y_R	Y_H	Θ_D
Si-III	93.9	93.9	93.9 (90.8)	68.6	68.4	68.5	165.5	165.1	165.3	645
Si-I	93.8	93.8	93.8 (94.0)	63.1	60.1	61.6	154.5	148.6	151.6	625
Si-V	116.0	115.1	115.6 (114.4)	69.3	46.0	57.7	173.4	121.7	147.6	578
Si-VII	96.2	92.9	94.6 (97.0)	38.8	36.3	37.6	102.6	96.4	99.5	465
Si-II	116.7	115.5	116.1 (117.3)	44.8	26.4	35.6	119.1	73.6	96.4	460
Si-X	89.9	89.9	89.9 (94.4)	9.6	6.5	8.1	27.9	18.9	23.4	219

The phonon dispersion plots for the various phases are given in Figures 4.27 to 4.31. These were done using the PBEsol functional at pressures slightly above the transition pressure for the previous phase. The dispersions were calculated at pressures slightly above the transition pressure for each structure. All show no soft modes. NOTE: The "soft mode" in Fig. 4.28 is most likely an artifact due to the long interaction between atoms causing missing force constants which resulted in a fake soft mode in the acoustic branch near Γ.

It is expected that at pressures close to the next phase transition for each allotrope, soft modes will appear in the dispersion plot indicative of an impending structural transition.

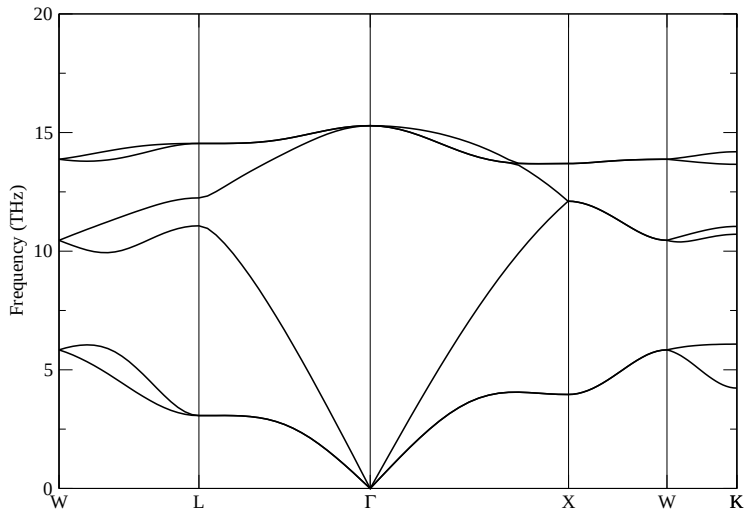

Figure 4.27: Si-I phonon dispersion at 0 GPa - Showing no soft modes.

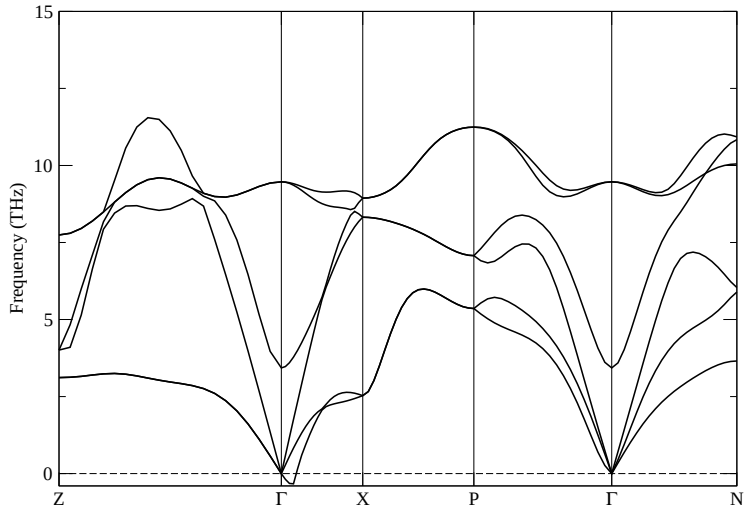

Figure 4.28: Si-II phonon dispersion at 7 GPa - Showing no soft modes except that at Γ which is a calculation artifact.

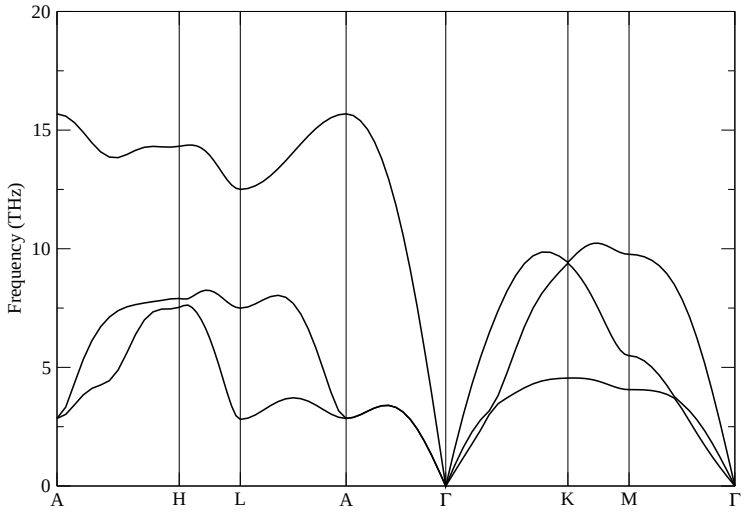

Figure 4.29: Si-V phonon dispersion at 10 GPa - Showing no soft modes.

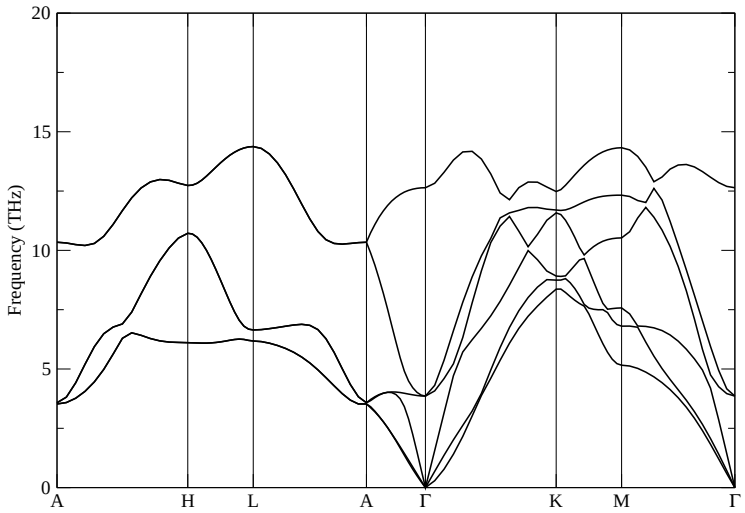

Figure 4.30: Si-VII phonon dispersion at 38 GPa - Showing no soft modes.

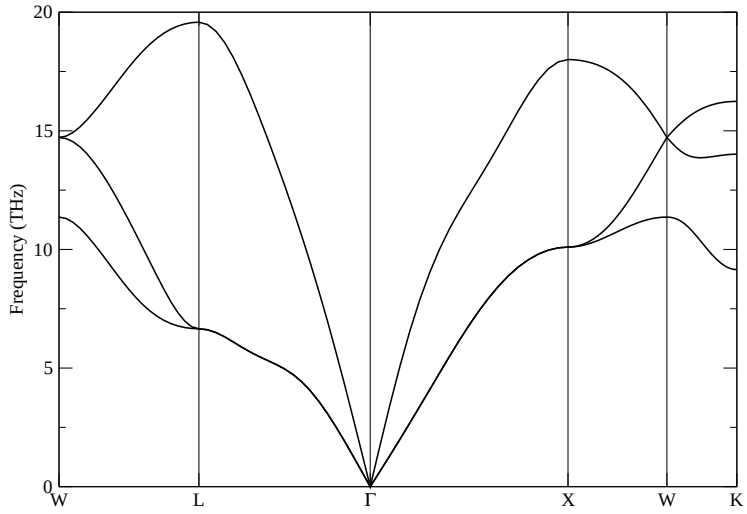

Figure 4.31: Si-X phonon dispersion at 75 GPa - Showing no soft modes.

4.3 Carbon

The two most commonly known forms of carbon are graphite and diamond. Recently, another allotrope has been proposed called the C_4 structure[35], possibly produced by the cold compression of graphite. A high pressure allotrope of carbon is thought to exist and two possible candidates are the BC8 structure[30] (as in silicon) and another body-centered structure called supercubane[29]. A fourth proposed phase for carbon is the theoretical allotrope for C called glitter[7]. The symmetry group, Wyckoff positions, crystal system and lattice type for each structure are given in Table. 4.6. The last four allotropes of BC8, Supercubane, C_4 and Glitter all have an internal parameter (x or in the case of glitter z) to describe the internal positions of the atoms.

Although diamond and graphite are well studied allotropes of carbon, BC8, C_4, supercubane and glitter have been under-reported in terms of their elastic, lattice dynamic and bonding properties which this study sought to rectify.

Table 4.6: Symmetries of carbon allotrope structures.

Structure	Symmetry Group	Wyckoff positions	Crystal system	Lattice type
Graphite	$P6_3/mmc$	2*b*,2*c*	hexagonal	primitive-centered
Diamond	$Fd\bar{3}m$	8*b*	cubic	face-centered
BC8	$Ia\bar{3}$	16*c*	cubic	body-centered
Supercubane	$Im\bar{3}m$	16*f*	cubic	body-centered
C_4	$I4/mmm$	8*h*	tetragonal	body-centered
Glitter	$P4_2/mmc$	2*e*,4*i*	tetragonal	primitive-centered

4.3.1 Bonding and electronic properties

As with silicon, the bonding in carbon was investigated and linked to the electronic properties of the various allotropes. Carbon also has an even valency so in principle, both metallic and insulating allotropes are possible.

Graphite, shown in Figure. 4.32 consists of stacked monolayers of carbon atoms in the honeycomb structure. We know that each carbon atom in graphite contributes three valence electrons for three covalent sp^2 bonds. This is reflected in the ELF plot for the (001) plane shown in the bottom row of Figure. 4.32 where it shows well defined regions of strong localization from each atom to its three nearest neighbors. The charge density plot also shows high concentrations of charge between atoms. The bond length for the sp^2 covalent bonding is d_{C-C}=1.42 Å. The ELF plot in the (110) plane, shown in the top row, shows that there is no localized covalent or delocalized metallic bonding between the layers. The inter-layer bonding is achieved through the weak van der Waals forces which are only mimicked by LDA. The fact that the material is metallic is shown in the band structure in Figure.4.33, where the touching of the upper valence band and the lower conduction bands at the H and K symmetry points indicate that graphite is a semi-metal.

Like silicon Si-I, each carbon atom in cubic diamond contributes four valence electrons to four directional tetrahedral covalent sp^3 bonds linking nearest neighbors. This is reflected in Figure. 4.34 where the ELF plot shows well defined areas of strong localization of bonding electron pairs between each atom and its nearest neighbors. As with silicon, it is expected that this material is an insulator since the charge density

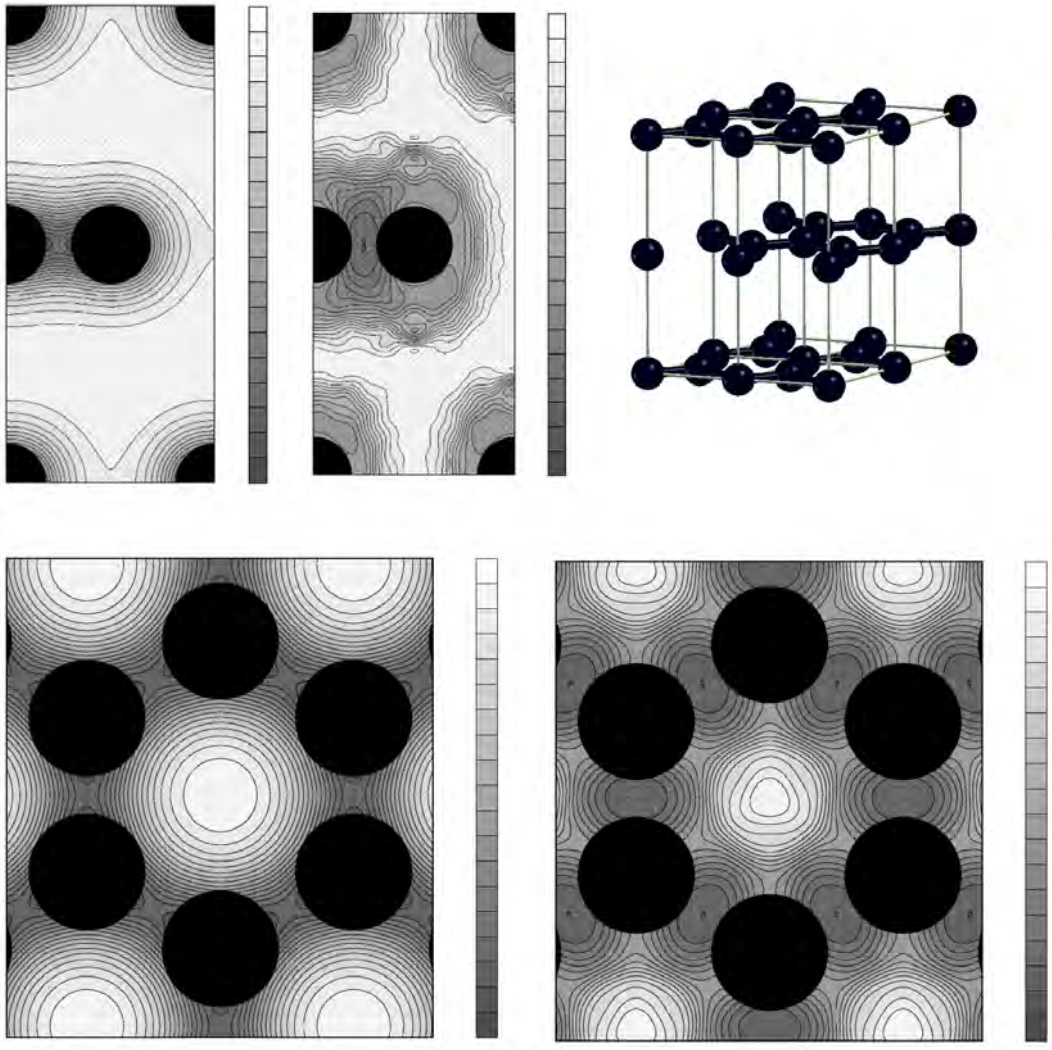

Figure 4.32: Graphite structure - Showing charge density plot (left) and ELF plot (right) for the (110) plane (top row) and for the (001) plane (bottom row).

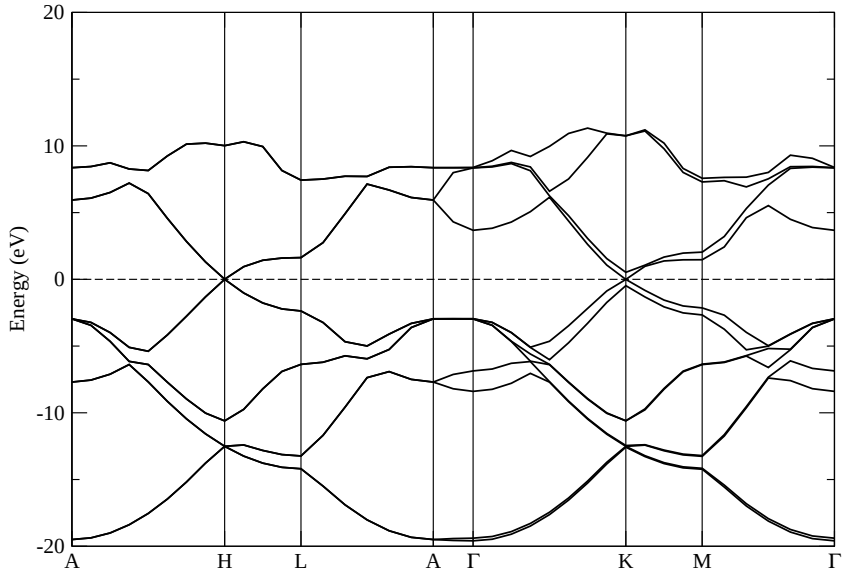

Figure 4.33: Graphite band structure - Showing it to be semi-metallic. Energies shifted to Fermi level.

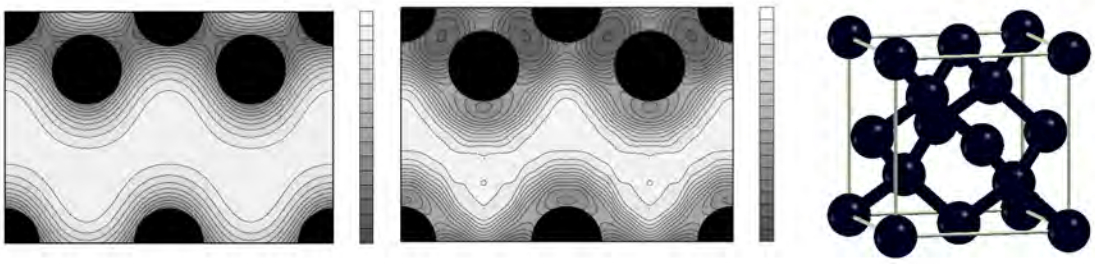

Figure 4.34: Diamond structure - Showing a charge density plot (left) and an ELF plot (middle) for the (110) plane.

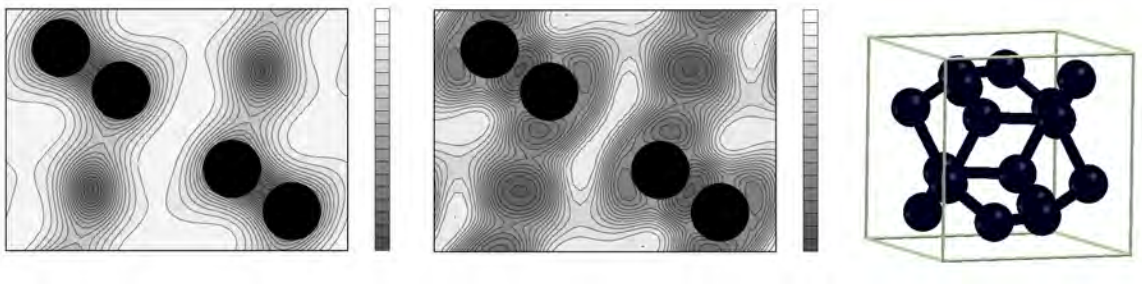

Figure 4.35: BC8 structure - Showing a charge density plot (left) and an ELF plot (middle) for the (110) plane.

plot shows no charge in the interstitial regions. This can be seen in the calculated band structure given in Figure.4.39 where an indirect band gap is clearly seen.

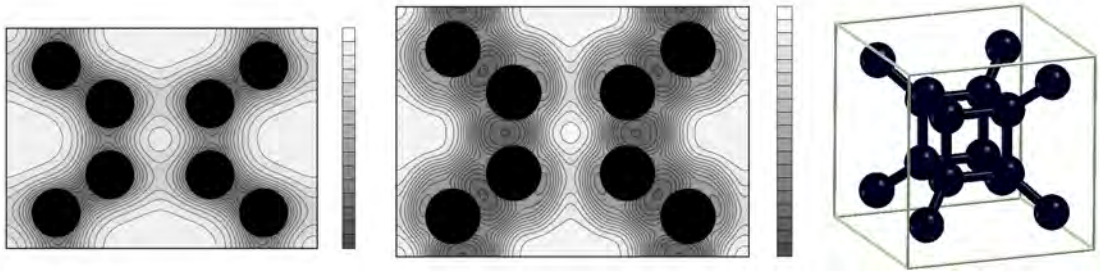

Figure 4.36: Supercubane structure - Showing a charge density plot (left) and an ELF plot (middle) for the (110) plane.

The bonding is similar for BC8, body-centered cubic supercubane and body-centered tetragonal C_4, seen in Figures. 4.35 to 4.37, as they all have 4-fold coordination with localized electron pairs and high concentrations of charge between nearest neighbors.

The tetragonal glitter structure is shown in Figure. 4.38 with the charge density and ELF plots shown in the left and middle for the (010) plane. The charge density plot shows that the charge is concentrated between nearest neighbors and the ELF plot shows covalent lobes between atoms. It has four-fold coordinated carbon atoms connected to trigonal bonded atoms.

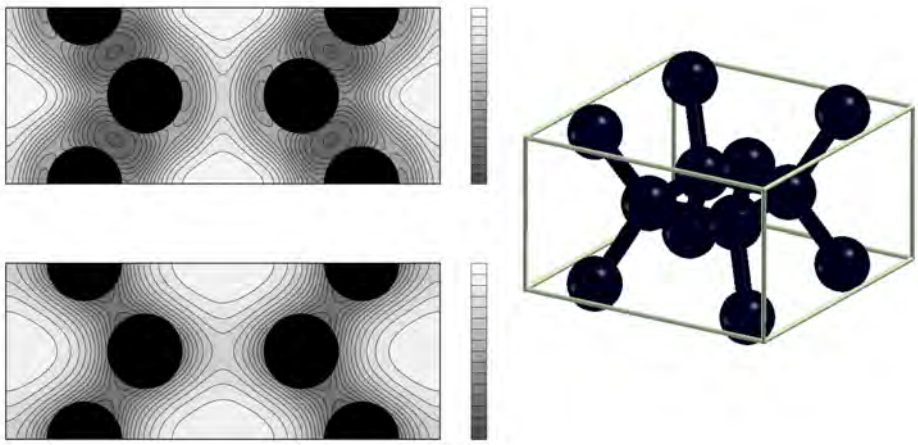

Figure 4.37: C_4 structure - Showing an ELF plot (upper) and a charge density plot (lower) for the (110) plane.

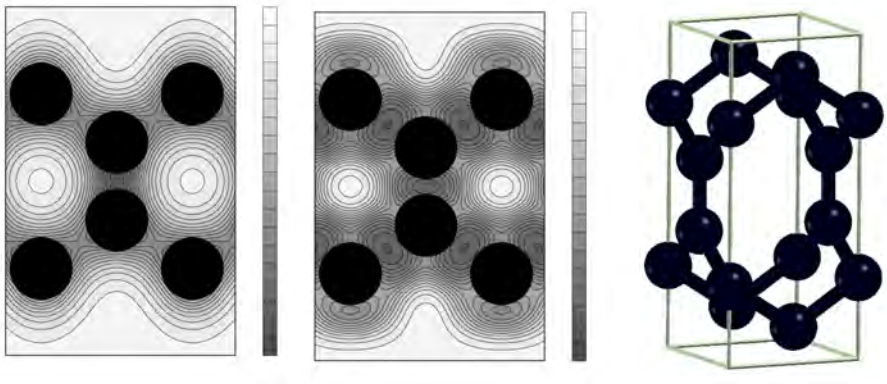

Figure 4.38: Glitter structure - Showing an ELF plot (middle) and a charge density plot (left) for the (010) plane.

Diamond has all six internal angles of 109.47°; BC8 has three angles of 101.2° and three of 116.3°; C_4 has four angles of 113.6°, one of 111.0° and one of 90°; supercubane has three angles of 90° and three of 125.26°; glitter has four angles of 106.9° and two of 114.7° for the four-fold coordinated atoms and two of 122.7° and one of 114.7° for the three-fold coordinated atoms. As with silicon, the MAO of these angles from their ideal values evaluates the amount of bonding distortion, assuming four-fold atoms should ideally be tetrahedrally bonded with six internal angles of 109.47° and three-fold atoms trigonally bonded with three internal angles of 120°. The tetrahedral bonding for the four-fold coordinated carbon atoms becomes increasingly distorted from diamond → glitter→ C_4 → BC8 → supercubane with MAO values of 0 %, 3.2 %, 5.7 %, 6.9 %, and 16.1 %. The MAO for the three-fold coordinated carbon atoms in glitter is 3.0 %. The bond lengths for diamond, BC8, and C_4 are d_{C-C}=1.54 Å (larger than that for sp^2 bonding) and for supercubane are d_{C-C}=1.47 and 1.58 Å. Glitter also has bond lengths of 1.53 Å but the three-fold coordinated carbon atoms are 1.35 Å apart, slightly larger than that for a carbon double bond where PBEsol predicts the double bond length in C_2H_4 to be d_{C-C}=1.33 Å. All structures have band gaps as is seen in Figures. 4.40 to 4.42. Graphite and glitter are the only structures that have a slight metallic nature, as seen in Figure. 4.43 and Figure. 4.33, with all structures being sp^3 covalent. The band structure for glitter is almost semi-metallic with a single lowest conduction band crossing the Fermi level at M as shown in Figure.4.43.

4.3.2 Diamond, BC8, Supercubane, C_4, Glitter - Equation of state and pressure transition

Fitting diamond, BC8, supercubane, C_4 and glitter to the Birch-Murnaghan equation of state using the PBEsol functional, as was done in the case of silicon, yields the values in Table. 4.7 and the fitted curves shown in Figure 4.44. The results for graphite are not discussed here as a different method was used to extract its EOS parameters.

Figure. 4.44 shows that supercubane is not directly accessible from diamond since no positive pressure tangent line can be drawn between their two EOS fit curves. C_4 and glitter are also not accessible for the same reason. BC8 is, however, accessible since its per atom volume is smaller than diamond. The enthalpy versus pressure plot in Figure. 4.45 predicts a transition pressure of 0.971 TPa for diamond to BC8, which is close to the value of 1.2 TPa predicted by Biswas et al. [30]. The plot also shows that

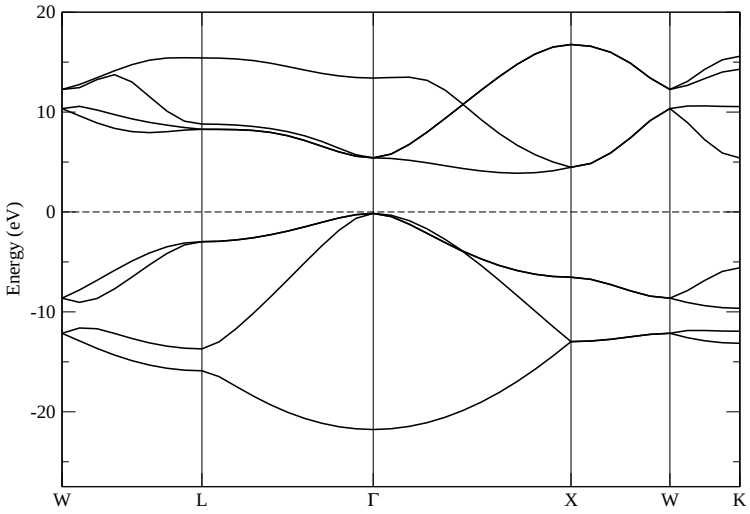

Figure 4.39: Diamond band structure - Showing an indirect band gap of 4.0 eV. Energies shifted to Fermi level.

the enthalpy curves for supercubane, C_4 and glitter do not intersect that of diamond.

Table 4.7: Carbon allotrope Birch-Murnaghan EOS fits (volume per atom in Å^3, lattice parameter a in Å, bulk modulus B_0 in GPa, B_0' dimensionless, B_0'' in GPa^{-1} and heat of formation H_f per atom in kJ mol^{-1}). Refer to section 4.3.4 Table 4.10 for graphite.

	V_0	a_0	c/a	B_0	B_0'	B_0''	H_f
Diamond	5.620	3.56		447.9	3.78	-0.0083	1.7
[a]BC8	5.515	4.45		406.6	3.81	-0.0092	67.1
[b]Supercubane	7.156	4.86		321.0	3.85	-0.012	67.2
[c]C_4	5.939	4.36	0.573	415.0	3.68	-0.0088	20.8
[d]Glitter	6.611	2.575	2.323	338.9	4.78	-0.0156	49.0

[a] x=0.16 [b] x=0.16 [c] x=0.18 [d] z=0.11

The results of Table. 4.7 show that the bulk modulus ranks, in decreasing order, as diamond → C_4 → BC8 → glitter → supercubane. This follows the same ranking as the increase in tetrahedral distortion except for glitter which has a value on the same

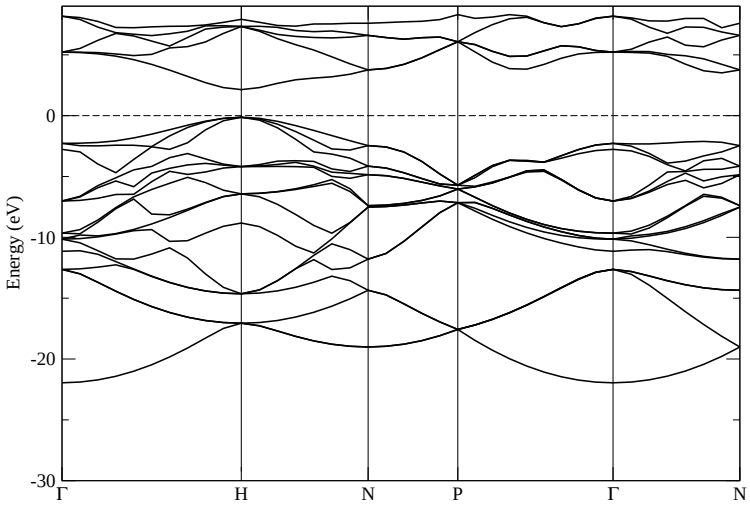

Figure 4.40: BC8 band structure - Showing a direct band gap of 2.26 eV at H. Energies shifted to Fermi level.

order as supercubane. This is due to the added effect of trigonal distortion.

Like silicon, all bulk modulus values respond in a near linear manner to changes in pressure around P=0 since $|B_0''| < B_0'$ with supercubane and glitter having the most parabolic response to pressure.

The heats of formation H_f are all positive, indicating that energy is required to form these structures.

The EOS values for diamond are very close to the experimental values with a_0 within 0.3% and the bulk modulus is within 2%[135]. The energy of formation for this structure is 1.7 kJ mol^{-1} since it is a metastable form of carbon made by the compression of graphite.

The values for C_4 compare well with the LDA calculations of Umemoto et al.[35] who gave a=4.33 Å with c/a=0.573 with an internal parameter of x=0.1804, a bulk modulus of 428.7 GPa with B_0'=3.57.

The values for supercubane compare well with the GGA results of Winkler[139] who calculated a_0=4.82Å, B_0=319 GPa with B_0'=3.7. The heats of formation of super-

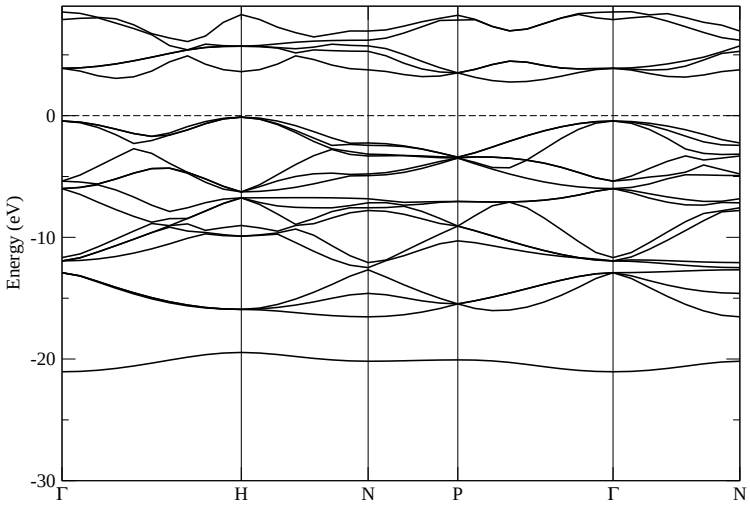

Figure 4.41: Supercubane band structure - Showing an indirect band gap of 2.89 eV. Energies shifted to Fermi level.

cubane and BC8 are calculated to be the same as reflected in the relative positions of their EOS fit curves in Figure. 4.44.

The values for glitter compare reasonably well with the results of Bucknum and Hoffmann [7] who used a model 1,4-cyclohexadiene model molecule to obtain a_0=2.53 Å with c/a=2.364.

4.3.3 Diamond, BC8, supercubane, C_4 - Elastic properties and stability

The calculated elastic constants of diamond, BC8, supercubane and C_4 are given in Table. 4.8 and the moduli in Table. 4.9. The elastic constants for graphite are given in subsection 4.3.4.

The elastic constants for diamond are very close to the experimental values of Vogelgesang et al. [140] with C_{12} being within 12%. Stiffness matrix eigenvalues are positive, as are the elastic moduli, indicating elastic stability of all allotropes. The calculated bulk moduli are close to their EOS derived equivalents shown in parentheses

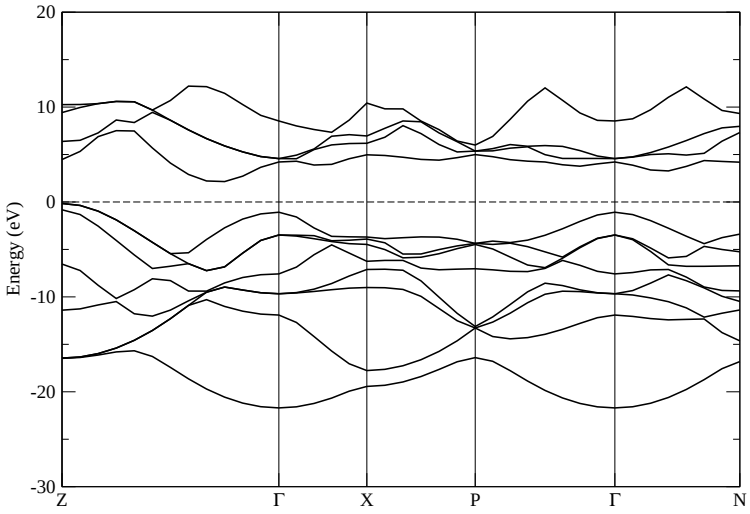

Figure 4.42: C_4 band structure - Showing an indirect band gap of 2.40 eV. Energies shifted to Fermi level.

in Table. 4.9. The values of the Young's and shear modulus for diamond and BC8 are almost identical due to their tetrahedral bonding (with an MAO for BC8 of 6.9 %) and their cubic conventional cells. Although supercubane is also cubic, it has an MAO for its distorted tetrahedral bonding that is more than twice that of BC8 therefore lower modulus values. C_4 is second in the ranking due to the combination of its low MAO and tetragonal conventional cell. Next is supercubane with its high MAO value and finally glitter with its added effect of distorted trigonal bonding.

The phonon dispersion plots for the allotropes are given in Figures. 4.46 to 4.50, and show no soft modes. The plots were calculated at 0 GPa for Diamond, supercubane, C_4 and glitter and at 1000 GPa for BC8 (slightly above the expected diamond to BC8 transition pressure).

For materials that expand with temperature, their dispersion bands will generally move up with increased pressure due to the higher presence of positive Grüneisen constants for each mode where these are given by

$$\gamma_i = \frac{B_0}{\omega_i}\frac{d\omega_i}{dP}. \tag{4.1}$$

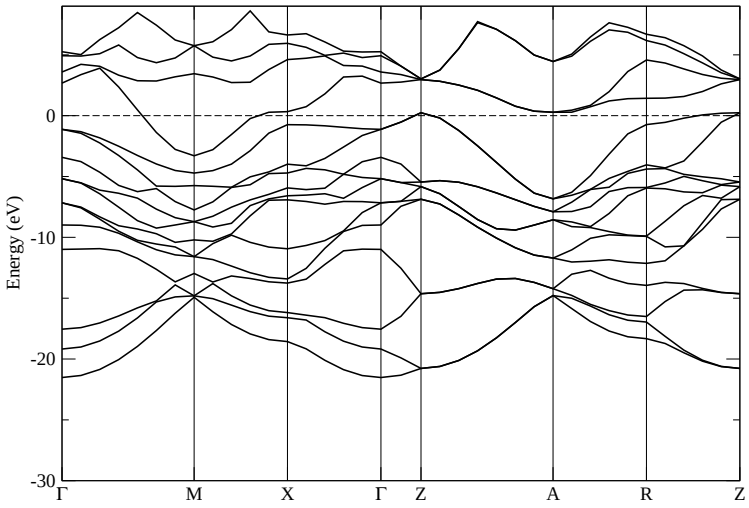

Figure 4.43: Glitter band structure - Showing it to be metallic. Energies shifted to Fermi level.

This will make the appearance of soft modes less likely (except in the case of a pressure transition). For this reason, the likely high-pressure phases of supercubane, C_4 and glitter are most probably stable at these pressures since no soft modes exist at zero pressure.

It is interesting to note that the dispersion plots for supercubane and glitter contain absolute band gaps around the 35∼40 THz range. This is a feature of phononic crystals where a mismatch of periodic elements in the crystal prevents the transmission of a band of acoustic waves. In this case, the gap prevents phonons with energies that exist in this optical range.

4.3.4 Graphite - Equation of state and elastic constants

In 1989, Hanfland et al.[141] proposed a 1-dimensional linear Murnaghan EOS to experimentally study the effect of bulk pressure on graphite. The equation related the change in lattice parameter r to the pressure as follows

$$P = B_0 \left((\frac{r_0}{r})^{B'_0} - 1 \right) / B'_0, \tag{4.2}$$

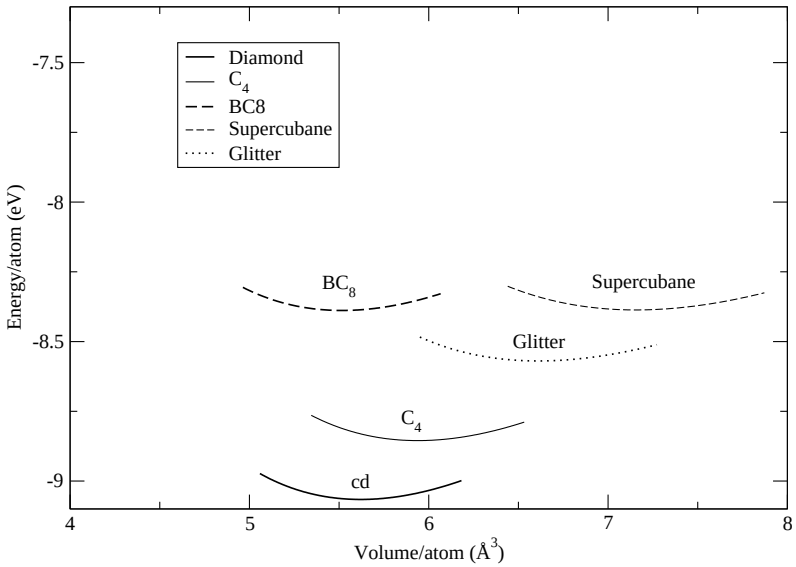

Figure 4.44: Carbon Birch-Murnaghan EOS fits - Showing energy vs volume EOS fit curves.

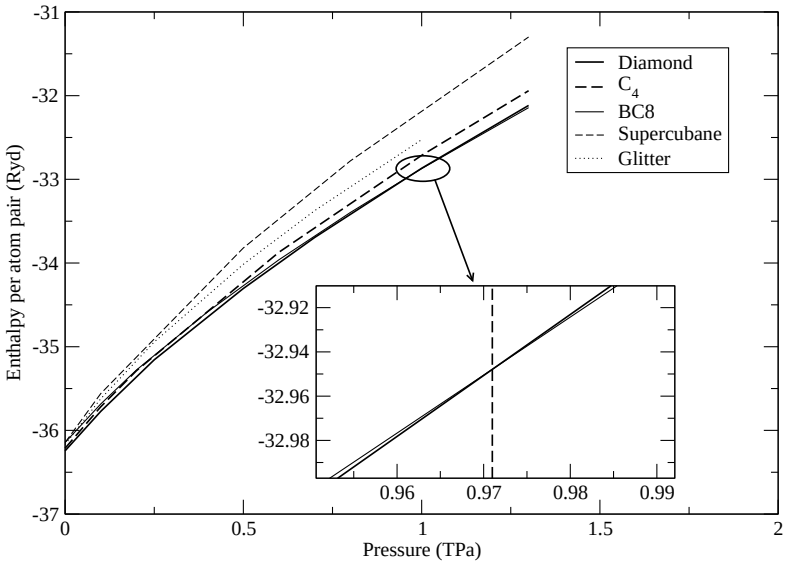

Figure 4.45: Carbon PBEsol phase transition - Showing transition from diamond to BC8 at 0.971 TPa.

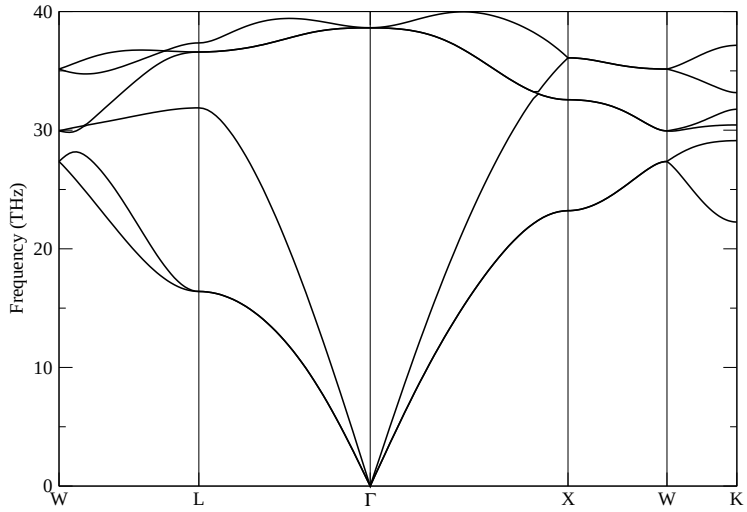

Figure 4.46: Diamond phonon dispersion at 0 GPa - Showing no soft modes.

Table 4.8: Calculated elastic constants for C allotropes (in GPa) showing numerical error estimates.

	C_{11}	C_{12}	C_{44}	C_{13}	C_{33}	C_{66}
Diamond	1072.1 ± 2.8	141.6 ± 2.8	577.2 ± 4.0			
Expt. Diamond[a]	1080.4	127.0	576.6			
BC8	1148.1 ± 9.5	40.1 ± 9.5	525.8 ± 13.4			
Supercubane	512.8 ± 1.2	227.1 ± 1.2	288.6 ± 1.7			
C_4	953.3 ± 6.7	183.0 ± 6.7	454.4 ± 9.6	67.3 ± 4.8	1224.1 ± 6.7	313.1 ± 6.72
Glitter	813.7 ± 4.0	50.8 ± 4.0	97.3 ± 5.7	81.9 ± 2.8	1207.7 ± 4.0	76.1 ± 5.7

[a] Vogelgesang et al.[140]

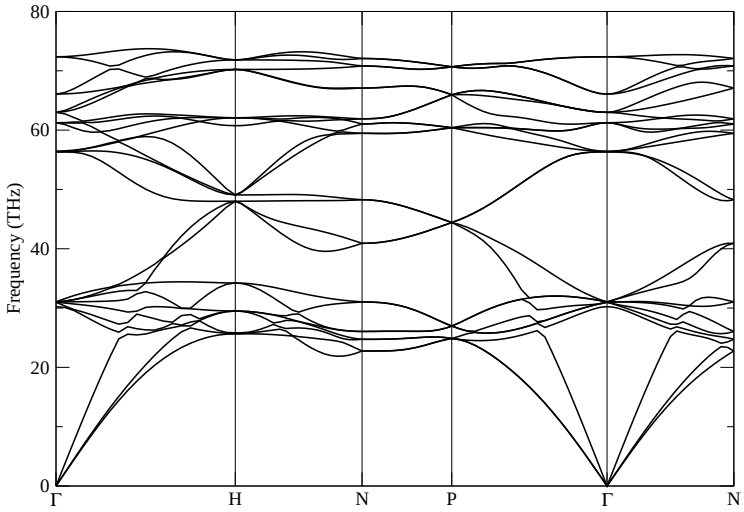

Figure 4.47: BC8 phonon dispersion at 1000 GPa - Showing no soft modes.

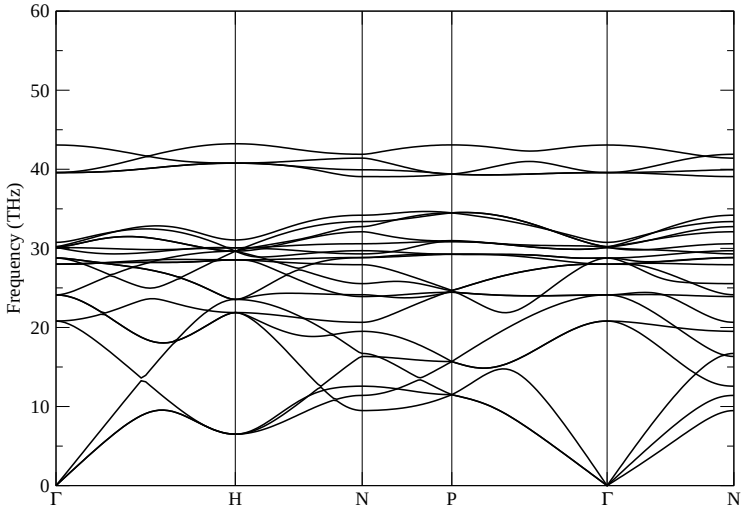

Figure 4.48: Supercubane phonon dispersion at 0 GPa - Showing no soft modes.

Table 4.9: Calculated elastic moduli for C allotropes in GPa showing Voigt, Reuss and geometric mean Hill values. EOS derived bulk moduli in parentheses. Debye temperature is expressed in Kelvin.

	B_V	B_R	B_H	G_V	G_R	G_H	Y_V	Y_R	Y_H	Θ_D
Diamond	451.8	451.8	451.8 (447.9)	532.4	526.5	529.5	1146.8	1137.6	1142.2	2231
BC8	409.5	409.5	409.5 (406.6)	537.1	536.7	536.9	1121.0	1120.5	1120.8	2233
Supercubane	322.3	322.3	322.3 (321.0)	230.3	205.0	217.6	558.0	507.3	532.7	1511
C_4	418.5	416.8	417.7 (415.0)	431.9	416.4	424.1	964.0	937.1	950.5	2023
Glitter	362.7	349.1	355.9 (338.9)	228.9	130.1	179.5	567.3	347.2	457.3	1364

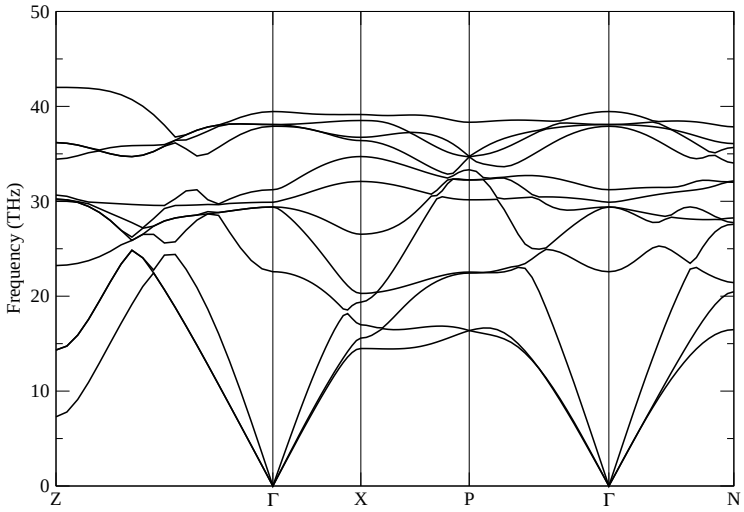

Figure 4.49: C_4 phonon dispersion at 0 GPa - Showing no soft modes.

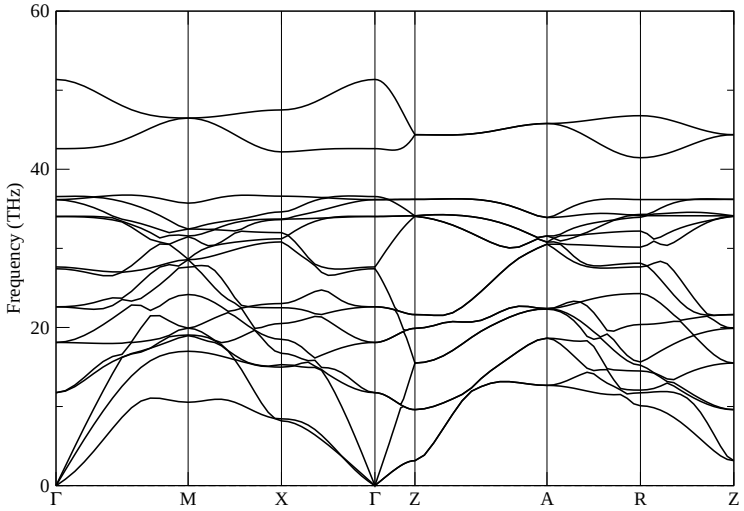

Figure 4.50: Glitter phonon dispersion at 0 GPa - Showing no soft modes.

where r could either be the in-plane parameter a or the out-of-plane parameter c and where

$$\beta_0 = -\left(\frac{\partial P}{\partial \ln r}\right)_{P=0} \tag{4.3}$$

is the linear modulus with respect to bulk pressure and β_0' is its pressure derivative.

The linear moduli β_a and β_c can be found for graphite by doing full LDA structural relaxations for a set of external pressures. The resulting lattice parameter values can then be fitted to Eqn. 4.2. A Birch-Murnaghan fit of the energy versus volume will also obtain the bulk modulus. These calculated fit parameters are given in Table. 4.10.

In 1989, Hanfland et al. [141] placed graphite into a diamond anvil cell and measured its response to pressure. They found that β_c=35.7∼36.6 GPa with β_c'=10.8 which are extremely close to the calculated values in Table. 4.10. Assuming β_a'=1, they also estimated that β_a=1250 GPa although they were not confident in their measurement of a over the entire pressure range used. With this in mind, the calculated value of 1228.3 GPa with β_a'=38.0 is within 2 % of their estimate. The results for the two linear-moduli show that graphite is more resilient to in-plane pressure as opposed to out-of-plane pressure. The linear-EOS fits also gave a_0=2.48 Å and c_0=6.58 Å which are close to their x-ray diffraction derived values of a_0=2.463 Å and c_0=6.712 Å [142]. The value for the bulk modulus is relatively close to the measured value of 34.6 GPa by Bosak et al. [142].

Table 4.10: Graphite linear/bulk EOS fits with vol in Å^3, lattice constants in Å and linear/bulk moduli in GPa, modulus prime dimensionless.

	V_0	a_0	c_0	B_0 or β_0	B_0' or β_0'
Bulk	34.14			29.5	13.2
Linear-c			6.58	33.8	10.82
Linear-a		2.48		1228.3	38.0

Using Eqn. 4.3 with the following relations

$$C_{11} + C_{12} = \frac{1}{\sqrt{3}c_0}\frac{\partial^2 E}{\partial a^2}$$

$$C_{33} = \frac{2c_0}{\sqrt{3}a_0^2}\frac{\partial^2 E}{\partial c^2} \tag{4.4}$$

$$C_{13} = \frac{1}{\sqrt{3}a_0}\frac{\partial^2 E}{\partial a \partial c},$$

the linear moduli become

$$\begin{aligned} \beta_a &= C_{11} + C_{12} + 2\,C_{13} \\ \beta_c &= C_{33} + C_{13}. \end{aligned} \tag{4.5}$$

Since the bulk modulus for graphite is given as [143]

$$B = \frac{(C_{11} + C_{12})\,C_{33} - 2\,C_{13}^2}{C_{11} + C_{12} + 2\,C_{33} - 4\,C_{13}}, \tag{4.6}$$

it and the other two modulus values can be used to calculate the values for the elastic constants $C_{11} + C_{12}$, C_{33} and C_{13}.

In 2007, Bosak et al. [142] measured the elastic constants of graphite using inelastic x-ray scattering. They measured that $C_{11} + C_{12}$=1248 GPa, C_{33}=38.7 GPa with C_{13}=0. The moduli values of Table. 4.10 give elastic constants of $C_{11} + C_{12}$=1222.1 GPa, C_{33}=30.7 GPa and C_{13}=3.1 GPa which are very close to the measured values. The results show that the in-plane elastic constants $C_{11} + C_{12}$ are much larger than the out-of-plane C_{33} due to the strong sp^2 bonding.

These calculations for graphite also show that LDA is an effective XC functional to use for layered materials.

4.4 Silicon carbide polytypes

Silicon carbide comes in over ∼200 different polytypes plus a rocksalt (RS) high pressure phase. The polytypes are made up of repeated units composed of the stacking of silicon hexagonal layers in various orderings, with each silicon atom tetrahedrally bonded to a carbon atom.

The hexagon of Figure. 4.51 has three atom positions: A at the white circles, B at the grey circles and C at the black circles. The first hexagonal layer of Si atoms in the

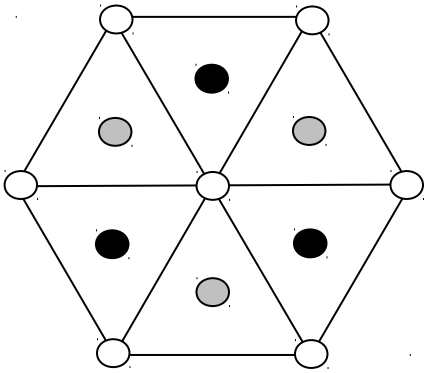

Figure 4.51: Hexagonal stacking - A=white circles, B=grey circles, C=black circles.

stacking sequence is arbitrarily placed at the white circles (labeling the layer A). The next highest layer of atoms then has a choice to be located at either the grey circles (labeling the layer B) or at the black circles (labeling the layer C). Since this choice is arbitrarily, the next layer is chosen to be B. If the third layer is now placed back at A, the stacking sequence can be stopped giving the sequence $ABABABAB\cdots$. otherwise the sequence is continued with the third layer placed at C. Subsequent series of layers are then similarly placed until the desired stacking pattern repeats.

The hexagonal polytypes are denoted by nH-SiC where n is the periodicity of the stacking. The simplest hexagonal polytype is the AB stacking of wurtzite 2H-SiC. Two other common stackings are $ABCB$ (4H-SiC) and $ABCACB$ (6H-SiC). Zinc blende SiC has the repeating ABC stacking of fcc and is called 3C-SiC since it is considered a cubic phase. These structures can be seen in Figure. 4.52.

The symmetry group, Wyckoff positions, crystal system and lattice type for each polytype are given in Table. 4.11.

4.4.1 Bonding and electronic properties

Since carbon has a greater electronegativity, it is expected that the bonding in SiC will be slightly ionic with the carbon atoms having a greater concentration of electronic charge surrounding them and silicon having a relative absence of negative charge.

The electronic structure for 3C-SiC is given in the middle row of Figure. 4.53 showing it to be isostructural to diamond (shown in the top row) with perfect tetrahedral

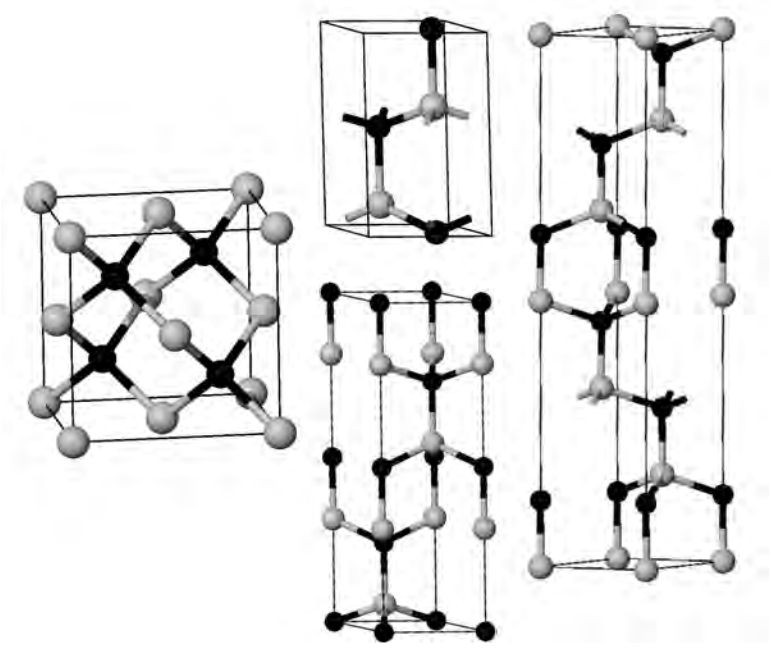

Figure 4.52: SiC polytypes - Showing 3C left, 2H upper-middle, 4H lower-middle and 6H right.

Table 4.11: Symmetries of SiC polytypes.

Structure	Symmetry Group	Wyckoff positions	Crystal system	Lattice type
NaCl	$Fm\bar{3}m$	$C:4a\ \ Si:4b$	cubic	face-centered
3C-SiC	$F\bar{4}3m$	$Si:4a\ \ C:4c$	cubic	face-centered
2H-SiC	$P6_3mc$	$Si:2b\ \ C:2b$	hexagonal	primitive-centered
4H-SiC	$P6_3mc$	$Si:2a,2b\ \ C:2a,2b$	hexagonal	primitive-centered
6H-SiC	$P6_3mc$	$Si:2a,2b,2b\ \ C:2a,2b,2b$	hexagonal	primitive-centered

bonding except with silicon atoms at the FCC sites and carbon at the tetrahedral sites. The hexagonal allotropes have slightly distorted tetrahedral bonding with a slight elongation in the c direction. The charge density plot in the middle-left of Figure. 4.53 shows that the majority of the electron charge is located away from the silicon atoms defined by closed triangular rings of contour surrounding each carbon atom as opposed to the case in diamond where the plot shows more or less unbroken contour lines from atom

to atom. The ELF plot for 3C-SiC in the middle of the 2nd row shows covalent lobes between nearest neighbors, as in the case of diamond, but with a greater localization of valence electrons in close proximity to the carbon atoms. This shows that, while elemental diamond has complete covalent bonding, bi-elemental SiC has a significant ionic character to its bonding. This bonding characteristic is shared by all SiC allotropes. The semi-ionic bonding has bond length d_{Si-C}=1.89 Å. The band structures for each main polytype are show in Figures 4.54 to 4.57. Each show an indirect band gap, indicating that the bonding has no metallic component and is sp^3 although with a slight ionic component. The PBEsol values of 1.25, 2.15, 2.11 and 1.91 eV for 3C, 2H, 4H and 6H compare well with the LDA calculated values of 1.24, 2.05, 2.14 and 1.98 eV by Park et al. [48], with both sets having the same symmetry points defining the gaps.

The high pressure rocksalt phase (RS-SiC) is shown in the bottom row of Figure. 4.53. The ELF plot for the (100) plane shows a large localization of valence electrons around each carbon atom with a slight covalent nature towards each of the six neighboring silicon atoms. The covalent lobes are not located in the midpoint between neighboring atoms, as in the case of full covalent bonding, but are closer to the more electronegative carbon atoms. The charge density plot shows that the negative charge is concentrated around the carbon atoms with a relative depletion of charge around the silicon atoms. These are the characteristics of ionic bonding with the carbons accepting the valence electrons from silicon making it a negative anion with the silicon atoms becoming cations. The coulomb attraction between ions creates the bonding. The nearest neighbor distance in ionic RS-SiC is d_{Si-C}=2.02 Å.

The band structure is shown in Figure. 4.58 showing a structure extremely close to that of a semi-metal with a depression of the conduction band at X closing the gap. This is the same result found by Karch et al. [53]. This suggests some semi-metallic bonding.

This admixture of semi-metallic/ionic/partly-covalent bonding is a result of the six-fold coordination of each atom as compared to the tetrahedral coordination of the other polytypes.

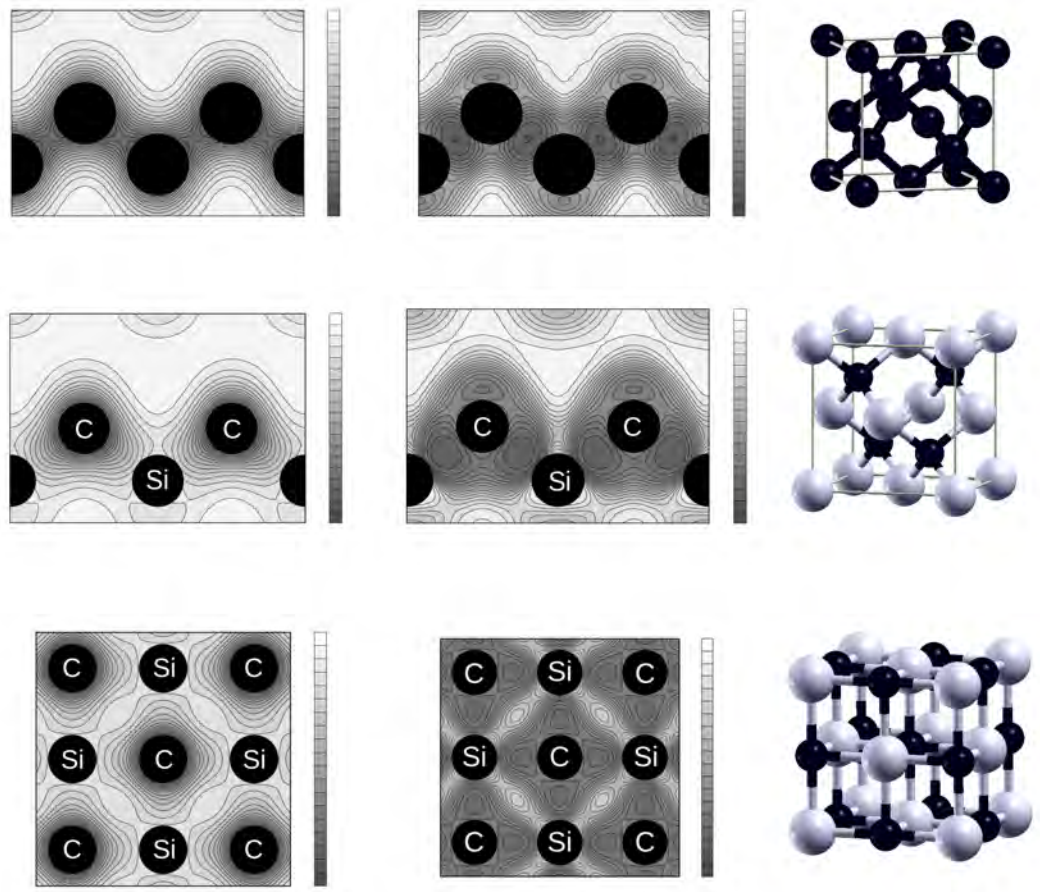

Figure 4.53: Diamond, 3C-SiC and RS-SiC structures - Showing charge density plots (left column) and ELF plots (middle column) for the (110) plane in the case of diamond and 3C-SiC (top and middle row) and the (100) plane in the case of RS-SiC (bottom row).

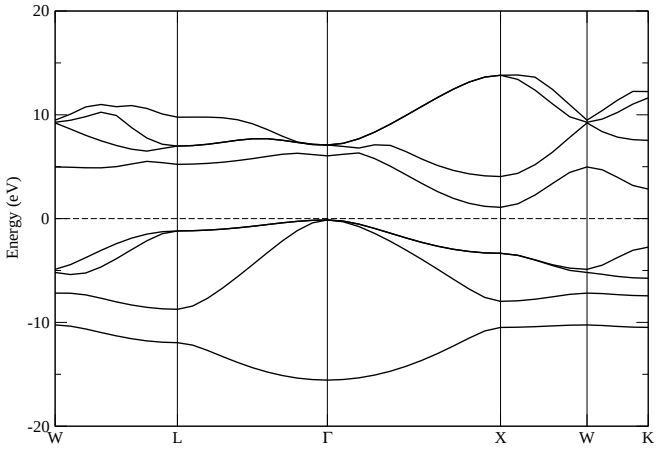

Figure 4.54: 3C-SiC band structure - Showing an indirect band gap of 1.25 eV between Γ and X. Energies shifted to Fermi level.

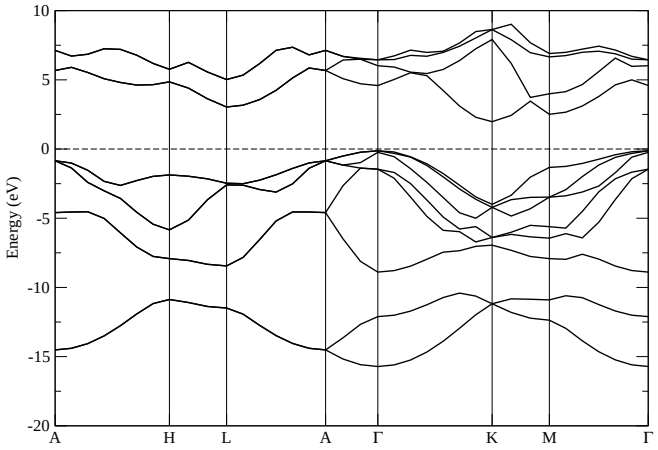

Figure 4.55: 2H-SiC band structure - Showing an indirect band gap of 2.15 eV between Γ and K. Energies shifted to Fermi level.

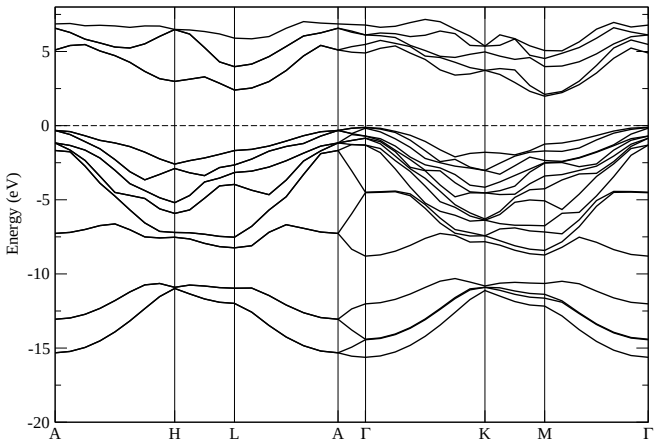

Figure 4.56: 4H-SiC band structure - Showing an indirect band gap of 2.11 eV between Γ and M. Energies shifted to Fermi level.

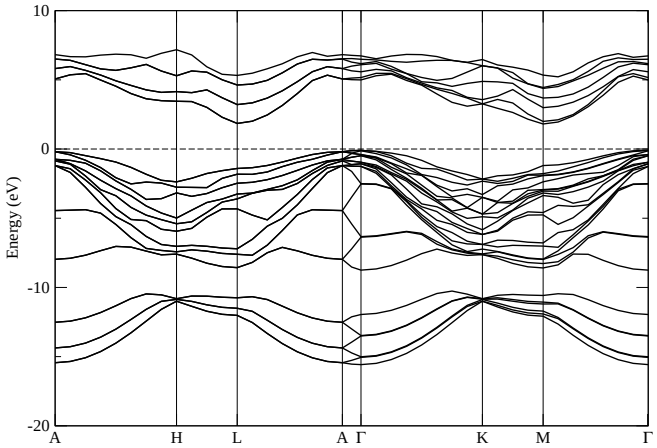

Figure 4.57: 6H-SiC band structure - Showing an indirect band gap of 1.91 eV between Γ and M. Energies shifted to Fermi level.

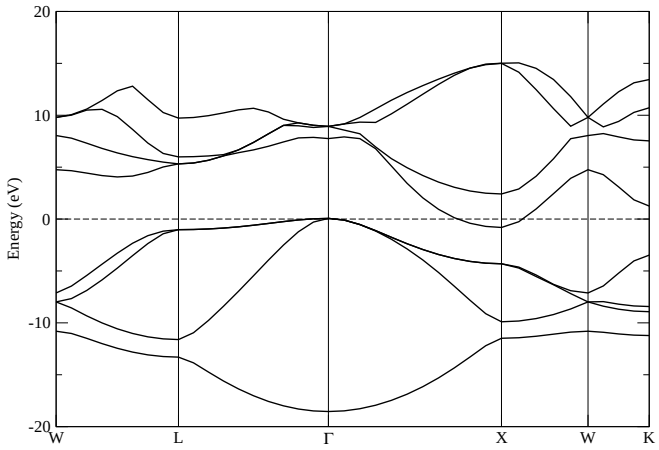

Figure 4.58: RS-SiC band structure - Showing it to be metallic. Energies shifted to Fermi level.

4.4.2 Equation of state and pressure transition

The PBEsol Birch-Murnaghan EOS fits for SiC are shown in Table.4.12 with the curves given in Figure. 4.59. The values for 3C, 2H and 4H compare well to the LDA results of Karch et al. [53] given in the middle section of Table.4.12. The available experimental data is also comparable to the PBEsol results.

The bulk modulus of the hexagonally stacked polytypes 2H, 4H and 6H are the same which is not surprising since these polytypes share the same bonding. The higher value for the bulk modulus of RS-SiC could be due to the coulomb repulsion between each atom and its second nearest neighbors which are of the same ionic charge.

The EOS fit values show that the bulk modulus values for the SiC polytypes react to pressure in exactly the same manner. The high pressure RS phase has the same B_0'' parabolic term but a differing linear B_0' term due to its differing bonding. The heats of formation indicate that only the rock-salt phase does not form spontaneously whereas the others have approximately the same negative value allowing these structures to form spontaneously. This is reflected in Figure. 4.59 where the curves for 3C, 2H, 4H and 6H almost overlap each other. Their small equilibrium differences, as illustrated by the curves in the inset, are due to the fact that each polytype may be considered a

variant with a different periodic stacking fault.

The second to last column in Table. 4.12 shows the difference between each equilibrium energy and that of 3C-SiC. The energy differences rank in decreasing order as RS→2H→3C→6H→4H. The ranking is the same as found by Jiang et al. [144] and the values compare very well to their LDA values listed in the middle section of Table. 4.12.

The curves in Figure. 4.59 predict a pressure transition from 3C-SiC to RS-SiC at

Table 4.12: SiC polytype Birch-Murnaghan EOS fits (volume per SiC in Å^3, lattice parameters a and c in Å, bulk modulus B_0 in GPa, B_0' dimensionless, B_0'' in GPa^{-1} and energy difference per SiC in meV).

This work								
	V_0	a_0	c_0	B_0	B_0'	B_0''	$E_0 - E_0^{3C}$	H_f
RS	16.435	4.04		257.5	4.41	-0.0174	1313	74.2
2H	20.711	3.08	5.050	221.8	3.88	-0.0171	4.00	-52.1
3C	20.706	4.36		220.9	3.87	-0.0171	0	-52.5
6H	20.700	3.08	15.114	221.4	3.89	-0.0171	-2.40	-52.7
4H	20.699	3.08	10.081	221.4	3.88	-0.0171	-2.79	-52.7
Previous work[a]								
	V_0	a_0	c_0	B_0	B_0'	B_0''	$E_0 - E_0^{3C}$	
2H	20.600	3.065	5.039	225	3.78		4.00[b]	
3C	20.706	4.343		223.6	3.77		0	
6H							-2.40[b]	
4H	20.699	3.068	10.051	224.3	3.72		-2.9[b]	
Experimental[a]								
	V_0	a_0	c_0	B_0	B_0'	B_0''	$E_0 - E_0^{3C}$	
2H	20.711	3.079	5.052	223				
3C	20.7110	4.359		227	3.57			
6H								
4H	20.550	3.073	10.052					

[a] Karch et al. [53]

[b] Jiang et al. [144]

57 GPa (a result verified by enthalpy versus pressure curves). The PBEsol value is well below the experimentally measured value of 100 GPa by Yoshida et al. [46] and slightly below the LDA value of 66 GPa by Chang and Cohen [45]. Using a greater **k**-mesh to

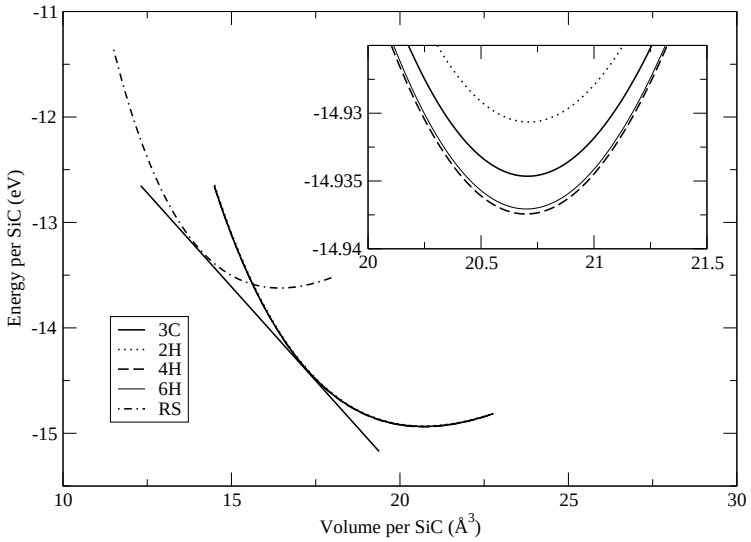

Figure 4.59: Silicon carbide Birch-Murnaghan EOS fits - Showing energy vs volume data and a phase transition between 3C and RS-SiC at P_t=57 GPa. Insert shows detail around equilibrium values for 3C, 2H, 4H and 6H.

better sample around the Fermi surface did not improve the value.

One would expect PBEsol to accurately predict this high pressure transition as it was shown to be more accurate for high pressure silicon transitions. A possible factor is that, whereas the high pressure Si phases became increasingly metallic with pressure, here the phase transition is from covalent semi-conducting to ionic. It has been noted that when pressure transitions involve a drastic change in electronic structure, non-canceling errors in the two phases can lead to a large bias in the predicted transition pressure[145]. This may explain why PBEsol does not accurately describe this high pressure covalent to ionic transition.

4.4.3 Elasticity and stability

The calculated elastic constants are shown in Table. 4.13 with the values for 3C within 4% and the values for 6H within 11% of the listed experimental values. The elastic constants of the hexagonal polytypes all have very similar values due their tetrahedral bonding. The values for RS-SiC have higher numerical error which did not improve with a larger **k**-point sampling.

The elastic moduli are listed in Table. 4.14 and have similar values for these polytypes. Cubic 3C-SiC shares the same bonding and has the same elastic moduli as the hexagonal polytypes. The rocksalt structure has the highest values, within the nu-

Table 4.13: Calculated elastic constants for SiC polytypes (in GPa) showing numerical error estimates.

	C_{11}	C_{12}	C_{44}	C_{13}	C_{33}
RS	414.0 ± 11.6	169.1 ± 11.6	306.5 ± 16.4		
3C	384.0 ± 1.5	140.7 ± 1.5	237.2 ± 2.2		
Expt. 3C[a]	395 ± 12	132 ± 9	236 ± 7		
2H	501.9 ± 3.3	114.2 ± 3.3	147.6 ± 4.7	55.7 ± 2.3	546.7 ± 3.3
4H	502.1 ± 2.0	108.3 ± 2.0	153.3 ± 2.8	58.8 ± 1.4	541.5 ± 2.0
6H	501.4 ± 1.9	106.3 ± 1.9	155.8 ± 2.7	60.3 ± 1.3	541.8 ± 1.9
Expt. 6H[b]	501 ± 4	111 ± 5	163 ± 4	52 ± 9	553 ± 4

[a] Mat. Sc. Eng. A 387 302 (2004) Brillouin scattering

[b] Kamitani et al.[146]

merical error, due to its ionic bonding. For all low pressure phases, the bulk moduli match the EOS derived values shown in brackets. Due to the large numerical errors for RS-SiC, it is not possible to verify the EOS value for the bulk modulus.

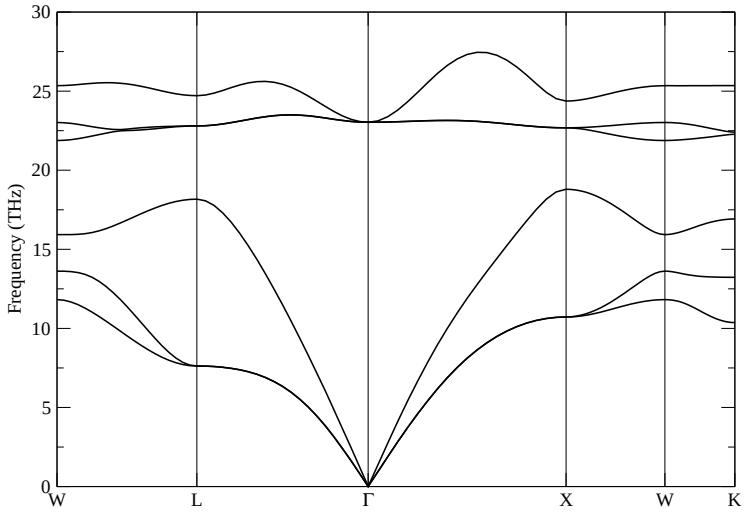

Figure 4.60: 3C-SiC phonon dispersion at 0 GPa - Showing no soft modes.

The phonon dispersion curves for zero pressure 3C-SiC and RS-SiC at 60 GPa are given in Figures 4.60 and 4.61. No soft modes are present and the structures are dynamically stable.

4.5 Conclusions

These calculations on the elemental and 50:50 silicon-carbon systems were done in order to choose suitable calculation parameters and to validate methods used to evaluate structural strength, stability and possible pressure phase transitions. In addition, these methods were used to predict some under-reported properties for three previously proposed hypothetical allotropes of carbon.

The first method to be validated was the use of valence charge density and electron localization function plots to determine bonding properties. For the silicon allotropes,

Table 4.14: Calculated elastic moduli for SiC polytypes in GPa showing Voigt, Reuss and geometric mean Hill values. EOS derived bulk moduli in brackets. Debye temperature in Kelvin.

	B_V	B_R	B_H	G_V	G_R	G_H	Y_V	Y_R	Y_H	Θ_D
RS	250.7	250.7	250.7 (257.5)	232.9	191.4	212.2	533.5	457.8	495.7	1175
3C	221.8	221.8	221.8 (220.9)	191.0	171.9	181.5	445.2	409.9	427.5	1130
2H	222.4	222.4	222.4 (221.8)	186.2	179.2	182.7	486.6	423.8	430.2	1134
4H	222.0	222.0	222.0 (221.4)	188.7	183.1	185.9	441.1	430.7	435.9	1143
6H	222.0	222.0	222.0 (221.4)	189.7	184.5	187.1	442.9	433.4	438.2	1147

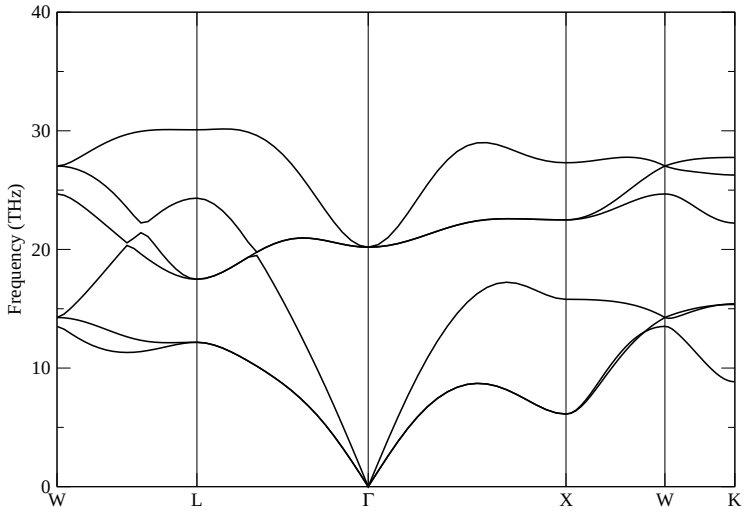

Figure 4.61: RS-SiC phonon dispersion at 60 GPa - Showing no soft modes.

analysis of these plots correctly predicted the increasing metallic component to the bonding with pressure when going, in order, from covalent diamond Si-I to fully metallic Si-X. The known covalent admixture for the Si-V phase was also verified. For the carbon allotropes, these plots correctly identified the covalent sp^2 bonding in graphite and the covalent sp^3 bonding in diamond, BC8, C_4 and supercubane. It was determined that the tetrahedral bonding for the four-fold coordinated carbon atoms becomes increasingly distorted from diamond $\rightarrow$ glitter$\rightarrow$ C_4 $\rightarrow$ BC8 $\rightarrow$ supercubane with the glitter structure contained both tetrahedral and trigonal covalent bonding. Investigation of the bonding in 3C-SiC verified that the covalent bonding is slightly ionic due to the larger electronegativity of carbon. The bonding in RS-SiC was determined to be mostly ionic with a small semi-metallic/covalent component.

Next the electronic properties for the three systems were investigated and validated. The calculated band structures for the silicon allotropes matched the previously investigated bonding properties. Covalently bonded diamond was correctly identified as a semi-conductor whereas all other structures were found to be metals. The non-layered covalently bonded carbon allotropes were all identified as semi-conductors (except glit-

ter which is predicted to be a metal, therefore having a metallic component to the bonding), while graphite was correctly identified as a semi-metal. The SiC polytypes were all determined to be semi-conductors with calculated band gaps matching previous calculations. RS-SiC was determined to be a near semi-metal, a result previously found by others. These results showed how the electronic properties could also be used to further describe bonding characteristics.

Using the Birch-Murnaghan equation of state, the bulk equilibrium properties of the three systems were investigated. The results for Si-I, Si-II and Si-III were found to compare well with previous calculations and known experimental results. The EOS fits for diamond compared well with experiment and those for C_4 and supercubane compared well with previous calculations. The calculated EOS lattice parameters for the SiC stacking polytypes closely matched available experimental data. This established PBEsol is a suitable functional for calculations predicting structural properties.

Elastic properties for the various structures were then investigated to see the influence of bonding on the elastic moduli and to determine structural stability. Phonon dispersions were also calculated to determine dynamic stability by looking for the presence of soft modes. The calculated elastic constants for diamond silicon, diamond carbon and select stacking polytypes of SiC were found to be reasonably close to experimental values. This correspondence was also reflected in the resulting elastic moduli. The eigenvalues of the stiffness matrices were all positive as were the calculated elastic moduli, which indicates elastic stability. The calculated phonon dispersion curves for each structure contained no soft modes, indicating dynamic stability. The modulus values for the various silicon allotropes were linked to the amount of metallic bonding present, and in the case of carbon, the amount of bonding distortion. This link between bonding and the elastic moduli was especially evident for the stacking polytypes of SiC where the nearly identical modulus values reflected the similarity in the bonding. This verified PBEsol as a suitable functional to be used to determine elastic properties and elastic/dynamic stability.

Lastly, pressure phase transitions were validated for the silicon and SiC systems and looked for in the case of the non-layered carbon allotropes. For the known silicon pressure phase transitions, it was found that while LDA predicted the transition pressures with reasonable accuracy, PBEsol was more accurate for the densely compacted high pressure phases. This is in accordance with the known behavior of the

PBEsol functional. It was also noted that the coordination of the atoms and degree of metallic bonding increased with pressure. For carbon, it was found that the only high pressure transition from diamond was to the BC8 structure at 0.971 TPa, a result close to previous predictions. This reveals that the three theoretical allotropes of C_2, supercubane and glitter are not accessible under pressure from diamond although they could possibly be made from the shock-compression of graphite. For silicon carbide, the phase transition between 3C-SiC and RS-SiC was verified but the predicted pressure transition of 57 GPa was well below the experimental value of 100 GPa. It is thought that one possible explanation for this is that this pressure transition involves a drastic change in electronic structure causing non-canceling errors in the two phases which results in a large bias in the predicted transition pressure. This revealed a limitation of the PBEsol functional.

For completeness, graphite was fitted to the linear EOS of Hanfland et al. [141] using the LDA functional. The resulting linear moduli, bulk modulus and elastic constants all compared well to existing calculations and experimental data. The results also verified that the in-plane strength of graphite is much higher than that due to the inter-plane interaction. This result validates that LDA mimics the weak inter-plane van der Waals interaction.

The methods and calculation parameters refined here as well as the observed bonding trends are now applied in the next chapter to the study of off-50:50 alloys.

5

Bulk off-50:50 Si-C alloys

Some of the work presented in this chapter has been published:

R C Andrew et al. Computational Materials Science 55, 186 (2012) [147]

The tools that are available to investigate off-50:50 structures are wide ranging. The preliminary calculations of the previous chapter presented some methods which can now be used to investigate Si-C systems and the stability of candidate structures:

- The coordination of the atoms will indicate the plausibility of the locations for each carbon and silicon atom, since silicon atoms can occupy atom positions with 4 to 12-fold coordination whereas carbon atoms can only occupy those with 3, 4 or 6-fold coordination
- Charge density and ELF plots will show where charge is concentrated and where bonding electrons are localized to give an indication of the amount of covalent, ionic or metallic bonding
- Electronic band structure will also show if there is any metallic character to the bonding.
- Distances between atoms and comparing them with the bond distances in the various C, Si and SiC allotropes will also give an indication of bonding type
- Positive elastic moduli and eigenvalues for the stiffness matrix will indicate elastic stability

- Soft modes in the phonon dispersion will indicate dynamic instability
- Enthalpy versus pressure curves for stable phases will indicate possible pressure phase transitions

An additional condition for structure plausibility is that the bond lengths must satisfy the following ordering: $d_{Si-Si} > d_{Si-C} > d_{C-C}$.

The guiding principle in looking for candidate structures was to look for open structures with a strong covalent component to the bonding as well as those with high coordination that could be accessible under conditions of pressure. The first candidate alloy structure considered was the perovskite structure of $CaTiO_3$ because it could represent a range of possible off 50:50 alloys with high coordination. The next three candidate structures focused on the study of the two alloy stoichiometries, silicon dicarbide (SiC_2) and disilicon carbide (Si_2C), and had the possibility of strong, open covalent bonding. These structures were the pyrite structure based on FeS_2, a previously suggested tetragonal structure based on the hypothetical carbon allotrope glitter [7] and another tetragonal structure based on a suggested hypothetical structure for diamond-like boron dicarbide [8].

In the first section, the perovskite structure is investigated for a variety of Si-C alloy stoichiometries. Section 5.2 shows the results for pyrite SiC_2 and Si_2C while sections 5.3 and 5.4 show the results for the glitter and diamond-like boron-dicarbide structures respectively. Based on these studies, the stability of SiC_2 is discussed in section 5.5.

5.1 Perovskite structure

The perovskite structure is shown in Figure. 5.1. It is a structure with chemical formula ABX_3 with the spacegroup $Pm\bar{3}m$. For $CaTiO_3$, oxygen atoms are located at X, calcium atoms at A and a titanium atom at B. Generic perovskite is comprised of cations at A and B with an anion at X bonded to both. For the structure to be perfectly cubic, the cation at A must be larger than that at the body-center position else a distorted perovskite structure will result. The cation at A has 12-fold coordination while that at B has six. The various candidate off 50:50 alloy stoichiometries possible by placing

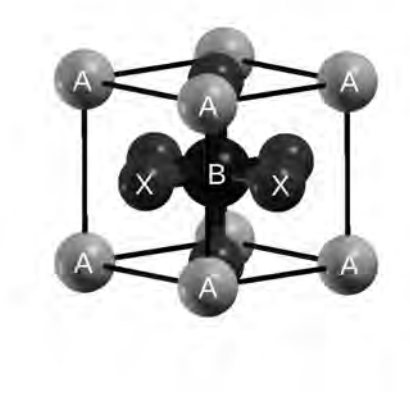

Figure 5.1: Perovskite structure - Showing atoms at the corners (A), atoms at the face-centers (X) and an atom at body-center (B).

carbon and silicon atoms in various combinations of the A, B and X positions are SiC_4, Si_2C_3, Si_3C_2 and Si_4C. The combinations are given in Table. 5.1.

Table 5.1: Various perovskite derived Si-C alloys.

	X	A	B
Si_2C_3	C	Si	Si
Si_3C_2	Si	C	C
SiC_4	C	C	Si
SiC_4	C	Si	C
Si_4C	Si	C	Si
Si_4C	Si	Si	C
coordination	2	12	6

For a Si-C perovskite alloy, the X anions would have to be carbon atoms since they have the greater electronegativity and based on the results of the preliminary calculations, the A atoms can only be silicon because of its ability to have high coordination. This leaves the Si_2C_3 alloy with Si as the cation at B. The structure is shown in Figure. 5.2 along with charge density and ELF plots showing the nature of the bonding between the atoms. The plots for the (110) plane cutting diagonally through the structure show that the carbon atoms on the upper and lower faces at X have a

large concentration of charge surrounding them with covalent lobes extending towards the center silicon at B, indicative of the same covalent/ionic bonding found in 3C-SiC. In fact, the carbon to silicon distance is d_{Si-C}=1.87 Å, the same as the bonding in 3C-SiC. The plots also show that the corner silicon atoms at A are not bonded to the face-center carbon atoms. There is no charge extending from the carbon atoms to the silicon atoms and no covalent lobes between the atoms. In fact, valence electrons are spherically localized around the silicon atoms. The plots for the (100) plane intersecting the mid-line of the structure shown in the middle row of Figure. 5.2 also show that the carbon atoms at X are bonded to the central silicon atom. The last set of plots for the (100) plane for each cube-face also show that although the face-center carbon atom has a large concentration of charge, the electrons for the corner silicon atoms at A are not involved in bonding as they are spherically localized around the silicon atoms. All of this shows that while the carbon atoms at X are covalently/ionically bonded to the central silicon, the silicon atoms at the corners are left as isolated atoms. For this reason, this structure can be discounted.

5.2 Pyrite structure

The pyrite structure has chemical formula AB_2 and is based on FeS_2 (also ThC_2 Pearson #529710). Studies on the dinitrides CN_2, SiN_2 and GeN_2 in 2011 also considered the pyrite structure as a possible candidate[148]. The pyrite structure is an open structure with the possibility of strong covalent bonds. The two possible Si-C alloys with this structure are SiC_2 and Si_2C.

This structure has space group $Pa\bar{3}$ (primitive-centered cubic lattice) with the A atoms at fcc sites and the B atoms placed at lattice position (x, x, x) and other symmetry-equivalent positions as shown in the left of Figure. 5.3. In terms of the Wyckoff positions, the A atoms are at the $4a$ positions while the B atoms are at the $8c$ positions.

This structure is identical to the fluorite structure, shown on the right of Figure. 5.3, when the internal parameter x=$\frac{1}{4}$ giving the structure the spacegroup $Fm\bar{3}m$. The B atom in both structures has four-fold coordination while the coordination of the A atoms is dependent on the value of x. For the fluorite structure, each A atom has 8-fold coordination while those in a general pyrite structure with $x \neq \frac{1}{4}$ can have a

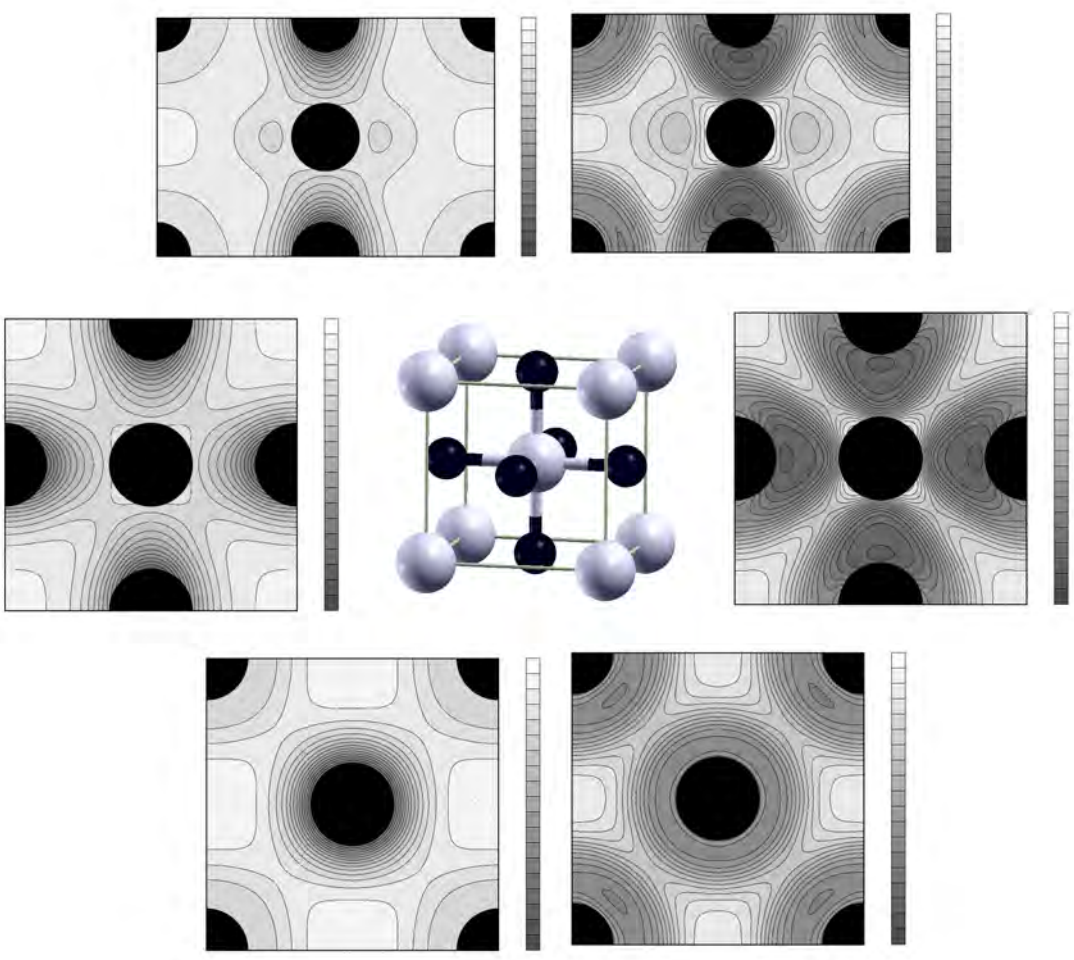

Figure 5.2: Perovskite Si_2C_3 structure - Showing charge density plots (on left) and ELF plots (on the right) for the diagonal (110) plane (upper row) and for the (100) plane going through the body-center atom (second row) and that for the face-centers (last row).

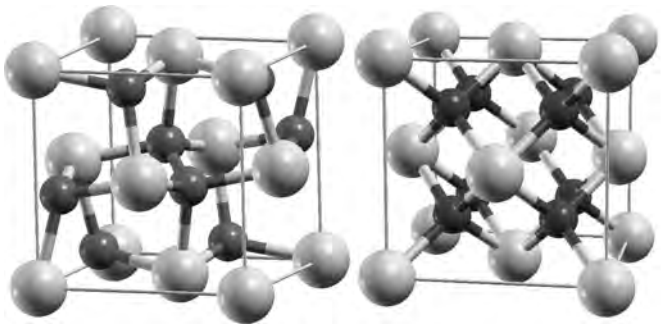

Figure 5.3: Pyrite/Fluorite structure - Pyrite structure on left with A atoms in an FCC arrangement and grey B atoms at (x, x, x) and symmetry-equivalent positions (structure shown with x=0.417). Fluorite structure on right with x=$\frac{1}{4}$.

coordination of six. Because of this, only the alloy SiC_2 can have the fluorite structure with silicon atoms occupying the higher coordinated A sites and carbon the B sites. The other possible alloy, Si_2C, may however have a general pyrite structure where the carbon at A can have the lower six-fold coordination.

5.2.1 Pyrite-SiC_2

Since the internal parameter x allows for a variety of possible pyrite structures, including the fluorite structure, it remains to be found which is the most energetically stable configuration. This is especially true since full geometric relaxations of the structure either resulted in a general pyrite structure with x=0.417 or the special case of the fluorite structure as shown in Figure. 5.3. For this reason, the total energy for pyrite SiC_2 is plotted as a function of the internal parameter x at the geometrically optimized lattice constant of a=4.75Å, making a continuous transition over all possible pyrite structures between $0.175 < x < 0.44$. This range was chosen since any values near $x = 0.0$ or $x = 0.5$ results in near atom overlap. The resulting plot is shown in Figure. 5.4 where we find a local minimum in the energy for the fluorite structure at x=0.25 and a global minimum at x=0.417. Another set of calculations were done (shown in Figure. 5.5) to test the effect of relaxing the cell volume at each fixed x value. The resulting plot yields the same local and global minima as before showing no effect.

An analysis of the dispersion spectra for the fluorite structure shows it to be dynamically unstable: the phonon dispersion Fig. 5.6 indicates the presence of soft modes.

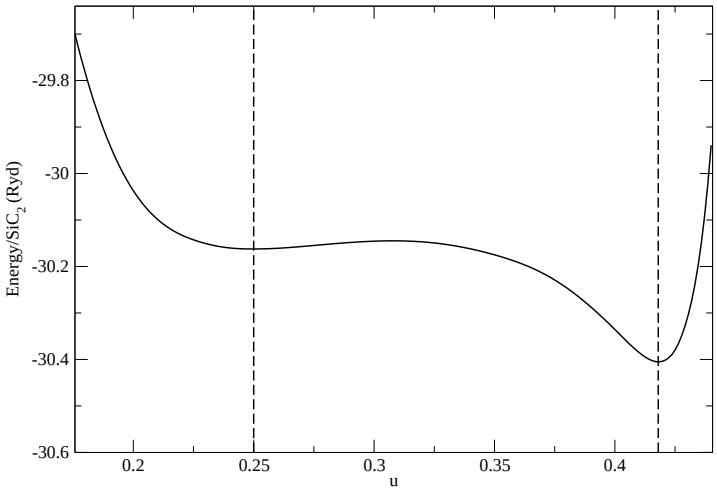

Figure 5.4: Pyrite SiC_2 x parameter plot at $a = 4.75\,\AA$ - Showing a local minimum at x=0.25 and a global at 0.417.

The pyrite structure at the global minimum, on the other hand, is dynamically stable at zero pressure as indicated by the positive phonon frequencies shown in Fig. 5.7.

Therefore, pyrite SiC_2 relaxes into a structure with lattice parameter a=4.75 Å (larger than the value of 4.36 Å, for 3C-SiC) with the previously determined internal parameter x=0.417. This gave a density of 3.225 g cm^{-3}, slightly greater than the value of 3.216 g cm^{-3} for 3C-SiC. It has six-fold coordinated silicon atoms surrounded by carbon atoms which are in turn, in close proximity to three silicon atoms and one other carbon atom. This effectively has the silicon atoms connected to a six-fold coordinated carbon-carbon pair with three silicon atoms connected to each carbon.

The charge density and ELF plots in the left half of Figure. 5.8 are taken for the (011) plane which not only contains the central carbon-carbon pair, but also two attached silicon atoms on either side of the pair as well. This way the bonding between the carbon atoms, as well as that between each silicon atom and its carbon neighbors, could be investigated.

The charge density plot on the lower-left shows that after the SCF cycle, the valence charge concentrates around the carbon atoms, shown by the concentric rings around the carbon pair, with a significant amount of charge concentrated between the atoms.

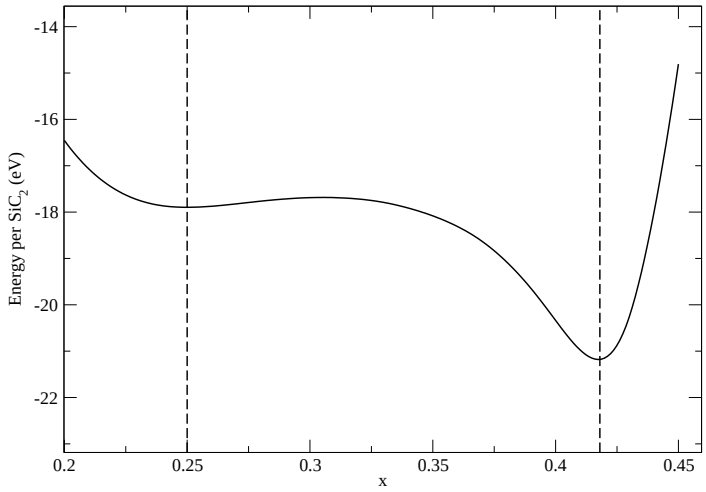

Figure 5.5: Pyrite SiC_2 x parameter plot with volume relaxations - Showing a local minimum at x=0.25 and a global at 0.417.

The higher charge density is directed slightly towards the silicon atoms with each silicon atom having a relativity dilute charge density surrounding it.

The ELF slice on the upper-left shows covalent lobes from each carbon atom to the surrounding silicon atoms and one between the carbon atoms. These plots indicate that the Si-C bonding is a mix of ionic and covalent and that the C-C bonding is strictly covalent.

The carbon atoms have three bonding angles of Si-Ĉ-Si=109.34° and three of C-Ĉ-Si=109.60° giving a slightly distorted tetrahedral nature to the bonding around each C atom (refer to Fig. 5.9). The angles have an MAO (mean absolute offset)[1] of 0.12 % from the ideal value of 109.47°. Through each Si atom, the opposing Si-C bonds form three straight C-Si-C segments which are not fully orthogonal to each other but either form an angle of 87.91° or the complimentary angle of 92.09°, giving a distorted octahedral character to the bonding with an MAO from the ideal angle 90° of 2.3 %.

The carbon-carbon bond distance is d_{C-C}=1.36 Å, the same as the bond length in glitter. The silicon-carbon bond distance is d_{Si-C}=2.06 Å which is slightly higher than

[1] where $MAO = \frac{1}{N}\sum_{n=1}^{N}\left|\frac{X_0 - X_n}{X_0}\right| \times 100\%$

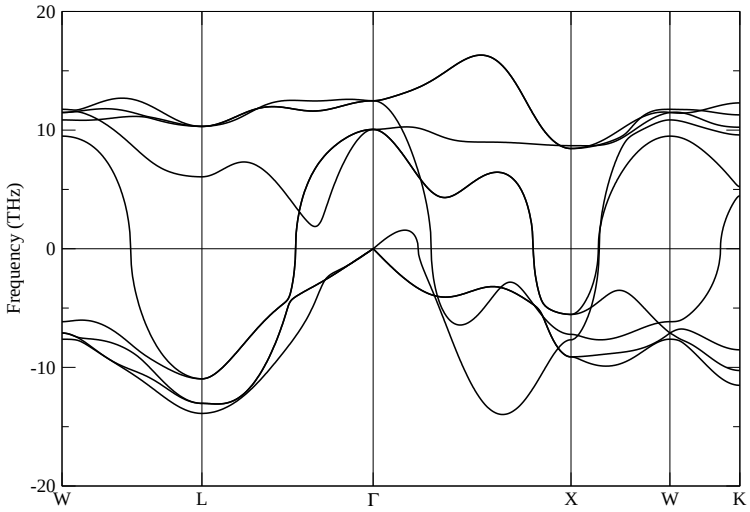

Figure 5.6: Fluorite SiC_2 phonon dispersion at 0 GPa - Showing soft modes.

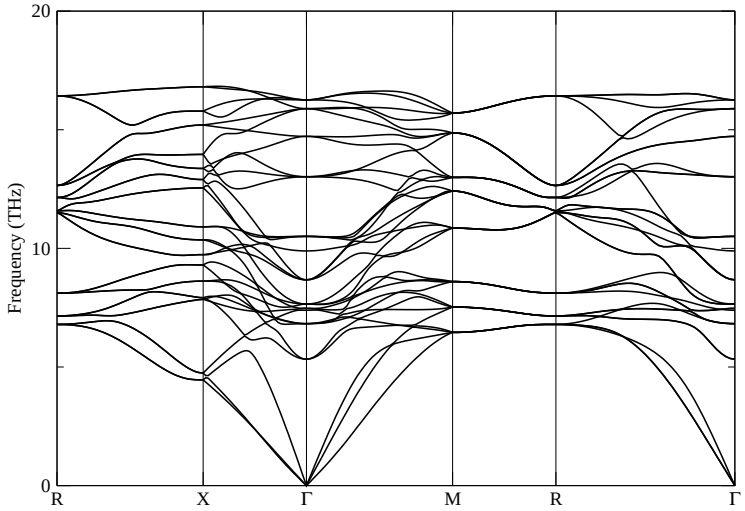

Figure 5.7: Pyrite SiC_2 phonon dispersion at 0 GPa - Showing no soft modes.

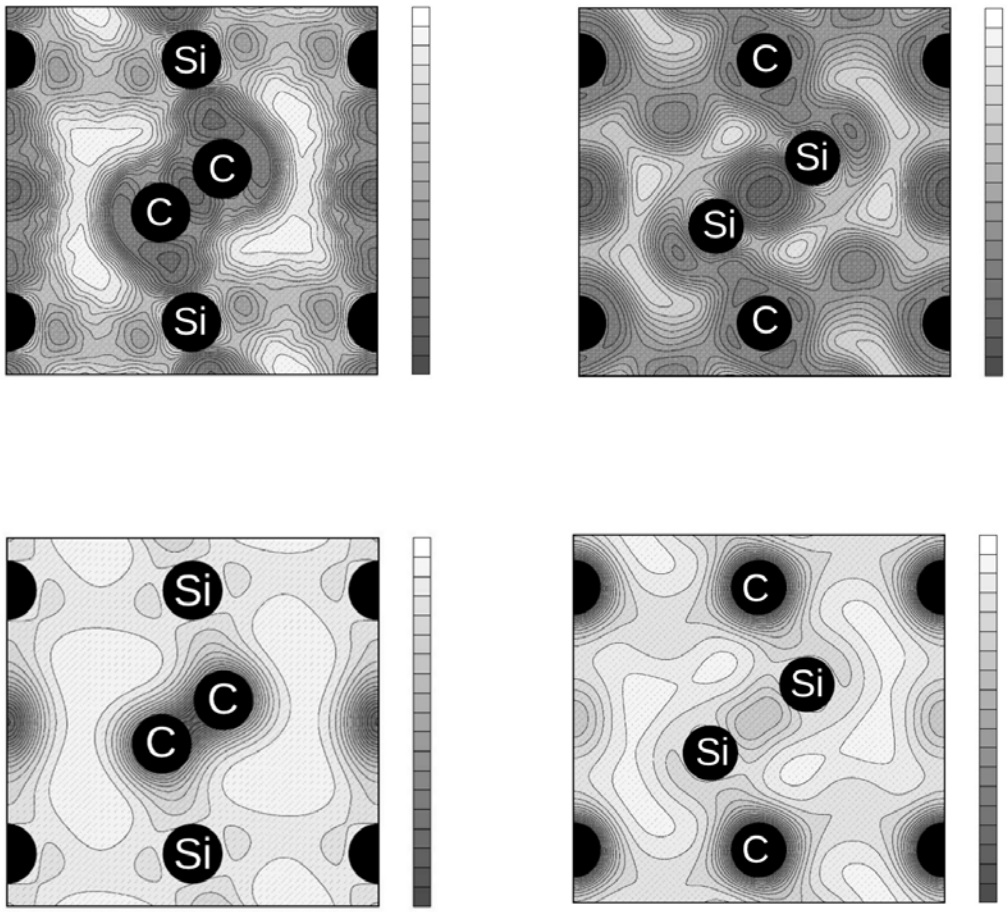

Figure 5.8: Pyrite SiC_2 and Si_2C bonding - Showing ELF (upper) and charge density (lower) plots in the (011) plane for the pyrite alloys SiC_2 (left half) and Si_2C (right half).

that found in ionic rocksalt SiC where PBEsol predicts d_{Si-C}=2.02 Å. These lengths also indicate that the bonding between the carbon atoms is strongly covalent while the bonding between the silicon and carbon atoms is largely ionic (the silicon atoms transferring charge to the carbon pairs).

The carbon pairs are strongly bound to the surrounding silicon atoms resulting in a strong structure. Figure. 5.10 shows an isosurface of the charge density with an ISO value of 0.25 e $Å^{-3}$. It indicates that there is charge within the interstitial spaces between atoms. This gives the bonding a slight metallic character.

The slight metallic bonding is reflected in the band structure plot of Figure. 5.11 where no bad gap exists at the Fermi level. This structure does have an energy gap above the Fermi energy; the high lying states above the gap have the potential to overlap with the conduction band states under pressure. This suggests that the pyrite structure is not a simple metal.

The elastic constants are shown in Table. 5.2 and elastic moduli are given in Table. 5.3. The constants are all positive and the resulting stiffness matrix has positive eigenvalues indicating elastic stability. This stability is also reflected in the resulting positive moduli. This and the fact that the phonon dispersion has no soft modes, indicates that the pyrite structure is a feasible, stable phase for SiC_2.

5.2.2 Pyrite-Si_2C

For Si_2C, the pyrite structure geometrically relaxes into one with lattice parameter a=5.13 Å and internal parameter x=0.365 (shown in Figure. 5.12). As with SiC_2, the total energy is plotted as a function of the internal parameter x at the geometrically optimized lattice constant of a=5.13 Å, making a continuous transition over all possible pyrite structures between $0.175 < x < 0.4$. The resulting plot is shown in Figure. 5.13 where we find a local minimum at x=0.21 and a global minimum at x=0.365. It is interesting to note that the local minimum is not the fluorite structure. The structure of the global minimum has a density of 3.347 g cm^{-3}, greater than the value of 3.216 g cm^{-3} for 3C-SiC and greater than the value for pyrite SiC_2. It has six-fold coordinated carbon atoms connect to six-fold coordinated silicon-silicon pairs.

The charge density plot in the lower-right of Figure. 5.8 for the (011) plane shows that the charge is highly concentrated around each carbon atom whereas the charge around and between the silicon pairs is largely dilute. The ELF plot on the upper-right

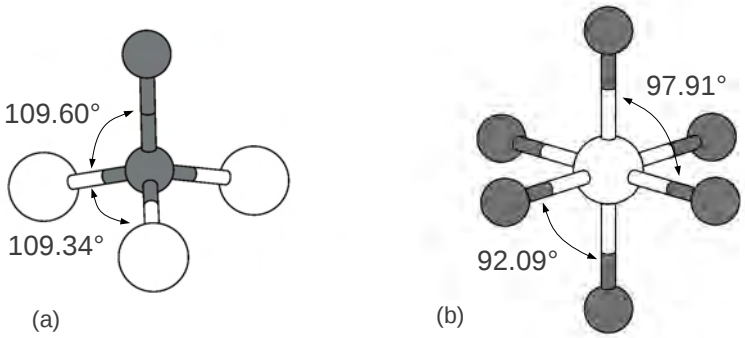

Figure 5.9: Pyrite SiC_2 bonding angles - Showing a) distorted tetrahedral bonding around each carbon b) distorted octahedral bonding around each silicon.

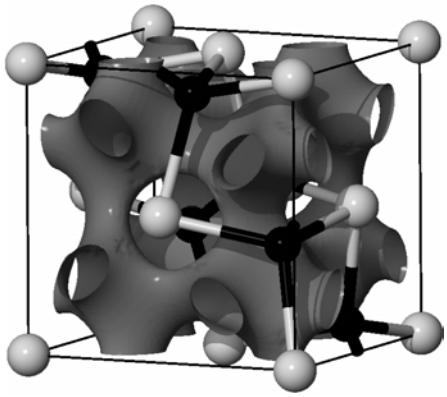

Figure 5.10: Pyrite SiC_2 interstitial valence charge density - Showing charge density in the spaces between atoms. ISO value 0.25 e $Å^{-3}$ (0.037 e $bohr^{-3}$).

Table 5.2: Optimized structural properties and elastic constants C_{ij} calculated from a least-squares fit for Si_2C and SiC_2 (lattice constants in Å, density in g cm^{-3}, C_{ij} in GPa with stated error bars indicating the numerical uncertainty of the fit).

	a	c/a	ρ	C_{11}	C_{12}	C_{13}	C_{33}	C_{44}	C_{66}	Eigenvals
Pyrite SiC_2	4.75		3.225	415.8 ± 1.3	83.1 ± 1.3			65.9 ± 1.8		pos
Pyrite Si_2C	5.13		3.347	100.7 ± 2.8	156.3 ± 2.8			2.6 ± 3.9		neg
Glitter SiC_2	3.16	2.17	2.523	333.5 ± 1.2	15.4 ± 1.2	101.5 ± 0.9	521.9 ± 1.2	33.2 ± 1.7	8.4 ± 1.7	pos
Glitter Si_2C	3.03	2.99	2.728	222.9 ± 2.3	50.4 ± 2.3	72.8 ± 1.6	335.3 ± 2.3	52.8 ± 3.3	40.6 ± 3.3	pos
t-SiC_2	2.93	4.27	3.239	566.2 ± 2.4	22.0 ± 2.4	141.5 ± 1.7	503.5 ± 2.4	246.2 ± 3.4	149.9 ± 3.4	pos
t-Si_2C	3.22	4.62	2.939	263.4 ± 0.9	94.2 ± 0.9	107.9 ± 0.6	284.8 ± 0.9	88.3 ± 1.2	64.9 ± 1.2	pos

Table 5.3: Calculated elastic moduli based on elastic constants for Si_2C and SiC_2 showing upper bound Voigt, lower bound Reuss and geometric mean Hill values in GPa along with the Poisson ratio σ and Debye temperature in Kelvin.

	B_V	B_R	B_H	G_V	G_R	G_H	Y_V	Y_R	Y_H	σ	Θ_D
3C-SiC	221.8	221.8	221.8	191.0	171.9	181.5	445.2	409.9	427.5	0.18	1130
Pyrite SiC_2	194.0	194.0	194.0	106.1	86.9	96.5	269.2	226.8	248.0	0.29	875
Pyrite Si_2C	137.8	137.8	137.8	-9.5	4.7	-2.4	-29.3	13.9	-7.7		
glitter SiC_2	180.6	163.7	172.2	79.6	26.0	52.8	208.3	74.0	141.2	0.34	681
glitter Si_2C	130.3	124.1	127.2	68.2	59.7	64.0	174.3	154.3	164.3	0.28	670
t-SiC_2	249.5	248.8	249.2	217.2	205.7	211.5	505.1	483.7	494.4	0.17	1277
t-Si_2C	159.0	158.5	158.8	81.7	80.6	81.2	209.4	206.8	208.1	0.57	745

shows that there is a significant covalent lobe between the silicon atoms with weaker delocalization between these silicon pairs and their surrounding carbon atoms. No strong ionic bonding exists between the silicon and carbon atoms as opposed to the strong ionic bonding in SiC_2. Compared to the covalency between the silicon atoms, the silicon-carbon bonding is relatively metallic with a very slight ionic character. The covalency between the silicon atoms reduces the effect of the larger electronegativity of the carbon atoms, resulting in weaker bonding as compared to SiC_2.

The silicon atoms have bonding angles C-$\hat{\text{Si}}$-C=118.25° and Si-$\hat{\text{Si}}$-C=97.68° giving a very distorted tetrahedral nature to the bonding around each Si atom with a MAO of 9.4 % compared to 0.12 % for the carbon atom in pyrite-SiC_2. Through each C atom, the opposing Si-C bonds form three straight Si-C-Si segments which are not fully orthogonal to each other but either form an angle of 83.84° or the complimentary angle of 96.16°, giving a distorted octahedral character to the bonding with an MAO of 6.8 %, more distorted than the silicon atoms in pyrite-SiC_2.

The Si-Si bond length of 2.40 Å, close to that for a single covalent bond in diamond Si, shows significantly weaker bonding than the strong bonding between the carbon atoms in pyrite-SiC_2. The Si-C distance is d_{Si-C}=2.12 Å which is much too large for a covalent or ionic bond. The silicon pairs do not strongly bind to the surrounding carbon atoms, due to the strong delocalization in the bonding as opposed to the stronger ionic C-Si bonding in pyrite-SiC_2. All of this results in a weaker, more open structure for pyrite-Si_2C as compared to the SiC_2 structure.

An inspection of the phonon dispersion in Figure. 5.14 shows that this alloy structure is in fact dynamically unstable at zero pressure and although the elastic constants in Table. 5.2 are positive, they define a stiffness matrix with negative eigenvalues. The value for C_{44} is also calculated as zero within the numerical error resulting in negative values for the shear and Young's modulus. This elastic instability is a consequence of the weak bonding along with the increased tetrahedral and octahedral distortion around each silicon atom as compared to similar bonding in pyrite-SiC_2. For these reasons, the pyrite structure is not a feasible structure for Si_2C.

5.3 Glitter structure

In 2005, Bucknum et al.[75] suggested a tetragonal structure for SiC_2 derived from a theoretical allotrope for C called glitter (as discussed in the previous chapter) where the four-fold coordinated carbon atoms are replaced by silicon. For the general binary glitter structure with chemical formula AB_2, the four-fold coordinated A atoms and the three-fold B carbons have atomic positions as given in Table. 5.4 as defined by an internal structural parameter z. This structure (henceforth referred to as the glitter structure) has the space group $P4_2/mmc$ with a primitive-centered tetragonal lattice.

5.3.1 Glitter-SiC_2

The lattice parameters for the glitter SiC_2 structure relax to a=3.16 Å and c/a=2.17 with internal parameter z=0.10, giving a density of 2.523 g cm^{-3}, higher than that for the pyrite structure but lower than the value of 3.216 g cm^{-3} for 3C-SiC. Bucknum et al. obtained cell length parameters of a=3.07 Å and c/a=2.287 though their method is not clear.

Charge density and ELF plots were done in the (100) plane since each face of the glitter structure has the same features as the faces of the tetragonal cell. The charge density plot in the lower-left of Figure. 5.15 shows that the valence charge concentrates around the central carbon-carbon pair in much the same manner as the pair in the pyrite structure. It also shows that this charge extends between silicon atoms. The ELF plot in the upper-left shows covalent lobes between all atoms with those between the carbon and silicon atoms having a slight asymmetry.

The distorted tetrahedral bonding around each Si atom, as shown in Fig. 5.16, has two angles of C-$\hat{S}$i-C=113.40° and another four of C-$\hat{S}$i-C=107.54° giving an MAO of 2.4 %. The distorted trigonal bonding around each C atom has Si-$\hat{C}$-Si=113.40° and Si-$\hat{C}$-C=123.30° with an MAO of 3.7 %. The bond length between the carbon atoms is d_{C-C}=1.36 Å, the same as for the carbon-carbon pair in the pyrite and carbon-glitter structures. The bond length between each carbon atom and its silicon neighbor is d_{Si-C}=1.89 Å, the same as a single covalent Si-C bond in 3C-SiC. This indicates that the bonding is mostly covalent with double bonds between the three-fold coordinated carbon atoms and single bonds between the four-fold coordinated silicon atoms and

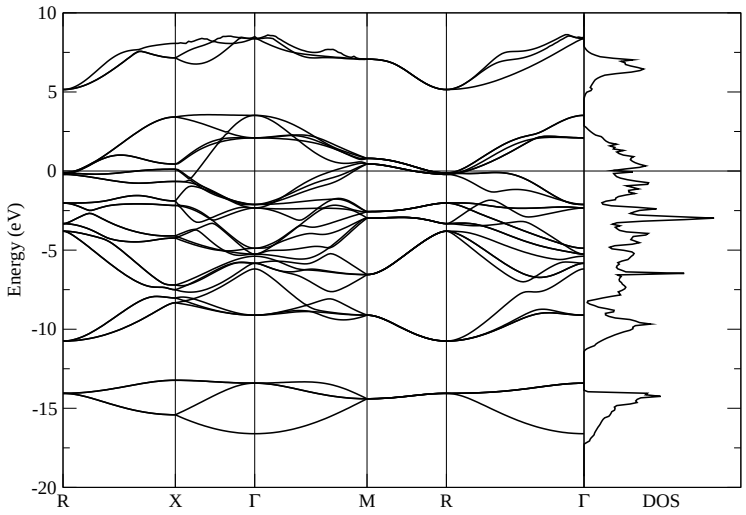

Figure 5.11: Pyrite SiC_2 band structure - Showing it to be metallic. Energies shifted to Fermi level.

Table 5.4: Atomic positions for the tetragonal binary glitter unit cell with chemical formula AB_2 defined as ratios of the cell length parameters a and c and the internal parameter z.

atom	x/a	y/a	z/c
A	0	0	$\frac{1}{4}$
A	0	0	$\frac{3}{4}$
B	0	$\frac{1}{2}$	$\frac{1}{2}+z$
B	0	$\frac{1}{2}$	$\frac{1}{2}-z$
B	$\frac{1}{2}$	0	$1-z$
B	$\frac{1}{2}$	0	z

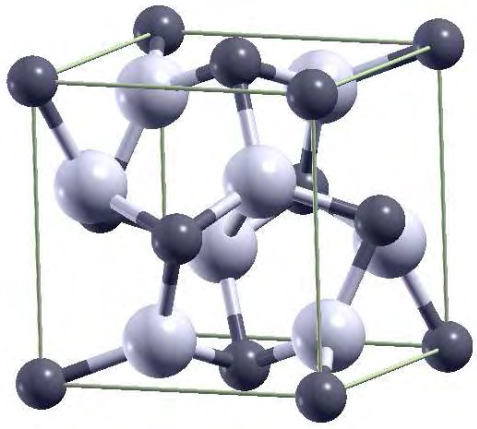

Figure 5.12: Si_2C Pyrite structure - Pyrite structure with x=0.365.

their neighbors. Due to the larger electronegativity of the carbon atoms, the silicon-carbon bonding is slightly ionic.

There are no soft modes present in the phonon dispersion for glitter SiC_2 (shown in Figure. 5.17) indicating that this structure is dynamically stable. It has the same feature of a phonon band gap as was seen in glitter and supercubane carbon indicative of forbidden phonons. The elastic constants in Table. 5.2 have a stiffness matrix with positive eigenvalues and give positive elastic moduli shown in Table. 5.3, both indicating elastic stability. For these reasons, the glitter structure is a feasible, stable phase of SiC_2.

The band structure in Fig. 5.18 indicates that this form of SiC_2 is metallic, therefore there is a metallic character to the bonding. The band structure is close to that of a semi-metal with a depression in the lower conduction band at M as in the carbon glitter phase. This can be better seen in the density of states (DOS) given in Figure. 5.19.

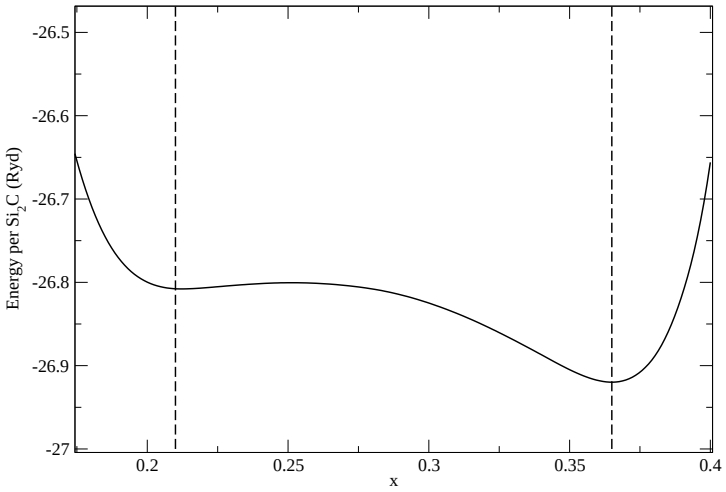

Figure 5.13: Pyrite Si_2C x parameter plot at $a = 5.13\,\AA$ - Showing a local minimum at x=0.21 and a global at 0.365.

5.3.2 Glitter-Si_2C

The lattice parameters for the glitter Si_2C structure relaxed to a=3.03 Å and c/a=2.99 with internal parameter z=0.13, giving a density of 2.728 g cm^{-3}, higher than that for glitter-SiC_2 but lower than the value of 3.216 g cm^{-3} for 3C-SiC.

The charge density plot in the lower-right of Figure. 5.15 shows that the valence charge concentrates around each carbon atom and between the silicon atoms in the central silicon-silicon pair. The ELF plot in the upper-right shows covalent lobes between all atoms with a significantly larger lobe between the silicon atoms. The distorted tetrahedral bonding around each C atom has two angles of Si-$\hat{C}$-Si=103.83° and another four of Si-$\hat{C}$-Si=110.76°, giving an MAO of 2.5 %, the same as glitter-SiC_2 with its MAO of 2.4 %. The distorted trigonal bonding around each Si atom has C-$\hat{Si}$-C=110.76° and C-$\hat{Si}$-Si=124.62° giving an MAO of 5.1 %, larger than in glitter-SiC_2. The bond length between the silicon atoms is d_{Si-Si}=2.34 Å, the same as a single covalent bond as in diamond silicon. The bond length between each silicon atom and its carbon neighbor is d_{Si-C}=1.87 Å, the same as a Si-C bond in 3C-SiC. This indicates that the bonding between all atoms is covalent with the silicon-carbon bonding being slightly ionic. The

band structure plot in Figure. 5.20 shows that unlike glitter-SiC_2, there is no depression near the Fermi level indicating that the bonding has a relatively greater metallic character. Therefore, the bonding is weaker than that in glitter-SiC_2 and due to the relatively loosely bound silicon pair, the structure is more open.

There are soft modes present in the phonon dispersion (shown in Figure. 5.21) indicating that this is not a stable, feasible phase for Si_2C. This even though the elastic constants in Table. 5.2 give a stiffness matrix with positive eigenvalues and positive elastic moduli.

5.4 t-BC_2 structure

In 2010, Xu et al.[8] proposed a tetragonal structure for diamond-like boron dicarbide called t-BC_2. The structure has the symmetry group $I4_1/amd$ with boron atoms at the 4*a* Wyckoff positions and carbon atoms at the 8*e* positions with internal parameter z=0.533. Its underlying bravias lattice is body-centered tetragonal. This structure also allows for the off 50:50 alloys of SiC_2 and Si_2C.

5.4.1 t-SiC_2

The alloy t-SiC_2, shown in Figure. 5.22, has silicon atoms in place of the boron atoms in t-BC_2 with four silicon atoms and eight carbon atoms per conventional cell. It relaxed into a structure with lattice parameters a=2.93 Å and c/a=4.27 with internal parameter z=0.534. This gave a density of 3.239 g cm^{-3}, slightly greater than the value of 3.216 g cm^{-3} for 3C-SiC. The two ELF plots in Figure. 5.22 show that there is significant localization of bonding electrons between each atom and its neighbors with none in the interstitial regions. This is also reflected in the charge density plots. The distorted tetrahedral bonding around each Si atom has an MAO of 4.7 % with two angles of C-$\hat{Si}$-C=101.9° and another four of C-$\hat{Si}$-C=113.4°. The distorted tetrahedral bonding around each C atom has an MAO of 5.3 % with one angle of Si-$\hat{C}$-Si=101.9°, another four of C-$\hat{C}$-Si=106.7° and one more of C-$\hat{C}$-C=125.7°. The calculated neighbor to neighbor lengths are d_{C-C}=1.64 Å, larger than a single covalent bond in diamond, and d_{Si-C}=1.88 Å, the same as a single covalent bond in 3C-SiC. This indicates that there is a strong covalent nature to the bonding. The band structure shown in Figure. 5.25

shows a direct band gap of 0.76 eV, indicating that the valence electrons are extremely localized.

The elastic constants in Table. 5.2 are all positive and the resulting stiffness matrix has positive eigenvalues. This and the fact that the resulting moduli shown in Table. 5.3 are also all positive indicates elastic stability. The phonon dispersion shown in Figure. 5.24 shows no soft modes, also indicating dynamic stability. For these reasons, this tetragonal structure is a stable, feasible phase for silicon dicarbide.

5.4.2 t-Si_2C

The alloy t-Si_2C, shown in Figure. 5.23, has four carbon atoms and eight silicon atoms per cell. The structure relaxed to a=3.22 and c/a=4.62 with internal parameter z=0.555. This gave a density of 2.939 g cm^{-3}, less than the value of 3.216 g cm^{-3} for 3C-SiC. The ELF and charge density plots show similar features to t-SiC_2. The distorted tetrahedral bonding around each C atom has two angles of Si-$\hat{C}$-Si=115.6° and another four of Si-$\hat{C}$-Si=106.5° giving an MAO of 3.7 % which is comparable to the value for the Si atom in SiC_2. The distorted tetrahedral bonding around each Si atom has one angle of C-$\hat{Si}$-C=115.6°, another four of Si-$\hat{Si}$-C=112.7° and one more of Si-$\hat{Si}$-Si=87.3° giving an MAO of 6.3 % showing that the tetrahedral bonding around the Si atom is more distorted than that around the C atoms in SiC_2. The C-Si bond length is d_{Si-C}=1.90 Å (close to that in 3C-SiC), whereas the d_{Si-Si}=2.33 Å (close to that in diamond silicon). The band structure plot of Figure. 5.26 shows that there is a metallic component to the bonding.

The elastic constants given in Table. 5.2 give a stiffness matrix with positive eigenvalues. This and the fact that the elastic moduli in Table. 5.3 are all positive, indicates elastic stability. The phonon dispersion in Figure. 5.21 shows soft modes indicating dynamic instability. This instability persisted up to a pressure of 800 GPa indicating that this structure is not a feasible phase for Si_2C.

5.5 Stable silicon dicarbide

The previous calculations have determined three feasible phases for SiC_2 namely the pyrite, glitter and t-SiC_2 structures. These structures have the required elastic and

dynamical stability due to their geometry and bonding type. Pyrite-SiC_2 has four-fold coordinated carbon atoms and six-fold coordinated silicon atoms with close to ideal tetrahedral and octahedral bonding. Because of this, the bonding is a mixture of covalent, ionic and metallic bonding and the structure is a metal. Glitter has four-fold coordinated silicon atoms with three-fold coordinated carbons with slightly distorted tetrahedral and trigonal bonding. The bonding is mostly covalent with slight ionic and metallic character making the material almost a semi-metal. The last structure, t-SiC_2, has distorted tetrahedral covalent bonding, making the material a semi-conductor. The trend in increasing metallic character is from t-SiC_2 $\rightarrow$ glitter-SiC_2 $\rightarrow$ pyrite-SiC_2.

5.5.1 Pressure transitions and formation energies

By relaxing the three stable structures under pressure using the PBEsol functional, the enthalpy versus pressure curves in Figure. 5.28 were obtained. It is clear that the t-SiC_2 structure is stable over the entire pressure range. There are no pressure transitions from this structure to any of the others. A possible pressure transition exists from glitter to pyrite at 24.7 GPa.

The heats of formation are ΔH_{t-SiC_2}=112 kJ mol^{-1}, $\Delta H_{glitter}$=124 kJ mol^{-1} and ΔH_{pyrite}=221 kJ mol^{-1}. The positive heats of formation indicate that these phases do not form spontaneously under ambient conditions. The glitter and t-SiC_2 phases have very similar values at zero pressure. Possibly C-rich conditions of growth under pressure and temperature are needed to explore the synthesis of this new material.

5.5.2 Comparison of elastic properties

The calculated Hill elastic moduli in Table. 5.3 for the three SiC_2 phases rank according to Debye temperature. The Debye temperature is another measure of material stiffness since a stiffer material results in higher acoustic velocities, meaning a higher Debye temperature. The silicon dicarbide materials rank in order of increasing stiffness, with 3C-SiC included for comparison, as glitter $\rightarrow$ pyrite $\rightarrow$ 3C-SiC $\rightarrow$ t-SiC_2.

The Debye temperature and elastic moduli values for t-SiC_2 are highly comparable to 3C-SiC since both materials share many structural properties. All of their atoms are four-fold coordinated with t-SiC_2 having slightly distorted strong covalent tetrahedral bonding, very similar to 3C-SiC. The t-SiC_2 structure has the larger values since 1/3

of its bonds are strong C-C bonds, instead of all the bonding being homogeneous Si-C bonds as in 3C-SiC.

The bonding in t-SiC_2 gives it the highest bulk modulus of the three silicon dicarbide phases since it has a geometrical configuration that is relatively more resistant to isotropic compressive strain. Pyrite has a lower value since one out of three atoms have six-fold coordination and the bonding to the silicon atoms has a strong ionic character. The pyrite structure has a higher value than that of glitter due to the fact that it contains C atoms in the center of near-perfect tetrahedra and Si atoms in the center of near-perfect octahedra, whereas glitter has more distorted tetrahedral bonding around each silicon atom, with each carbon atom having distorted trigonal bonding. It should be noted that Bucknum et al. calculated a bulk modulus value for glitter of 230 GPa (on par with 3C-SiC and t-SiC_2) using a semi-empirical formula by Cohen [76]. This value, 34 % higher than the Hill value for glitter SiC_2 in Table. 5.2, is obviously a gross over-estimation. The low shear modulus for the glitter structure is due to its greater anisotropy. The low value for its Young's modulus is due to bending of the trigonal bonds around each C atom. The Poisson ratios for pyrite and glitter structures are similar and they are significantly greater than that for SiC, suggesting they have a higher ductility [149]. This is consistent with the metallic nature of both SiC_2 structures. The large value for glitter is due to a decrease in the Si-$\hat{C}$-Si angles causing a significant reduction in the cross-sectional area of the unit cell when under strain in the [001] direction. As expected, the Poisson ratios for 3C-SiC and t-SiC_2 are almost the same.

5.6 Conclusions

This study has focused on three candidate structures for the two possible alloy combinations of SiC_2 and Si_2C. For all three structures, silicon rich Si_2C was found to be unstable since the structures now contained longer Si-Si bonds in comparison to the C-C bonds found in SiC_2 which resulted in more open structures with even greater distortion in the tetrahedral, octahedral and trigonal bonding. The shorter C-C bonds in SiC_2 have less distortion in the bonding yielding more stable structures. From this observation, it seems likely that carbon rich alloys are more favorable to their silicon-rich counterparts due to the smaller size of the carbon atoms and the more compact

carbon-carbon bonds which result in less distorted bonding. SiC_2 shows the greatest promise as a new material that could be synthesized.

Analysis of the charge distribution and ELF plots revealed that the bonding in pyrite Si_2C is weaker compared to stable SiC_2 due to greater valence electron pair delocalization existing between the silicon atoms and the six-fold coordinated carbons. The density of states plot for glitter-Si_2C also revealed that its bonding is more metallic than SiC_2 therefore weaker by comparison. The relative weakness of the glitter and t-Si_2C structures is seen in the lower elastic moduli values of Table. 5.3 as compared to their SiC_2 counterparts. It was found that t-Si_2C is a metal indicating its bonding to be weaker compared to the covalent bonding in semi-conducting t-SiC2. This shows that the larger silicon content of these silicon-carbon alloys increases their metallic nature thereby weakening the bonding.

Of the stable SiC_2 structures, the tetragonal phase had the lowest heat of formation with ΔH_{t-SiC_2}=112 kJ mol^{-1}, followed by glitter with $\Delta H_{glitter}$=124 kJ mol^{-1} and finally pyrite with the highest at ΔH_{pyrite}=221 kJ mol^{-1}. Pyrite and glitter exhibit metallic character whereas t-SiC_2 is a semi-conductor and the pyrite phase is predicted to not be a simple metal because of the existence of an energy band gap above the Fermi level. The glitter phase almost has the same electronic structure as a semi-metal due to the existence of a depression in the density of states near the Fermi level. The metallic nature of these two materials manifests itself in elastic moduli that are considerably lower that those for 3-SiC despite the higher C content and shorter C-C bond lengths. The moduli for the three structures were found to rank according to their Debye temperatures with t-SiC_2 having the highest values followed by pyrite-SiC_2 and finally glitter-SiC_2. The Debye temperature and moduli values for t-SiC_2 were found to be highly comparable to 3C-SiC since both materials share many structural properties: Their atoms are four-fold coordinated with t-SiC_2 having slightly distorted strong covalent tetrahedral bonding, very similar to 3C-SiC. The t-SiC_2 structure has the larger values since 1/3 of its bonds are strong C-C bonds instead of all the bonding being homogeneous as in 3C-SiC. In terms of ductility, both the pyrite and glitter structures had similar Poisson ratios well higher than that for 3C-SiC while t-SiC_2 had the same value as 3C-SiC.

It is likely that C-rich conditions of growth under pressure and temperature are needed to explore the synthesis of silicon dicarbide.

This concludes the *ab initio* study of bulk Si-C alloys. The next chapter explores two dimensional Si-C systems by introducing a novel 2D equation of state which is then used to evaluate the strength properties of various structures. Included are the C, Si and SiC honeycomb structures, four graphene allotropes, layered graphenes and the off-50:50 2D alloy silagraphene (SiC_2).

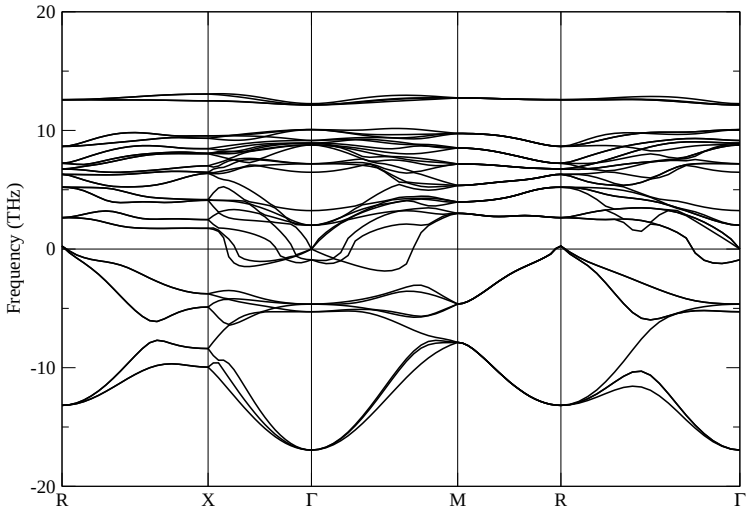

Figure 5.14: Pyrite Si_2C phonon dispersion at 0 GPa - Showing soft modes.

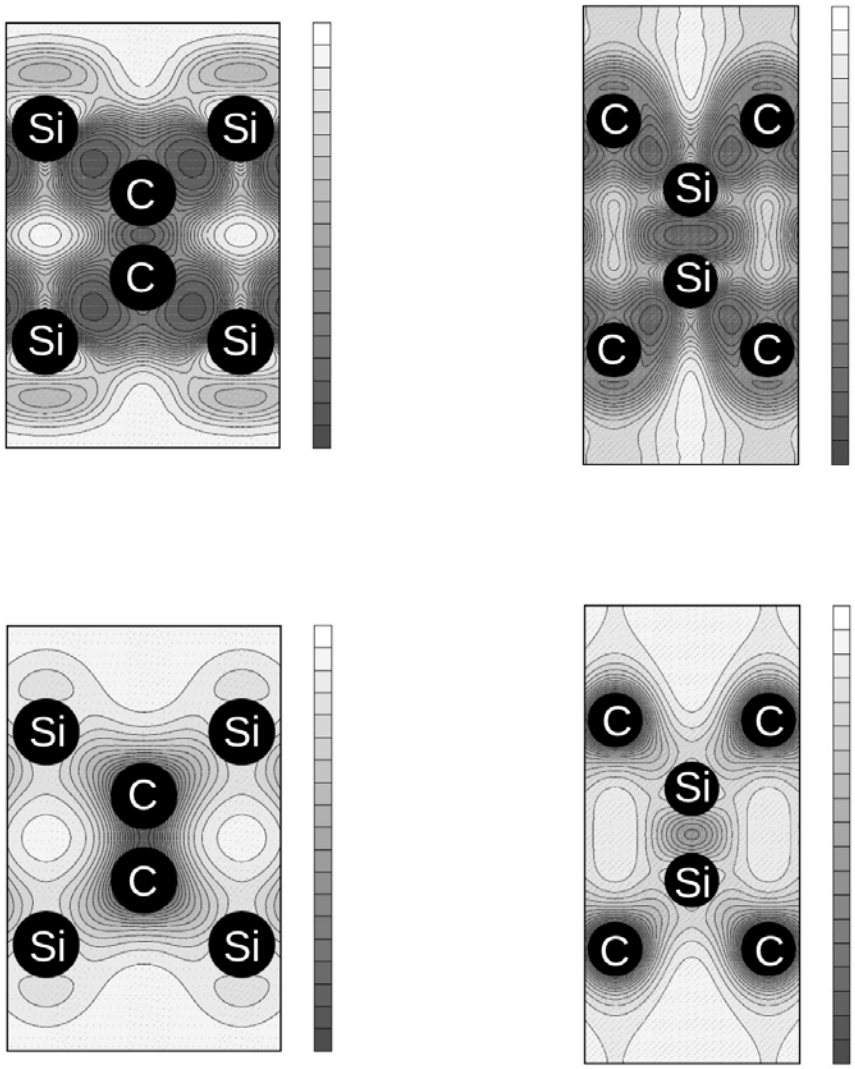

Figure 5.15: Glitter SiC_2 and Si_2C bonding - Showing ELF (upper) and charge density (lower) plots in the (011) plane for the alloys SiC_2 (left half) and Si_2C (right half).

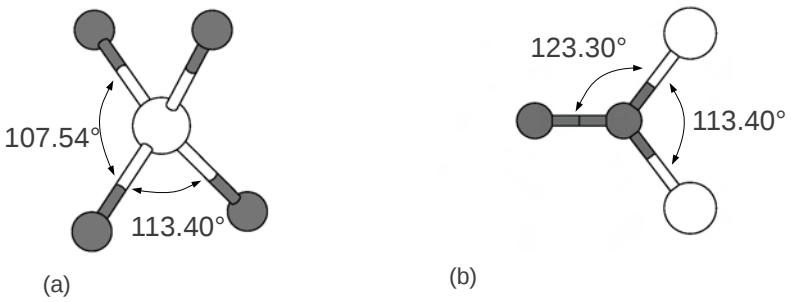

Figure 5.16: Glitter SiC_2 bonding angles - Showing a) distorted tetrahedral bonding around each silicon b) distorted trigonal bonding around each carbon.

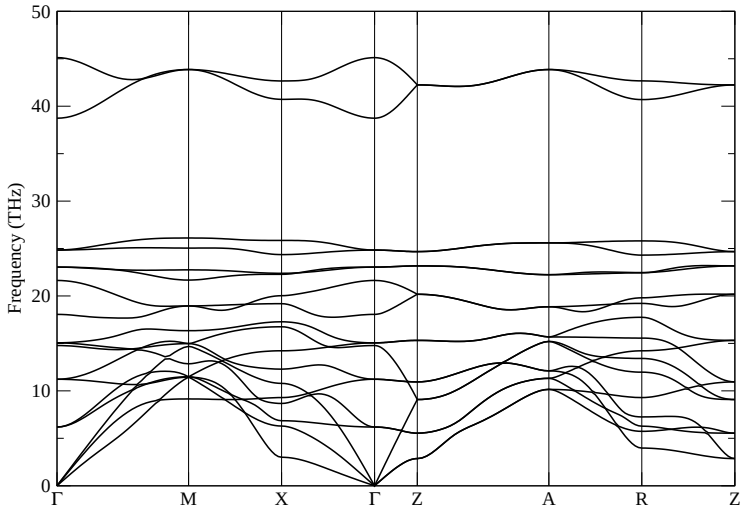

Figure 5.17: Glitter SiC_2 phonon dispersion at 0 GPa - Showing no soft modes.

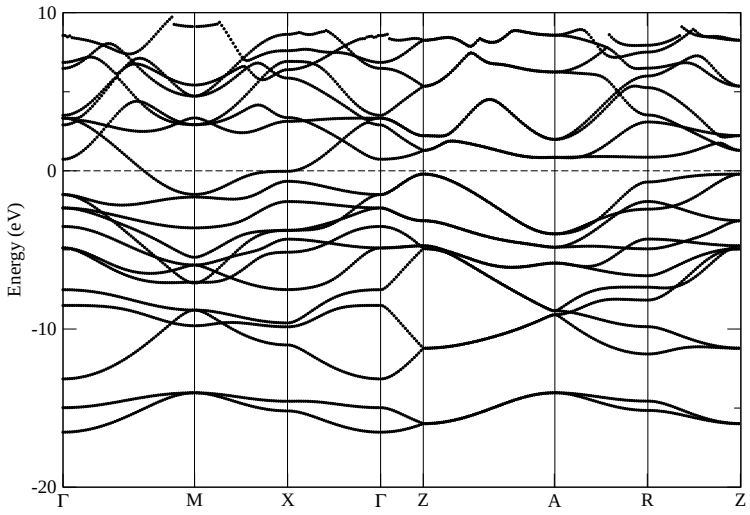

Figure 5.18: Glitter SiC_2 band structure - Showing it to be metallic. Energies shifted to Fermi level.

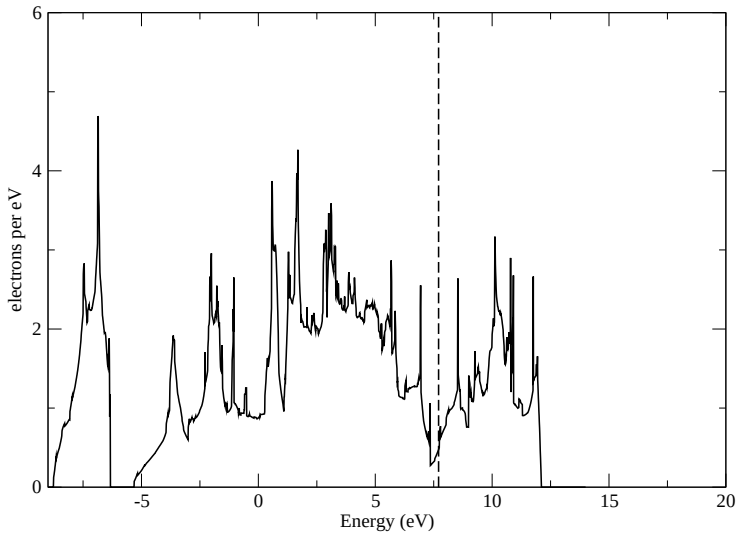

Figure 5.19: Glitter SiC_2 density of states - Showing a depression near the Fermi level.

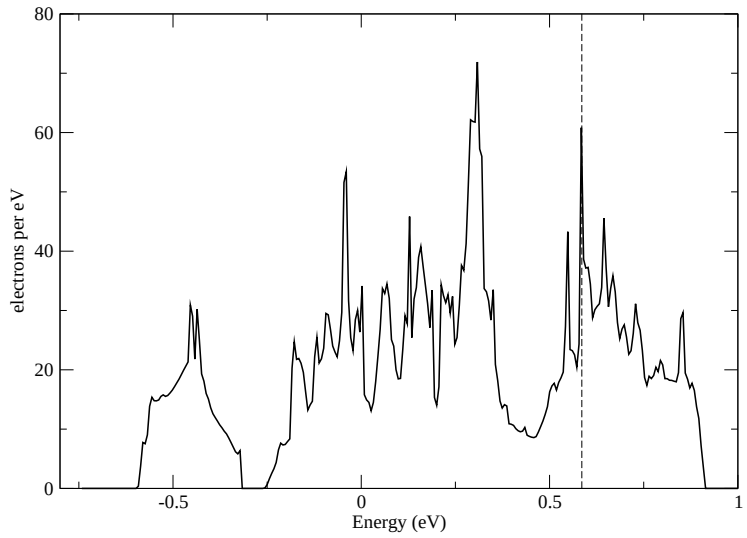

Figure 5.20: Glitter Si_2C density of states - Showing a no depression near the Fermi level.

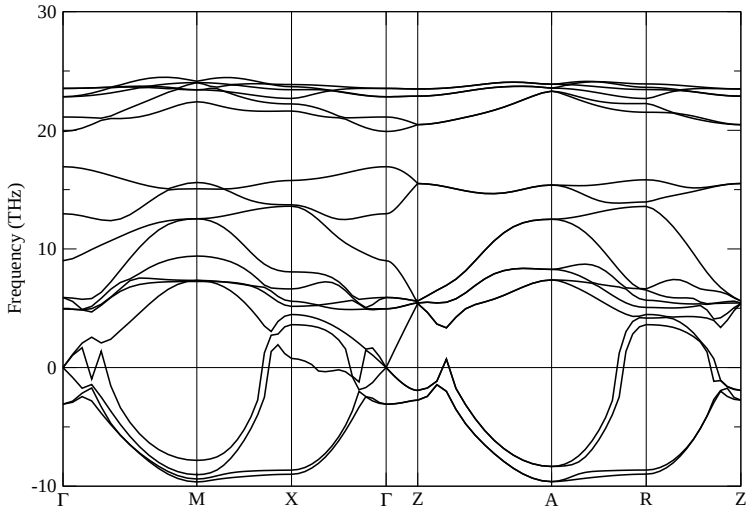

Figure 5.21: Glitter Si_2C phonon dispersion at 0 GPa - Showing soft modes.

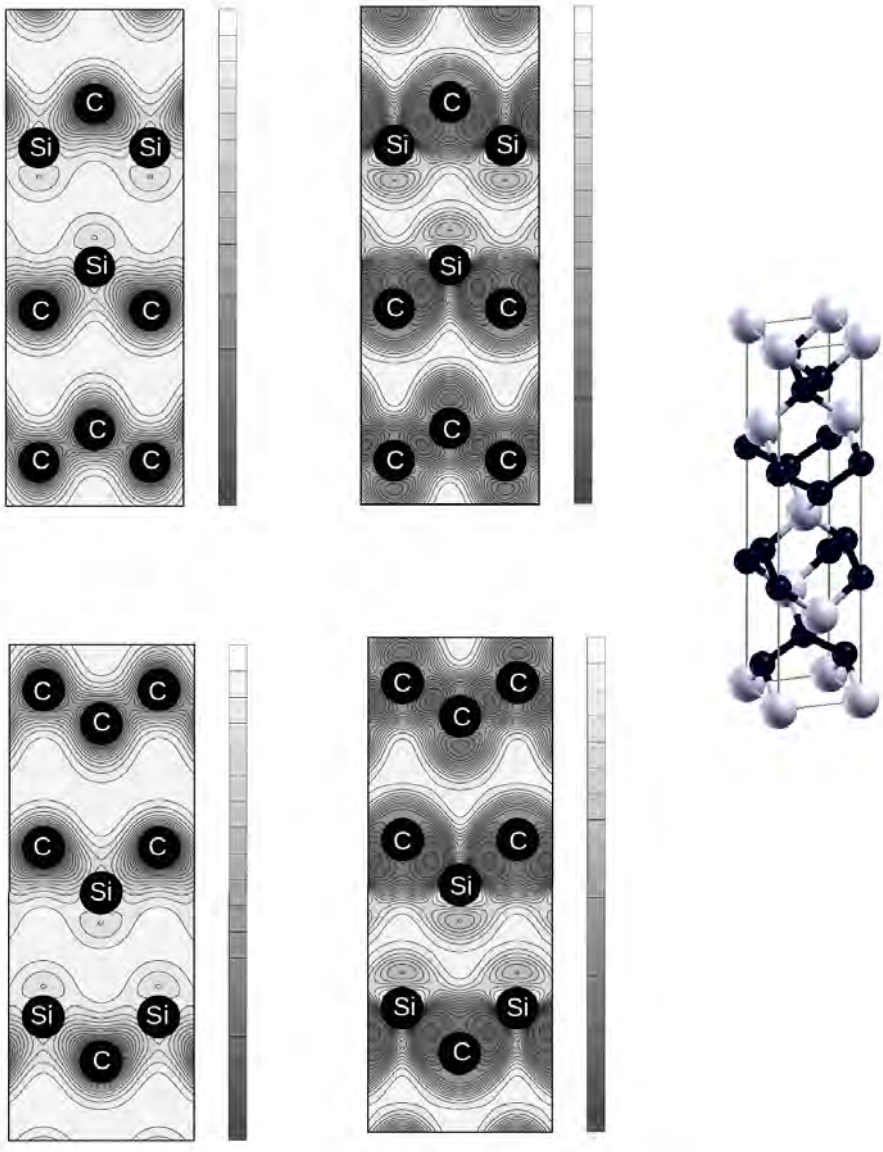

Figure 5.22: t-SiC_2 structure - Showing charge density plots (left) and ELF plots (right) for the (100) plane in the top row and (010) plane on the bottom.

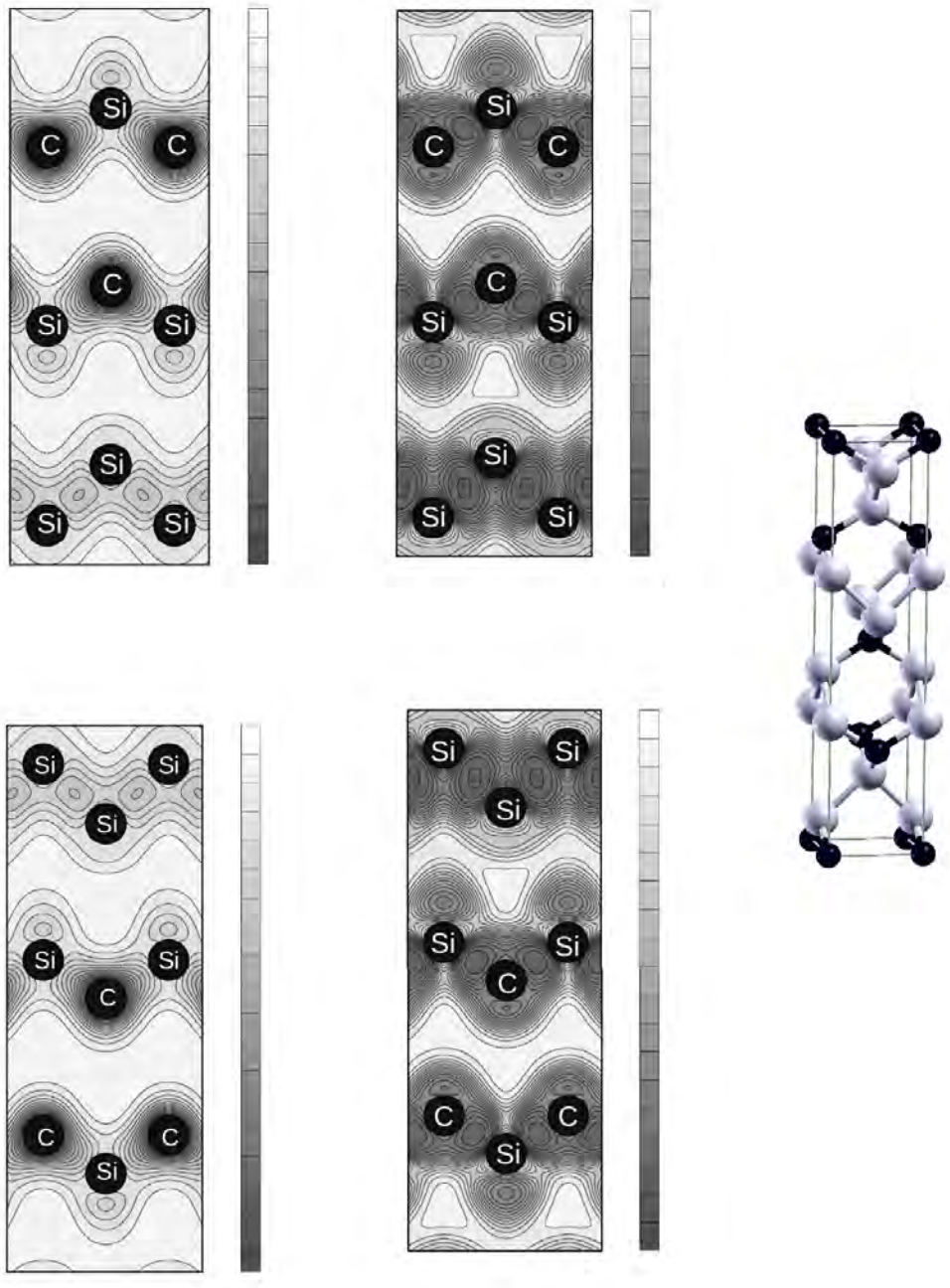

Figure 5.23: t-Si_2C structure - Showing charge density plots (left) and ELF plots (right) for the (100) plane in the top row and (010) plane on the bottom.

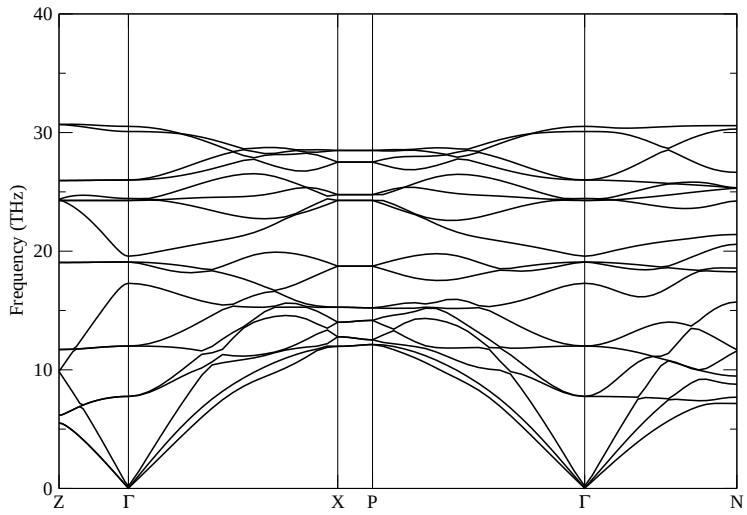

Figure 5.24: t-SiC_2 phonon dispersion at 0 GPa - Showing no soft modes.

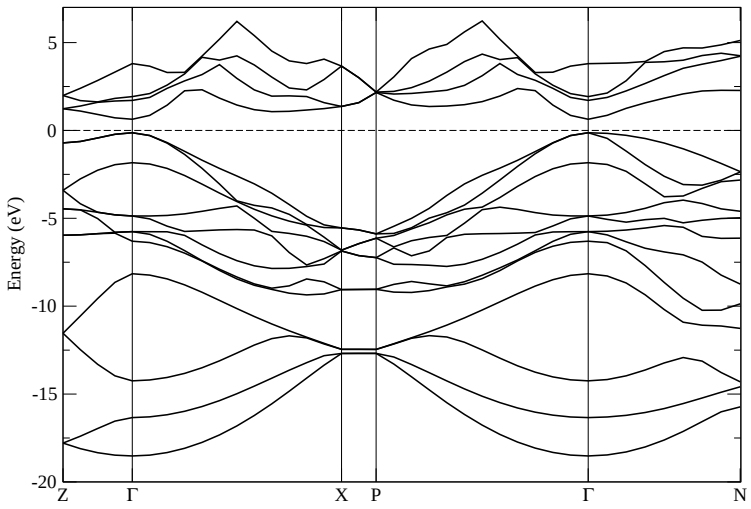

Figure 5.25: t-SiC_2 band structure - Showing a direct band gap of 0.76 eV. Energies shifted to the Fermi level.

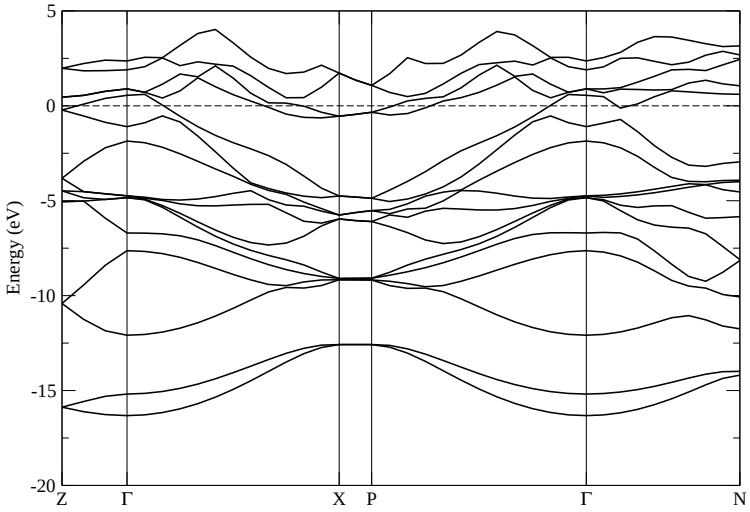

Figure 5.26: t-Si_2C band structure - Showing it to be a metal. Energies shifted to the Fermi level.

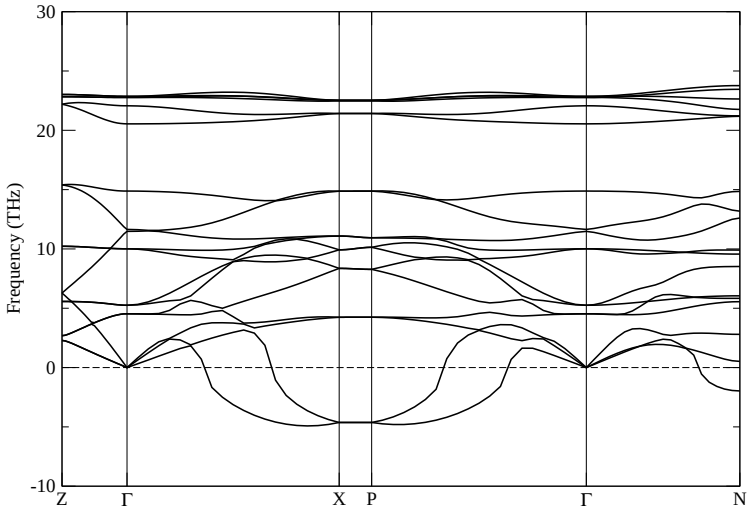

Figure 5.27: t-Si_2C phonon dispersion at 0 GPa - Showing soft modes.

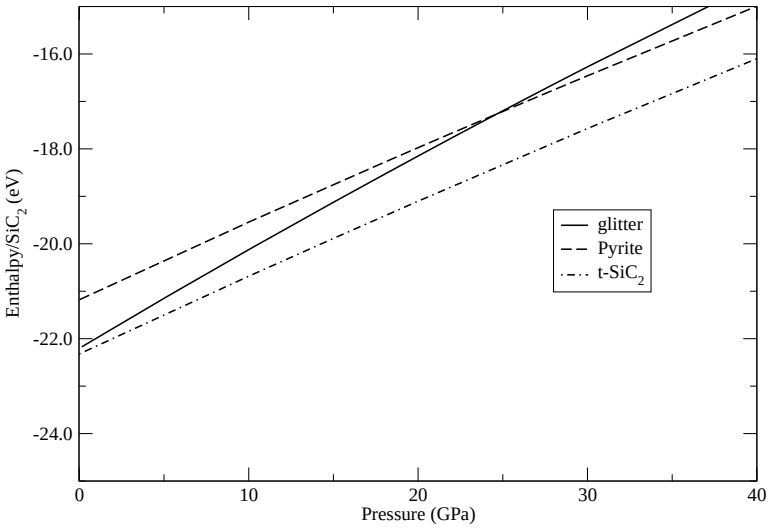

Figure 5.28: Silicon dicarbide PBEsol enthalpy-pressure curves - Showing curves for glitter, pyrite and t-SiC_2 with a possible phase transition from glitter to pyrite at 24.7 GPa.

6

Two dimensional Si-C systems and the 2D equation of state

The bulk of the work presented in this chapter has been published:

R C Andrew et al. Physical Review B 85, 125428 (2012) [150]

With the recent discoveries of graphene [9], a two dimensional (2D) allotrope of carbon in the honeycomb structure, and of boronitrene [151], also in the honeycomb structure, one is once again alerted to the iso-structural nature of these elements which prompts questions about the relative hardness and strength of these materials. The resistance to uni-axial strain (2D Young's modulus) of graphene and boronitrene has been compared theoretically [84], and experimentally measured [83,152] showing that graphene is the stronger material in this respect. A 2D bulk modulus has been calculated for both materials based on empirically derived elastic constants [81,153] and it is apparent that boronitrene has a value approximately 85% the value for graphene. The full significance of this result and how it describes the reaction of these materials to conditions of applied 2D pressure (now referred to as force per unit length $\mathcal{F}$) has not been investigated. Also, since graphene and boronitrene are, in effect, amongst the first two dimensional systems to be synthesized, the notion of hardness in two dimensional systems is yet to be fully investigated and tested. For example, while three dimensional crystal systems are compliant to positive isotropic pressure, it is generally considered not feasible to apply negative isotropic pressure in a carefully controlled manner to three dimensional systems. Two dimensional systems, on the other hand, open the prospects of applying

a negative $\mathcal{F}$, which amounts to a uniform stretch of the material. In fact, it could be argued that stretching a two dimensional material is mechanically more stable than uniformly compressing it in two dimensions. Stretching constrains the system in two dimensions, whereas compressing could result in buckling. Because of this latter point, it is essential that one views graphene and boronitrene as quasi-two dimensional systems rather than truly two dimensional systems. Also, puckering can occur for example by the inclusion of adatoms. Notwithstanding this, both stretching and compressing forces can, in principle, be applied in the plane of a two dimensional material, and this opens a new terrain for investigating the mechanical properties of these materials. For instance, although the 2D bulk modulus is readily computed from the elastic constants, there exists no equation of state (EOS), as is the case for bulk materials, where this property can be deduced from the relationship of the hydrostatic change in surface area to $\mathcal{F}$. The possibility of 2D allotropes, as in the case of graphene[154,155,156,157], also poses the question of whether phase transitions exist between these structures, something which can easily be tested by an EOS.

Here an EOS applicable to 2D structures is presented which provides a simple way to calculate the 2D bulk modulus. This modulus is a measure of the material's resilience to an externally applied isotropic $\mathcal{F}$ that is applied in two dimensions. It has units of force per unit length (Nm^{-1}) and may be defined for a single layer as well as for multi-layers. Because of this and the fact that a bulk modulus is associated with bulk pressure, this 2D equivalent is referred to as the layer modulus (symbol γ). This property has many analogies in other fields of study such as the "membrane stretching modulus" (also known as the "area-stretching elastic constant") used in the study of lipid bilayer membranes[158] and other soft materials.

This novel EOS is used to extract fit parameters, including the layer modulus, for the monolayer systems of graphene (now referred to as C) and also included are results for SiC and Si in the isostructural honeycomb structure for comparison. The EOS is also used to investigate the 2D strength of a planar SiC_2 structure first proposed by Li et al.[159] which they refer to as silagraphene. Four graphene allotropes are considered to test the possibility of 2D phase transitions from graphene. Bilayer, trilayer and four-layered graphene (henceforth denoted as 2-graphene, 3-graphene and 4-graphene) are also considered to investigate whether the EOS can indicate any trends. In all cases, the elastic properties are calculated and the EOS is used to predict intrinsic strength.

In Section 6.1, the theoretical concepts and equation of state used to investigate the two dimensional systems are presented as well as the computational parameters used. In Section 6.2 the 2D systems are investigated and the results discussed. Lastly, in Section 6.3, conclusions are given.

6.1 Theoretical framework

6.1.1 The two dimensional equation of state

The two dimensional equivalent of bulk pressure is force per unit length (denoted $\mathcal{F}$) where an in-plane hydrostatic force causes a uniform change in area of the two dimensional lattice. Force per unit length is expressed as the first derivative of the energy with respect to surface area:

$$\mathcal{F} = -\frac{\partial E}{\partial A}, \tag{6.1}$$

and has units Nm^{-1}. Positive $\mathcal{F}$ represents a hydrostatic 2D compression while negative $\mathcal{F}$ represents a uniform stretching. The two dimensional equivalent of the bulk modulus, the layer modulus, is then defined as

$$\gamma = -A\frac{\partial \mathcal{F}}{\partial A}. \tag{6.2}$$

The bulk modulus represents the resistance of a bulk material to compression, whereas the layer modulus represents the resistance of a 2D material to stretching.

The layer modulus for a monolayer of graphitic material can be estimated from the in-plane linear modulus obtained from the 1-dimensional linear Murnaghan EOS of Hanfland et al.[141] by the following

$$\gamma_0 \simeq \frac{t\,\beta_0}{2}, \tag{6.3}$$

where t is the layer thickness.

Using the procedure described in Appendix A, one can derive a two dimensional EOS relating the applied $\mathcal{F}$ to the surface area for any 2D material:

$$\mathcal{F}(A) = -2\,\gamma_0 \left[\epsilon + (1-\gamma_0')\,\epsilon^2 + \frac{2}{3}\left((1-\gamma_0')(2-\gamma_0') + \gamma_0\,\gamma_0''\right)\,\epsilon^3\right], \tag{6.4}$$

where the equibiaxial Eulerian strain is given by

$$\epsilon = \frac{1}{2}\left[1 - \frac{A_0}{A}\right], \tag{6.5}$$

and A_0, γ_0, γ_0' and γ_0'' are the equilibrium values for the unit cell area, layer modulus, the force per unit length derivative and second derivative of the layer modulus at $\mathcal{F}=0$. Integrating Eqn. 6.4 with respect to A, the energy EOS is obtained,

$$E(A) = E_0 + 4\,A_0\,\gamma_0\left[\frac{1}{2}\,\epsilon^2 + \frac{1}{3}(5-\gamma_0')\,\epsilon^3 + \frac{1}{6}\left((1-\gamma_0')\,(8-\gamma_0') + \gamma_0\,\gamma_0'' + 18\right)\,\epsilon^4\right],$$

which can be fitted to hydrostatic expansion and compression data to extract A_0, γ_0, γ_0' and γ_0''. The resulting γ versus $\mathcal{F}$ curve is then given by

$$\gamma(\mathcal{F}) = \gamma_0 + \gamma_0'\,\mathcal{F} + \frac{1}{2}\,\gamma_0''\,\mathcal{F}^2. \tag{6.6}$$

The fitted energy vs area curves of various candidate allotropes will give an indication of the presence of phase transitions between structures.

6.1.2 Elastic theory

In-plane stress is related to in-plane strain through the elastic constants where

$$\begin{bmatrix}\sigma_1\\ \sigma_2\\ \sigma_6\end{bmatrix} = \begin{bmatrix}c_{11} & c_{12} & c_{16}\\ c_{12} & c_{22} & c_{26}\\ c_{16} & c_{26} & c_{66}\end{bmatrix}\begin{bmatrix}\varepsilon_1\\ \varepsilon_2\\ 2\,\varepsilon_6\end{bmatrix} \tag{6.7}$$

The four non-zero 2D elastic constants for square, rectangular or hexagonal lattices are c_{11}, c_{22}, c_{12} and c_{66} (using the standard Voigt notation: 1-xx, 2-yy, 6-xy) where, due to symmetry, the square and hexagonal structures have $c_{11}=c_{22}$ and hexagonal structures have the additional relation that $c_{66}=\frac{1}{2}(c_{11}-c_{12})$. The units for the elastic constants are the same as $\mathcal{F}$.

In terms of these elastic constants, the layer modulus is

$$\gamma = \frac{1}{4}(c_{11}+c_{22}+2\,c_{12}), \tag{6.8}$$

the 2D Young's moduli (in-plane stiffness) for strains in the Cartesian [10] and [01] directions are

$$Y^{2D}_{[10]} = \frac{c_{11}\,c_{22}-c_{12}^2}{c_{22}} \quad \text{and} \quad Y^{2D}_{[01]} = \frac{c_{11}\,c_{22}-c_{12}^2}{c_{11}}, \tag{6.9}$$

the corresponding Poisson ratios are

$$\nu^{2D}_{[10]} = c_{12}/c_{22} \quad \text{and} \quad \nu^{2D}_{[01]} = c_{12}/c_{11}, \tag{6.10}$$

and 2D shear modulus is

$$G^{2D} = c_{66}. \tag{6.11}$$

For isotropic materials, the 2D Young's modulus and Poisson ratio are defined by the following relations[81]

$$Y^{2D} = \frac{4\gamma\, G^{2D}}{\gamma + G^{2D}} \tag{6.12}$$

$$\nu^{2D} = \frac{\gamma - G^{2D}}{\gamma + G^{2D}}. \tag{6.13}$$

It can be easily shown that Eqns. 6.9 and 6.10 for hexagonal structures are equivalent to Eqns. 6.12 and 6.13 indicating that these structures are truly isotropic. Using this fact, a measure of anisotropy can be defined where

$$ISO = \frac{4c_{66}}{c_{11} + c_{22} - 2c_{12}} \tag{6.14}$$

with a value of $ISO = 1$ indicating full isotropy.

Since the modulus equations apply only to the underlying 2D lattice of the material, they ignore the fact that the material has an out-of-plane thickness t. They can be re-expressed in the bulk units of Nm^{-2} by dividing the desired modulus by the material thickness.

6.1.3 Computational details

All calculations were done within the framework of density functional theory[88] (DFT) using the PAW[113] formalism as implemented in VASP[101]. The PBE GGA exchange-correlation functional[96] is used except for multi-layer graphene where LDA was used since it better incorporates the bonding between layers. The **k**-point sampling was done on a 10×10×1 Monkhorst-Pack[105] grid for honeycomb and layered graphene structures. A grid of 4×4×1 was used for structures with 4 or 8 atom unit cells and 2×2×1 for 18 atom unit cells. The total energy calculations were converged to within 10^{-5} eV and the Fermi distribution function with a smearing parameter 0.2 eV was used to integrate the bands at the Fermi level. Each structure was relaxed so that the forces converged to within 0.01 eV $\mathrm{Å}^{-1}$.

In all cases, a kinetic energy cut-off of 500 eV was used. For the monolayer materials and 2-graphene, the unit cell height was set to $c = 15$ Å in order to prevent spurious interactions between unit cells repeating perpendicular to the layer plane. A height of

20 Å was used for 3-graphene and a height of 30 Å for 4-graphene to incorporate the extra layers while still preventing these interactions.

Elastic constants were obtained using the method of least-squares fit [120] as implemented in the MedeA-MT module. Phonon dispersions were obtained using the direct method as implemented in the MedeA-PHONON [126] module.

6.2 Results and discussion

6.2.1 Structures considered

In this study, C, SiC and Si in the honeycomb structure, off-50:50 SiC_2 as well as the four allotropes of graphene shown in Fig. 6.1 were considered. Multi-layered graphene was also studied to investigate layer effects.

The relaxed honeycomb structures gave lattice constants calculated in GGA of 2.47 Å, 3.10 Å, and 3.87 Å for C, SiC, and Si respectively. These values are in good agreement with the LDA results of 2.46 Å, 3.07 Å, and 3.83 Å given by Ref. [84] with them being slightly higher as is expected with GGA. Graphene and SiC are planar structures, whereas Si is buckled. Sahin et al. [84] calculated a buckling parameter of $\Delta_{Si} = 0.44$ Å for Si which is similar to the value calculated here of 0.45 Å.

Fig. 6.1a shows the structure for C1 where the planar surface consists of distorted heptagons and pentagons with 8 atoms per unit cell and *cmm* symmetry. This structure, called pentaheptite, has been previously studied using tight-binding methods which predict it to be metallic [154,157]. The relaxed optimized structure has unit cell parameters of $a = 7.48$ Å and $b = 4.75$ Å with an internal angle of 38.05° which corresponds to a rectangular conventional cell of $a = 7.48$ Å and $b = 5.86$ Å. This compares well with the values of $a = 7.54$ Å and $b = 4.78$ Å obtained by Crespi et al. [154] and the conventional cell values of $a = 7.56$ Å and $b = 5.70$ Å obtained by Enyashin and Ivanovskii [157]. Each pentagon is symmetrical about a mid-line that bisects an angle of 105.4°. The angles in circular order are 105.4°, 106.9°, 110.4°, 110.4°, and 106.9° all which are distorted from the ideal value of 108° giving an MAO of 2.2%. Each heptagon is symmetrical about a mid-line bisecting an angle of 139.2° with angles in circular order of 139.2°, 122.7°, 130.4°, 127.3°, 127.3°, 130.4°, and 122.7° all distorted from the ideal value of 128.6° giving an MAO of 3.2%. The average bond distance is $d_{C-C} = 1.43$ Å.

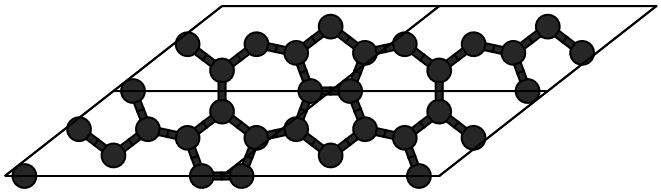

(a) 2x2 supercell

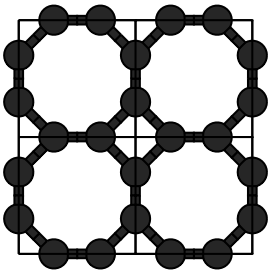

(b) 2x2 supercell

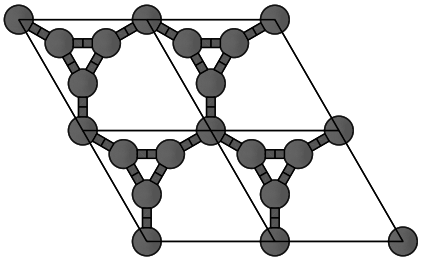

(c) 2x2 supercell

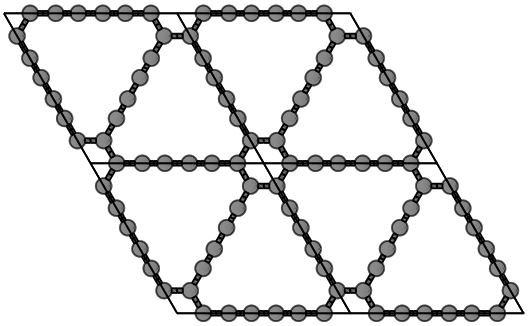

(d) 2x2 supercell

Figure 6.1: The four graphene allotropes: (a) C1 (pentaheptite) consisting of pentagons and heptagons (b) C2 consisting of squares and octagons (c) C3 consisting of triangles and enneagons (d) C4 (graphdiyne) consisting of two acetylenic linkages between hexagons.

The anisotropic graphene allotrope C2 shown in Fig. 6.1b is predicted to be a planar metallic[157] structure composed of squares connecting distorted octagons with 4 atoms per unit cell and *p4m* symmetry. The relaxed unit cell lattice parameter of $a = 3.45$ Å compares well with the value of 3.47 Å obtained by Ref.[157]. The internal angles for the octagons all have the same ideal value of 135° and the squares have $d_{C-C} = 1.46$ Å. The average bond distance is $d_{C-C} = 1.44$ Å.

The graphene allotrope C3, shown in Fig. 6.1c, is obtained from the honeycomb structure by replacing the second atom in the unit cell by a group of three atoms in an equilateral triangular cluster giving 4 atoms per unit cell with *p3m1* symmetry. The relaxed planar structure has a cell parameter of $a = 3.84$ Å with the triangle having $d_{C-C} = 1.40$ Å. The average bond length is $d_{C-C} = 1.41$ Å.

The C4 shown in Fig. 6.1d is known as graphdiyne[160] and consists of hexagons connected together by two acetylenic linkages in *p6m* symmetry forming a planar structure. This allotrope is predicted to be metallic[161,157] and has recently been synthesized using a cross-coupling reaction[162]. The relaxed structure has a lattice parameter of $a = 9.47$ Å which compares well with the value of 9.44 Å obtained by Ref.[161] using a full potential LDA linear combination of atomic orbitals (LCAO) method. Each hexagon has $d_{C-C} = 1.43$ Å while the acetylenic linkages have C-C bond lengths going between each hexagon of 1.40 Å, 1.23 Å, 1.34 Å, 1.23 Å and 1.40 Å.

The monolayer and multi-layered graphene structures used to study layer effects all had the same LDA calculated lattice parameter of $a = 2.45$ Å with the multi-layered structures having a layer thickness of 3.33 Å in the conventional Bernal stacking arrangement.

The planar-SiC_2 structure (silagraphene) , shown in Fig. 6.2, has *pmm* symmetry with three atoms per unit cell with a carbon pair in the middle and a silicon at (0,0). The relaxed structure has lattice parameters a=2.84 Å and b=3.92 Å which compare well with values of a=2.864 Å and b=3.879 Å by Li et al. who used the DMol code with the PW91 GGA functional. The charge density and ELF plot in Fig. 6.2 are very reminiscent of those found for glitter-SiC_2, with the same features. The structure has very similar bond lengths of d_{C-C}=1.33 Å (the same as the double carbon bond in ethylene) and d_{Si-C}=1.92 Å (slightly larger than the single Si-C bond in 3C-SiC). It has a trigonal bonding angle of C-$\hat{\text{C}}$-Si=132.04° and the angles C-$\hat{\text{Si}}$-C=95.25° and C-$\hat{\text{Si}}$-C=84.76° defining the planar tetra-coordinate bonding around each silicon atom.

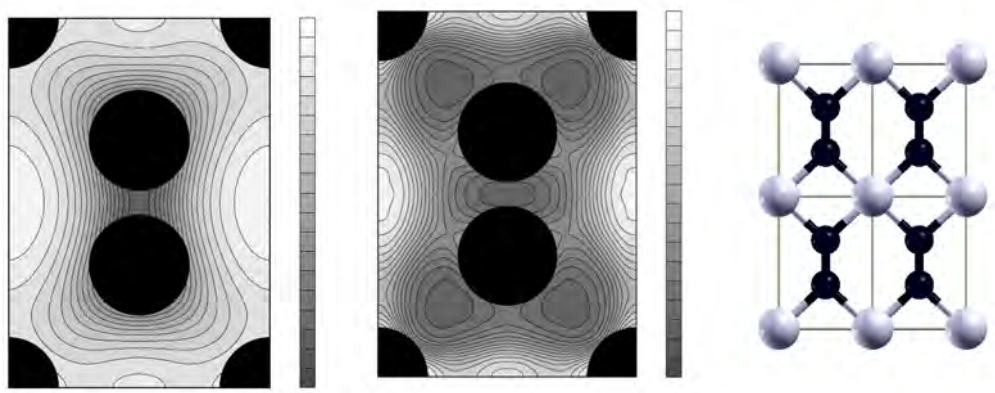

Figure 6.2: Planar SiC_2 structure - Showing a 4x4 supercell (black carbon atoms and white silicons) with a charge density plot (left) and an ELF plot (middle).

6.2.2 Mechanical properties

Bulk equations of state such as the Birch equation, are only valid for expansions and compressions in a range ±10% about the equilibrium volume. The range of validity for the 2D energy EOS was found by fitting energy versus unit cell area points for graphene. Calculations were done for 14 points in the range of 90% to 170% of the expected equilibrium area. [1] One fit used 9 points within 10% on either side of the expected equilibrium point while a second fit used the entire range. These are shown in Fig. 6.3 with the first fit shown as a dashed line and the second shown as a solid line. Although both fits overlap within the ±10% range as shown by the insert plot for this range, it is clear that the narrower fit deviates from the calculated data points for predicted expansions beyond about 130%∼140% of the equilibrium area. The first fit gave EOS fit parameters of equilibrium lattice constant a=2.47 Å, layer modulus of γ=206.7 Nm^{-1}, force per unit length derivative γ'=4.33, double force per unit length derivative γ''=-0.0306 mN^{-1} and a cohesive energy per atom pair of 15.2 eV while the second fit gave a=2.47 Å, γ=207.1 Nm^{-1}, γ'=3.93, γ''=-0.0670 mN^{-1} and the same cohesive energy. These fit parameters can be used in Eqn. 6.4 to predict the $\mathcal{F}(A)$ curves for each fit. Fig. 6.4 shows these curves for graphene using the two different sets of EOS fit parameters. The dashed line is the curve predicted by the first fit while the

[1] It should be noted that when compressed graphene with an area in the range 90-100% was given an artificial buckling, the atoms relaxed back into a fully planar structure

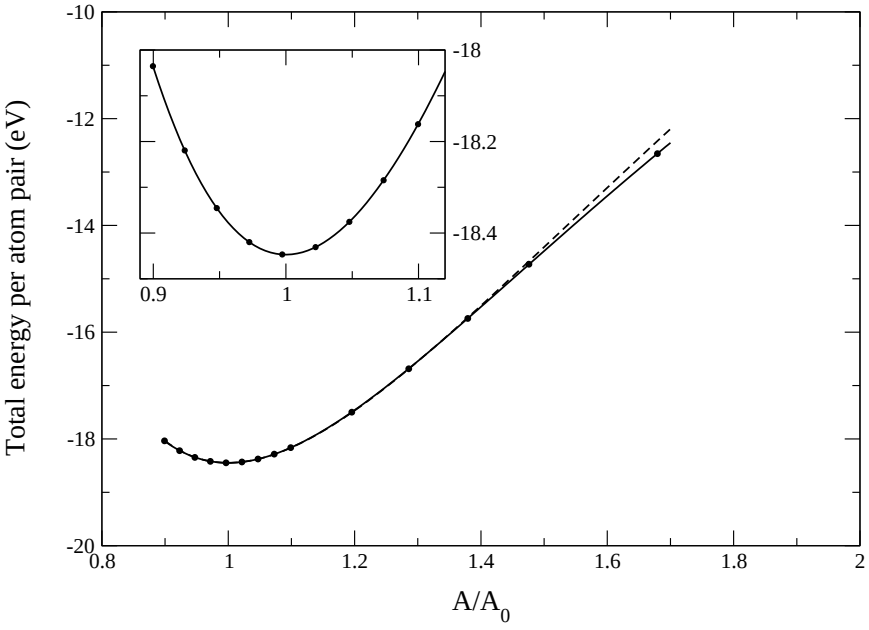

Figure 6.3: Graphene EOS fit - Showing total energy versus relative area A/A_0. Solid line shows fit for all 14 calculated points in the range $0.9 < A/A_0 < 1.7$ (insert shows detail) and dashed line shows fit for first 9 points in the range $0.9 < A/A_0 < 1.1$ extended to 1.7.

solid line is that for the larger fit. The solid data points are the force per unit length values calculated by VASP at each unit cell area point. The figure shows that the two curves pass through the calculated $\mathcal{F}$ points up to $A/A_0 \sim 1.10$ but that the curve based on the larger fit deviates from the points beyond $A/A_0 \sim 1.15$. For this reason, it was decided to use the shorter range of $\pm 10\%$ to obtain EOS fit parameters for all materials.

The EOS fits in the upper section of Table 6.1 for the monolayer honeycomb structures and silagraphene are listed in order of decreasing layer modulus. They give lattice constant values that are identical to those obtained by structural relaxation. The results for SiC_2 were obtained by keeping the ratio of the lattice parameters a and b fixed at the value obtained by structural relaxation thereby creating isotropic bi-axial strain (only the atoms were relaxed at each area value).

The results show that graphene is the most resilient to stretching with a value of

Table 6.1: EOS fit parameters for honeycomb structures, graphene allotropes and layered graphene (equilibrium area per atom pair A_0 in Å^2, lattice constants a and b, relaxed interlayer distance t and buckling parameter Δ in Å, layer modulus γ_0 in Nm^{-1}, γ_0' dimensionless, γ_0'' in mN^{-1}, cohesive energy per atom pair E_{coh} in eV.

	A_0	a	b	γ_0	γ_0'	γ_0''	E_{coh}
C	5.277	2.47		206.6	4.33	-0.0306	15.2
SiC	8.303	3.10		116.5	4.79	-0.0688	11.2
SiC_2	11.13	2.84	3.92	114.5	5.68	-0.138	18.0
Si	12.959	3.87[a]		44.5	1.79	-0.6826	7.2
C1	5.480	7.48	4.75	192.3	4.35	-0.0338	14.7
C2	5.944	3.45		174.7	4.33	-0.0361	14.2
C3	6.399	3.84		153.2	4.55	-0.0511	13.8
C4	8.629	9.47		110.2	4.51	-0.0742	13.7
4-graphene (LDA)	5.187	2.45[b]		863.4	4.29	-0.0072	17.0
3-graphene (LDA)	5.187	2.45[b]		647.6	4.29	-0.0096	17.0
2-graphene (LDA)	5.187	2.45[b]		431.8	4.28	-0.0146	17.0
graphene (LDA)	5.186	2.45		215.9	4.28	-0.0286	17.0

[a] $\Delta = 0.45$

[b] atom relaxation for 2D EOS gave $t = 3.33$

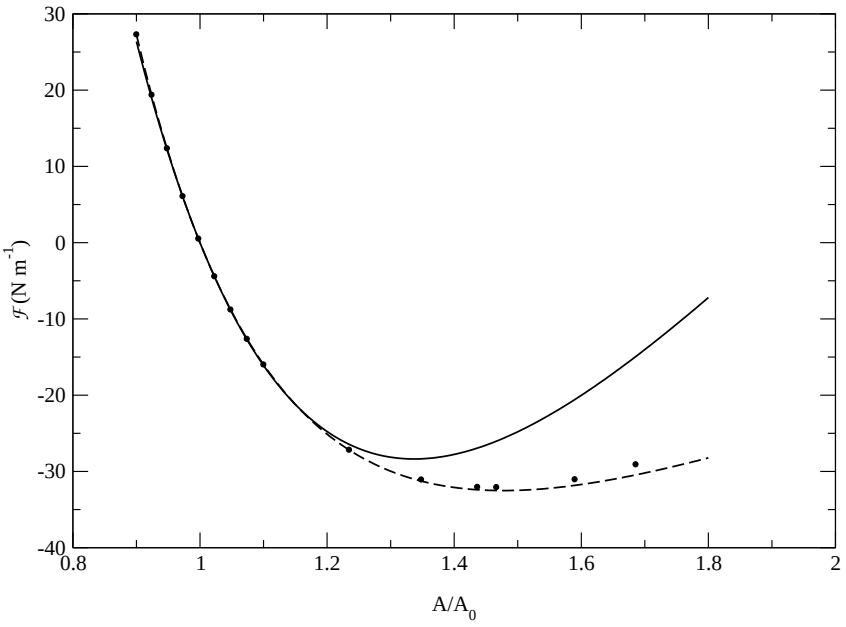

Figure 6.4: Graphene $\mathcal{F}$ versus relative area - Force per unit length versus relative area (A/A_0) for graphene showing a dashed line for the curve predicted by the $0.9 < A/A_0 < 1.1$ EOS fit and a solid line for the $0.9 < A/A_0 < 1.7$ prediction. Solid circles indicate calculated $\mathcal{F}$.

$\gamma_C = 206.6$ Nm^{-1}. This is in agreement with the estimated average value of 209.4 Nm^{-1} derived from the value of β_0 for graphite measured by Hanfland et al. with their linear Murnaghan EOS. Second is SiC with a value of $\gamma_{SiC} = 116.5$ Nm^{-1} which is 56% that of C followed by $\gamma_{SiC_2} = 114.5$ Nm^{-1} being 54% that of graphene. The value for silagraphene is almost the same as that for SiC therefore they should have similar strength properties. The value for buckled Si is $\gamma_{Si} = 44.5$ Nm^{-1}, which is substantially lower than the result for graphene. This establishes the relative expandability of these materials with Si being the most expandible and graphene the least and it verifies that graphene is an ideal material to use in applications that require structural integrity and a rigid membrane.

The results for the graphene allotropes are shown in the middle section of Table 6.1 The results for C1 were also obtained by using isotropic bi-axial strain.

The layer modulus values decrease from C→C1→C2→C3→C4 with values of $\gamma_{C1} = 192.3$ Nm^{-1}, $\gamma_{C2} = 174.7$ Nm^{-1}, $\gamma_{C3} = 153.2$ Nm^{-1} and $\gamma_{C4} = 110.2$ Nm^{-1}. This establishes the relative expandability of these graphene allotropes with C4 being the most expandible and graphene the least. The EOS fits shown in Fig. 6.5 show graphene as the most energetically stable 2D carbon allotrope with a possible phase transition existing from graphene to C4 at $\mathcal{F} = $-7.0 Nm^{-1}. Although, it is more likely that graphene will continue to stretch to failure rather than undergo such a transition since it will be shown in 6.2.4 that no soft mode is observed near the expected transition pressure.

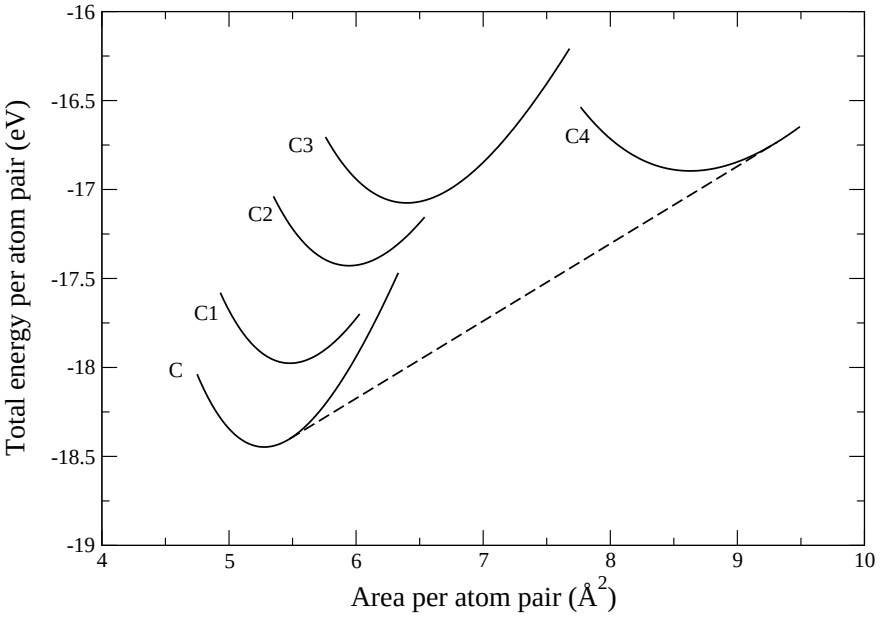

Figure 6.5: Graphene allotrope phase transition - EOS for graphene and four allotropes showing a phase transition from graphene to C4 at $\mathcal{F} = $-7.0 Nm^{-1}.

The force per unit length derivatives of γ for the honeycomb planar structures are γ'_C=4.33 and γ'_{SiC}=4.79 with $|\gamma''| < 0.0688$ mN^{-1}. This means that according to Eq. A.2, the layer moduli for these materials change in a similar near-linear manner in response to small changes in $\mathcal{F}$ around their equilibrium structures. The buckled structure of Si and SiC_2 react in a more parabolic manner with the layer modulus for

Si having more curvature than SiC_2 since $|\gamma''_{SiC_2}| < |\gamma''_{Si}|$. This is the result of the buckling only found in Si.

The lower section of Table 6.1 shows the LDA EOS fits for 1, 2, 3 and 4 layered graphene. The layer modulus for 2-graphene is exactly twice that of monolayer graphene with a value of 431.8 Nm^{-1} while 3-graphene and 4-graphene have values exactly three times and four times as much respectively. This establishes γ as a true property of layered structures with its value scaling with the number of atomic layers n as $\gamma = 215.9\,n$. The material becomes more resilient to stretching with the addition of extra layers as would be expected. All have values for γ' around 4.28 indicating that to first order, the layer modulus for these layered structures all change by the same amount for the same change in $\mathcal{F}$. The values for γ'' are inversely proportional to the number of layers scaling as $\gamma'' = -0.0286/n$. This indicates that $\gamma(\mathcal{F})$ becomes increasingly linear around the equilibrium value with an increase in the number of layers.

The calculated cohesive energies per atom pair show a general decreasing trend going down the column with C having the largest value and Si the lowest (except silagraphene which has the highest value). The values for honeycomb C, SiC and Si are lower than the values of 20.08 eV, 15.25 eV, and 10.32 eV given by Şahin et al. [84] due to the under binding nature of GGA. The value of 18.0 eV for silagraphene is very close to the value of 18.12 eV calculated by Li et al. [159]. The C allotropes have similar cohesive energies as do the layered graphenes.

6.2.3 Elastic properties

The two-dimensional elastic constants c_{ij} were obtained by first doing a least-squares fit on various *ab initio* stress calculations for carefully chosen strain states on the relaxed volume unit cell to extract the bulk elastic constants [120]. These were then multiplied by the unit cell height to obtain the corresponding 2D values. Due to the increased length of the unit cell heights, all bulk elastic constants containing 4 or 5 in their subscripts equated to zero within the numerical error of the fit. Monolayer materials also had all elastic constants containing 3 in their subscripts calculated to zero.

The elastic constants for the various structures and other derived elastic properties are listed in Table 6.2. For all structures, the principle-minors of the stiffness matrix and the calculated modulus values are all positive indicating elastic stability. The values

Table 6.2: Elastic properties for honeycomb structures, graphene allotropes and layered graphene (Elastic constants c_{ij}, shear modulus G^{2D}, calculated layer modulus γ_{calc}, EOS-derived layer modulus given in brackets and Young's modulus Y^{2D} in Nm^{-1}. Poisson ratio ν and anisotropic factor ISO dimensionless).

		c_{11}	c_{22}	c_{12}	$c_{66} = G^{2D}$	γ_{calc}	$Y^{2D}_{[10]}$	$Y^{2D}_{[01]}$	$\nu_{[10]}$	$\nu_{[01]}$	ISO
C	This work	352.7	352.7	60.9	145.9	206.8 (206.6)	342.2	342.2	0.173	0.173	1.0
	VASP (PBE)[163]	358.1	358.1	60.4	148.9[a]	209.3[a]	348	348	0.169	0.169	1.0
	estimated[142]	372.2	372.2	46.6	162.8	209.4	366.4	366.4	0.125	0.125	1.0
SiC	This work	179.7	179.7	53.9	62.9	116.8 (116.5)	163.5	163.5	0.300	0.300	1.0
SiC_2	This work	144.9	237.4	38.5	39.1	114.9 (114.5)	138.7	227.2	0.162	0.266	0.51
Si	This work	68.3	68.3	23.3	22.5	45.8 (44.5)	60.6	60.6	0.341	0.341	1.0
	VASP (LDA)[164]	68.9	68.9	23.3	22.8[a]	46.1[a]	61.0	61.0	0.33	0.33	1.0
C1	This work	309.6	325.2	67.6	117.8	192.5 (192.3)	295.5	310.4	0.208	0.218	0.94
$C2_0$	This work	295.3	295.3	54.5	49.1	174.9 (174.7)	285.2	285.2	0.185	0.185	0.41
$C2_{\frac{\pi}{4}}$	This work	222.8	222.8	127.4	127.0	175.1 (174.7)	150.0	150.0	0.572	0.572	2.66
C3	This work	219.4	219.4	87.7	65.9	153.6 (153.2)	184.3	184.3	0.400	0.400	1.0
C4	This work	152.1	152.1	69.0	41.6	110.6 (110.2)	120.8	120.8	0.454	0.454	1.0
4-graphene (LDA)	This work	1456.2	1456.2	273.8	591.2	865.0 (863.4)	1404.7	1404.7	0.188	0.188	1.0
3-graphene (LDA)	This work	1091.9	1091.9	204.7	443.9	648.3 (647.6)	1053.5	1053.5	0.187	0.187	1.0
2-graphene (LDA)	This work	728.5	728.5	135.9	296.3	432.2 (431.8)	703.1	703.1	0.186	0.186	1.0
graphene (LDA)	This work	364.6	364.6	67.3	148.7	216.0 (215.9)	352.2	352.2	0.185	0.185	1.0

[a] Calculated from given elastic constants

for the anisotropic measure ISO indicate that the only three anisotropic materials are silagraphene, C1 and C2 with all other structures being fully isotropic.

In order to validate the method used, the results for C and Si were compared to previous calculations and results based on available experimental data. The results for graphene compare very well with those of Wei et al. [163] who used a least-squares fit of Cauchy stress calculations done in VASP using the PBE GGA functional. As with this method, they converted bulk volume unit cell values to planar values by multiplying by the cell height. As can be seen in Table 6.2, the values in Ref. [163] for the elastic constants, the moduli and the Poisson ratio are very close. The values also compare reasonably well with those derived from elastic constant estimates taken from inelastic x-ray data for graphite [142] and the calculated value of 342.2 Nm^{-1} for the 2D Young's modulus compares well to the experimental value of 340±50 Nm^{-1} measured by Lee et al. [83] For the non-planar Si, the values for the elastic constants, moduli and Poisson ratio compare very well with those calculated by Zhang and Wang [164] who used various strain-energy LDA calculations to obtain their elastic constants.

The first thing that is apparent about the values in Table 6.2 is that the γ_{calc} values derived from the elastic constants are almost exactly the same as the layer modulus values obtained from the EOS fits (shown in brackets). In the case of C1 and silagraphene, the calculated values matched the EOS values obtained by isotropic bi-axial strain. This independently establishes that the 2D EOS correctly determines the layer modulus for planar 2D materials as well as buckled and layered quasi-two dimensional systems.

The elastic properties for the three honeycomb systems and silagraphene are shown in the top section of Table 6.2, the graphene allotropes in the middle section and the layered graphenes on the bottom.

For the honeycomb structures, all the moduli show a decreasing trend going down the columns from C → SiC → Si. The Young's moduli values of 342.2 Nm^{-1}, 163.5 Nm^{-1} and 60.6 Nm^{-1} are in general agreement with the LDA values of 335 Nm^{-1}, 166 Nm^{-1} and 62 Nm^{-1} given by Şahin et al. [84]. The Poisson ratios show an increasing trend. Since these structures are isostructural, these trends are indicative of the relative bonding strengths between the atoms and not of the geometry of the materials except in the case of Si where the added effect of surface buckling further reduces its elastic moduli.

The values for silagraphene show that the Young's modulus has an anisotropy due to the symmetry. It is more resistant to stretching in the [01] direction due to the strong C-C bond. The averaged value of 183.0 Nm^{-1} is larger than the value for SiC. The shear modulus is lower than SiC due to the fact that the honeycomb structure is very rigid compared to that of SiC_2. The Poisson ratio in the [01] direction is basically the same as SiC whereas the value for the [10] direction is lower due to the C-C bond.

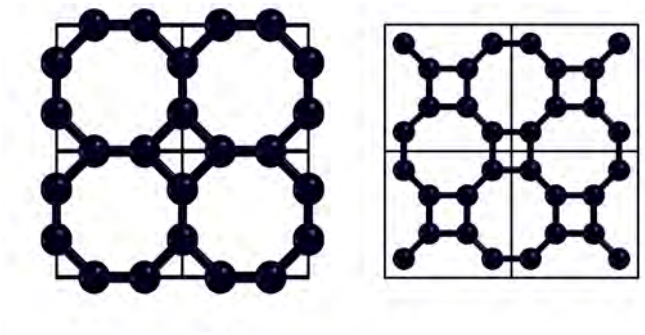

(a) 2x2 supercell for $C2_0$ **(b)** 2x2 supercell for $C2_{\frac{\pi}{4}}$

Figure 6.6: The graphene allotrope C2: (a) $C2_0$ showing the unrotated state (b) $C2_{\frac{\pi}{4}}$ showing the rotated state with a rotation angle of $\frac{\pi}{4}$.

The C1 structure has anisotropic Young's modulus values of $Y^{2D}_{[10]} = 295.5$ Nm^{-1} and $Y^{2D}_{[01]} = 310.4$ Nm^{-1}. Due to the fact that the pentagons are symmetrical about their y-axis and the enneagons about their x-axis, C1 is slightly more structurally rigid to elongations along the [01] direction. The averaged Young's modulus of 303.0 Nm^{-1} is 88% that of graphene.

The C2 structure seems isotropic on inspection due to its square symmetry. In order to test this, calculations were done on the unrotated structure shown in Fig. 6.6a and a rotated structure with the [10] and [01] directions rotated by $\frac{\pi}{4}$ as shown in Fig. 6.6b. It is clear that the anisotropic Young's modulus, shear modulus and Poisson ratio values in Table. 6.2 are vastly different between the unrotated case ($C2_0$) and the rotated case ($C2_{\frac{\pi}{4}}$). This large anisotropy can be seen in the calculated ISO values. As is expected, the values for γ are the same for both cases. If one then uses Eqns. 6.12

and 6.13 with the respective layer modulus and shear modulus values to calculated the supposed isotropic values for the Young's modulus and Poisson ratio, then $C2_0$ has values of Y^{2D}=153.3 Nm^{-1} and ν_{2D}=0.562, while those for $C2_{\frac{\pi}{4}}$ are Y^{2D}=294.4 Nm^{-1} and ν_{2D}=0.159. Clearly this is not an isotropic material. In fact, it seems as if the anisotropic values for the unrotated case match the isotropic values for the rotated case and vice-versa. The orientation of the uni-axial strain is important in determining this materials stiffness with it being more rigid in its unrotated state with a value approximately twice that of the rotated case. The reason for this is whereas $C2_0$ has strong bonds between each square that are orientated along the [01] and [10] uni-axial strain directions, $C2_{\frac{\pi}{4}}$ has these connections angled with respect to the rotated [01] and [10] directions which are prone to bending under uni-axial strain in these directions.

Isotropic C3 has a Young's modulus value 54% that of graphene. This is due to increased bond bending as compared to the graphene and C1.

Isotropic C4 has the lowest Young's modulus value, it being 35% that of graphene and 66% that of C3. The long acetylenic linkages cause structural weakness compared the other more compact structures.

Graphene has the highest shear modulus due to the fact that its honeycomb structure is very rigid. The shear modulus of C1 is ∼81% that of graphene due to its strong network of slightly distorted polygons. For $C2_0$, the bonds that make it very stiff to uni-axial strain are less resistant to shear whereas for $C2_{\frac{\pi}{4}}$, the angled bonds that made this orientation less stiff, make it more rigid to shear. There seems to be a trade-off between the two modulus values that depends on the orientation of the uni-axial directions. The shear moduli of C3 is more than half that of graphene showing it to be more prone to bond bending under shear strain. Even through C4 has a generalized honeycomb structure similar to graphene, it has a shear modulus ∼30% that of graphene due the long acetylenic chains making up this structure. The Poisson ratio for C3 and C4 are significantly higher than C1 and whereas that for C2 depends on the orientation of the uni-axial strain. These results show that of all the allotropes, metallic C1 would best compliment graphene for nano-applications since both have comparable moduli, and therefore similar hardness properties.

The last section of Table 6.2 shows the results for the layered graphene structures. The elastic constants c_{11}, c_{22}, c_{12} and c_{66} (and therefore all derived elastic moduli) scale in the same manner as found for γ. The Poisson ratios for the layered materials

are in the range $0.185 \leq \nu \leq 0.188$ showing that the widths of the materials all decrease the same with the same amount of linear strain.

For isotropic hexagonal materials, the Young's and shear moduli rank in the same order as the layer modulus making comparisons between materials straightforward. For anisotropic materials, these moduli depend on the orientation of the material making comparisons difficult. It would be useful to be able to place upper and lower bounds on these values. For these reasons, the layer modulus is a good and simple measure of the relative hardness of 2D materials.

6.2.4 Intrinsic strength

When a 2D material is stretched, the applied stress increases with the strain until it reaches a maximum beyond which the stress decreases. This extremum point indicates the isotropic intrinsic stress and strain for the material at which point the material fails. These values can be obtained by using Eqn. 6.4 with the fit parameters from the 2D EOS fit for a given material. Fig. 6.7 shows the stress (negative $\mathcal{F}$) versus relative area (A/A_0) curves for graphene using two different EOS fits. The dashed curve is from a fit over the range $0.9 < A/A_0 < 1.1$ and predicts a breaking stress of 32.5 Nm^{-1} at an area 47.7% larger than the equilibrium value. The onset of soft modes in the calculated phonon dispersion occurs when the structure is compressed below its equilibrium area and when it is stretched to $A/A_0 = 1.340$ (the solid vertical line in Fig. 6.7). [1] The stress curve over estimates this range of stability by 10.2%. The solid curve in Fig.6.7 uses an EOS fit that has the previously predicted relative area of 1.477 as an upper bound. It predicts a slightly lower failure stress of 29.4 Nm^{-1} at a relative area of 1.372. This predicted area is closer to the phonon prediction, being only 2.4% higher.

The predicted results using this method are summarized in Table 6.3. The materials in the upper section are listed in order of decreasing layer modulus. The relative area and breaking stress x_A and σ_A are based on a $\pm$ 10% EOS fit while x_B and σ_B use the extended range. The predicted phonon results for selected examples of planar, buckled and layered materials are compared to the EOS predictions by calculating the relative percentage difference between the two.

[1] Nowhere in this stretching range does a soft mode appear at the previously mentioned pressure phase transition at $\mathcal{F}$=-7 Nm^{-1}

Table 6.3: Intrinsic strength based on EOS fits for honeycomb structures, silagraphene, graphene allotropes and layered graphene (x_A is the relative area at failure from EOS fit over $0.9 < A/A_0 < 1.1$, σ_A is the hydrostatic stress at failure from same fit in Nm^{-1}, x_B is the relative area at failure from EOS fit over $0.9 < A/A_0 < x_A$, σ_B is the hydrostatic stress at failure from same fit in Nm^{-1}, x_{phonon} is the relative area where the first onset of a soft mode occurs in the phonon dispersion, RD is the relative percentage difference between x_B and x_{phonon}.

	x_A	σ_A	x_B	σ_B	x_{phonon}	$RD\,(\%)^a$
C	1.477	32.5	1.372	29.4	1.340	2.4
SiC	1.414	16.4	1.292	14.2	1.427	-9.5
SiC_2	1.284	12.5	1.253	11.7		
Si	1.301	6.6	1.201	4.9	1.420	-15.4
C1	1.469	30.0	1.278	24.3	1.309	-2.4
C2	1.464	27.5	1.298	22.7	1.309	-0.8
C3	1.422	22.3	1.304	19.4	1.308	-0.3
C4	1.414	16.0	1.307	14.0		
4-graphene (LDA)	1.481	137.0	1.381	125.0		
3-graphene (LDA)	1.481	102.8	1.381	93.8	1.32	4.6
2-graphene (LDA)	1.478	68.4	1.381	62.5	1.363	1.3
graphene (LDA)	1.483	34.4	1.383	31.3	1.363	1.5

[a] Relative difference; $\frac{x_B - x_{phonon}}{x_{phonon}} \times 100\%$

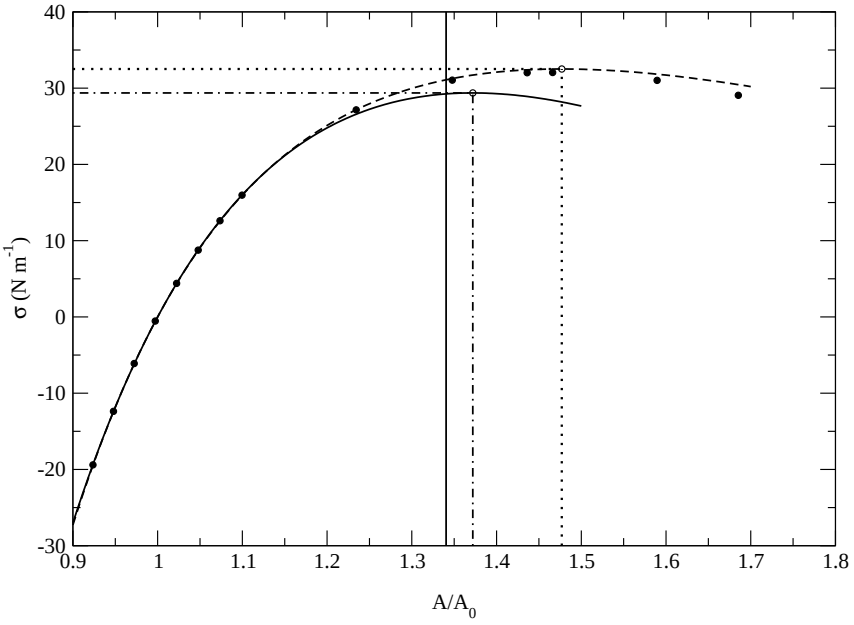

Figure 6.7: Graphene stress versus relative area - Showing dashed line for $0.9 < A/A_0 < 1.1$ fit and solid line for $0.9 < A/A_0 < 1.477$ fit. Dotted and dot-dash lines show predicted maximum values for each fit while solid vertical line is the value at which the phonon dispersion has an onset of a soft mode at K.

The results in the upper two sections of Table 6.3 show that C, C1, C2 and C3 give predictions no greater than $\sim 3\%$ off the phonon results while the results for SiC and Si are more than 10% off. Of the elemental honeycomb structures only buckled Si shows a vast discrepancy between the EOS prediction and phonon result. Binary SiC also has a vast discrepancy between EOS and phonon predictions. The layered materials of 2-graphene and 3-graphene show predicted EOS values no more than 5% off the phonon values. The discrepancies are likely due to anharmonic effects that are not accounted for by the phonon calculations when the structures are extended too far from their equilibrium states.

The honeycomb structures in the upper section of Table 6.3 show decreasing intrinsic stress σ_B in the same ranking order as their layer moduli with graphene having the highest value of 29.4 Nm^{-1}. SiC and silagraphene are second with comparable values

that are 48% and 40% that of C with buckled Si having the lowest value, 17% that of graphene.

The ordering of the intrinsic relative area x_B goes in decreasing order from C → SiC → Silagraphene → Si. Graphene fails at an area ∼40% greater than the equilibrium value. SiC and silagraphene fail at areas ∼25 and 29% greater while Si fails at a relative area 20% higher than its equilibrium value, about half that of C. These results indicate that C is able to withstand greater isotropic strains than the other honeycomb materials at a higher stress, a result reflected by its relatively high layer modulus. They also show that the higher carbon content of silagraphene does not increase its strength compared to SiC. This is reflected in the fact that their layer modulus values are very close.

The intrinsic stress values of the four graphene allotropes, shown in the middle section of Table 6.3, decrease from C1 → C2 → C3 → C4 with C1 having a value 83% that of graphene, C2 (77%), C3 (66%) and C4 a value 48%. This correlates well with the ordering of their layer moduli. All of the structures fail at approximately the same strain with an area ∼30% higher than their equilibrium values. This is slightly lower than graphene, once again showing the honeycomb structure to be the strongest.

As with the elastic moduli, the intrinsic stress values of the layered graphene structures, shown in the lower section of Table 6.3, scale with the number of layers. The values scale as $\sigma = 31.2\,n$ where n is the number of layers present while the relative area at failure remains fixed at ∼1.38 indicating these structures all fail at the same lattice parameter of $a = 2.88$ Å. This shows that each added layer increases the strength of the multi-layered structure but does not increase the amount of stretching the structure can withstand.

6.3 Conclusions

In this study an equation of state (EOS) for 2D materials is proposed that equates 2D pressure (force per unit length $\mathcal{F}$) with a change in surface area. This was then used to fit energy versus area data to extract equilibrium fit parameters including the layer modulus (symbol γ) which measures a material's resilience to hydrostatic stretching. The results for the monolayer systems of graphene, SiC and Si in the isostructural honeycomb structure are given for comparison. For these structures, the layer moduli were ranked showing graphene to be the most resilient to stretching with

$\gamma_C = 206.6$ Nm^{-1} with the buckled structure of Si the least resilient. SiC_2 was found to be very comparable to SiC. It was found that $\gamma(\mathcal{F})$ around $\mathcal{F}$=0 is more linear for honeycomb planar structures and more parabolic for buckled Si and silagraphene. Four graphene allotropes were considered including pentaheptite and graphdiyne. For the graphene allotropes, the ranking for γ in decreasing order went C1→C2→C3→C4 with C1 (pentaheptite) having a value comparable to graphene. C4 (graphdiyne) was shown to be the softest of the four. The EOS fits for these structures showed a possible, though unlikely, phase transition from graphene to C4 at a force per unit length of -7 Nm^{-1}. Multi-layered graphene was considered and it was found that the curve $\gamma(\mathcal{F})$ is more linear around $\mathcal{F} = 0$ as the number of layers is increased.

The planar elastic constants for all the structures were calculated and it was found that the layer modulus derived from the elastic constants matched those from the EOS fits, thereby independently verifying the EOS. The EOS was used to predict the isotropic intrinsic strength of the various structures. The results show that the intrinsic stress correlated well with the layer modulus with graphene having the highest intrinsic strength of 29.4 Nm^{-1}. The EOS showed that although silagraphene and SiC are different elastically, their strengths are comparable due to the similarity of their layer moduli.

These results show that the layer modulus is a good indicator of relative strength for planar, buckled and layered 2D structures and is applicable to both isotropic and anisotropic materials. They also show that the proposed EOS correctly extracts this value as one of its fit parameters and is a useful tool to investigate a materials response to $\mathcal{F}$ as well as to look for possible phase transitions.

The results of the last three chapters allow general conclusions to be drawn about the Si-C systems investigated. These are given in the next chapter.

7

General conclusions

This study involved the investigation of silicon-carbon systems. It was motivated by the search for off-50:50 alloys and a way to quantify the strengths of 2D silicon-carbon materials.

7.1 Elemental and 50:50 systems

The elemental and 50:50 silicon-carbon systems were investigated in order to validate the *ab initio* methods used in this study as well as predict some under-reported properties for three previously proposed hypothetical allotropes of carbon. It was found that the use of valence charge density and electron localization function plots accurately determined bonding properties. Electronic properties could be used to further describe bonding characteristics. Birch equation of state fits established that PBEsol is a suitable functional for structural properties. The calculation of elastic properties and phonon dispersions correctly determined the elastic stability for all structures as well as predicted the stability of C_4, supercubane and glitter-carbon. These results verified PBEsol as a suitable functional to be used to determine elastic properties and elastic/dynamic stability. The link between the elastic properties and structural bonding was made. The moduli values for the various silicon allotropes were linked to the amount of metallic bonding present, and in the case of carbon, the amount of bonding distortion. Pressure phase transitions were validated for the silicon and SiC systems and it was found that while LDA predicted the transition pressures with reasonable accuracy, PBEsol was more accurate for the densely compacted high pressure phases. For carbon, it was found that the three theoretical allotropes of C_2, supercubane and

glitter are not accessible under pressure from diamond but perhaps can be made from graphite through such methods as shock compression. The phase transition between 3C-SiC and RS-SiC was verified but the predicted pressure transition was well below the experimental value. It was thought that because this pressure transition involves a drastic change in electronic structure, non-canceling errors in the two phases resulted in this large bias in the predicted transition pressure.

7.2 Off-50:50 alloys

The search for off-50:50 alloys revealed that of the possible alloy combinations and candidate structures considered, only the pyrite-FeS_2, glitter-SiC_2 and t-BC_2 structures for SiC_2 were found to be elastically and dynamically stable. The first aim of this study has been achieved.

The results show that carbon rich SiC_2 has the greatest promise as a new material that could be synthesized. The stiffness of the silicon dicarbide structures were found to rank, in increasing order with 3C-SiC included for comparison, as glitter $\rightarrow$ pyrite $\rightarrow$ 3C-SiC $\rightarrow$ t-SiC_2. The modulus values for t-SiC_2 were found to be very comparable to 3C-SiC since for both materials, all atoms are four-fold coordinated with t-SiC_2 having slightly distorted strong covalent tetrahedral bonding. Its bonding was found to give it the highest bulk modulus of the three silicon dicarbide phases. Pyrite had a lower value since one out of three atoms are six-fold coordinated and the bonding to the silicon atoms has a strong ionic character. It has a higher modulus value than glitter due to the fact that it contains near-perfect tetrahedral and near-perfect octahedral bonding, whereas glitter has more distorted tetrahedral bonding with each carbon atom having distorted trigonal bonding. The Poisson ratios for pyrite and glitter structures are significantly greater than that for SiC, suggesting they have a higher ductility. These structures exhibit metallic character whereas t-SiC_2 is a semi-conductor with the pyrite phase not being a simple metal because of the existence of an energy band gap above the Fermi level. The glitter phase almost has the same electronic structure as a semi-metal due to the existence of a depression in the density of states near the Fermi level.

Analysis of the instability of these three structures for silicon-rich Si_2C revealed some interesting observations. The Si-Si bonds and their corresponding longer bond lengths results in more open unstable structures with even greater distortion in the

tetrahedral, octahedral and trigonal bonding. From this observation, it seems likely that carbon rich alloys are more favorable to their silicon-rich counterparts due to the smaller size of the carbon atoms and the more compact carbon-carbon bonds which result in less distorted bonding. The bonding in pyrite Si_2C is weaker compared to stable SiC_2 due to greater valence electron pair delocalization existing between the silicon atoms and the six-fold coordinated carbons resulting in more metallic bonding. This is also the case when comparing metallic t-Si_2C to the covalently bonded, semi-conducting t-SiC_2. The trend for silicon-rich alloys is increased metallic nature, weakening the bonding, and more open unstable structures with greater bond distortion.

7.3 2D systems and the novel EOS

The need to quantify the strengths of 2D Si-C materials led to the derivation of an equation of state (EOS) that equates in-plane pressure (force per unit length $\mathcal{F}$) with a change in surface area. This was then used to extract equilibrium fit parameters including the layer modulus (symbol γ) which measures a material's resilience to hydrostatic stretching. It could now be used to rank the relative strengths of various 2D materials thereby satisfying the second aim of this study.

Graphene was shown to be the most resilient to stretching with $\gamma_C = 206.6$ Nm^{-1} with the buckled structure of Si the least resilient. Silagraphene SiC_2 was found to be very comparable to SiC. It was found that $\gamma(\mathcal{F})$ around $\mathcal{F}$=0 is more linear for honeycomb planar structures and more parabolic for buckled Si and silagraphene. Four graphene allotropes were considered including pentaheptite and graphdiyne. For the graphene allotropes, the ranking for γ in decreasing order went C1→C2→C3→C4 with C1 (pentaheptite) having a value comparable to graphene. C4 (graphdiyne) was shown to be the softest of the four. The EOS fits for these structures predict a phase transition from graphene to C4 at a force per unit length of -7 Nm^{-1}, although this transition seems unlikely. Multi-layered graphene was considered and it was found that the curve $\gamma(\mathcal{F})$ is more linear around $\mathcal{F} = 0$ as the number of layers is increased. The planar elastic constants for all the structures were calculated and it was found that the layer modulus derived from the elastic constants matched those from the EOS fits, thereby independently verifying the EOS. It was also found, that in general, the other moduli rank according to the layer modulus. The EOS was used to predict the isotropic intrinsic

strength of the various structures. The results show that the intrinsic stress correlated well with the layer modulus with graphene having the highest intrinsic strength of 29.4 Nm^{-1}.

These results show that the layer modulus is a good indicator of relative hardness in planar, buckled and layered 2D structures and that the proposed EOS correctly extracts this value as one of its fit parameters. Also, the EOS is a useful tool to investigate a materials response to $\mathcal{F}$ and can be used to look for possible phase transitions.

7.4 Conclusion

Not only has this work demonstrated that, in principle, off-50:50 alloys of carbon and silicon are plausible, it has also provided information on how the strength and elastic properties of these materials are effected by increased silicon content. This has filled in a significant lack of knowledge about these bulk systems.

The novel 2D equation of state presented here opens up new ways to study and compare the strength properties of mono or multi-layered 2D materials, especially how their resilience to isotropic stretching responds to in-plane pressure.

7.5 Future investigations

The work presented here leads to opportunities for further investigations. Future work that involves using an evolutionary crystal structure search algorithm to identify candidate structures for other Si-C stoichiometries which can then be tested for stability using the methods presented here is foreseen. This will indicate if, in general, carbon-rich alloys are in fact more favorable. Experimentally it could then be investigated if these compounds can be manufactured.

Further work on 2D systems will include studying how the effect of adatoms on monolayer and layered graphenes change their mechanical properties. The use of various non-local exchange-correlation functionals on the calculation of the mechanical properties of layered materials can be investigated and compared. The mechanical properties of graphene with extended defects and "grain boundaries" can also be studied to see the effects of these structural features.

Appendix A

Derivation of the 2D EOS

This derivation for the in-plane pressure and energy equation of states given in Eqn. 6.4 and Eqn. 6.1.1 used the seminal paper by Francis Birch as inspiration [123].

A point in a 2D material is displaced from an initial position (a_1, a_2) to a strained position (x_1, x_2) where $u_i = x_i - a_i$ is the displacement vector. Considering a strain composed of a hydrostatic strain defined by a universal scaling factor α and a homogeneous strain defined by four coefficients β_{ij}, the displacements can be written as

$$x_1 = (1-\alpha)[(1+\beta_{11})a_1 + \beta_{12}a_2]$$
$$x_2 = (1-\alpha)[(1+\beta_{22})a_2 + \beta_{21}a_1]$$

Ignoring higher order terms of β_{ij}, the ratio of the unstrained area and strained area is

$$A_0/A = (1-\beta_{11}-\beta_{22})/(1-\alpha)^2$$

Using Eulerian strain, where the strained coordinates are taken to be independent, the strain components are defined as

$$\varepsilon_{ij} = \delta_{ij}\varepsilon + \beta_{ij}(1-2\varepsilon)$$

where $(1-\alpha)^2 = (1-2\varepsilon)^{-1}$.

Using the free energy defined in terms of the elastic constants

$$E = \rho_0\phi = \frac{1}{2}c_{ij}\varepsilon_i\varepsilon_j$$

and the definition for stress

$$T_{ij} = \rho \left(\frac{\partial \phi}{\partial \varepsilon_{ij}} - 2\varepsilon_{ik} \frac{\partial \phi}{\partial \varepsilon_{kj}} \right)$$

under the condition of a hydrostatic strain, an expression for the hydrostatic in-plane pressure is found

$$\mathcal{F} = B_1\,\varepsilon + B_2\,\varepsilon^2 + B_3\,\varepsilon^4 + \cdots + B_n\,\varepsilon^n$$

where $\varepsilon = \frac{1}{2}(1 - A_0/A)$ and the coefficients contain elastic constants of various orders.

These coefficients are determined by using the following relations for the layer modulus, the first in-pressure derivative of the layer modulus and the second derivative of the layer modulus

$$\gamma = -A\frac{\partial \mathcal{F}}{\partial A} \quad \gamma' = \frac{\partial \gamma}{\partial \mathcal{F}} \quad \gamma'' = \frac{\partial \gamma'}{\partial \mathcal{F}}$$

Keeping only up to the cubic term in ε yields the following 2D equation of state that relates the in-plane pressure to the surface area

$$\mathcal{F}(A) = -2\,\gamma_0 \left[\epsilon + (1 - \gamma_0')\,\epsilon^2 + \frac{2}{3}\left((1 - \gamma_0')(2 - \gamma_0') + \gamma_0\,\gamma_0'' \right)\,\epsilon^3 \right], \tag{A.1}$$

where A_0, γ_0, γ_0' and γ_0'' are the equilibrium values for the unit cell area, layer modulus, the force per unit length derivative and second derivative of the layer modulus at $\mathcal{F} = 0$.

These parameters define the response of the layer modulus to in-plane pressure where

$$\gamma(\mathcal{F}) = \gamma_0 + \gamma_0'\,\mathcal{F} + \frac{1}{2}\,\gamma_0''\,\mathcal{F}^2. \tag{A.2}$$

Using the fact that

$$\mathcal{F} = -\frac{\partial E}{\partial A}$$

and integrating Eqn. A.1, the following energy equation of state is obtained

$$E(A) = E_0 + 4\,A_0\,\gamma_0 \left[\frac{1}{2}\,\epsilon^2 + \frac{1}{3}(5 - \gamma_0')\,\epsilon^3 + \frac{1}{6}\left((1 - \gamma_0')\,(8 - \gamma_0') + \gamma_0\,\gamma_0'' + 18 \right)\,\epsilon^4 \right].$$

References

[1] Arthur Holmes. *PRINCIPLES OF PHYSICAL GEOLOGY*. Thomas Nelson and sons LTD, 1944. [1]

[2] Dieter H Hofmann and Matthias H Müller. Prospects of the use of liquid phase techniques for the growth of bulk silicon carbide crystals. *Materials Science and Engineering: B*, 61-62:29, July 1999. [2]

[3] M. W. Dashiell, L. V. Kulik, D. Hits, J. Kolodzey, and G. Watson. Carbon incorporation in $Si_{1-y}C_y$ alloys grown by molecular beam epitaxy using a single silicon-graphite source. *Applied Physics Letters*, 72(7):833, 1998. [2]

[4] K Eberl, K Brunner, and W Winter. Pseudomorphic $Si_{1-y}C_y$ and $Si_{1-x-y}Ge_xC_y$ alloy layers on Si. *Thin Solid Films*, 294:98–104, 1997. [2, 13]

[5] K H Chung, J C Sturm, E Sanchez, K K Singh, and S Kuppurao. The high growth rate of epitaxial silicon-carbon alloys by using chemical vapour deposition and neopentasilane. *Semiconductor Science and Technology*, 22(1):S158, January 2007. [2]

[6] Matthew P Grumbach and Richard M Martin. PHASE DIAGRAM OF CARBON AT HIGH PRESSURE : ANALOGY TO SILICON. *Solid State Communications*, 100(2): 61–65, 1996. [3, 46]

[7] Michael J Bucknum and Roald Hoffmann. A Hypothetical Dense 3, 4-Connected Carbon Net and Related B_2C and CN_2 Nets Built from 1, 4-Cyclohexadienoid Units. *J. Am. Chem. Soc.*, 116:11456, 1994. [4, 14, 72, 81, 108]

[8] Lifang Xu, Zhisheng Zhao, Li min Wang, Bo Xu, Julong He, Zhongyuan Liu, and Yongjun Tian. Prediction of a Three-Dimensional Conductive Superhard Material : Diamond-like BC_2. *J. Phys. Chem. C*, 114:22688–22690, 2010. [4, 108, 126]

[9] K S Novoselov, a K Geim, S V Morozov, D Jiang, Y Zhang, S V Dubonos, I V Grigorieva, and A A Firsov. Electric field effect in atomically thin carbon films. *Science*, 306:666, October 2004. ISSN 1095-9203. doi: 10.1126/science.1102896. URL `http://www.ncbi.nlm.nih.gov/pubmed/15499015`. [4, 14, 143]

[10] M T Yin and Marvin L Cohen. Microscopic Theory of the Phase Transformation and Lattice Dynamics of Si. *Physical Review Letters*, 45(12):1004–1007, 1980. [6]

[11] S Minomura and H G Drickamer. PRESSURE INDUCED PHASE TRANSITIONS IN SILICON, GERMANIUM AND SOME III-V COMPOUNDS. *J Phys Chem Solids*, 23: 451–456, 1962. [6]

[12] John C Jamieson. Crystal Structures at High Pressures of Metallic Modifications of Silicon and Germanium. *Science*, 139(3556):762, 1963. [6]

[13] H Olijnyk, S K Sikka, and W B Holzapfel. Structural phase transitions in Si and Ge under pressure up to 50 Gpa. *Physics Letters*, 103(3):1–4, 1984. [6, 7, 8]

[14] M T Yin and Marvin L Cohen. Theory of static structural properties, crystal stability, and phase transformations: Applications to Si and Ge. *Physical Review B*, 26(10):5668–5687, 1982. [7]

[15] R H Wentorf and J S Kasper. Two New Forms of Silicon. *Science*, 139(3552):338, 1963. [7, 65]

[16] A K McMahan and John A Moriarty. Structural phase stability in third-period simple metals. *Physical Review B*, 27(6):3235–3251, 1983. [7]

[17] John A Moriarty. Density-functional formulation of the generalized pseudopotential theory. *Physical Review B*, 16(6):2537, 1977. [7]

[18] O K Andersen. Linear method in band theory. *Physical Review B*, 12(8):3060, 1975. [7]

[19] Richard J Needs and Richard M Martin. Transition from β-tin to simple hexagonal silicon under pressure. *Physical Review B*, 30(9):5390, 1984. [8]

[20] Steven J Duclos, Yogesh K Vohra, and Arthur L Ruoff. hcp-to-fcc Transition in Silicon at 78 GPa and Studies to 100 GPa. *Physical Review Letters*, 58(8):775, 1987. [8]

[21] Rana Biswas, Richard M Martin, R J Needs, and O H Nielsen. Complex tetrahedral structures of silicon and carbon under pressure. *Physical Review B*, 30(6):3210–3213, 1984. [8, 58]

[22] M T Yin. Si-III (BC-8) crystal phase of Si and C: Structural properties, phase stabilities, and phase transitions. *Physical Review B*, 30(4):1773–1776, 1984. [8]

[23] Jing Zhu Hu, Larry D Merkle, Carmen S Menoni, and Ian L Spain. Crystal data for high-pressure phases of silicon. *Physical Review B*, 34(7):4679–4684, 1986. [8, 68]

[24] M I McMahon and R J Nelmes. New high-pressure phase of Si. *Physical Review B*, 47 (13):8337, 1993. [8]

[25] Steven P Lewis and Marvin L Cohen. Theoretical study of high-pressure orthorhombic silicon. *Physical Review B*, 48(21):16144, 1993. [8]

[26] M I McMahon, R J Nelmes, N G Wright, and D R Allan. Pressure dependence of the Imma phase of silicon. *Physical Review B*, 50(2):739, 1994. [8]

[27] F. P. Bundy and J. S. Kasper. Hexagonal diamond-a new form of carbon. *Journal of Chemical Physics*, 46:3437, 1967. [8]

[28] V. E. Strel'nitskii, V. G. Padalka, and S. I. Vakula. *Sov. Phys. Tech. Phys.*, 23:222, 1978. [8]

[29] N. N. Matyushenko, V. E. Strel'nitskii, and V. A. Gusev. *JETP Lett.*, 30:199, 1979. [8, 72]

[30] R Biswas, Richard M Martin, R J Needs, and O H Nielsen. Stability and electronic properties of complex structures of silicon and carbon under pressure: Density-functional calculations. *Physical Review B*, 35(18):9559, 1987. [8, 65, 72, 78]

[31] Ken-Ichi Kondo. The shock compression and rapid quenching method for exploring new phases of carbon. *Diamond and Related Materials*, 5:13–18, 1996. [8]

[32] Hongliang He, T Sekine, and T Kobayashi. Direct transformation of cubic diamond to hexagonal diamond. *Applied Physics Letters*, 81(4):610–612, 2002. doi: 10.1063/1.1495078. [8]

[33] Quan Li, Yanming Ma, Artem Oganov, Hongbo Wang, Hui Wang, Ying Xu, Tian Cui, Ho-Kwang Mao, and Guangtian Zou. Superhard Monoclinic Polymorph of Carbon. *Physical Review Letters*, 102(17):1–4, April 2009. ISSN 0031-9007. doi: 10.1103/PhysRevLett.102.175506. URL `http://link.aps.org/doi/10.1103/PhysRevLett.102.175506`. [8]

[34] Roy L Johnston and Roald Hoffmann. Superdense Carbon , C8 : Supercubane or Analogue of γ-Si? *J. Am. Chem. Soc.*, 111:810, 1989. [8]

[35] Koichiro Umemoto, Renata M Wentzcovitch, Susumu Saito, and Takashi Miyake. Body-Centered Tetragonal C_4: A Viable sp^3 Carbon Allotrope. *Physical Review Letters*, 104 (12):125504, March 2010. ISSN 0031-9007. doi: 10.1103/PhysRevLett.104.125504. URL `http://link.aps.org/doi/10.1103/PhysRevLett.104.125504`. [8, 72, 80]

[36] Xiang-Feng Zhou, Guang-Rui Qian, Xiao Dong, Lixin Zhang, Yongjun Tian, and Hui-Tian Wang. Ab initio study of the formation of transparent carbon under pressure. *Physical Review B*, 82(13):1–5, October 2010. ISSN 1098-0121. doi: 10.1103/PhysRevB.82.134126. URL `http://link.aps.org/doi/10.1103/PhysRevB.82.134126`. [8]

[37] A Jayaraman. Diamond anvil cell and high-pressure physical investigations. *Reviews of Modern Physics*, 55(1):65–108, 1983. [8]

[38] M T Yin and Marvin L Cohen. Will diamond transform under Megabar Pressures? *Physical Review Letters*, 50(25):2006–2009, 1983. [8]

[39] S Fahy and Steven G Louie. High-pressure structural and electronic properties of carbon. *Physical Review B*, 36(6):3373–3385, 1987. [8]

[40] Matthew P Grumbach and Richard M Martin. Phase diagram of carbon at high pressures and temperatures. *Physical review B*, 54(22):15730–15741, December 1996. ISSN 0163-1829. [9]

[41] Xiaofei Wang, Sandro Scandolo, and Roberto Car. Carbon Phase Diagram from Ab Initio Molecular Dynamics. *Physical Review Letters*, 95:185701, 2005. doi: 10.1103/PhysRevLett.95.185701. [9, 45]

[42] Neville Churcher, Karel Kunc, and Volker Heine. GROUND STATE PROPERTIES OF THE GROUP IV IONIC COMPOUND SILICON CARBIDE. *Solid state communications*, 56(2):177, 1985. [9]

[43] P J H Denteneer and Van W Haeringen. Ground-state properties of polytypes of silicon carbide. *Physical Review B*, 33(4):2831, 1986. [9]

[44] P J H Denteneer and Van W Haeringen. Ground-state properties of wurtzite silicon carbide. *Solid state communications*, 65(2):115–119, 1988. [9]

[45] K J Chang and Marvin L Cohen. Ab initio pseudopotential study of structural and high-pressure properties of SiC. *Physical Review B*, 35(15):8196–8201, 1987. [10, 12, 99]

[46] Minoru Yoshida, Akifumi Onodera, Masaki Ueno, Kenichi Takemura, and Osamu Shimomura. Pressure-induced phase transition in SiC. *Physical Review B*, 48(14):10587–10590, 1993. [10, 99]

[47] W R L Lambrecht, B Segall, M Methfessel, and M Van Schilfgaarde. Calculated elastic constants and deformation potentials of cubic SiC. *Physical Review B*, 44(8):3685, 1991. [10]

[48] C H Park, Byoung-Ho Cheong, Keun-Ho Lee, and K J Chang. Structural and electronic properties of cubic, 2H, 4H and 6H SiC. *Physical Review B*, 49(7):4485–4493, 1994. [10, 94]

[49] P Käckell, B Wenzien, and F Bechstedt. Electronic properties of cubic and hexagonal SiC polytypes from ab initio calculations. *Physical Review B*, 50(15):10761–10768, 1994. [10]

[50] P Käckell, B Wenzien, and F Bechstedt. Influence of atomic relaxations on the structural properties of SiC polytypes from ab initio calculations. *Physical Review B*, 50(23):17037, 1994. [10]

[51] M Hofmann, A Zywietz, K Karch, and F Bechstedt. Lattice dynamics of SiC polytypes within the bond-charge model. *Physical Review B*, 50(18):13401, 1994. [11]

[52] K Karch, P Pavone, W Windl, O Schütt, and D Strauch. Ab initio calculation of structural and lattice-dynamical properties of silicon carbide. *Physical Review B*, 50(23):17054, 1994. [11]

[53] K Karch, F Bechstedt, P Pavone, and D Strauch. Pressure-dependent properties of SiC polytypes. *Physical Review B*, 53(20):13400–13413, May 1996. ISSN 0163-1829. [11, 46, 94, 98, 99]

[54] K Karch, F Bechstedt, P Pavone, and D Strauch. Pressure-dependent dynamical and dielectric properties of cubic SiC. *J Phys Condens Matter*, 8:2945–2955, 1996. [11]

[55] F Bechstedt, P Käckell, A Zywietz, K Karch, B Adolph, K Tenelsen, and J Furthmüller. Polytypism and Properties of Silicon Carbide. *Physica Status Solidi (B)*, 202:35, 1997. [12]

[56] P Käckell, J Furthmüller, and F Bechstedt. Stacking faults in group-IV crystals : An ab initio study. *Physical Review B*, 58(3):1326, 1998. [12]

[57] Ulf Lindefelt, Hisaomi Iwata, Sven Oberg, and Patrick R Briddon. Stacking faults in 3C- , 4H- , and 6H-SiC polytypes investigated by an ab initio supercell method. *Physical Review B*, 67:155204, 2003. doi: 10.1103/PhysRevB.67.155204. [12]

[58] J Pollmann, K Peter, and M Sabisch. Atomic and Electronic Structure of SiC Surfaces from ab-initio Calculations. *Physica Status Solidi (B)*, 202:421, 1997. [12]

[59] Jakub Kedzierski, Pei lan Hsu, Paul Healey, Peter W Wyatt, Craig L Keast, Mike Sprinkle, Claire Berger, and Walt A de Heer. Epitaxial Graphene Transistors on SiC Substrates. *IEEE Transactions on Electron Devices*, 55(8):2078, 2008. [12]

[60] J B Posthill, R A Rudder, S V Hattangady, G G Fountain, and R J Markunas. On the feasibility of growing dilute C_xSi_{x-1} epitaxial alloys. *Applied Physics Letters*, 56(8):734, 1990. [13]

[61] Richard A Soref. Optical band gap of the ternary semiconductor $Si_{1-x-y}Ge_xC_y$. *Journal of Applied Physics*, 70(4):2470, 1991. [13]

[62] Alexander A Demkov and Otto F Sankey. Theoretical investigation of random Si-C alloys. *Physical Review B*, 48(4):2207–2214, 1993. [13]

[63] H Rücker, M Methfessel, E Bugiel, and H J Osten. Strain-Stabilized Highly Concentrated Pseudomorphic $Si_{1-x}C_x$ Layers in Si. *Physical Review Letters*, 72(22):3578, 1994. [13]

[64] S Knief and Von Wolfgang Niessen. The electronic structure of amorphous silicon-carbon alloys. *Journal of Non-Crystalline Solids*, 255(2-3):242–249, October 1999. ISSN 00223093. doi: 10.1016/S0022-3093(99)00416-0. URL `http://linkinghub.elsevier.com/retrieve/pii/S0022309399004160`. [13]

[65] Tsung yang Liow, Student Member, Kian ming Tan, Doran Weeks, Rinus Tek, Po Lee, Ming Zhu, Keat mun Hoe, Chih hang Tung, Senior Member, Matthias Bauer, Jennifer Spear, Shawn G Thomas, Ganesh S Samudra, N Balasubramanian, and Yee chia Yeo. Strained n-Channel FinFETs Featuring In Situ Doped Silicon-Carbon ($Si_{1y}C_y$) Source and Drain Stressors With High Carbon Content. *IEEE Transactions on Electron Devices*, 55(9):2475–2483, 2008. [13]

[66] Fabio Finocchi, Giulia Galli, Michele Parrinello, and Carlo M Bertoni. Microscopic Structure of Amorphous Covalent Alloys Probed by Ab Initio Molecular Dynamics: SiC. *Physical Review Letters*, 68(20):3044, 1992. [13]

[67] Fabio Finocchi, Giulia Galli, Michele Parrinello, and Carlo M Bertoni. Chemical order in amorphous covalent alloys. *Physica B*, 185:379–383, 1993. [13]

[68] V.I. Ivashchenko and V.I. Shevchenko. Effects of short-range disorder upon electronic properties of a-SiC alloys. *Applied Surface Science*, 184(1-4):137–143, December

2001. ISSN 01694332. doi: 10.1016/S0169-4332(01)00671-7. URL http://linkinghub.elsevier.com/retrieve/pii/S0169433201006717. [13]

[69] P Kelires. Total-energy and entropy considerations as a probe of chemical order in amorphous silicon carbide. *Journal of Non-Crystalline Solids*, 231(1-2):200–204, July 1998. ISSN 00223093. doi: 10.1016/S0022-3093(98)00539-0. URL http://linkinghub.elsevier.com/retrieve/pii/S0022309398005390. [13]

[70] A Chehaidar, A Zwick, and R Carles. Investigation of structural and chemical ordering in Si-rich amorphous SiC alloys via Raman spectroscopy. *J Phys Condens Matter*, 13: 10743–10755, 2001. [13]

[71] Prachi Pradhan and Asok K Ray. A density functional study of the structures and energetics of small hetero-atomic silicon–carbon nanoclusters. *Journal of Molecular Structure: THEOCHEM*, 716(1-3):109–130, March 2005. ISSN 01661280. doi: 10.1016/j.theochem.2004.11.019. URL http://linkinghub.elsevier.com/retrieve/pii/S0166128004008899. [13]

[72] H Wang, W Lu, J Sun, Z Li, and C Sun. Theoretical investigation on the structures of silicon and carbon hetero clusters. *Chemical Physics Letters*, 423(1-3):87–93, May 2006. ISSN 00092614. doi: 10.1016/j.cplett.2006.03.031. URL http://linkinghub.elsevier.com/retrieve/pii/S0009261406003800. [13]

[73] B Agrawal, P Yadav, R Yadav, and S Agrawal. Ab initio theoretical study of SiC microclusters. *Progress in Crystal Growth and Characterization of Materials*, 52(1-2):15–20, March 2006. ISSN 09608974. doi: 10.1016/j.pcrysgrow.2006.03.003. URL http://linkinghub.elsevier.com/retrieve/pii/S0960897406000040. [13]

[74] P Yadav, R Yadav, S Agrawal, and B Agrawal. Theoretical study of the physical properties of binary SimCn ($m + n \leq 5m + n \leq 5$) clusters: An ab initio study. *Physica E: Low-dimensional Systems and Nanostructures*, 33(1):249–262, June 2006. ISSN 13869477. doi: 10.1016/j.physe.2006.03.132. URL http://linkinghub.elsevier.com/retrieve/pii/S1386947706002608. [13]

[75] Michael J Bucknum, Andrea Ienco, and Eduardo A Castro. Electronic structure and bulk modulus of silicon dicarbide: a glitter phase. *Journal of Molecular Structure: THEOCHEM*, 716:73, March 2005. ISSN 01661280. doi: 10.1016/j.theochem.2004.10.066. [14, 122, 129]

[76] Marvin L Cohen. PREDICTING PROPERTIES AND NEW MATERIALS. *Solid state communications*, 92:45–52, 1994. [14, 129]

[77] Daniel Sanchez-Portal, Emilio Artacho, Jose M Soler, Angel Rubio, and Pablo Ordejon. Ab initio structural , elastic , and vibrational properties of carbon nanotubes. *Physical Review B*, 59(19):12678, 1999. [14]

[78] C Thomsen, S Reich, and P Ordejon. Ab initio determination of the phonon deformation potentials of graphene. *Physical Review*, 65:073403, 2002. doi: 10.1103/PhysRevB.65.073403. [14]

[79] Nicolas Mounet and Nicola Marzari. First-principles determination of the structural, vibrational and thermodynamic properties of diamond, graphite, and derivatives. *Physical Review B*, 71:205214, 2005. doi: 10.1103/PhysRevB.71.205214. [14]

[80] Vibhor Singh, Shamashis Sengupta, Hari S Solanki, Rohan Dhall, Adrien Allain, Sajal Dhara, Prita Pant, and Mandar Deshmukh. Probing thermal expansion of graphene and modal dispersion at low-temperature using graphene nanoelectromechanical systems resonators. *Nanotechnology*, 21:165204, 2010. doi: 10.1088/0957-4484/21/16/165204. [14]

[81] K H Michel and B Verberck. Theory of the evolution of phonon spectra and elastic constants from graphene to graphite. *Physical Review B*, 78:085424, 2008. doi: 10.1103/PhysRevB.78.085424. [14, 15, 143, 147]

[82] K H Michel and B Verberck. Theory of the elastic constants of graphite and graphene. *Physica Status Solidi (B)*, 245(10):2177, 2008. doi: 10.1002/pssb.200879604. [14]

[83] C Lee, X Wei, J. W Kysar, and J Hone. Measurement of the elastic properties and intrinsic strength of monolayer graphene. *Science*, 321(5887):385, July 2008. ISSN 1095-9203. doi:

10.1126/science.1157996. URL http://www.ncbi.nlm.nih.gov/pubmed/18635798. [14, 143, 158]

[84] H Şahin, S Cahangirov, M Topsakal, E Bekaroglu, E Akturk, R T Senger, and S Ciraci. Monolayer honeycomb structures of group-IV elements and III-V binary compounds : First-principles calculations. *Physical Review B*, 80:155453, 2009. doi: 10.1103/PhysRevB.80.155453. [14, 143, 148, 156, 158]

[85] Paolo Giannozzi. *Metodi Numerici in Struttura Elettronica*. 2010. lecture notes. [16]

[86] Richard M Martin. *Electronic Structure: Basic Theory and Practical Methods*, chapter 3, page 63. Cambridge University Press, 2004. [18]

[87] Richard M Martin. *Electronic Structure: Basic Theory and Practical Methods*, chapter 3, page 64. Cambridge University Press, 2004. [18]

[88] P Hohenberg and W Kohn. Inhomogeneous Electron Gas. *Physical Review*, 136(3B):864, 1964. [20, 147]

[89] Richard M Martin. *Electronic Structure: Basic Theory and Practical Methods*, chapter 6, pages 122–124. Cambridge University Press, 2004. [20]

[90] W Kohn and L J Sham. Self-Consistent Equations Including Exchange and Correlation Effects. *Physical Review B*, 140(4A):A1133, 1965. [22]

[91] Richard M Martin. *Electronic Structure: Basic Theory and Practical Methods*, chapter 7, pages 137–138. Cambridge University Press, 2004. [22]

[92] Richard M Martin. *Electronic Structure: Basic Theory and Practical Methods*, chapter 8, page 153. Cambridge University Press, 2004. [23]

[93] Richard M Martin. *Electronic Structure: Basic Theory and Practical Methods*, chapter 5, page 106. Cambridge University Press, 2004. [23]

[94] J P Perdew and A Zunger. Self-interaction correction to density-functional approximations for many-electron systems. *Physical Review B*, 23(10):5048, 1981. [24]

[95] D M Ceperley and B J Alder. Ground State of the Electron Gas by a Stochastic Method. *Physical Review Letters*, 45(7):566, 1980. [24]

[96] John P Perdew, Kieron Burke, and Matthias Ernzerhof. Generalized Gradient Approximation Made Simple. *Physical Review Letters*, (3):3865–3868, 1996. [24, 147]

[97] John P Perdew, Adrienn Ruzsinszky, Gábor I Csonka, Oleg A Vydrov, Gustavo E Scuseria, Lucian A Constantin, Xiaolan Zhou, and Kieron Burke. Restoring the Density-Gradient Expansion for Exchange in Solids and Surfaces. *Physical Review Letters*, 100: 136406, April 2008. ISSN 0031-9007. doi: 10.1103/PhysRevLett.100.136406. [25, 44]

[98] R Armiento and A E Mattsson. Functional designed to include surface effects in self-consistent density functional theory. *Physical Review B*, 72(8):085108, August 2005. ISSN 1098-0121. doi: 10.1103/PhysRevB.72.085108. URL `http://link.aps.org/doi/10.1103/PhysRevB.72.085108`. [25]

[99] Ann E Mattsson, Rickard Armiento, Joachim Paier, Georg Kresse, John M Wills, and Thomas R Mattsson. The AM05 density functional applied to solids. *The Journal of chemical physics*, 128(8):084714, March 2008. ISSN 0021-9606. doi: 10.1063/1.2835596. URL `http://www.ncbi.nlm.nih.gov/pubmed/18315079`. [25]

[100] Richard M Martin. *Electronic Structure: Basic Theory and Practical Methods*, chapter 9, page 173. Cambridge University Press, 2004. [26]

[101] G Kresse and J Furthmuller. Efficiency of ab-initio total energy calculations for metals and semiconductors using a plane-wave basis set. *Computational Materials Science*, 6: 15–50, 1996. [25, 39, 44, 147]

[102] Paolo Giannozzi, Stefano Baroni, Nicola Bonini, Matteo Calandra, Roberto Car, Carlo Cavazzoni, Davide Ceresoli, Guido L Chiarotti, Matteo Cococcioni, Ismaila Dabo, Andrea Dal Corso, Stefano de Gironcoli, Stefano Fabris, Guido Fratesi, Ralph Gebauer, Uwe Gerstmann, Christos Gougoussis, Anton Kokalj, Michele Lazzeri, Layla Martin-Samos, Nicola Marzari, Francesco Mauri, Riccardo Mazzarello, Stefano Paolini, Alfredo Pasquarello, Lorenzo Paulatto, Carlo Sbraccia, Sandro Scandolo, Gabriele

Sclauzero, Ari P Seitsonen, Alexander Smogunov, Paolo Umari, and Renata M Wentzcovitch. QUANTUM ESPRESSO: a modular and open-source software project for quantum simulations of materials. *Journal of Physics: Condensed Matter*, 21 (39):395502, September 2009. ISSN 0953-8984. doi: 10.1088/0953-8984/21/39/395502. URL `http://stacks.iop.org/0953-8984/21/i=39/a=395502?key=crossref.c21336c286fa6d3db893262ae3f6e151`. [25, 44]

[103] Neil W. Ashcroft and N. David Mermin. *Solid State Physics*, pages 762–763. Thomson Learning Inc., 1976. [25]

[104] M C Payne, M P Teter, D C Allan, T A Arias, and J D Joannopoulos. Iterative minimization techniques for ab initio total-energy calculations: molecular dynamics and conjugate gradients. *Reviews of Modern Physics*, 64(4):1045, 1992. [27, 30]

[105] Hendrik J Monkhorst and James D Pack. Special points for Brillouin-zone integration. *Physical Review B*, 13(12):5188, 1976. [28, 147]

[106] Peter E Blöchl, O Jepsen, and O K Andersen. Improved tetrahedron method for Brillouin-zone integrations. *Physical Review B*, 49(23):16223, 1994. [28]

[107] M Methfessel and A T Paxton. High-precision sampling for Brillouin-zone integration in metals. *Physical Review B*, 40(6):3616, 1989. [28]

[108] Richard M Martin. *Electronic Structure: Basic Theory and Practical Methods*, chapter 11, page 213. Cambridge University Press, 2004. [29]

[109] G B Bachelet, D R Hamann, and M Schluter. Pseudopotentials that work: H to Pu. *Physical Review B*, 26(8):4199, 1982. [30]

[110] David Vanderbilt. Optimally smooth norm-conserving pseudopotentials. *Physical Review B*, 32(12):8412, 1985. [30]

[111] N Troullier and Luis Jose Martins. Efficient pseudopotentials for plane-wave calculations. *Physical Review B*, 43(3):1993, 1991. [30]

[112] Leonard Kleinman and D M Bylander. Physical review letters 17. *Physical Review B*, 48: 1425, 1982. [30]

[113] P E Blöchl. Projector augmented-wave method. *Physical Review B*, 50(24):17953, 1994. [30, 147]

[114] R P Feynman. Forces in molecules. *Physical Review*, 56:340, 1939. [33]

[115] J D Renton. *Applied Elasticity: Matrix and Tensor Analysis of Elastic Continua*. Horwood Pub Ltd, 2003. ISBN 1-898563-85-3. [34]

[116] Open - No copyright-accessed Nov 2011, . URL `http://en.wikipedia.org/wiki/File:2D_geometric_strain.svg#file`. [35]

[117] Attribution-ShareAlike 3.0 Unported (CC BY-SA 3.0) License-accessed Nov 2011, . URL `http://en.wikipedia.org/wiki/File:Stress_in_a_continuum.svg#file`. [37]

[118] O H Nielsen and Richard M Martin. First-Principles Calculation of Stress. *Physical Review Letters*, 50(9):697, 1983. [36]

[119] P C Waterman. Orientation Dependence of Elastic Waves in Single Crystals. *Physical Review*, 113:1240, 1959. [37]

[120] Yvon Le Page and Paul Saxe. Symmetry-general least-squares extraction of elastic data for strained materials from ab initio calculations of stress. *Physical Review B*, 65:104104, February 2002. ISSN 0163-1829. doi: 10.1103/PhysRevB.65.104104. [39, 44, 148, 156]

[121] R. Hill. The elastic behaviour of a crystalline aggregate. *Proceedings of the Physical Society, Section A*, 65(5):349, 1952. [39]

[122] O L Anderson. A simplified method for calculating the Debye temperature from elastic constants. *J Phys Chem Solids*, 24:909, November 1963. [40]

[123] Francis Birch. Finite Elastic Strain of Cubic Crystals. *Physical Review*, 71(11):809, 1947. [40, 170]

[124] Richard M Martin. *Electronic Structure: Basic Theory and Practical Methods*, chapter 19, page 388. Cambridge University Press, 2004. [42]

[125] Max Born and Kun Huang. *Dynamical theory of crystal lattices*, chapter IV, pages 173–174. Oxford University Press, 1954. [43]

[126] K Parlinski, Z Q Li, and Y Kawazoe. First-Principles Determination of the Soft Mode in Cubic ZrO_2. *Physical Review Letters*, 78(21):4063–4066, 1997. [44, 148]

[127] S Baroni, S de Gironcoli, A Dal Corso, and P Giannozzi. Phonons and related crystal properties from density-functional perturbation theory. *Rev. Mod. Phys.*, 73:515, 2001. [44]

[128] Gábor I Csonka, John P Perdew, Adrienn Ruzsinszky, Pier H T Philipsen, Sébastien Lebègue, Joachim Paier, Oleg Vydrov, and János Ángyán. Assessing the performance of recent density functionals for bulk solids. *Physical Review B*, 79(15):155107, April 2009. ISSN 1098-0121. doi: 10.1103/PhysRevB.79.155107. [44]

[129] G Kresse and D Joubert. From ultrasoft pseudopotentials to the projector augmented-wave method. *Physical Review B*, 59(3):1758, 1999. [47]

[130] George Kresse, Martijn Marsman, and Jürgen Furthmüler. *VASP the GUIDE*, chapter 7, page 117. 2009. [52]

[131] Georg Kresse. Vasp: Accurate force calculations and vasp dataset. Presentation. [52]

[132] Neil W. Ashcroft and N. David Mermin. *Solid State Physics*, page 566. Thomson Learning Inc., 1976. [55]

[133] Richard M Martin. *Electronic Structure: Basic Theory and Practical Methods*, chapter 2, page 43. Cambridge University Press, 2004. [55]

[134] K J Chang and Marvin L Cohen. Structural and electronic properties of the high-pressure hexagonal phases of Si. *Physical Review B*, 30(9):5376, 1984. [60]

[135] Charles Kittel. *Introduction to Solid State Physics*. University of California, Berkeley, 2004. [64, 80]

[136] R G Hennig, A Wadehra, K P Driver, W D Parker, C J Umrigar, and J W Wilkins. Phase transformation in Si from semiconducting diamond to metallic β-Sn phase in QMC and DFT under hydrostatic and anisotropic stress. *Physical Review B*, 82(1):014101, July 2010. ISSN 1098-0121. doi: 10.1103/PhysRevB.82.014101. URL `http://link.aps.org/doi/10.1103/PhysRevB.82.014101`. [64]

[137] Steven J Duclos, Yogesh K Vohra, and Arthur L Ruoff. Experimental study of the crystal stability and equation of state of Si to 248 GPa. *Physical Review B*, 41(17):12021, 1990. [68]

[138] H J McSkimin. Measurement of the Elastic Constants of Silicon Single Crystals and Their Thermal Coefficients. *J. Acoust. Soc. Am.*, 22:413, 1950. [68]

[139] B Winkler. Structure and properties of supercubane from density functional calculations. *Chemical Physics Letters*, 293(3-4):284–288, August 1998. ISSN 00092614. doi: 10.1016/S0009-2614(98)00762-3. URL `http://linkinghub.elsevier.com/retrieve/pii/S0009261498007623`. [80]

[140] R Vogelgesang, A K Ramdas, S Rodriguez, M Grimsditch, and T R Anthony. Brillouin and Raman scattering in natural and isotopically controlled diamond. *Physical Review B*, 54(6):3989, 1996. [81, 86]

[141] M Hanfland, H Beister, and K Syassen. Graphite under pressure: Equation of state and first-order Raman modes. *Physical Review B*, 39(17):12598, 1989. [83, 90, 106, 145]

[142] Alexey Bosak, Michael Krisch, Marcel Mohr, Janina Maultzsch, and Christian Thomsen. Elasticity of single-crystalline graphite: Inelastic x-ray scattering study. *Physical Review B*, 75(15):153408, April 2007. ISSN 1098-0121. doi: 10.1103/PhysRevB.75.153408. URL `http://link.aps.org/doi/10.1103/PhysRevB.75.153408`. [90, 91, 157, 158]

[143] H J F Jansen and A J Freeman. Structural and electronic properties of graphite via an all-electron total-energy local-density approach. *Physical Review B*, 35(15):8207–8214, 1987. [91]

[144] Zhenyi Jiang, Xiaohong Xu, Haishun Wu, Fuqiang Zhang, and Zhihao Jin. Ab initio calculation of SiC polytypes. *Solid State Communications*, 123(6-7):263, August 2002. ISSN 00381098. doi: 10.1016/S0038-1098(02)00307-1. URL `http://linkinghub.elsevier.com/retrieve/pii/S0038109802003071`. [99]

[145] Sandro Sorella, Michele Casula, Leonardo Spanu, and Andrea Dal Corso. Ab initio calculations for the β-tin diamond transition in silicon: Comparing theories with experiments. *Physical Review B*, 83(7):075119, February 2011. ISSN 1098-0121. doi: 10.1103/PhysRevB.83.075119. URL `http://link.aps.org/doi/10.1103/PhysRevB.83.075119`. [101]

[146] K Kamitani, M Grimsditch, J C Nipko, C Loong, M Okada, and I Kimura. The elastic constants of silicon carbide : A Brillouin-scattering study of 4H and 6H SiC single crystals. *J. Appl. Phys.*, 82(6):3152, 2001. [101]

[147] R C Andrew, M Braun, and N Chetty. A theoretical investigation of the stability of crystalline silicon dicarbide. *Computational Materials Science*, 55:186, April 2012. ISSN 09270256. doi: 10.1016/j.commatsci.2011.10.040. URL `http://linkinghub.elsevier.com/retrieve/pii/S0927025611006112`. [107]

[148] Y.C. Ding, A.P. Xiang, X.J. He, and X.F. Hu. Structural, elastic constants, hardness, and optical properties of pyrite-type dinitrides (CN_2, SiN_2, GeN_2). *Physica B: Condensed Matter*, 406(8):1357–1362, April 2011. ISSN 09214526. doi: 10.1016/j.physb.2011.01.003. URL `http://linkinghub.elsevier.com/retrieve/pii/S0921452611000159`. [110]

[149] S F Pugh. Relations between the Elastic Moduli and the Plastic Properties of Polycrystalline Pure Metals. 45(367), 1954. [129]

[150] R C Andrew, R E Mapasha, A M Ukpong, and N Chetty. Mechanical properties of graphene and boronitrene. *Physical Review B*, 85(12):125428, March 2012. ISSN 1098-0121. doi: 10.1103/PhysRevB.85.125428. URL `http://link.aps.org/doi/10.1103/PhysRevB.85.125428`. [143]

[151] K S Novoselov, D Jiang, F Schedin, T J Booth, V V Khotkevich, S V Morozov, and A K Geim. Two-dimensional atomic crystals. *PNAS*, 102(30):10451, 2005. [143]

[152] Li Song, Lijie Ci, Hao Lu, Pavel B Sorokin, Chuanhong Jin, Jie Ni, Alexander G Kvashnin, Dmitry G Kvashnin, Jun Lou, Boris I Yakobson, and Pulickel M Ajayan. Large Scale Growth and Characterization of Atomic Hexagonal Boron Nitride Layers. *Nano letters*, 10:3209, 2010. doi: 10.1021/nl1022139. [143]

[153] K. H. Michel and B. Verberck. Theory of elastic and piezoelectric effects in two-dimensional hexagonal boron nitride. *Physical Review B*, 80:224301, December 2009. ISSN 1098-0121. doi: 10.1103/PhysRevB.80.224301. URL `http://link.aps.org/doi/10.1103/PhysRevB.80.224301`. [143]

[154] V H Crespi, L X Benedict, Marvin L Cohen, and Steven G Louie. Prediction of a pure-carbon planar covalent metal. *Physical Review B*, 53(20):R13303, May 1996. ISSN 0163-1829. URL `http://www.ncbi.nlm.nih.gov/pubmed/9983172`. [144, 148]

[155] H Terrones, M Terrones, E Hernández, N Grobert, J-C Charlier, and P M Ajayan. New Metallic Allotropes of Planar and Tubular Carbon. *Physical Review Letters*, 84(8):1716, 2000. [144]

[156] M Deza, P W Fowler, M Shtogrin, and K Vietze. Pentaheptite Modifications of the Graphite Sheet. *J. Chem. Inf. Comput. Sci.*, 40:1325, 2000. [144]

[157] Andrey N Enyashin and Alexander L Ivanovskii. Graphene allotropes. *Physica Status Solidi (B)*, 248(8):1879, January 2011. ISSN 03701972. doi: 10.1002/pssb.201046583. URL `http://doi.wiley.com/10.1002/pssb.201046583`. [144, 148, 150]

[158] Sergej Kakorin, Thomas Liese, and Eberhard Neumann. Membrane Curvature and High-Field Electroporation of Lipid Bilayer Vesicles. *J. Phys. Chem. B*, 107:10243, 2003. [144]

[159] Yafei Li, Fengyu Li, Zhen Zhou, and Zhongfang Chen. SiC_2 Silagraphene and Its One-Dimensional Derivatives : Where Planar Tetracoordinate Silicon Happens. *Journal of the American Chemical Society*, 133:900, 2011. [144, 150, 156]

[160] Michael M Haley, Stephen C Brand, and Joshua J Pak. Carbon Networks Based on Dehydrobenzoannulenes: Synthesis of Graphdiyne Substructures. *Angewandte Chemie*, 36(8):835–838, 1997. [150]

[161] Nobuo Narita, Sumiaki Nagai, Shugo Suzuki, and Kenji Nakao. Optimized geometries and electronic structures of graphyne and its family. *Physical Review B*, 58(16):11009, 1998. [150]

[162] Guoxing Li, Yuliang Li, Huibiao Liu, Yanbing Guo, Yongjun Li, and Daoben Zhu. Architecture of graphdiyne nanoscale films. *Chemical communications (Cambridge, England)*, 46(19):3256, May 2010. ISSN 1364-548X. doi: 10.1039/b922733d. URL `http://www.ncbi.nlm.nih.gov/pubmed/20442882`. [150]

[163] X Wei, B Fragneaud, C.A Marianetti, and J. W. Kysar. Nonlinear elastic behavior of graphene: Ab initio calculations to continuum description. *Physical Review B*, 80(20): 205407, November 2009. ISSN 1098-0121. doi: 10.1103/PhysRevB.80.205407. URL `http://link.aps.org/doi/10.1103/PhysRevB.80.205407`. [157, 158]

[164] Huili Zhang and Rui Wang. The stability and the nonlinear elasticity of 2D hexagonal structures of Si and Ge from first-principles calculations. *Physica B: Condensed Matter*, 406(21):4080, November 2011. ISSN 09214526. doi: 10.1016/j.physb.2011.07.052. URL `http://linkinghub.elsevier.com/retrieve/pii/S0921452611007290`. [157, 158]